PHYSICAL PRINCIPLES OF MEMBRANE MECHANICS,

MEMBRANE DOMAIN FORMATION, AND CELLULAR

SIGNAL TRANSDUCTION

by

Carlos D. Alas

A Dissertation Presented to the
FACULTY OF THE USC GRADUATE SCHOOL
UNIVERSITY OF SOUTHERN CALIFORNIA
In Partial Fulfillment of the
Requirements for the Degree
DOCTOR OF PHILOSOPHY
(PHYSICS)

December 2023

Acknowledgements

With heartfelt gratitude to those who profoundly influenced my academic journey I give thanks:

I extend a deep appreciative thank you to my father, Vinicio Alas, who, from an early age, taught me about computers, instilled in me a curiosity in math and science, discipline, and encouraged higher education, supporting me throughout childhood and early higher education. My deepest appreciation also goes to my mother, Evelyn Alas, whose resilience during her battle with cancer initiated my existential exploration. This challenging period sparked my interest in philosophy, leading me to trace human knowledge, read and discuss philosophy, and research historical narratives shaping modern perspectives.

applying computational methods to solve problems. She also provided me with a first example on how theorists approach and model phenomena. After working with Tatiana, I knew I belonged in the field of computational and theoretical biophysics. Tatiana also gave me the best advice on the value of a PhD education and educated me on my options after earning a PhD, including gifting me a very valuable book called "A PhD is not enough" by Peter J. Feibelman, which gave me great insight into the journey of a PhD in physics and reasonable expectations for what I could do with my PhD after. Tatiana is also the best lecturer in classical mechanics, and I owe her much gratitude for her very effective style of teaching the fundamentals, which helped me succeed in graduate school.

To   a   few   others:
A heartfelt thanks to Dr. Cheol Park at the Soft Materials Research Center, University of Colorado, Boulder for his support and levity throughout my study of hydrodynamic flow in liquid crystal films. His guidance and encouragement were invaluable in shaping my academic journey.

I give thanks to the Margeat and Doucet labs from the French National Centre for Scientific Research (CNRS) who met with our group to discuss the experimental phenomenology of emerin nanodomain assembly at the nuclear envelope, every other Tuesday morning.

I give thanks to my orange tabby feline friend Jeremy, who has given my wife and I endless joy and inspired us with his deep commitment to studying door mechanics and high-pitched sound waves at wee hours every morning. I often stare at Jeremy's patterned coat of fur and wonder if the pattern comes from a Turing mechanism. Interestingly, a recent study [C. B. Kaelin, K. A. McGowan, and G. S. Barsh. *Nature Communications*,

Armen Tokadjian, a dear friend of mine who I would team up with to tackle difficult courses together, and from time to time meet up with to play billiards and talk about tech.

Marco Olguin, for his technical support in using CARC.

Dr. Krzysztof Pilch, for his role as Faculty Graduate Advisor during my first few years in graduate school, and help in learning about the dual degree program which allowed me to supplement my PhD physics degree electives with courses in computer science for my Master's degree in Computer Science. I also thank him for letting me win in billiards after I was down a hundred dollars :).

Dr. Rosa Di Felice, for her guidance in research during my first year in the PhD program. She taught me a lot about molecular dynamics simulations and Gromacs software for implementing such simulations.

Dr. James Boedicker, for convincing me to join the PhD program at USC, helping me obtain a USC graduate school DIA fellowship which provided me with additional financial support, for all the background tasks he helped me with in his role as my Faculty Graduate Advisor during my latter years in graduate school, and for participating in both my Qualification Exam and PhD Thesis Defense committees.

Dr. Aiichiro Nakano, for his lectures on methods in computational physics, high-performance computation, and other topics in computer science. I really appreciated the structure of his courses, especially in regards to course projects which gave me space to run with my ideas. From these projects, I learned a lot and applied what I learned throughout my thesis work. Aiichiro also gave me great advice on coursework towards

always will continue to capture my imagination. Over the past five years, Christoph has strategically fostered my development into a professional, including guiding me in forming ideas and hypotheses in biophysics, constructing quantitative physical models to describe biological phenomena, writing manuscripts, rebutting peer-reviewers, reporting the progress to our collaborators, reporting our research through presentations at research conferences, mentoring newer students in our lab, recommending me as a peer reviewer to journals, writing grant proposals, and managing my time to meet multiple deadlines. Christoph has also given me crucial advice in regards to choosing a career path after graduate school. It was Christoph who suggested I look into pursuing data science and always encouraged me to take advantage of the physics department's dual degree program to study and earn a Master's degree in Computer Science for technical skills and knowledge that would transfer directly to industry. Even though I know I still have a lot to learn, I have never been more confident in myself as a physicist and professional, and this is largely due to Christoph. I am deeply honored to have had the opportunity to learn from Christoph.

Last of all, but not least, I have to thank the love of my life and best friend, my wife Zhibek Mukhamedina-Alas, who has supported me throughout my PhD journey. Zhibek also worked part-time to help support us all while pursuing her own academic studies. Since meeting Zhibek, she has brought much structure and stability to my life and, in many ways, helped me mature as a person. She is my north star, guiding me and helping me work towards a future for both of us. I'm very grateful to have had her support during this very exciting, challenging, and rewarding journey. This accomplishment is as much hers as it is mine.

Carlos D. Alas

December 2023

Table of Contents

List of Figures

Abstract

Over recent years, a diverse range of experiments have provided much quantitative data on the role of membrane proteins in cellular signal transduction and the adaptation of cells to dynamic environments. Membrane proteins exhibit diverse molecular mechanisms for sensing stimuli, initiating signaling pathways through structural changes, and engaging in collective signaling activities. In particular, protein clustering into domains dedicated to specialized functions provides important mechanisms for cell membrane organization. Furthermore, the perturbation of the lipid bilayer by membrane proteins is thought to play an important role in membrane protein function. This thesis comprises a set of interconnected studies that employ theoretical physics to investigate fundamental aspects of the intricate coupling between membrane proteins and cellular responses to stimuli. Chapter 1 provides a general introduction to cell membranes, membrane proteins, and the diverse functions they serve in cell membranes, and as well as the theory of membrane mechanics. Chapter 2 introduces a novel boundary value method (BVM) that bridges structural biology with membrane elasticity theory, enabling the analytic determination of protein-induced lipid bilayer deformations, even for non-circular protein cross-sections, in

excellent agreement with finite element solutions. Inspired by our BVM, Chapter 3 formulates a simple analytic approximation of the bilayer thickness deformation energy associated with general protein shapes and shows that, for modest deviations from rotational symmetry, this analytic approximation is in good agreement with BVM solutions. The BVM and analytical approximation are utilized to explore how variations in protein shape influence elastic bilayer thickness deformations. Our findings reveal that alterations in protein shape induce changes to the lipid bilayer deformation energy exceeding $10\ k_BT$, which may have important implications for protein conformational changes and protein oligomerization processes. Chapter 4 examines the interplay between membrane mechanics and thermosensing, revealing how, mediated by lipid bilayer properties such as hydrophobic thickness and bending rigidity, temperature changes influence the conformational transitions of membrane proteins. We thus investigate the fundamental principles underlying the coordination of thermosensing and mechanosensing in living systems. Chapter 5 explores the physical principles underlying the self-assembly of emerin nanodomains at the inner nuclear membrane, which may shed new light on the role of emerin nanodomains in mechanotransduction. By employing a comprehensive modeling approach rooted in the Turing mechanism of nonequilibrium pattern formation, we develop a simple model quantifying the intricate reaction-diffusion properties of proteins and their nuclear binding partners. On this basis, we provide insight into the wild-type properties of emerin nanodomains and their response to applied forces, as well as the mechanisms underlying the observed defects in the self-assembly of emerin nanodomains for mutated forms of emerin associated with Emery-Dreifuss muscular dystrophy. Chapter 6 provides an overview and conclusions from our studies, and suggests potential future directions of

research inspired by our findings. By integrating these diverse research strands, our work contributes to a deeper understanding of the fundamental principles governing membrane mechanics and pattern formation, with implications for both physics and biology.

Most of the material described in this thesis is/will be discussed in the following publications:

I. C. D. Alas and C. A. Haselwandter. Dependence of protein-induced lipid bilayer deformations on protein shape. *Phys. Rev. E*, 107:024403, 2023.

II. C. D. Alas, O. Kahraman, and C. A. Haselwandter. Thermosensing through membrane mechanics, (expected submission in early 2024).

III. C. D. Alas, F. Pinaud, and C. A. Haselwandter. Physical mechanism for the self-assembly of emerin nanodomains at the inner nuclear membrane, (expected submission in 2023).

Chapter 1

Introduction

This chapter provides an introduction to the research topics addressed in this PhD thesis. We start by exploring the fundamental components of cell membranes in Section 1.1. In Section 1.2, we dive into various intricate aspects of transmembrane proteins in cell membranes, including their influence on membrane shape (Section 1.2.1), their responsiveness to physical stimuli such as temperature (Section 1.2.2), and their collective response to mechanical stress (Section 1.2.3). Finally, Section 1.3 motivates the boundary value method (BVM) for calculating protein-induced membrane deformations developed as part of this PhD thesis.

1.1 Proteins and phospholipids: the building blocks of cell membranes

Cell membranes maintain cellular integrity, and serve as dynamic barriers for nutrient, signal, and waste exchange with the external environment [1]. Comprising membrane
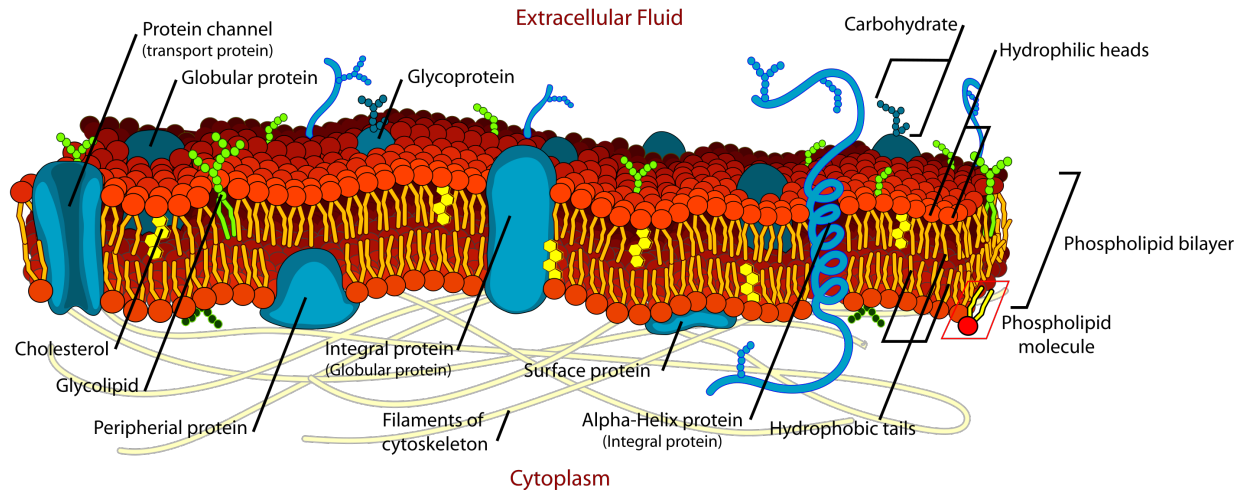
Figure 1.1: Illustration (from Ref. [3]) depicting various membrane proteins within lipid bilayer environments.

proteins and phospholipids, these structures facilitate vital cellular functions. Phospholipids form bilayers that interlock with membrane proteins, as illustrated in Figure 1.1, ensuring structural integrity, while membrane proteins govern essential processes such as ion transport, signal transduction, and membrane shape regulation [2].

Phospholipids possess an amphiphilic nature, with hydrophobic tail chains repelling water and hydrophilic head groups favorably interacting with it [4]. This amphiphilic property drives the self-assembly of lipid aggregates when introduced into an aqueous environment. The specific type of lipid aggregate formed depends on factors such as hydrocarbon chain characteristics, ionic conditions, and temperature. For instance, double-chained lipids with a large head group area tend to prefer, energetically, bilayer structures. These self-assembled lipid aggregates typically exhibit characteristic lateral sizes on the order of magnitude of micrometers while being only a few nanometers in the thickness.

Transmembrane proteins exhibit a consistent structural framework composed of three fundamental constituents [5]. First and foremost, the transmembrane segments are pivotal for anchoring the protein within the membrane. These segments traverse the lipid bilayer, showing hydrophobic amino acid residues that establish favorable interactions with the hydrophobic core of the lipid bilayer. Their role extends to providing structural stability and ensuring the protein's secure integration within the lipid bilayer. Furthermore, membrane proteins encompass extracellular domains that project into the external environment. These domains frequently serve as sites for interactions with neighboring cells, specific ligands, or extracellular molecules. Consequently, membrane proteins actively engage in essential processes such as cell signaling, adhesion, and recognition, contributing significantly to cellular function [6, 7]. In addition to extracellular domains, intracellular domains project into the cellular interior. These segments play multifaceted roles, often involving intracellular signal transduction and interactions with various components within the cell. Intriguingly, they can also be instrumental in anchoring the protein to the cell's cytoskeleton, thereby enhancing the protein's structural stability.

It is noteworthy that the precise composition and arrangement of the above constituent elements of membrane proteins can exhibit substantial variations among different membrane proteins. This diversity allows membrane proteins to fulfill a wide spectrum of functions, underscoring their significance in various cellular processes. A profound understanding of the structural organization of membrane proteins is indispensable for unraveling their contributions to cellular functions and the maintenance of cell membrane integrity.

1.2 Coordinators of cellular responses: the multifaceted functions of transmembrane proteins

The strategic placement of transmembrane proteins empowers them to fulfill a wide range of functions, including cellular gatekeeping activities such as the regulation of molecular transport, and pivotal roles as receptors for various signaling pathways [4].

A primary function of transmembrane proteins is the precise regulation of molecular transport across cell membranes [4, 8]. This function is facilitated by various types of transmembrane proteins, including ion channels, transporters, and pumps, responsible for maintaining the delicate balance of ions, small molecules, and nutrients inside and outside the cell. They act as gatekeepers, controlling the passage of substances to ensure the proper functioning of cellular processes. For example, ion channels enable the controlled flow of ions, which is vital for maintaining the electrochemical balance necessary for nerve impulses and muscle contraction.

Beyond their gatekeeping duties, transmembrane proteins also serve as primary receptors for numerous signaling pathways, as illustrated in Figure 1.2, allowing cells to detect and respond to various external stimuli [4, 6, 9]. Upon binding specific ligands, such as hormones or neurotransmitters, transmembrane receptors initiate cascades of intracellular events, culminating in the activation of essential cellular processes, such as gene expression, cell growth, and differentiation. Conformational changes triggered by ligand binding enable the transmission of signals across the cell membrane, ensuring the coordination of complex cellular activities.
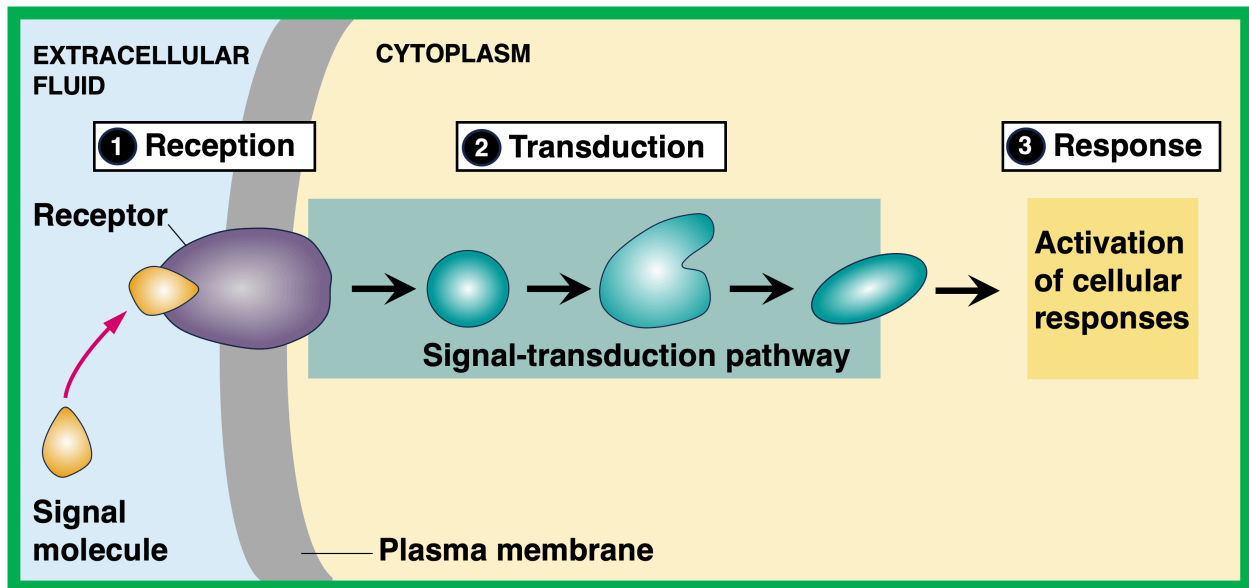
Figure 1.2: Illustration (adapted from Ref. [10]) depicting a transduction process initiated by a transmembrane protein. In particular, in this illustration, a signaling molecule binds to a receptor protein in the plasma membrane seperating the cell's cytoplasm from the extracellular environment, which sets off a signal transduction pathway leading to a response that involves the activation of cellular process.

Moreover, transmembrane proteins contribute to the organization of specialized membrane domains critical for cellular signal transduction [11, 12]. Through their collective actions, these proteins form defined clusters or domains within the cell membrane, facilitating the initiation of intricate signaling pathways and the recruitment of various signaling molecules. This protein clustering enables the efficient coordination of cellular responses to diverse environmental stimuli, ensuring the proper regulation of cellular processes, including adaptation to mechanical stress. Some notable examples are synaptic protein domains in neuronal membranes, which regulate synaptic transmission essential for cognitive function and learning, and inner nuclear membrane (INM) emerin nanodomains in mammalian cells, which facilitate the regulation of signals between the nucleoskeleton and the cytoskeleton vital for cellular adaptation to mechanical stress.

5

Transmembrane proteins also play a significant role in detecting physical stimuli, responding to mechanical forces, temperature changes, and osmotic pressure variations [8, 12, 13]. In particular, transmembrane proteins can undergo conformational changes in response to these stimuli, activating various cellular processes and signaling cascades [6, 14–16]. By sensing alterations in the cell's external environment, transmembrane proteins contribute to maintaining cellular homeostasis, enabling cells to adapt and respond to environmental fluctuations.

The multifaceted functionality of transmembrane proteins underscores their indispensable role in maintaining cellular homeostasis and regulating complex cellular processes. Their intricate structural arrangement within the cellular membrane enables them to act as gatekeepers for molecular transport, as receptors for various signaling pathways, and as sensors for physical stimuli, ensuring cells can adapt and respond to environmental changes. The collective behavior of transmembrane proteins in forming specialized domains plays a critical role in efficiently regulating cellular function and maintaining cellular integrity. Understanding the intricate functionality of transmembrane proteins offers valuable insights into the complex mechanisms governing cellular life and may lead to the development of novel therapeutic strategies for various diseases and disorders.

1.2.1 The influence of membrane proteins on membrane shape

Membrane proteins spanning the lipid bilayer are characterized by large hydrophobic regions that approximately match up with the thickness of the lipid bilayer hydrophobic

core [1, 4, 17–20]. However, distinct membrane proteins often show distinct hydrophobic thicknesses, and transitions in protein conformational state can change the protein's hydrophobic thickness. Figure 1.3, for instance, illustrates the gating of the mechanosensitive ion channel of large conductance (MscL), for which the change in protein shape is thought to impact the lipid bilayer hydrophobic thickness of the surrounding membrane area. Moreover, the lipid composition in cell membranes tends to be highly heterogeneous, with distinct lipids often showing distinct unperturbed lipid bilayer thicknesses. As a result, membrane proteins are generally expected to show a (modest) hydrophobic mismatch with the surrounding lipid bilayer, resulting in protein-induced lipid bilayer thickness deformations [21–31]. Membrane proteins may also deform the lipid bilayer membrane without perturbing the lipid bilayer thickness [32–38] as, for instance, in the case of bilayer midplane (curvature) deformations (see Appendix. B.1). The energy cost of such protein-induced lipid bilayer deformations depends on the protein shape and conformational state, the lipid composition, membrane mechanical properties such as membrane tension, as well as membrane organization, and can thus regulate, or even determine, membrane protein function. Membrane elasticity theory provides a beautiful framework for the quantitative description of protein-induced lipid bilayer deformations with, at least in the most basic models, all physical parameters being determined directly from experiments [21–25, 27–34, 36–40]. As a result, membrane elasticity theory yields definite predictions for the energy cost of protein-induced lipid bilayer deformations and, hence, the coupling between lipid bilayer mechanics and membrane protein function, allowing direct comparisons between theoretical predictions and experimental measurements.
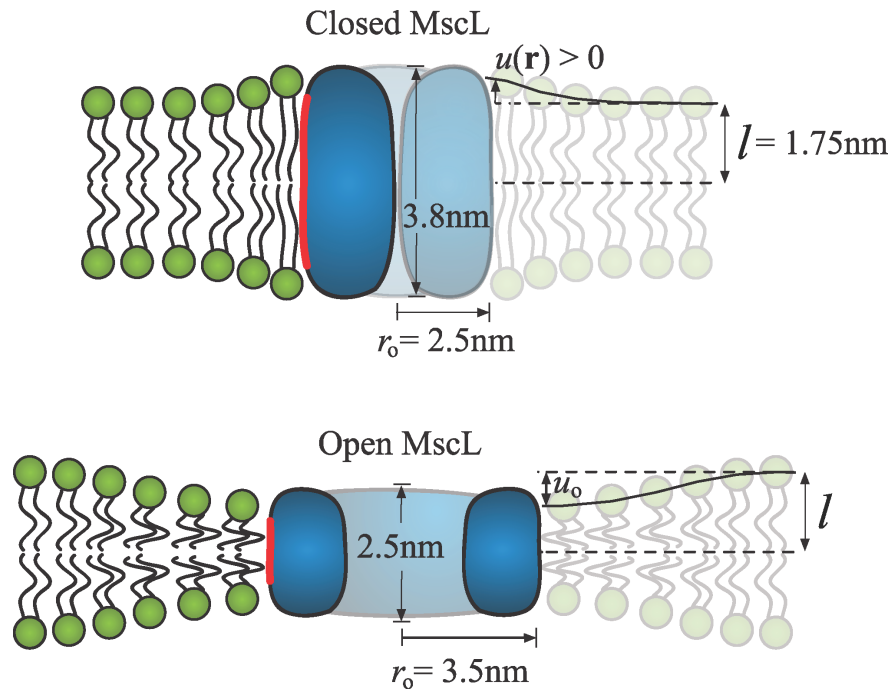
Figure 1.3: Illustration (from Ref. [41]) depicting the change in lipid bilayer hydrophobic thickness as MscL transitions from its closed state to its opened state.

Over the past two decades, breakthroughs in membrane protein crystallography and, more recently, cryo-electron microscopy have yielded enormous insight into the shape of membrane proteins [42–53]. Despite the large diversity in protein shape revealed by these experiments, mathematical difficulties associated with the description of protein-induced lipid bilayer deformations for general protein shapes have meant that the elasticity theory of bilayer-protein interactions has largely been limited to idealized, rotationally symmetric protein shapes. However, membrane protein shape may have important consequences for membrane morphology, membrane elastic properties, membrane curvature sensing and mechanosensing, the lateral organization and orientation of membrane proteins, bilayer-mediated protein interactions, and the regulation of protein function [30,

8

54–61]. This PhD thesis aims to address these issues by providing a versatile mathematical methodology allowing for the description of bilayer-protein interactions for the protein shapes observed in structural studies (see Chapters 2 and 3).

1.2.2 Temperature sensing in cells: the convergence of membrane mechanics and function

Living organisms are inherently attuned to their ever-changing surroundings, relying on a plethora of environmental cues to orchestrate vital biological processes. Among these cues, temperature is a crucial factor, exerting a significant influence on cellular physiology. The capacity to detect and respond to temperature variations is essential for survival, enabling organisms to thrive in diverse thermal environments. For instance, many cells employ temperature as a critical determinant in decision-making processes. Many microorganisms utilize temperature as a cue for optimal growth conditions, adjusting not only their metabolic activities but also their motion to flourish within specific thermal niches [13, 62–69]. Moreover, extreme cold temperatures can inhibit vital cellular processes, leading organisms to employ thermosensory mechanisms to evade or adapt to adverse conditions [70–79]. Conversely, excessive high temperatures can pose a severe threat to cell viability, necessitating rapid responses to mitigate the damaging effects of extreme warmth [16, 80–84]. In recent decades, a diverse range of experiments have significantly advanced our understanding of how organisms perceive and respond to environmental cues, particularly temperature fluctuations. This progress has been punctuated

by the identification of key molecular players, including temperature and touch transmembrane protein sensors, that play pivotal roles in these sensory processes. While these insights have provided valuable pieces of the puzzle, the precise physical mechanisms governing temperature sensing at the molecular level continue to be elusive.

In recent decades, extensive research has uncovered the mechanical properties of cellular membranes, revealing a coupling between protein function and membrane mechanics [8, 14, 15, 22, 23, 27, 38, 46, 47, 49, 59, 85–112]. These specialized proteins, often called mechanosensors, couple to membrane mechanical properties such as membrane thickness and rigidity. Additionally, various lines of experimental research suggest that biological membranes, typically considered soft materials, exhibit substantial changes as temperatures rise, making them easier to deform and thinner [15, 113–117]. While our quantitative understanding of the effect of temperature changes on membrane deformability continues to evolve, available evidence, albeit limited, permits a basic quantification of the relationship between temperature and membrane mechanical properties within physiologically relevant temperature ranges. As we shall discuss in this thesis (see Chapter 4), this interplay between protein functionality and membrane mechanics, influenced by temperature, suggests that cells might possess the inherent capacity to detect temperature variations through membrane mechanics. On this basis, we develop a basic framework allowing quantification of the potential consequences of temperature fluctuations on membrane mechanics and protein conformational states. In the scope of our investigation, membrane elasticity theory [21, 23, 27, 32–34, 59, 102, 118, 119], which we discuss in Chapter 2, serves to establish a direct link between the mechanics of the lipid bilayer and the functional behavior of membrane proteins. Notably, different conformational states

of membrane proteins often yield distinct protein-induced membrane deformations, with resultant changes in the energy of bilayer-protein interactions. On this basis, we employ membrane elasticity theory to connect measured temperature-dependent changes in bilayer mechanical properties to transitions in protein conformational state.

1.2.3   Collective protein behavior in specialized membrane domains

Proteins, both individually and collectively, are fundamental for a cell's ability to sense and respond to physical stimuli. An example of this is the organized clustering of proteins into specialized domains, a prevalent occurrence in cells. These protein-rich domains, composed of an assortment of proteins, often act as hubs for specific cellular functions. Take neurons, for instance. Neuron synaptic protein domains trigger complex signal pathways, transmitting information through neurotransmitter release, receptor binding, synaptic function, vesicle recycling, structural integrity, and material transport, ultimately supporting learning, memory, and neural communication [9, 11, 120–122]. The precise arrangement and organization of these domains are critical for dynamic and regulated synaptic communication. Any disruption or dysregulation in this intricate protein network can lead to various neurological disorders and cognitive impairments. In our exploration of collective protein behavior, we place a specific focus on the self-assembly of emerin nanodomains located at the INM and their role in initiating signaling pathways in response to mechanical stress.

Emerin, a nuclear membrane protein within mammalian cells, is a fundamental component of the INM [12]. It plays a pivotal role in mechanotransduction, as illustrated in

Figure 1.4, a process through which mechanical forces are detected and converted into biochemical signals. This function is intricately connected to emerin's role as a key link between the plasma membrane, the cytoskeleton, and the nucleoskeleton.

Emerin is a key component of the Linker of Nucleoskeleton and Cytoskeleton (LINC) complex. This complex acts as a bridge, connecting the nuclear lamina inside the nucleoplasm to the cytoskeleton on the cytoplasmic side. The LINC complex has the ability to sense and relay mechanical signals from the plasma membrane to the cell nucleus, which, consequently, can be perceived by emerin.

Emerin can affect gene expression involved in the processes of mechanotransduction. For example, by influencing genes such as β-catenin and Lmo7, emerin can affect cytoskeletal dynamics and cell shape [123–126]. Numerous studies have highlighted the significance of emerin's intrinsically disordered region in performing many of its vital functions. This structural flexibility allows emerin to adopt various conformations, form oligomers, and engage with multiple partners at the INM [12, 127–139]. Mutations in emerin or its absence have been correlated with abnormal responses of the nuclear envelope to mechanical stress, ultimately resulting in Emery-Dreifuss muscular dystrophy (EDMD).

A recent study utilizing single-molecule tracking and super-resolution fluorescence microscopy has provided intriguing insights into the steady-state distributions and mobilities of wild-type and mutated emerin at the INM under various conditions, including mechanical stress [12]. In particular, these experiments revealed two distinct distributions of emerin species at the INM, slow and fast diffusers, and that emerin generally forms
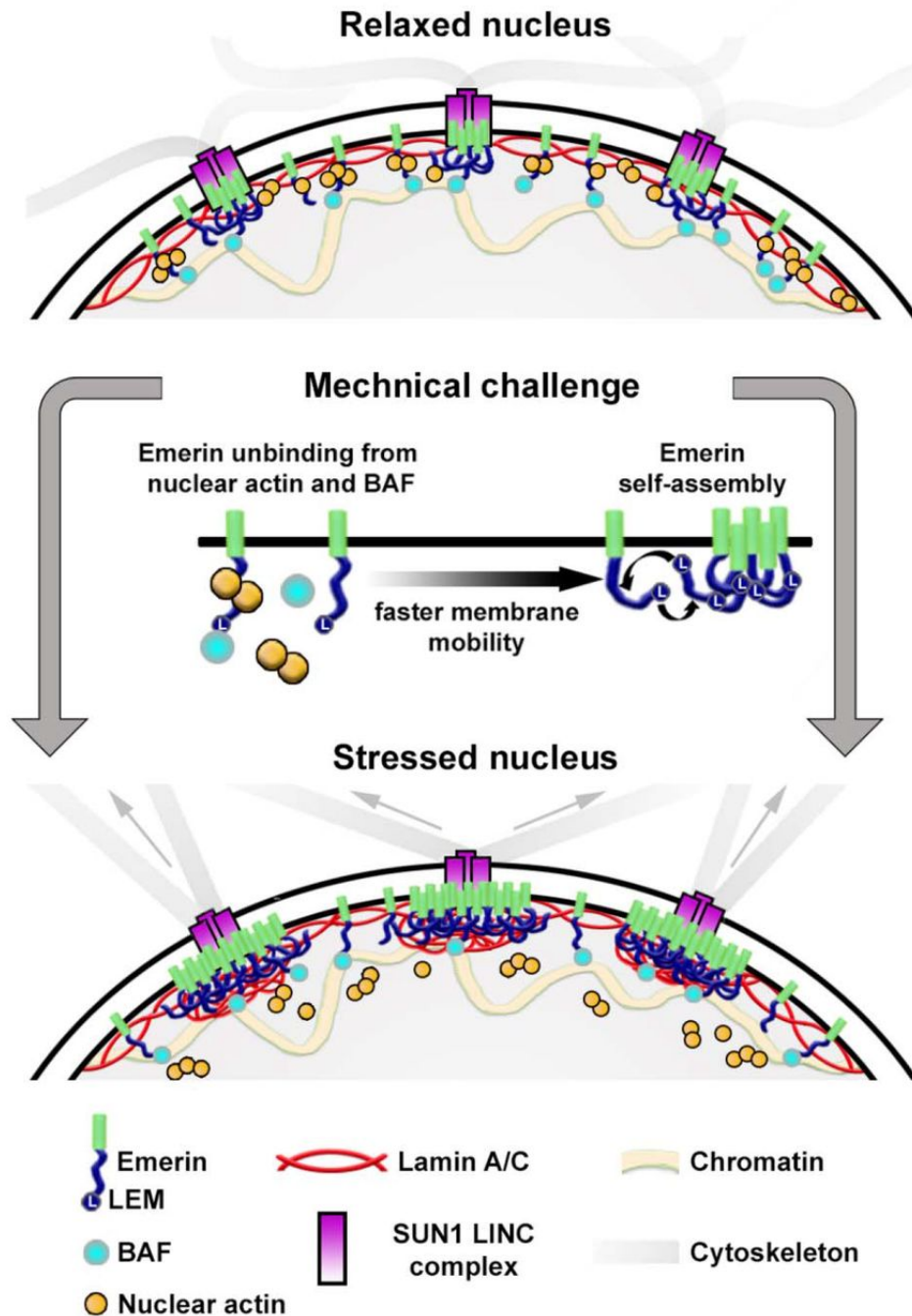
Figure 1.4: Schematic (from Ref. [12]) depicting the reorganization of emerin at the NE in response to mechanical stress. Increased lateral mobility at the INM is initiated by emerin monomer unbinding from nuclear actin and BAF, facilitating LEM domain interactions with binding sites along the intrinsically disordered region of other emerin molecules. This controlled process leads to the formation of emerin oligomers at SUN1 LINC complexes, subsequently stabilized by lamin A/C.

stable nanodomains of elevated emerin concentrations which are maintained through interactions with emerin and other nuclear binding partners (NBPs) [e.g., SUN1, lamin A/C, barrier-to-autointegration factor (BAF), and nuclear actin]. Mutations of emerin and mechanical stress were found to perturb the distributions of emerin and its oligomerization potential.

The INM spatial pattern of emerin nanodomains of increased concentrations and the distinction between slower and faster diffusing emerin species resembles the properties of molecular domains self-assembled through a Turing mechanism in an activator-inhibitor reaction-diffusion model [9, 11, 120–122, 140–144]. In this model, inhibitors, which diffuse rapidly, act to restrain increased molecular concentrations via steric constraints. On the other hand, activators diffuse at a slower pace compared to inhibitors but activate elevated molecular concentrations of both inhibitors and other activators. In Chapter 5, we show that the self-assembly of stable emerin nanodomains may be attributed to the self-stabilization of slow-diffusing, activating emerin-complexes and fast-diffusing, inhibiting emerin-complexes at the INM, coupled with the steric repulsion of the inhibitors.

1.3 Shortcomings of former approaches for calculating protein-induced lipid bilayer deformations

While it is relatively straightforward to derive analytical solutions for bilayer deformations induced by idealized proteins with approximately circular cross-sections [4], structural biology has revealed that membrane proteins often deviate significantly from this
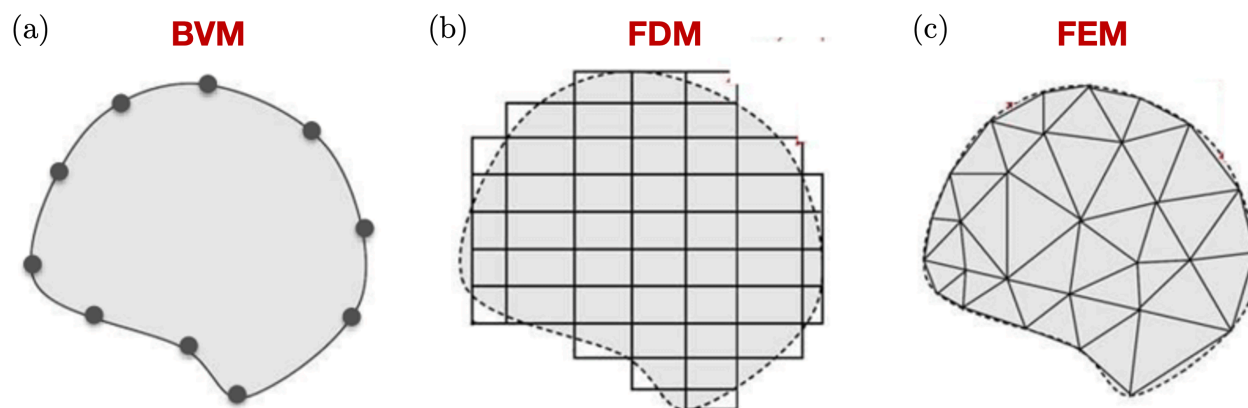
Figure 1.5: Diagrams (from Ref. [145]) of the general system domain discetization schemes utilized in (a) BVM, (b) FDM, and (c) FEM [145].

idealized shape. As a result, a more precise assessment of protein-induced bilayer deformations, incorporating the complex protein shapes observed in structural biology, typically relies on numerical methods. In previous studies [30], both finite element methods (FEM) and finite difference methods (FDM) have been employed to address bilayer deformations caused by proteins of arbitrary shapes. However, these methods show various limitations and, in some cases, are unable to provide accurate solutions. The BVM developed in this thesis (see Chapter 2) provides an alternative approach for calculating protein-induced bilayer deformations, and allows accurate calculation of protein-induced bilayer deformations for proteins with arbitrary shape. Our investigation reveals that the BVM offers several advantages over FEM and FDM when it comes to addressing lipid bilayer deformations.

FEM is a versatile numerical technique employed to solve partial differential equations by dividing the computational domain into smaller elements, often triangular in shape [see Fig. 1.5(c)]. It excels in addressing complex problems characterized by intricate geometries, diverse material properties, and complex boundary conditions. However, FEM

can be computationally intensive, particularly when dealing with numerous elements due to large sized systems and complex boundary geometries. Its implementation often demands expertise in tasks such as mesh generation, element selection, and boundary condition specification to achieve exceptional accuracy. It is noteworthy that, in the case of protein-induced lipid bilayer deformations, standard FEM software is often not suitable, as it requires a non-standard approach [30]. Conversely, FDM adopts a grid-based approach, discretizing the domain and approximating derivatives using finite differences [30] [see Fig. 1.5(b)]. FDM, like FEM, produces limited success when dealing with large and intricately shaped system domains, necessitating a substantial number of elements or grid points for high accuracy. Implementing parallelized computing structures to handle such situations can help to alleviate these issues but adds complexity to the process. These challenges become particularly evident when dealing with bilayer deformations with large decay lengths, demanding extensive computational resources and often rendering FEM and FDM impractical.

BVM solutions, characterized by their focus on boundary conditions and minimal discretization [see Fig. 1.5(a)], offer several distinct advantages over FEM and FDM. Notably, their simplicity in problem setup is a key strength. BVM involves the definition of boundary conditions, which are often known in advance, reducing the necessity for an extensive grid or mesh. This streamlined process enhances computational efficiency and simplifies implementation. In the context of bilayer deformations, BVM excels in scenarios where significant bilayer deformation attenuation lengths are expected. This advantage arises from BVM's discretization scheme, which relies solely on the boundary geometry rather than the size of the system enclosed by the boundary, a key contrast with FEM and FDM.

Consequently, BVM imposes a considerably lighter computational load. Another distinctive feature of BVM is its capacity to yield analytic solutions, in contrast to the numerical solutions provided by FEM and FDM.

Nonetheless, the very simplicity that makes BVM advantageous can, in certain scenarios, become a constraint. Its strong computational reliance on boundary shape can result in significant requirements on computational resources, such as situations involving many proteins. In such instances FEM, which tends to show a computational efficiency that is only mildly dependent on boundary geometry, is the optimal choice. In Chapter 2 we demonstrate, through rigourous benchmarks, that for many of the types of protein shapes observed in structural biology, a BVM, often effortlessly, generates accurate analytic (if complicated) solutions for the protein-induced lipid bilayer deformations and their associated energies.

Chapter 2

A boundary value method for lipid bilayer deformations

The objective of this chapter is to develop, describe, and test a straightfoward and easy to implement BVM suited for the construction of analytic solutions of protein-induced lipid bilayer deformations for protein shapes with arbitrarily large deviations from a circular cross section. This BVM allows for constant as well as variable boundary conditions along the bilayer-protein interface. In particular, we consider here, as test cases for the BVM, four generic classes of protein shapes breaking the rotational symmetry of protein-induced lipid bilayer thickness deformations, which are illustrated in Fig. 2.1. Inspired by observed molecular structures of membrane proteins [5, 146], we consider two classes of non-circular membrane protein cross sections: Clover-leaf [see Fig. 2.1(a)] and polygonal [see Fig. 2.1(b)] protein shapes. Furthermore, we allow for variations in the bilayer-protein hydrophobic mismatch [see Fig. 2.1(c)] as well as in the bilayer-protein contact slope [see Fig. 2.1(d)] along the bilayer-protein interface. Such variations in the bilayer-protein boundary conditions can arise, on the one hand, as inherent features of the protein structure or, on the other hand, as a result of, for instance, the binding of small peptides, such as spider toxins, or other molecules along the bilayer-protein interface [5, 22, 146,
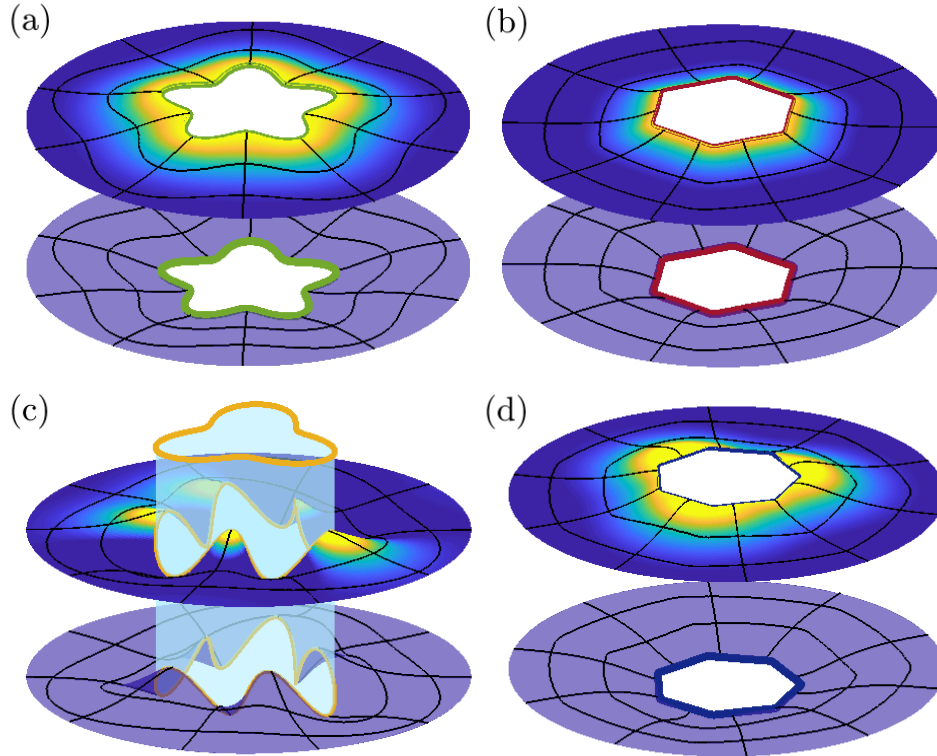
Figure 2.1: Protein-induced lipid bilayer thickness deformations for selected families of protein shapes: (a) Clover-leaf protein cross section with five-fold symmetry, constant protein hydrophobic thickness, and zero bilayer-protein contact slope, (b) polygonal protein cross section with six-fold symmetry, constant protein hydrophobic thickness, and constant bilayer-protein contact slope $U' = 0.3$, (c) clover-leaf protein cross section with three-fold symmetry, a five-fold symmetric (sinusoidal) variation in protein hydrophobic thickness, and zero bilayer-protein contact slope, and (d) polygonal protein cross section with seven-fold symmetry, constant protein hydrophobic thickness, and a three-fold symmetric (sinusoidal) variation in the bilayer-protein contact slope. The color map and purple surfaces show the positions of the upper and lower lipid bilayer leaflets, respectively. The bilayer-protein boundaries are color-coded according to their symmetries (see also Fig. 2.3 in Sec. 2.1). For panels (a) and (c) we used $\epsilon = 0.2$ and $\epsilon = 0.3$ in Eq. (2.17), respectively, and for panels (b) and (d) we used $P = 5$ in Eqs. (2.18) and (2.19). All bilayer surfaces were calculated using the reference parameter values in Sec. 2.1 and the BVM for protein-induced lipid bilayer thickness deformations described in Sec. 2.2.

147]. For each of these four classes of protein shapes we use the BVM to obtain the energy cost of protein-induced lipid bilayer thickness deformations, and test these results against corresponding numerical solutions obtained through the FEM for bilayer thickness deformations [30, 60, 61]. Our BVM reproduces available analytic solutions for proteins

with circular cross section and yields, for proteins with non-circular cross section, excellent agreement with the numerical, finite element solutions. Crucially, our BVM does not suffer from the membrane areal domain size limitations exhibited by FEM and FDM, with a computational demand that only scales with the complexity of the bilayer boundary geometry, making it the preferred choice for addressing bilayer deformations with potentially long decay lengths.

This chapter is organized as follows. Section 2.1 summarizes the elasticity theory of protein-induced lipid bilayer thickness deformations. In Sec. 2.2 we describe in detail the BVM for bilayer thickness deformations, test this BVM against FEM solutions, and discuss how the BVM can be used to calculate protein-induced lipid bilayer thickness deformations, and their associated elastic energy, for general protein shapes. We summarize the conclusions of our work and discuss limitations and further potential applications of our BVM in Sec. 6.1.

2.1   Modeling protein-induced lipid bilayer thickness deformations

The preferred hydrophobic thickness of lipid bilayers depends strongly on the lipid chain length [1, 4, 17–20] while different membrane proteins, and even different conformational states of the same membrane protein, often have distinct hydrophobic thicknesses. For membrane proteins that offer a rigid interface to the lipid bilayer and show a modest hydrophobic mismatch with the unperturbed lipid bilayer, the lipid bilayer thickness is

expected to deform in the vicinity of the membrane protein so as to achieve hydropho-

bic matching at the bilayer-protein interface [21–31]. The resulting protein-induced lipid

bilayer thickness deformations can result in a pronounced dependence of the protein con-

formational state, and protein function, on lipid chain length [14, 23, 102, 118, 148, 149].

The purpose of this section is to summarize the elasticity theory of protein-induced lipid

bilayer thickness deformations [21–25, 27–30, 39, 58, 59]. We first outline the standard

elasticity theory of lipid bilayer thickness deformations (see Sec. 2.1.1). We then describe

how protein shape couples to lipid bilayer thickness, and discuss the models of protein

shape considered in Chapters 2–4 (see Sec. 2.1.2).

2.1.1 Continuum elasticity theory of lipid bilayer deformations

Lipid bilayer thickness deformations tend to decay rapidly, with a characteristic decay

length ≈ 1 nm [22, 28]. When modeling protein-induced lipid bilayer thickness deforma-

tions it is therefore convenient to represent the positions of the two lipid bilayer leaflets in

the Monge parameterization of surfaces, $h_\pm = h_\pm(x, y)$, with Cartesian coordinates (x, y)

(see Fig. 2.2). It is instructive to express $h_+(x, y)$ and $h_-(x, y)$ in terms of the midplane

deformation field $h = h(x, y)$,

$$h = \frac{h_+ + h_-}{2} \,, \tag{2.1}$$

and in terms of the thickness deformation field $u = u(x, y)$,

$$u = \frac{h_+ - h_- - 2a}{2} \,, \tag{2.2}$$

Figure 2.2: Notation used for the calculation of protein-induced lipid bilayer thickness deformations in (a) angled and (b) side views. As an example, we consider here a membrane protein with a non-circular (clover-leaf) bilayer-protein boundary curve, $C(\theta)$, constant hydrophobic thickness, $W(\theta) = W_0$, and zero bilayer-protein contact slope, $U'(\theta) = 0$. The positions of the upper and lower lipid bilayer leaflets are denoted by h_+ and h_-, from which the bilayer midplane and bilayer thickness deformation fields h and u can be obtained via Eqs. (2.1) and (2.2), respectively. We denote one-half the unperturbed bilayer thickness by a, resulting in a hydrophobic mismatch $U = W/2 - a$ at the bilayer-protein interface. The unit vectors $\hat{t}$ and $\hat{n}$ denote the directions tangential and perpendicular (pointing towards the protein) to the bilayer-protein boundary, respectively.

where a is one-half the unperturbed lipid bilayer thickness (Fig. 2.2). The value of a depends on, for instance, the chain length of the lipid species under consideration, and can be directly measured in experiments [21, 22, 40].

The membrane elasticity theory describing the shape of lipid bilayers [4, 150–152] dates back to the classic work of W. Helfrich [32], P. B. Canham [33], E. A. Evans [34], and H. W. Huang [23]. Interestingly, one finds that the elastic energies governing h and u in Eqs. (2.1) and (2.2) decouple from each other to leading order [27, 39]. In the most straightforward model of bilayer-protein interactions [21–25, 27–30, 150–154], the energy cost of protein-induced lipid bilayer midplane deformations is then captured by the classic Helfrich-Canham-Evans energy [32–34], and the energy cost of protein-induced lipid bilayer thickness deformations is given by [21, 23–25, 27–30]

$$G = \frac{1}{2} \int dxdy \left[K_b \left(2H \right)^2 + K_t \left(\frac{u}{a} \right)^2 + \tau \left(\nabla u \right)^2 + 2\tau \frac{u}{a} \right] , \qquad (2.3)$$

where the integral runs over the (in-plane) lipid bilayer surface, K_b is the lipid bilayer bending rigidity, the mean curvature $H = \frac{1}{2}\nabla^2 u$, K_t is the bilayer thickness deformation modulus, and τ is the lateral membrane tension.

The terms $K_b \left(\nabla^2 u \right)^2$, $K_t \left(u/a \right)^2$, $\tau \left(\nabla u \right)^2$, and $2\tau \frac{u}{a}$ in Eq. (2.3) provide lowest-order descriptions of the energy cost of bilayer bending, the compression/expansion of the bilayer hydrophobic core, changes in the projection of the bilayer area onto the reference plane used in the Monge representation, and stretching deformations tangential to the leaflet surfaces, respectively. Equation (2.3) has been successfully employed to describe bilayer-protein interactions in a variety of experimental systems [4, 14, 21–23, 27, 28, 30,

59, 102, 118, 155–157]. In general, the protein-induced lipid bilayer thickness deformations captured by Eq. (2.3) compete with protein-induced bilayer midplane deformations [22, 32–38, 54–56, 107, 153, 154, 158]. Depending on the specific bilayer-protein system under consideration, both contributions to the elastic energy of bilayer-protein interactions may need to be considered [22, 27]. We also assume in Eq. (2.3) that the lipids forming the bilayer have zero intrinsic curvature. A nonzero lipid intrinsic curvature could also be included in the formalism employed here [24, 25, 119]. Furthermore, the elastic energy of protein-induced lipid bilayer deformations involves, in general, contributions due to lipid tilt deformations [32, 56, 159–161], in addition to contributions due to bilayer thickness and bilayer midplane deformations. Finally, we note that one could extend Eq. (2.3) to include a bending term associated with the Gaussian membrane curvature. Previous work on bilayer-protein interactions indicates that Gaussian curvature contributions to Eq. (2.3) tend to be negligible in experiments [27, 119]. We employ here Eq. (2.3) as a simple model system for investigating the effect of protein shape on the elastic energy of protein-induced lipid bilayer deformations while noting that, as illustrated above, Eq. (2.3) can be extended and modified in a variety of ways.

Similarly as the unperturbed lipid bilayer thickness $2a$, the effective parameters K_b and K_t in Eq. (2.3) characterizing the elastic properties of the bilayer membrane depend on the lipid composition, and can be directly measured in experiments [21, 22, 40]. Typical values of K_b, K_t, and a for cell membranes are $K_b = 20 \ k_B T$, $K_t = 60 \ k_B T/\text{nm}^2$, and $a = 1.6 \ \text{nm}$ [28, 40, 114, 116]. In Chapters 2 and 3 we use these values of K_b, K_t, and a; in Chapter 4 we will assign to K_b, K_t, and a temperature dependent relations. When studying the dependence of protein-induced bilayer thickness deformations on lipid chain

length we follow Refs. [27, 40, 162] and assume, for simplicity, a linear dependence of a on lipid chain length:

$$a = \frac{1}{2} \left(0.13m + 1.7 \right) \text{ nm} .\tag{2.4}$$

The integer m in Eq. (2.4) denotes the lipid chain length (number of carbon atoms comprising each lipid chain), with the approximate range $13 \leq m \leq 22$ for phospholipids in cell membranes [1, 17, 19, 40]. For simplicity, we take K_b and K_t to be independent of m while noting that, in general, K_b and K_t may have a (weak) dependence on m [40].

The effective parameters K_b, K_t, and a in Eq. (2.3) yield the characteristic length scale

$$\lambda = \left(\frac{a^2 K_b}{K_t} \right)^{1/4} ,\tag{2.5}$$

which corresponds to the characteristic decay length of bilayer thickness deformations [27]. As alluded to above, we have $\lambda \approx 1$ nm [22, 28]. Similarly, the bilayer bending rigidity K_b defines a characteristic energy scale in Eq. (2.3). It is therefore convenient to recast the bilayer thickness deformation energy in Eq. (2.3) in terms of the characteristic spatial and energy scales, λ and K_b. In Chapters 2 and 3, we use a dimensionless form of Eq. (2.3) such that $\bar{G}K_b \to G$, $\bar{x}\lambda \to x$, $\bar{y}\lambda \to y$, $\bar{u}\lambda \to u$, $\bar{a}\lambda \to a$, $\bar{K}_t K_b / \lambda^2 \to K_t$, and $\bar{\tau} K_b / \lambda^2 \to \tau$, resulting in

$$\bar{G} = \frac{1}{2} \int d\bar{x} d\bar{y} \left[\left(\bar{\nabla}^2 \bar{u} \right)^2 + \bar{u}^2 + \bar{\tau} \left(\bar{\nabla} \bar{u} \right)^2 + 2\bar{\tau} \frac{\bar{u}}{\bar{a}} \right] ,\tag{2.6}$$

where $\bar{\nabla} \equiv \lambda \nabla$.

We assume that, for a given protein conformational state, the dominant bilayer thickness deformation field $\bar{u}(\bar{x}, \bar{y})$ minimizes Eq. (2.6) subject to suitable boundary conditions [21, 23–25, 27, 28, 30]. The Euler-Lagrange equation associated with Eq. (2.6) is given by

$$\left(\bar{\nabla}^2 - \bar{\nu}_+\right)\left(\bar{\nabla}^2 - \bar{\nu}_-\right)\bar{u} = -\frac{\bar{\tau}}{\bar{a}} \tag{2.7}$$

with $\bar{\nu}_\pm = \frac{1}{2}\left(\bar{\tau} \pm \mathbf{i}\sqrt{4 - \bar{\tau}^2}\right)$, where $\mathbf{i}$ is the imaginary unit, and $\bar{u}$ is composed of a general solution $\bar{u}_g\left(\bar{x}, \bar{y}\right)$ and a particular solution $\bar{u}_p = -\bar{\tau}/\bar{a}$. To construct the general solution of Eq. (2.7) for protein-induced bilayer thickness deformations it is useful to transform $(\bar{x}, \bar{y})$ to the dimensionless polar coordinates $(\bar{r}, \theta)$ with the protein center as the origin of the polar coordinate system. Assuming that protein-induced bilayer thickness deformations form a localized membrane footprint $\bar{u}_g \to 0$ as $\bar{r} \to \infty$ [23, 118, 119], in which case Eq. (2.7) yields [30, 58, 59]

$$\bar{u}\left(\bar{r}, \theta\right) + \frac{\bar{\tau}}{\bar{a}} = \bar{f}^+\left(\bar{r}, \theta\right) + \bar{f}^-\left(\bar{r}, \theta\right) , \tag{2.8}$$

where the Fourier-Bessel series

$$\bar{f}^\pm(\bar{r}, \theta) = A_0^\pm K_0\left(\sqrt{\bar{\nu}_\pm}\bar{r}\right) + \sum_{n=1}^{\infty}\left[A_n^\pm K_n\left(\sqrt{\bar{\nu}_\pm}\bar{r}\right)\cos\left(n\theta\right) + B_n^\pm K_n\left(\sqrt{\bar{\nu}_\pm}\bar{r}\right)\sin\left(n\theta\right)\right], \tag{2.9}$$

in which the K_n are the modified Bessel functions of the second kind [163] and the values of the coefficients $A_0^\pm$, $A_n^\pm$, and $B_n^\pm$ are determined by the bilayer-protein boundary conditions.

The bilayer thickness deformation energy in Eq. (2.6) is conveniently evaluated for the stationary bilayer thickness deformation field in Eq. (2.8) by noting that, via Eq. (2.7), Eq. (2.6) can be transformed to a line integral along the bilayer-protein boundary $\bar{C}$ [27, 30, 59] (Fig. 2.2). For simplicity, we thereby take the bilayer-protein boundary to be specified by the polar curve $\bar{\mathbf{r}} = \bar{C}(\theta)\hat{\mathbf{r}}$, where $\hat{\mathbf{r}}$ is the radial unit vector pointing away from the protein center. We thus have

$$\bar{G} = \frac{1}{2} \int_0^{2\pi} d\theta \, \bar{l} \, \hat{\mathbf{n}} \cdot \left[\bar{\nabla}\bar{u}\bar{\nabla}^2\bar{u} - \left(\bar{u} + \frac{\bar{\tau}}{\bar{a}}\right) \bar{\nabla}^3\bar{u} + \bar{\tau}\left(\bar{u} + \frac{\bar{\tau}}{\bar{a}}\right) \bar{\nabla}\bar{u} \right]\Bigg|_{\bar{r}=\bar{C}(\theta)} + \bar{G}_\infty \,, \qquad (2.10)$$

where the line element $\bar{l} = \sqrt{\left[\bar{C}(\theta)\right]^2 + \left[\bar{C}'(\theta)\right]^2}$, the unit vector $\hat{\mathbf{n}}$ is normal to the tangent of $\bar{\mathbf{r}} = \bar{C}(\theta)\hat{\mathbf{r}}$ and points towards the protein (Fig. 2.2), and $\bar{G}_\infty = -\left(\bar{\tau}/\bar{a}\right)^2 \int d\bar{x}d\bar{y}$. The constant term $\bar{G}_\infty$ emerges from the relaxation of the "loading" device producing tension $(\tau > 0)$ and diverges under the assumption of an asymptotically flat, infinite membrane. Since $\bar{G}_\infty$ does not contribute to the energy cost of protein-induced bilayer thickness deformations we shift $\bar{G}$ so as to subtract $\bar{G}_\infty$ from $\bar{G}$, $\bar{G} - \bar{G}_\infty \to \bar{G}$. Note that the term in brackets in Eq. (2.10) may be interpreted as a bilayer-protein line tension along the bilayer-protein boundary [27, 30, 102]. The normal vector $\hat{\mathbf{n}}$ in Eq. (2.10) is obtained by differentiating the bilayer-protein boundary curve $\bar{\mathbf{r}} = \bar{C}(\theta)\hat{\mathbf{r}}$ with respect to θ and rotating the resulting tangent vector by $\pi/2$ so as to point towards the protein,

$$\hat{\mathbf{n}} = \frac{-\bar{C}(\theta)\hat{\boldsymbol{r}} + \bar{C}'(\theta)\hat{\boldsymbol{\theta}}}{\bar{l}} \,, \qquad (2.11)$$

where we have noted that the (counterclockwise) angular unit vector $\hat{\boldsymbol{\theta}} = d\hat{\mathbf{r}}/d\theta$ in polar coordinates (Fig. 2.2). Equation (2.10) with Eq. (2.11) allows calculation of $\bar{G}$ in Eq. (2.6) and, hence, G in Eq. (2.3) along a one-dimensional curve rather than over a two-dimensional surface, which provides a computationally efficient method for evaluating $\bar{G}$.

2.1.2   Modeling protein shape

The coefficients $A_0^{\pm}$, $A_n^{\pm}$, and $B_n^{\pm}$ in Eq. (2.9) are fixed by the boundary conditions at the bilayer-protein interface. The general mathematical form of these boundary conditions, which encode the key protein properties governing protein-induced lipid bilayer thickness deformations, follows from the calculus of variations [164, 165]. Based on previous work on protein-induced bilayer thickness deformations [21–26, 118], we assume that the lipid bilayer thickness deforms in the vicinity of membrane proteins so as to achieve hydrophobic matching at the bilayer-protein interface. We thus have the boundary condition

$$\bar{u}(\bar{r}, \theta)\big|_{\bar{r}=\bar{C}(\theta)} + \frac{\bar{\tau}}{\bar{a}} = \bar{U}(\theta) + \frac{\bar{\tau}}{\bar{a}} \,, \tag{2.12}$$

where the bilayer-protein hydrophobic mismatch

$$\bar{U}(\theta) = \frac{1}{2}\left[\bar{W}(\theta) - 2\bar{a}\right] \,, \tag{2.13}$$

in which $W(\theta) = \lambda\bar{W}(\theta)$ is the protein hydrophobic thickness along the bilayer-protein boundary (Fig. 2.2). For large enough magnitudes of U, membrane proteins or lipids may

expose parts of their hydrophobic regions to water, which would amount to an offset of $\bar{W}$ in Eq. (2.13). For a given membrane protein, $W(\theta)$ can be estimated from the molecular structure of the membrane protein [21, 22, 30, 59, 60] and/or computer simulations [31, 166]. We explore here protein-induced bilayer thickness deformations for generic models of $W(\theta)$ inspired by the molecular structure of the mechanosensitive channel of large conductance (MscL) [42, 91, 167, 168].

In addition to Eq. (2.12), it is also necessary to specify boundary conditions on the (normal) derivative of u at the bilayer-protein interface [164, 165]. The appropriate choice for these boundary conditions has been a matter of debate, and is likely to depend on the specific system under consideration [21–25, 27–31, 39, 56, 102, 118, 160, 161, 169]. We generally focus on the fixed-value boundary condition

$$\hat{\mathbf{n}} \cdot \bar{\nabla}\bar{u}(\bar{r}, \theta)\big|_{\bar{r}=\bar{C}(\theta)} = \bar{U}'(\theta)\,, \tag{2.14}$$

but also explore choices for $\bar{U}'(\theta)$ minimizing the bilayer thickness deformation energy. One may physically interpret fixed-value boundary conditions on the derivative of u as corresponding to scenarios in which the lipid leaflet surfaces are normal to the protein hydrophobic surface at the bilayer-protein boundary [27], while natural boundary conditions minimizing the bilayer thickness deformation energy permit arbitrary slopes of u [118]. A more detailed molecular model of the gradients of the lipid bilayer leaflets at bilayer-protein interfaces can be developed by explicitly taking into account lipid tilt [26, 161, 170]. We allow for constant as well as varying $\bar{U}'(\theta)$ in Eq. (2.14).

For a (hypothetical) membrane protein with a perfectly circular cross section $\bar{C}(\theta) = \bar{R}$, where $\bar{R}$ is the (dimensionless) protein radius, and constant $\bar{U}$ and $\bar{U}'$, the bilayer-protein boundary conditions in Eqs. (2.12) and (2.14) are azimuthally symmetric about the protein center, and the resulting protein-induced bilayer thickness deformations also show azimuthal symmetry about the protein center [23, 27, 102, 118]. Equations (2.12) and (2.14) suggest three, not mutually exclusive, modes for protein structures to break rotational symmetry, and to hence endow protein-induced bilayer thickness deformations with a non-trivial structure [58, 59]. First, the value of $\bar{U}$ in Eq. (2.12) or, second, the value of $\bar{U}'$ in Eq. (2.14) may vary along the bilayer-protein interface. To explore generic effects of varying $\bar{U}$ or $\bar{U}'$ on protein-induced bilayer thickness deformations we consider the bilayer-protein hydrophobic mismatch

$$\bar{U}(\theta) = \bar{U}_0 + \bar{\beta}\cos(w\theta) \tag{2.15}$$

and the bilayer-protein contact slope

$$\bar{U}'(\theta) = \bar{U}'_0 + \bar{\gamma}\cos(v\theta)\,, \tag{2.16}$$

where $\bar{U}_0$ and $\bar{U}'_0$ denote the average bilayer-protein hydrophobic mismatch and bilayer-protein contact slope, $\bar{\beta}$ and $\bar{\gamma}$ denote the amplitudes of the perturbations about these average values, and w and v denote the protein symmetries associated with variations in $\bar{U}$ and $\bar{U}'$. In Chapters 2 and 3, we set $\bar{U}_0\lambda = -0.1$ nm and $\bar{\beta}\lambda = 0.5$ nm in Eq. (2.15) for all calculations involving a modulation in the bilayer-protein hydrophobic mismatch, and

$\bar{U}'_0 = 0$ and $\bar{\gamma} = 0.3$ in Eq. (2.16) for all calculations involving a modulation in the bilayer-protein contact slope. For all scenarios considered in Chapters 2 and 3 for which we keep $\bar{U}$ or $\bar{U}'$ constant along the bilayer-protein interface we set, unless stated otherwise, $\bar{U}\lambda = 0.3$ nm or $\bar{U}' = 0$. The values of U and U' employed here are in line with previous work on MscL and gramicidin channels [28, 31, 42, 91, 118].

Angular variations in $\bar{C}(\theta)$ along the bilayer-protein boundary $\bar{\mathbf{r}} = \bar{C}(\theta)\hat{\mathbf{r}}$ provide, in addition to Eqs. (2.15) and (2.16), a third mode for a protein structure to break azimuthal symmetry of protein-induced bilayer thickness deformations about the protein center. Inspired by molecular structures of tetrameric and pentameric MscL [42, 59, 60, 171] and other membrane proteins [5, 146], we consider here two generic classes of protein shapes breaking rotational symmetry. On the one hand, we consider clover-leaf protein cross sections specified by

$$\bar{C}(\theta) = \bar{R}\big[1 + \epsilon \cos(s\theta)\big], \tag{2.17}$$

where ϵ parameterizes the magnitude of deviations from a circular protein cross section, $\epsilon = 0$ for circular protein cross sections, and s denotes the symmetry of the boundary curve [see Figs. 2.2(a) and 2.3(a)]. On the other hand, we consider (rounded) polygonal protein cross sections specified by the series

$$\bar{C}(\theta) = \bar{A}_{\bar{R}}\sqrt{\left[\sum_{p=-P}^{P} \frac{\cos(sp+1)\theta}{(sp+1)^2}\right]^2 + \left[\sum_{p=-P}^{P} \frac{\sin(sp+1)\theta}{(sp+1)^2}\right]^2}, \tag{2.18}$$

where larger P yield sharper polygonal corners with $P = 0$ for circular protein cross sections, $\bar{A}_{\bar{R}}$ is a rescaling factor chosen so as to ensure that the polygons are inscribed
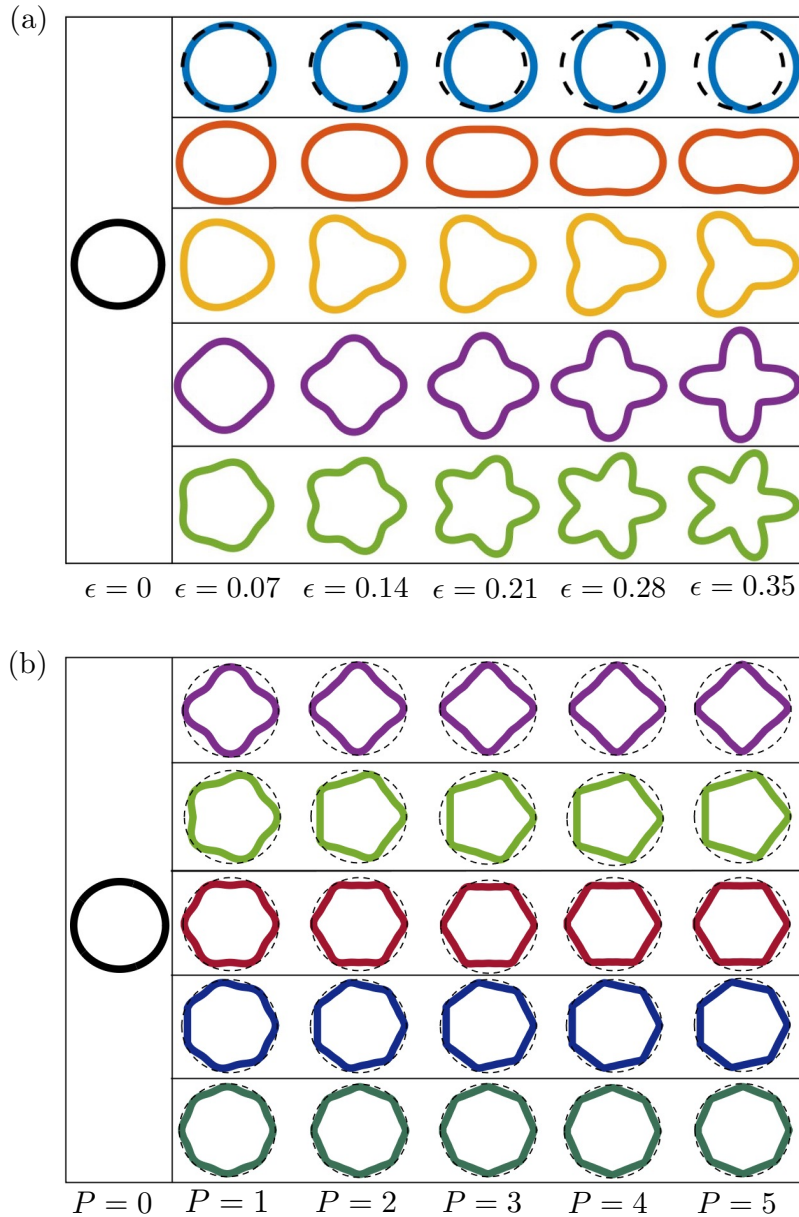
Figure 2.3: Cross sections of cylindrical protein shapes (left-most panels) and (a) clover-leaf and (b) polygonal protein shapes (right panels). The clover-leaf protein cross sections in panel (a) are obtained from Eq. (2.17) with $\epsilon = 0.07$, 0.14, 0.21, 0.28, and 0.35 (left to right) and $s = 1$, 2, 3, 4, and 5 (top to bottom), with $\epsilon = 0$ yielding a circular protein cross section. Note that the clover-leaf protein cross sections with $s = 1$ only show small deviations from the corresponding circular protein cross section obtained with $\epsilon = 0$ in Eq. (2.17) (dashed curves) for the values of ϵ considered here. The polygonal protein cross sections in panel (b) are obtained from Eq. (2.18) with $P = 1$, 2, 3, , 4, and 5 (left to right) and $s = 4$, 5, 6, 7, and 8 (top to bottom). As a guide to the eye, these polygonal protein cross sections are inscribed in circles obtained with $P = 0$ in Eq. (2.18) (dashed curves).

in circles of radius $\bar{R}$, and s denotes the polygonal symmetry [59, 172] [see Fig. 2.3(b)].
We have

$$\bar{A}_{\bar{R}} = \frac{\bar{R}}{\sum_{p=-P}^{P} \frac{1}{(sp+1)^2}} \ . \tag{2.19}$$

Unless stated otherwise, we set $P = 5$ in Eqs. (2.18) and (2.19). For the scenarios considered here we found that an increase in P beyond $P = 5$ only resulted in minor shifts in the bilayer thickness deformation energy (see Figure 2.8). For all the calculations described in Chapters 2 and 3 we use $\bar{R}\lambda \approx 2.3$ nm in Eqs. (2.17) and (2.19), which approximately corresponds to the observed size of a closed state of MscL [27, 42].

2.2 Boundary value method for bilayer thickness deformations

In this section we introduce a BVM for bilayer thickness deformations, which allows calculation of protein-induced bilayer thickness deformations, and their associated elastic energy, for general protein shapes. In the following sections we use this BVM to calculate the bilayer thickness deformation field $\bar{u}(\bar{r}, \theta)$ in Eq. (2.8), and the resulting bilayer thickness deformation energy G in Eq. (2.3), for the clover-leaf and polygonal protein shapes $\bar{\mathbf{r}} = \bar{C}(\theta)\hat{\mathbf{r}}$ in Eqs. (2.17) and (2.18) and the boundary conditions $\bar{U}(\theta)$ and $\bar{U}'(\theta)$ in Eqs. (2.15) and (2.16). We first provide a general formulation of the BVM for bilayer thickness deformations, and validate this BVM against exact analytic and FEM solutions (see Sec. 2.2.1). We then discuss how the numerical performance of the BVM for bilayer thickness deformations can be improved by employing an adaptive point distribution

(APD) that results in a nonuniform distribution of boundary points for non-circular protein cross sections (see Sec. 2.2.2). For simplicity, we set $\tau = 0$ in all of our calculations in Chapters 2 and 3, but we continue discussing our mathematical equations assuming a finite τ for completeness.

2.2.1 Formulation and validation of the boundary value method

The BVM for bilayer thickness deformations takes the analytic solution for $\left(\bar{u}(\bar{r}, \theta) + \frac{\bar{\tau}}{\bar{a}}\right)$ in Eq. (2.8) as its starting point, and assumes that the infinite series in this general solution can be truncated at some finite order N:

$$\bar{u}\left(\bar{r}, \theta\right) + \frac{\bar{\tau}}{\bar{a}} \approx \bar{f}_N^+\left(\bar{r}, \theta\right) + \bar{f}_N^-\left(\bar{r}, \theta\right) ,\tag{2.20}$$

where

$$\bar{f}_N^\pm(\bar{r}, \theta) = A_0^\pm K_0\left(\sqrt{\bar{\nu}_\pm}\bar{r}\right) + \sum_{n=1}^N \left[A_n^\pm K_n\left(\sqrt{\bar{\nu}_\pm}\bar{r}\right)\cos\left(n\theta\right) + B_n^\pm K_n\left(\sqrt{\bar{\nu}_\pm}\bar{r}\right)\sin\left(n\theta\right)\right].\tag{2.21}$$

The solution in Eq. (2.20) with Eq. (2.21) contains the $4N + 2$ unknown constants $A_0^\pm$, $A_n^\pm$, and $B_n^\pm$. In the BVM for bilayer thickness deformations, we fix these coefficients by imposing the boundary conditions in Eqs. (2.12) and (2.14) at $2N + 1$ boundary points along the bilayer-protein interface. For now, we take these boundary points to be uniformly distributed along the bilayer-protein interface, with a constant arc length separating adjacent boundary points along the bilayer-protein interface. We return to the distribution of boundary points in Sec. 2.2.2.

From the boundary conditions in Eqs. (2.12) and (2.14) we have

$$\bar{u}(\bar{r}, \theta_j)\big|_{\bar{r}=\bar{C}(\theta_j)} + \frac{\bar{\tau}}{\bar{a}} = \bar{U}(\theta_j) + \frac{\bar{\tau}}{\bar{a}}, \tag{2.22}$$

$$\hat{\mathbf{n}} \cdot \bar{\nabla}\bar{u}(\bar{r}, \theta_j)\big|_{\bar{r}=\bar{C}(\theta_j)} = \bar{U}'(\theta_j), \tag{2.23}$$

in which $j = 1, 2, \ldots, 2N+1$ denote the boundary points along the bilayer-protein interface, where $\bar{C}(\theta) = \bar{R}$ for proteins with a circular cross section, $\bar{C}(\theta)$ is as in Eq. (2.17) for cloverleaf protein shapes, and $\bar{C}(\theta)$ is as in Eq. (2.18) for polygonal protein shapes (Fig. 2.3). Equations (2.22) and (2.23) amount to a linear system of equations

$$\mathbf{A}\mathbf{x} = \mathbf{b}, \tag{2.24}$$

where the vector $\mathbf{x}$ has dimension $4N + 2$ and contains the unknown constants $A_0^{\pm}$, $A_n^{\pm}$, and $B_n^{\pm}$, the $4N + 2$ components of the vector $\mathbf{b}$ contain the boundary conditions on the right-hand sides of Eqs. (2.22) and (2.23), and $\mathbf{A}$ is a square matrix of order $4N + 2$ that has the coefficients of the constants $A_0^{\pm}$, $A_n^{\pm}$, and $B_n^{\pm}$ on the left-hand sides of Eqs. (2.22) and (2.23) as its entries. Equation (2.24) can be solved efficiently using the extensive numerical methods available for the solution of matrix equations. We employed here LU decomposition with partial pivoting to solve Eq. (2.24) for $\mathbf{x}$ [173, 174].

To quantify numerical errors in our BVM solutions it is useful to compute, based on the calculated $A_0^{\pm}$, $A_n^{\pm}$, and $B_n^{\pm}$ in Eq. (2.20) with Eq. (2.21), the values of $\left(\bar{u}(\bar{r}, \theta) + \frac{\bar{\tau}}{\bar{a}}\right)$ and $\hat{\mathbf{n}} \cdot \bar{\nabla}\bar{u}(\bar{r}, \theta)$ along the bilayer-protein boundary for a given set of reference points distinct from the boundary points employed for the BVM solution in Eq. (2.24). We compile these

computed boundary values of $\left(\bar{u}(\bar{r}, \theta) + \frac{\bar{\tau}}{\bar{a}}\right)$ and $\hat{\mathbf{n}} \cdot \bar{\nabla}\bar{u}\left(\bar{r}, \theta\right)$ in a vector $\tilde{\mathbf{b}}$, and compare $\tilde{\mathbf{b}}$ to the corresponding exact boundary values $\mathbf{b}'$ mandated by the boundary conditions in Eqs. (2.12) and (2.14),

$$\eta_{b'} = 100 \times \frac{||\tilde{\mathbf{b}} - \mathbf{b}'||_{L^2}}{||\mathbf{b}'||_{L^2}}, \qquad (2.25)$$

where $|| \cdot ||_{L^2}$ is the L^2 norm [173]. For all the results shown in this thesis, we used vectors $\mathbf{b}'$ and $\tilde{\mathbf{b}}$ with 800 components [400 components each for $\left(\bar{U}(\theta) + \frac{\bar{\tau}}{\bar{a}}\right)$ and $\bar{U}'(\theta)$] in Eq. (2.25), which we chose for a given protein shape so as to yield reference points with a uniform spacing in θ over the interval $0 \leq \theta \leq 2\pi$. Figure 2.4(a) shows $\eta_{b'}$ in Eq. (2.25) for the clover-leaf shapes in Eq. (2.17) with $s = 3$ and various values of ϵ. As expected, we find that $\eta_{b'}$ tends to decrease with increasing N in Eq. (2.20) with Eq. (2.21), indicating that a greater accuracy of BVM solutions is obtained at larger N. The local minima of $\eta_{b'}$ in Fig. 2.4(a) correspond to values of N that are multiples of s, which suggests that the accuracy of the BVM is improved if N matches the protein symmetry. Figure 2.4(b) indicates that the convergence of BVM solutions with increasing N can be improved substantially through an APD that allows for a nonuniform distribution of boundary points, which we discuss in Sec. 2.2.2.

We performed our BVM calculations in C++ using the arbitrary precision numerical library *Arb* [175]. Unless stated otherwise, we allowed for sufficient numerical precision so that the boundary error $\eta_{b'} \leq 0.1\%$ in Eq. (2.25) and we obtained changes in G and $\eta_{b'}$ of no more than $10^{-5}\%$ as the numerical precision was increased. We generated all figures in *MATLAB* [176]. To speed up our calculations, we multi-threaded some of the source code
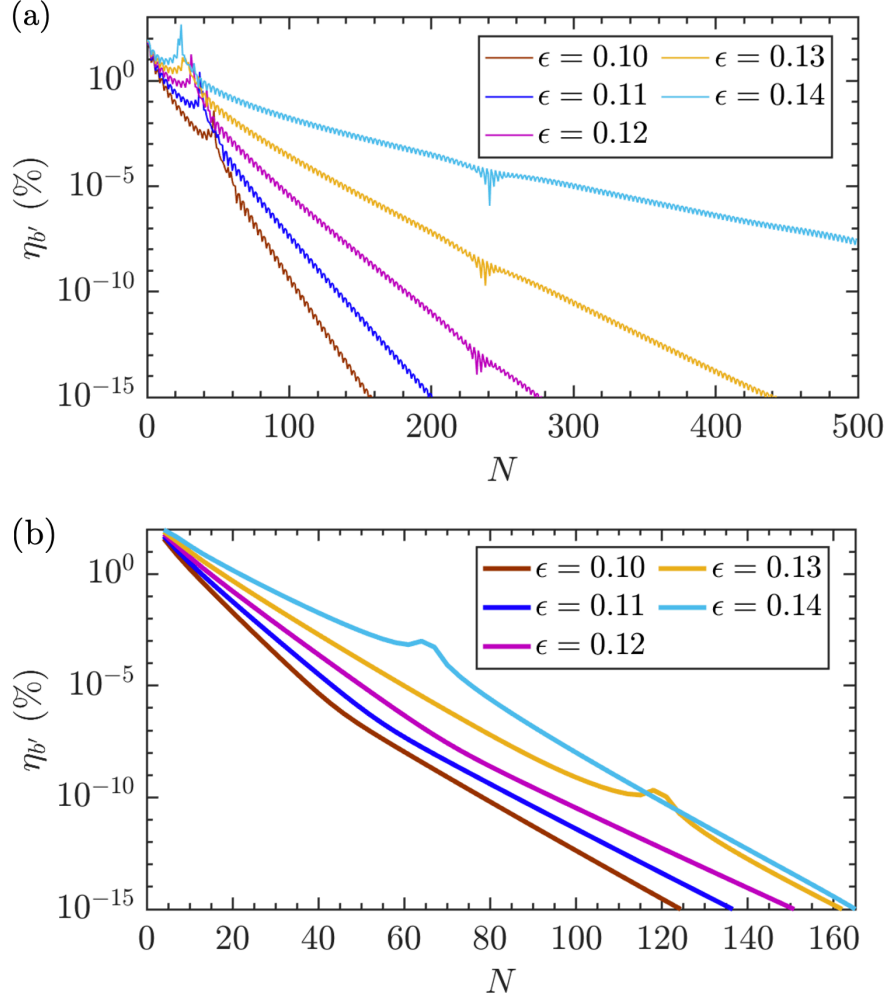
Figure 2.4: Percentage difference between the exact bilayer thickness deformation field along the bilayer-protein boundary and the bilayer thickness deformation field obtained from the BVM solution, $\eta_{b'}$ in Eq. (2.25), as a function of the number of terms in the Fourier-Bessel series in Eq. (2.20) with Eq. (2.21) for (a) uniformly distributed points along the bilayer-protein boundary and (b) the boundary point distributions implied by the APD method (see Sec. 2.2.2). For both panels we considered three-fold clover-leaf protein shapes ($s = 3$) in Eq. (2.17) with the indicated values of ϵ, $\bar{R}\lambda \approx 2.3$ nm, and the constant $\bar{U}\lambda = 0.3$ nm and $\bar{U}' = 0$ and set $\tau = 0$. In panel (b) we used, for ease of comparison, the same gap factor $\Omega = 0.25$ in Eq. (2.28) for all curves.

of the *Arb* library [177]. Appendix A.1 provides a more in-depth description of our computational implementation of the BVM, and discusses possible issues with the numerical solution of Eq. (2.24) arising from floating point errors and numerical instabilities. For the polygonal protein shapes considered here, with $P = 5$ in Eq. (2.18) with Eq. (2.19), and

for the clover-leaf protein shapes considered here with large s and/or large ϵ in Eq. (2.17) we found it convenient to perform the BVM calculations with numerical precision greater than double precision (64 bits). In Appendix A.2 we illustrate the extent to which double precision calculations could be used to approximate the BVM results described here.

In our BVM calculations we evaluate the bilayer thickness deformation energy G in Eq. (2.3) by numerically computing Eq. (2.10) using the same 400 reference points employed to calculate $\eta_{b'}$ in Eq. (2.25). To this end, we approximate $\bar{G}$ in Eq. (2.10) through Eq. (2.20) with Eq. (2.21),

$$\bar{G} \approx \frac{1}{4} \int_0^{2\pi} d\theta \bar{l} \left[\bar{U}' - \left(\bar{U} + \frac{\bar{\tau}}{\bar{a}} \right) \hat{\mathbf{n}} \cdot \bar{\nabla} \right] \left[\bar{\nu}_+ \bar{f}_N^+ + \bar{\nu}_- \bar{f}_N^- \right] \Big|_{\bar{r} = \bar{C}(\theta)}, \tag{2.26}$$

where we have used Eq. (2.7) and the boundary conditions in Eqs. (2.12) and (2.14). We have confirmed that, within the numerical accuracy used here, identical results for $\eta_{b'}$ and $\bar{G}$ are obtained with more than 400 reference points. Note that $\bar{l}$ in Eq. (2.26) is real and that Eq. (2.26) must evaluate to a real number, which means that the remaining terms in the integrand in Eq. (2.26) evaluate to a real number; in the scenarios considered here, we find $\bar{f}_N^+$ and $\bar{f}_N^-$ are complex conjugates so $\left(\bar{f}_N^+ - \bar{f}_N^- \right)$ evaluates to a purely imaginary number and $\left(\bar{f}_N^+ + \bar{f}_N^- \right)$ evaluates to a purely real number.

We validated the BVM for bilayer thickness deformations against exact analytic solutions obtained for proteins with circular cross sections [23, 27, 30, 58, 59, 118] and against FEM solutions [30, 60, 61] (see Fig. 2.5). In particular, we consider in Fig. 2.5 cylindrical membrane proteins with constant U and U' [see Fig. 2.5(a)], for which the exact analytic solution of bilayer thickness deformations simply amounts to the zeroth-order
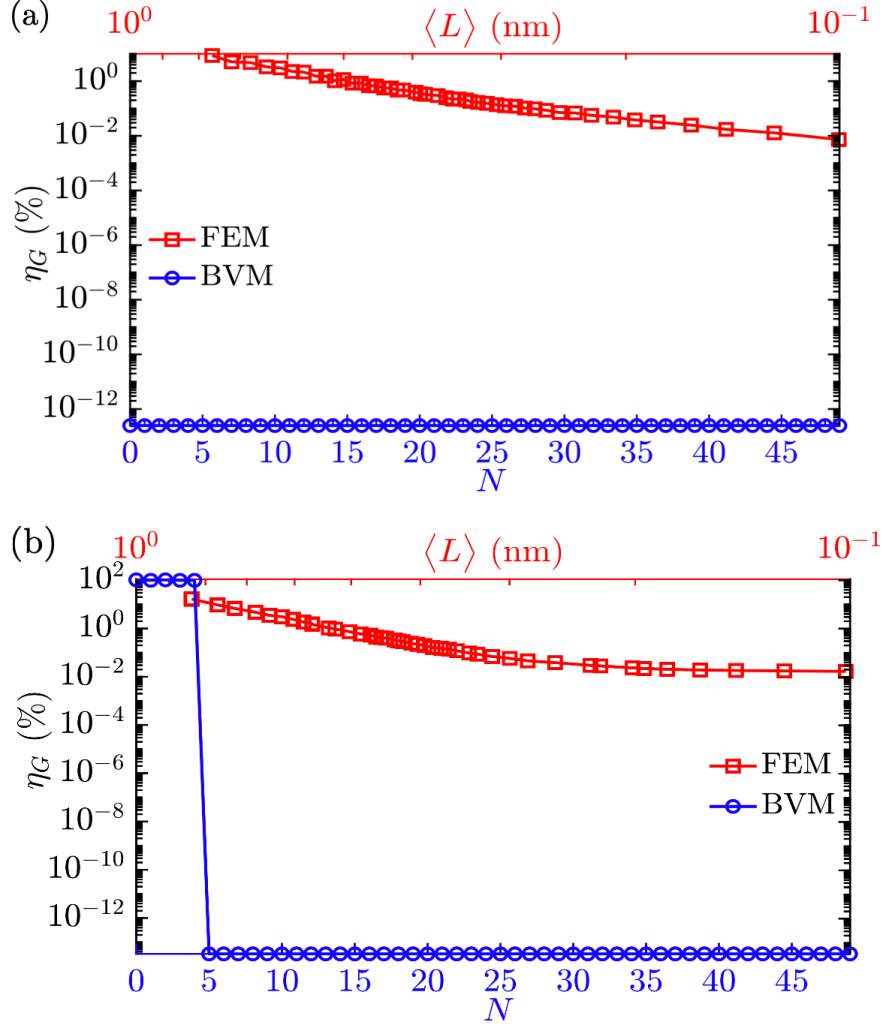
Figure 2.5: Percentage difference between exact analytic and FEM (red curves) or BVM (blue curves) solutions for the bilayer thickness deformation energy, η_G in Eq. (2.27), as a function of the average edge size $\langle L \rangle$ used in the FEM solution (upper axes) or the number of terms in Eq. (2.20) with Eq. (2.21) used in the BVM solution (lower axes) for (a) a cylindrical protein with $\bar{R}\lambda = 2.3$ nm and $\bar{U}\lambda = 0.3$ nm and (b) a crown-shaped protein with $\bar{R}\lambda = 2.3$ nm, $\bar{U}_0\lambda = -0.1$ nm, $\bar{\beta}\lambda = 0.5$ nm, and $w = 5$ in Eq. (2.15). We set $\bar{U}' = 0$ and $\tau = 0$ for both panels.

terms in Eq. (2.20) with Eq. (2.21) [23, 27, 118]. Furthermore, we consider in Fig. 2.5

crown-shaped membrane proteins with circular cross section, constant U', and the peri-

odically varying $U(\theta)$ in Eq. (2.15) [see Fig. 2.5(b)], for which the exact analytic solution

is obtained at order $N = w$ in Eq. (2.20) with Eq. (2.21) [30, 58, 59]. We quantified the

level of agreement between the BVM and FEM solutions and the corresponding exact

analytic solutions through the percentage difference in the calculated bilayer thickness deformation energy G in Eq. (2.3),

$$\eta_G = 100 \times \left| \frac{G - G_{\mathrm{analy}}}{G_{\mathrm{analy}}} \right|, \tag{2.27}$$

where G_{analy} denotes the analytic solution [23, 27, 30, 58, 59, 118] and G denotes the corresponding BVM or FEM solutions. We found, as expected, excellent numerical agreement between the BVM and the aforementioned exact analytic solutions for $N = 0$ [Fig. 2.5(a)] or $N \geq w$ [Fig. 2.5(b)] within floating point error. The FEM solutions in Fig. 2.5 are, up to their expected numerical precision [30], in good agreement with the exact analytic and BVM solutions, with the agreement improving with decreasing average edge size $\langle L \rangle$ in the FEM grid. For both cylindrical and crown-shaped membrane proteins, we have $\eta_G \approx 0.01\%$ for $\langle L \rangle \approx 0.1$ nm in the FEM solutions in Fig. 2.5.

2.2.2 Nonuniform boundary point distributions

As illustrated in Figs. 2.4 and 2.5, the BVM can provide a highly accurate method for calculating protein-induced bilayer thickness deformations. However, Fig. 2.4(a) also shows that, for large enough deviations from a circular protein cross section, accurate BVM solutions require a large number of terms in the Fourier-Bessel series in Eq. (2.20) with Eq. (2.21). For non-circular protein cross sections, the numerical performance of the BVM can be improved substantially by choosing suitable, nonuniform boundary point distributions. In particular, we found that boundary point distributions that assign more points

to, as viewed from the lipid bilayer, concave boundary regions yield a more rapid convergence of G with increasing N. This can be understood intuitively by noting that, in the concave regions of a boundary curve, different sections of the boundary curve can produce overlapping bilayer thickness deformation fields, inducing protein self-interactions. One expects that higher-order terms in the Fourier-Bessel series in Eq. (2.20) with Eq. (2.21) are required to capture such interactions [30, 58].

To assign more boundary points to the concave boundary regions of clover-leaf and (finite-P) polygonal protein shapes, we employ an APD of the BVM boundary points. In the APD method, we distribute the $2N + 1$ boundary points such that boundary points are always assigned to the apex points along the bilayer-protein boundary curves furthest away from the protein center (see Fig. 2.6). We distribute the remaining boundary points along the sections of the bilayer-protein boundary curves that are an arc length $\bar{l} \geq \bar{\ell}$ away from the apex points such that these points are uniformly spaced in arc length, with the gap length

$$\bar{\ell} = \Omega \frac{\bar{\Gamma}}{2s} \,, \tag{2.28}$$

where the gap factor Ω satisfies $0 < \Omega < 1$, $\bar{\Gamma}$ is the (dimensionless) protein circumference, and s is the symmetry of the clover-leaf or polygonal protein shape [see also Eqs. (2.17) and (2.18)] (Fig. 2.6). For even values of s, we consider in our APD method the general solution in Eq. (2.20) with Eq. (2.21) for $N = sM/2$ with integers $M \geq 3$. For odd values of s, we allow in Eq. (2.20) with Eq. (2.21) for $N = sM/2$ for even integers $M \geq 3$, and for $N = (sM - 1)/2$ for odd integers $M \geq 3$. To achieve an approximately periodic distribution of boundary points for even s and for odd s with even M, we found it convenient
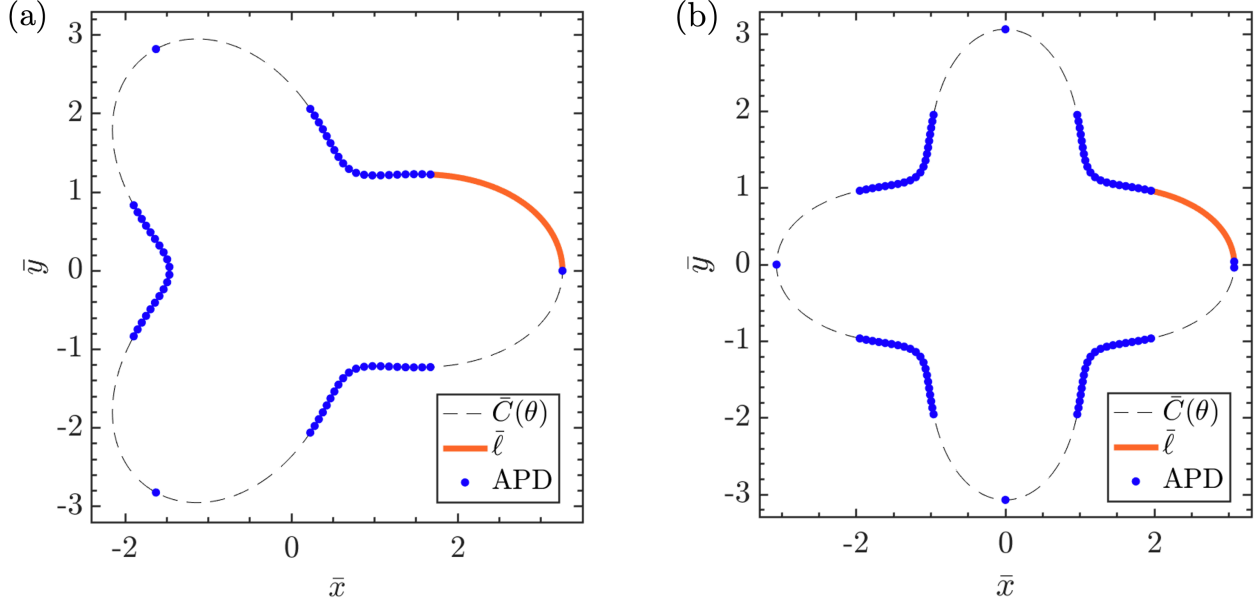
Figure 2.6: Illustration of the APD method used to increase the numerical efficiency of BVM solutions for (a) a three-fold clover-leaf protein shape ($s = 3$) and (b) a four-fold clover-leaf protein shape ($s = 4$) in Eq. (2.17). The boundary points used for the BVM solutions are indicated by blue dots. In panel (a) we set $\epsilon = 0.38$, $N = 31$, and $\Omega = 0.62$ for the gap length $\bar{\ell}$ in Eq. (2.28). In panel (b) we set $\epsilon = 0.30$, $N = 42$, and $\Omega = 0.72$. For both panels we set $\bar{R}\lambda \approx 2.3$ nm and $\tau = 0$. To achieve an approximately periodic distribution of boundary points for even s, we duplicated in panel (b) the boundary point at the right-most apex, and slightly offset the resulting two boundary points along the bilayer-protein interface (see main text). The values of N in panels (a) and (b) were chosen for illustrative purposes. We generally employ values of N greater than those considered here so as to meet the numerical precision criteria imposed here (see main text).

to duplicate one of the apex boundary points, with a slight offset in the duplicated boundary points by an equal arc length distance from the apex [see Fig. 2.6(b)]. For greater numerical accuracy, this distance from the apex could be optimized so as to reduce the boundary error $\eta_{b'}$ in Eq. (2.25), but we found it sufficient here to set it equal to one-half the arc length spacing between the boundary points in the concave boundary regions. Unless stated otherwise, we used the APD method for all BVM calculations described in

this article, fixing Ω in Eq. (2.28) and N in Eq. (2.20) with Eq. (2.21) such that the boundary error $\eta_{b'} \leq 0.1\%$ in Eq. (2.25) and we obtained changes in G and $\eta_{b'}$ of no more than $10^{-5}\%$ as the numerical precision was increased.

As illustrated in Fig. 2.4(b) for clover-leaf protein shapes, the APD method employed here improves considerably the convergence of the BVM with increasing N, particularly for proteins that show substantial deviations from a circular cross section. As a result, a given numerical accuracy of BVM solutions can be achieved with smaller N. We note that, for proteins with (discrete) rotational symmetry, the Fourier-Bessel series in Eq. (2.20) with Eq. (2.21) must show the same symmetry. Indeed, in our BVM calculations we find that, within the numerical precision employed here, the coefficients of terms in Eq. (2.20) with Eq. (2.21) that break the protein symmetry take values equal to zero. On this basis one could, for a given protein symmetry, further improve the numerical efficiency of the BVM by using the protein symmetry to remove some of the terms in the Fourier-Bessel series in Eq. (2.20) with Eq. (2.21). For the scenarios considered here the BVM was efficient enough so as not to require such further refinement.

Figure 2.7 illustrates the calculation of the bilayer thickness deformation energy, G in Eq. (2.3), using the BVM with APD for the clover-leaf protein shapes in Eq. (2.17) with various protein symmetries, s, and deviations from a circular protein cross section, ϵ. As expected [59, 61], we find in Fig. 2.7(a) that G increases with increasing s and ϵ. We also show in Fig. 2.7 the corresponding results obtained from the FEM with an average edge
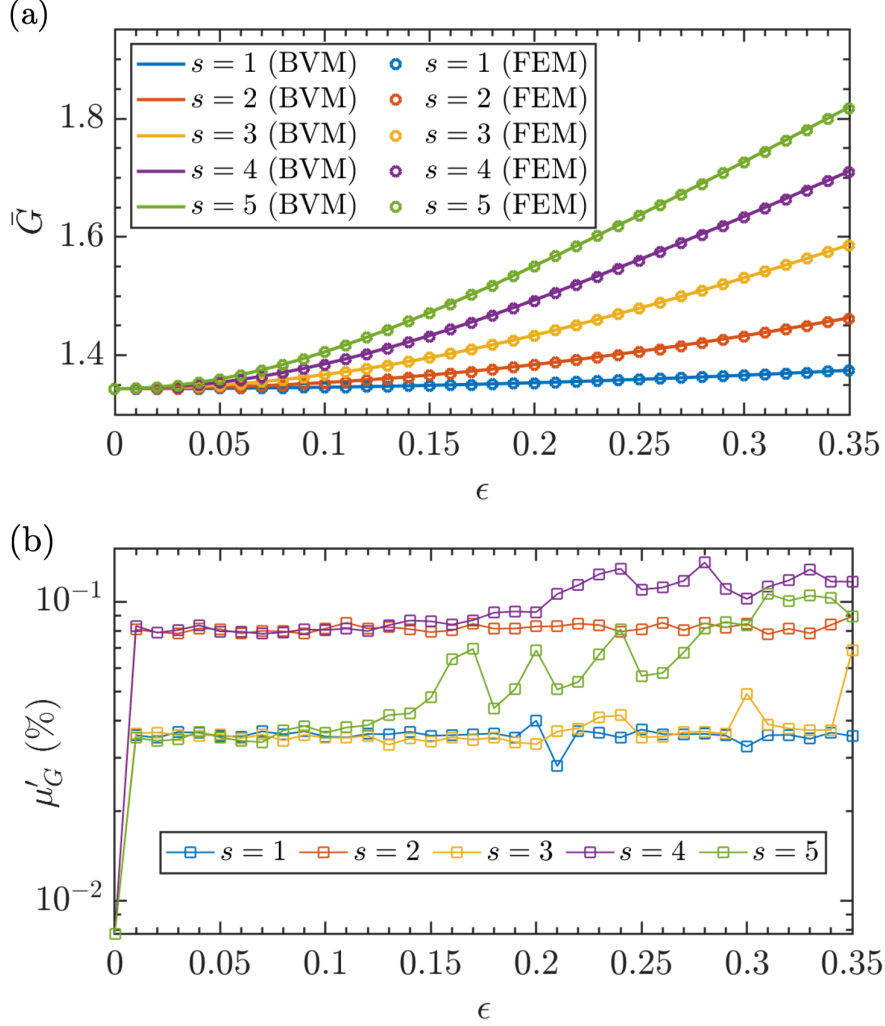
Figure 2.7: Comparing BVM and FEM solutions for the elastic energy of clover-leaf protein-induced bilayer thickness deformations. (a) Bilayer thickness deformation energy, $\bar{G}$ in Eq. (2.6), with $\tau = 0$, obtained using BVM and FEM solutions for $\bar{u}$ in Eq. (2.2) and (b) corresponding percentage difference between the BVM and FEM solutions for $\bar{G}$, μ'_G in Eq. (2.29), for the clover-leaf protein shapes in Eq. (2.17) as a function of ϵ with the indicated values of s, $\bar{R}\lambda \approx 2.3$ nm, $\bar{U}\lambda = 0.3$ nm, and $\bar{U}' = 0$. For the FEM solutions we employed an average edge size $\langle L \rangle \approx 0.1$ nm.

size $\langle L \rangle \approx 0.1$ nm. In Fig. 2.7(b) we quantify the agreement between our BVM and FEM

results through the percentage difference in G,

$$\mu'_G = 100 \times \left| \frac{G_{\text{BVM}} - G_{\text{FEM}}}{G_{\text{FEM}}} \right|, \tag{2.29}$$

44

where G_{BVM} and G_{FEM} correspond to the values of G in Eq. (2.3) obtained through the BVM and the FEM [30, 60, 61], respectively. Figure 2.8(a), shows the percentage error of the bilayer thickness deformation and contact slope fields at the protein-bilayer interface obtained from the BVM solution, $\eta_{b'}$ in Eq. (2.25), with APD as a function of the number of terms in the Fourier-Bessel series in Eq. (2.20) with Eq. (2.21) for the pentamer ($s = 5$) polygon protein shapes using the P values indicated, showing convergence with an increasingly smaller error with an increasing number of terms in the Fourier-Bessel series in Eq. (2.20) with Eq. (2.21). The local minima of $\eta_{b'}$ in Fig. 2.8(a) correspond to values of N that are multiples of s, which suggests that the accuracy of the BVM is improved if N matches the protein symmetry. We also performed calculations using the FEM, but for true polygon protein shapes, rather than those implied by Eqs. (2.18) and (2.19) with finite P. As such, the polygon protein shapes used in the FEM solutions differ slightly from those in the BVM solutions. As expected we find increasing agreement between the FEM and BVM solutions with increasing P in Eqs. (2.18) and (2.19) as these are expected to yield true polygonal protein shapes in the limit of $P \to \infty$ [see Figure 2.8(b)]. Our results indicate that using $P = 5$ is sufficient for our BVM solutions to agree remarkably well with the FEM solutions. We find in Figs. 2.7 and 2.8 that the BVM and FEM solutions yield excellent agreement for the energy of protein-induced bilayer thickness deformations for non-circular as well as circular protein cross sections, with the level of agreement between BVM and FEM solutions being in line with the accuracy of the FEM solutions expected from Fig. 2.5.
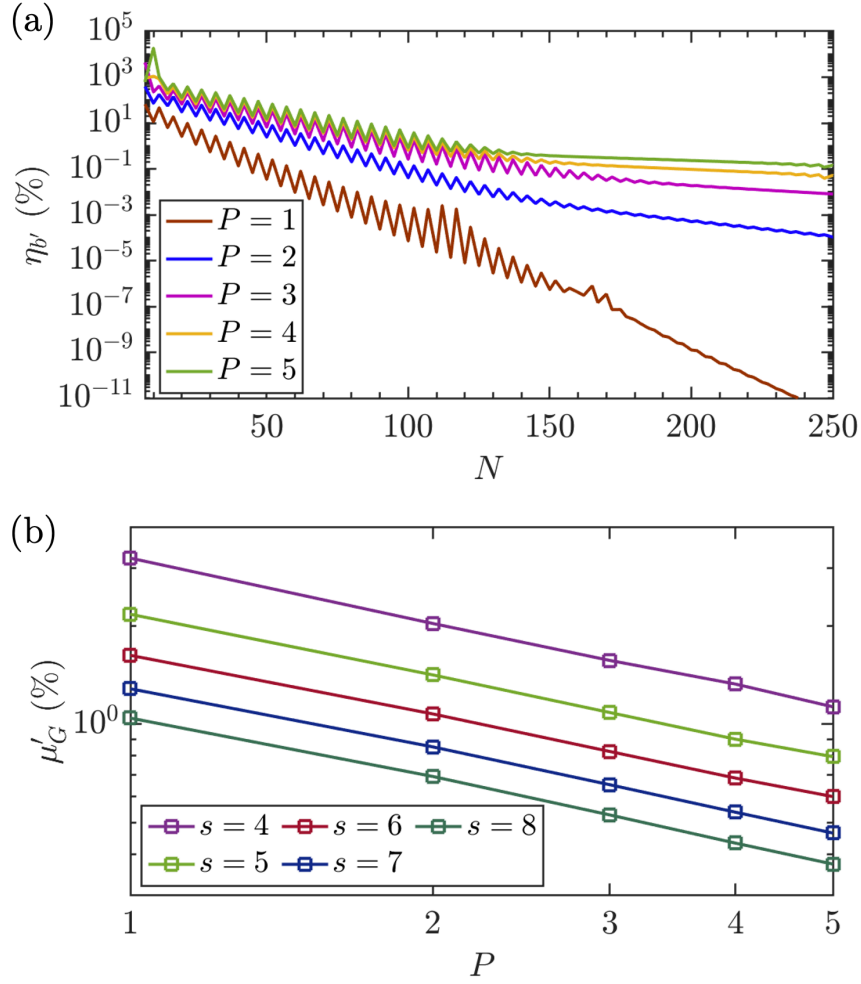
Figure 2.8: Convergence of BVM solutions for the elastic energy of polygon protein-induced bilayer thickness deformations. (a) Percentage difference between the exact bilayer thickness deformation field along the bilayer-protein boundary and the bilayer thickness deformation field obtained from the BVM solution, $\eta_{b'}$ in Eq. (2.25), as a function of the number of terms, N, in the Fourier-Bessel series in Eq. (2.20) with Eq. (2.21) for the boundary point distributions implied by the APD method (see Sec. 2.2.2), using the indicated values of P in Eq. (2.18) and (2.19) with $s = 5$. (b) Percentage difference between the FEM and BVM solutions for $\bar{G}$, μ'_G in Eq. (2.29), where we calculated the BVM solutions for the polygon protein shapes in Eqs. (2.18) and (2.19) as a function of P and with the indicated values of s, $\bar{R}\lambda \approx 2.3$ nm, $\bar{U}\lambda = 0.3$ nm, $\bar{U}' = 0$, $N = 750$, and $\Omega \approx 0.32$, 0.24, 0.18, 0.16, and 0.16, for symmetries $s = 4$, 5, 6, 7, and 8, respectively, in Eq. (2.28), while for the FEM solutions we employed an average edge size $\langle L \rangle \approx 0.1$ nm and used true polygon shapes, in contrast to those implied by Eqs. (2.18) and (2.19) with finite P. For all BVM and FEM solutions depicted here, we set $\tau = 0$.

Chapter 3

Dependence of protein-induced lipid bilayer deformations on protein shape

In this chapter we apply our BVM to survey the dependence of protein-induced lipid bilayer thickness deformations on protein shape. This chapter is organized as follows. In Sec. 3.1, inspired by the BVM (see Chapter 2), we develop a simple analytic scheme for estimating the energy of protein-induced lipid bilayer thickness deformations for membrane proteins with non-circular cross sections. In Secs. 3.2 and 3.3 we test this analytic approximation against BVM solutions. In Sec. 3.2, we survey the dependence of the bilayer thickness deformation energy on membrane protein shape, while in Sec. 3.3 we explore some implications of these results for the self-assembly of protein oligomers and transitions in protein conformational state. A summary and conclusions are provided in Sec. 6.2.

3.1 Analytic approximation of the bilayer thickness deformation energy

For membrane inclusions with circular cross section, the solution for the thickness deformation field $\bar{u}(\bar{r}, \theta)$ in Eq. (2.8) with Eq. (2.9) and the bilayer thickness deformation energy in Eq. (2.10) yield exact analytic expressions for the energy of protein-induced bilayer thickness deformations for arbitrary (angular) variations in the bilayer-protein boundary conditions [23–25, 30, 58, 59, 61]. The purpose of this section is to develop, on this basis, a simple analytic scheme for estimating the energy of protein-induced bilayer thickness deformations for membrane proteins with non-circular cross sections. In Sec. 3.2 we show that, for many protein shapes, these simple analytic estimates agree remarkably well with the corresponding BVM solutions.

As in Chapter 2, it is convenient to recast the bilayer thickness deformation energy in Eq. (2.3) in terms of the characteristic spatial and energy scales, the bilayer thickness deformation decay length scale λ and the bilayer bending ridigity K_b. Thus, consistent with Chapter 2, we reformulate Eq. (2.3) with the following parameter substitutions: $\bar{G}K_b \to G$, $\bar{x}\lambda \to x$, $\bar{y}\lambda \to y$, $\bar{u}\lambda \to u$, $\bar{a}\lambda \to a$, $\bar{K}_t K_b/\lambda^2 \to K_t$, and $\bar{\tau}K_b/\lambda^2 \to \tau$. We maintain specific values for $\bar{U}_0\lambda = -0.1$ nm and $\bar{\beta}\lambda = 0.5$ nm in Eq. (2.15) in calculations involving variations in the bilayer-protein hydrophobic mismatch. Furthermore, we set $\bar{U}_0' = 0$ and $\bar{\gamma} = 0.3$ in Eq. (2.16) in calculations involving variations in the bilayer-protein contact slope. In scenarios where we maintain $\bar{U}$ or $\bar{U}'$ constant along the bilayer-protein interface, we set $\bar{U}\lambda = 0.3$ nm or $\bar{U}' = 0$, unless otherwise specified. These parameter values align

with previous studies on MscL and gramicidin channels [28, 31, 42, 91, 118]. Additionally, unless explicitly stated, we adopt a value of $P = 5$ in Eqs. (2.18) and (2.19), and we assume $\bar{R}\lambda \approx 2.3$ nm in Eqs. (2.17) and (2.19), roughly corresponding to the observed size of a closed state of MscL [27, 42]. For the sake of simplicity, we exclude considerations of lateral membrane tension in this chapter by setting $\tau = 0$.

For a single membrane inclusion with circular cross section and arbitrary (angular) variations in $U(\theta)$ and $U'(\theta)$, the exact solution of the Euler-Lagrange equation in Eq. (2.7) is given by Eq. (2.8) with Eq. (2.9), and the corresponding bilayer thickness deformation energy follows from Eq. (2.10) [30, 58, 59, 61]. For the choices for $U(\theta)$ and $U'(\theta)$ in Eqs. (2.15) and (2.16), and assuming membrane tension $\tau = 0$, one thus finds the bilayer thickness deformation energy

$$
\begin{aligned}
\bar{G}_{\text{analy}} = \pi \bar{R}_{\text{analy}} (\bar{\nu}_+ - \bar{\nu}_-) \bigg[& \bar{U}_0^2 \bar{E}_0 + \bar{U}_0'^2 \bar{F}_0 + \bar{U}_0 \bar{U}_0' \bar{H}_0 \\
& + \frac{1}{2} \left(\bar{\beta}^2 \bar{E}_w + \bar{\gamma}^2 \bar{F}_v + \delta_{wv} \bar{\beta}\, \bar{\gamma} \bar{H}_w \right) \bigg] \bigg|_{\bar{r} = \bar{R}_{\text{analy}}}
\end{aligned}
\tag{3.1}
$$

with $v > 0$ and $w > 0$, where $\bar{R}_{\text{analy}}$ is the radius of the circular protein cross section, δ_{wv} is the Kronecker delta, and we have defined

$$
\begin{aligned}
\bar{D}_q &= K_q(\sqrt{\bar{\nu}_+}\bar{r})\partial_{\bar{r}} K_q(\sqrt{\bar{\nu}_-}\bar{r}) - K_q(\sqrt{\bar{\nu}_-}\bar{r})\partial_{\bar{r}} K_q(\sqrt{\bar{\nu}_+}\bar{r}) \,, \\
\bar{E}_q &= \frac{[\partial_{\bar{r}} K_q(\sqrt{\bar{\nu}_+}\bar{r})]\,[\partial_{\bar{r}} K_q(\sqrt{\bar{\nu}_-}\bar{r})]}{\bar{D}_q} \,, \\
\bar{F}_q &= \frac{K_q(\sqrt{\bar{\nu}_+}\bar{r}) K_q(\sqrt{\bar{\nu}_-}\bar{r})}{\bar{D}_q} \,, \\
\bar{H}_q &= \frac{K_q(\sqrt{\bar{\nu}_+}\bar{r})\partial_{\bar{r}} K_q(\sqrt{\bar{\nu}_-}\bar{r}) + K_q(\sqrt{\bar{\nu}_-}\bar{r})\partial_{\bar{r}} K_q(\sqrt{\bar{\nu}_+}\bar{r})}{\bar{D}_q} \,,
\end{aligned}
\tag{3.2}
$$

where $q = 0, 1, \ldots$, K_q denotes the qth order modified Bessel function of the second kind, and $\partial_{\bar{r}}$ denotes the partial derivative with respect to $\bar{r}$. The E_0, F_0, and H_0 terms in Eq. (3.1) are the contributions to $\bar{G}_{\text{analy}}$ due to the constant $\bar{U}_0$ and $\bar{U}'_0$ in Eqs. (2.15) and (2.16), while the remaining terms encapsulate the effects of the variations in $U(\theta)$ and $U'(\theta)$ in Eqs. (2.15) and (2.16) on $\bar{G}_{\text{analy}}$. We use here Eq. (3.1) to analytically estimate the energy of protein-induced bilayer thickness deformations for membrane proteins with non-circular cross sections. To this end, we choose $\bar{R}_{\text{analy}}$ in Eq. (3.1) such that the circumference of the circular membrane inclusion considered in Eq. (3.1) is equal to the circumference of the membrane protein under consideration,

$$\bar{R}_{\text{analy}} = \frac{\bar{\Gamma}}{2\pi} \,, \tag{3.3}$$

where, for the clover-leaf and polygonal boundary curves in Eqs. (2.17) and (2.18) with Eq. (2.19), the protein circumference Γ follows from $\bar{\Gamma} = \int_0^{2\pi} d\theta \bar{l}$, where, as in Eq. (2.10), $\bar{l}$ is the (dimensionless) line element.

The analytic estimate of the thickness deformation energy in Eq. (3.1) captures, for the choice of $\bar{R}_{\text{analy}}$ in Eq. (3.3), effects related to the overall shape of membrane proteins. However, Eq. (3.1) does not capture effects due to strong local variations in the protein cross section. For instance, the clover-leaf shapes in Eq. (2.17) can give, for large enough ϵ and s, protein cross sections with pronounced invaginations. If the protein size R is comparable to the decay length of bilayer thickness deformations, λ in Eq. (2.5), such protein invaginations can yield overlaps in the protein-induced lipid bilayer thickness deformations due to different portions of the bilayer-protein interface, resulting in
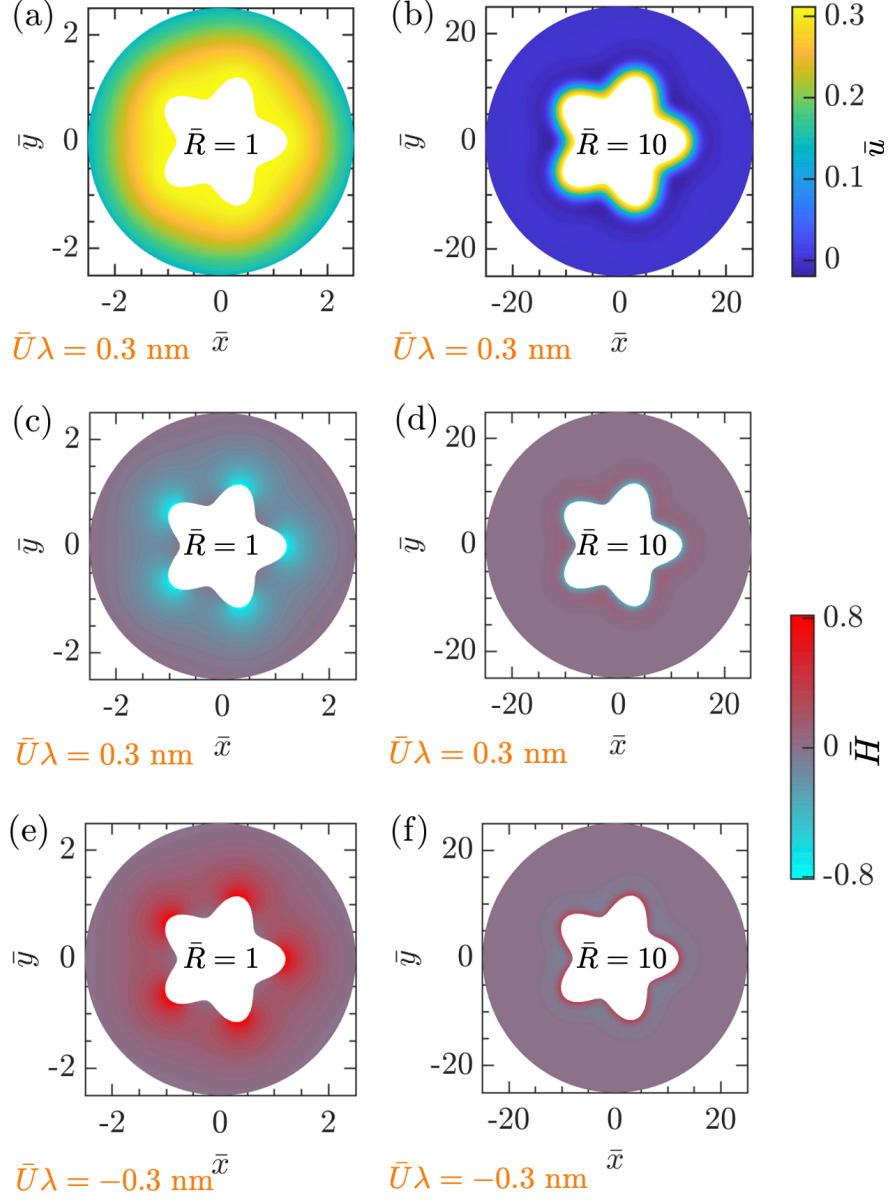
Figure 3.1: Color maps of the bilayer thickness deformation footprints due to clover-leaf protein shapes with (a) $\bar{R} = 1$ and (b) $\bar{R} = 10$ in Eq. (2.17) for $s = 5$, $\epsilon = 0.2$, $\bar{U}\lambda = 0.3$ nm in Eq. (2.15), and $\bar{U}' = 0$. Panels (c) and (d) show the mean curvature in units of $1/\lambda$, $\bar{H} = \lambda H$, associated with the thickness deformation fields in panels (a) and (b), respectively, while panels (e) and (f) show the corresponding mean curvature maps obtained for $\bar{U}\lambda = -0.3$ nm in Eq. (2.15) rather than $\bar{U}\lambda = 0.3$ nm. We set $2\bar{a}\lambda = 3.2$ nm and $\tau = 0$ for all panels. All results were obtained through the BVM.

protein self-interactions [see Fig. 3.1(a)]. As $\bar{R}$ is increased, these overlaps in protein-induced bilayer thickness deformations become less pronounced [see Fig. 3.1(b)]. Depending on the value of $\bar{R}$, one thus obtains distinct distributions of the mean curvature

of $\bar{u}$ about the protein [see Figs. 3.1(c,d)], which also depend on the value and sign of $\bar{U}$ [see Figs. 3.1(e,f)].

To quantify the protein self-interactions suggested by Fig. 3.1 it is useful to define, based on Eq. (2.10), the line tension along the bilayer-protein interface,

$$\bar{\Lambda} \equiv \left[\bar{U}'(\theta)\bar{\nabla}^2\bar{u} - \bar{U}(\theta)\hat{\mathbf{n}} \cdot \bar{\nabla}^3\bar{u} \right] \big|_{\bar{r}=\bar{C}(\theta)}, \tag{3.4}$$

where we used Eqs. (2.12) and (2.14) with lateral membrane tension $\tau = 0$. In Figs. 3.2(a) and 3.2(b) we compare, for the protein shapes in Figs. 3.1(a) and 3.1(b) with constant $\bar{U} > 0$ and $\bar{U}' = 0$, the line tensions $\bar{\Lambda}$ in Eq. (3.4) and their average values $\langle \bar{\Lambda} \rangle$ to the corresponding $\bar{\Lambda}$ associated with $\bar{G}_{\mathrm{analy}}$ in Eq. (3.1), which we denote by $\bar{\Lambda}_{\mathrm{analy}}$. As expected, Fig. 3.2 shows that the variations in $\bar{\Lambda}$ are more pronounced for smaller clover-leaf protein shapes. We also find in Fig. 3.2 that $\langle \bar{\Lambda} \rangle < \bar{\Lambda}_{\mathrm{analy}}$, with a larger $\left| \langle \bar{\Lambda} \rangle - \bar{\Lambda}_{\mathrm{analy}} \right|$ for smaller $\bar{R}$ in Fig. 3.2.

Interestingly, we can have $\bar{\Lambda} < 0$ in Fig. 3.2(a) for the smaller clover-leaf protein shape in Fig. 3.1(a), while $\bar{\Lambda} > 0$ in Fig. 3.2(b) for the larger clover-leaf protein shape in Fig. 3.1(b). The regime with $\bar{\Lambda} < 0$ in Fig. 3.2(a) can be understood by noting that, with a constant $\bar{U} > 0$ and $\bar{U}' = 0$, $\bar{\Lambda}$ in Eq. (3.4) is directly proportional to the change in the mean curvature of $\bar{u}$ at the protein boundary, in the direction perpendicular to the protein-bilayer boundary and into the bilayer $(-\hat{\mathbf{n}})$. For the points along the clover-leaf boundary closest and furthest away from the protein center, $\hat{\mathbf{n}}$ is anti-parallel with the radial direction $\hat{\mathbf{r}}$. For the points along the clover-leaf boundary shape in Figs. 3.1(a) and 3.1(b)
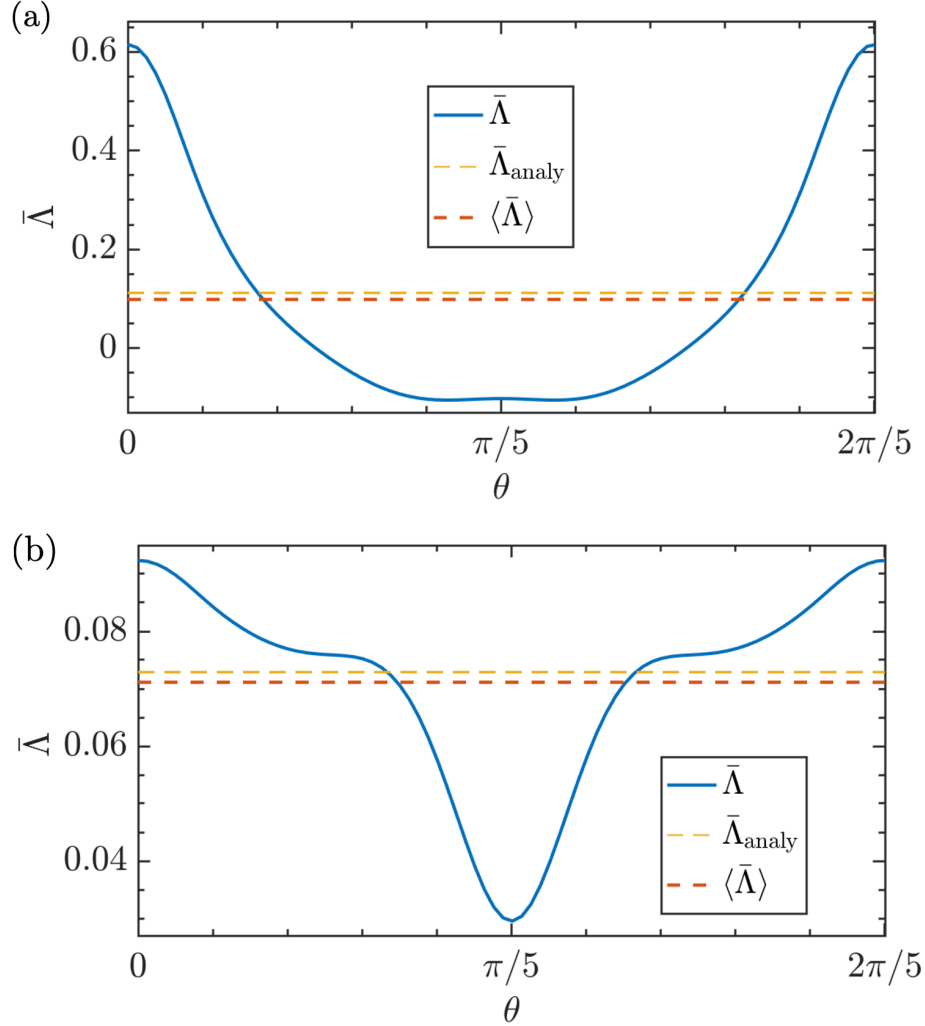
Figure 3.2: Line tension along the bilayer-protein boundary, $\bar{\Lambda}$ in Eq. (3.4), as a function of θ for (a) the protein shape in Fig. 3.1(a) and (b) the protein shape in Fig. 3.1(b), calculated using the same parameter values as in Fig. 3.1. The red dashed lines show the average of $\bar{\Lambda}(\theta)$ in Eq. (3.4) over the interval $0 \leq \theta \leq 2\pi/5$, $\langle \bar{\Lambda} \rangle$. The yellow dashed lines show $\bar{\Lambda}_{\mathrm{analy}} = \bar{G}_{\mathrm{analy}}/\bar{\Gamma}$, where $\bar{G}_{\mathrm{analy}}$ is given by Eq. (3.1) and $\bar{\Gamma}$ is the protein circumference in Eq. (3.3).

furthest away from the protein center the mean curvature is negative with the sign convention used here and decreases in magnitude as one radially moves away from the protein boundary, yielding $\bar{\Lambda} > 0$ [Figs. 3.1(c,d)]. In contrast, for the points along the clover-leaf boundary shape closest to the protein center in Fig. 3.1(a) [but not Fig. 3.1(b)], the mean curvature is approximately zero at the protein boundary and decreases as one radially

moves away from the protein boundary, yielding $\bar{\Lambda} < 0$. With a different sign convention for the mean curvature or a protein with a constant $\bar{U} < 0$ rather than $\bar{U} > 0$, analogous considerations apply [Figs. 3.1(e,f)]. Thus, protein self-interactions can effectively lower the energy cost of protein-induced lipid bilayer thickness deformations, in analogy to the energetically favorable bilayer-thickness-mediated protein interactions found for identical membrane proteins in close enough proximity [22, 24, 25, 30, 41, 57, 58, 60, 61, 157, 161, 178–183].

3.2 Dependence of bilayer thickness deformation energy on protein shape

In this section we survey the dependence of the bilayer thickness deformation energy in Eq. (2.3) on the shape of membrane proteins. In particular, we allow for three distinct, not mutually exclusive, modes for breaking rotational symmetry about the protein center (see also Sec. 2.1.2). In Sec. 3.2.1 we take the bilayer-protein boundary conditions to be constant along the protein circumference, but allow for protein cross sections that break rotational symmetry about the protein center. In Sec. 3.2.2 we explore the effect of variations in the protein hydrophobic thickness on protein-induced bilayer thickness deformations. Finally, in Sec. 3.2.3 we study protein-induced bilayer thickness deformations for proteins that show variations in the bilayer-protein contact slope along the bilayer-protein boundary. To test the analytic approximation of the bilayer thickness deformation energy described in Sec. 3.1 we compare, for all three scenarios considered in Secs. 3.2.1–3.2.3,

our BVM results to the corresponding analytic estimates by computing the signed percent error

$$\xi_G = 100 \times \frac{\bar{G}_{\mathrm{analy}} - \bar{G}}{\bar{G}}, \tag{3.5}$$

where $\bar{G}$ is the thickness deformation energy in Eq. (2.6) obtained through the BVM and the corresponding analytic estimate $\bar{G}_{\mathrm{analy}}$ is given by Eq. (3.1) with Eq. (3.2).

3.2.1 Constant bilayer-protein boundary conditions

In Fig. 3.3 we consider the energy of protein-induced bilayer thickness deformations for clover-leaf [see Figs. 3.3(a,b,c)] and polygonal [see Fig. 3.3(d)] protein shapes as a function of protein size $\bar{R}$ with a constant $\bar{U} \neq 0$ and $\bar{U}' = 0$. Previous work on the lipid bilayer thickness deformations induced by proteins with circular cross section [27, 102] suggests that, for $\bar{R} \gg 1$, $\bar{G}$ increases approximately linearly with $\bar{R}$. We find in Fig. 3.3 that we also approximately have $\bar{G} \propto \bar{R}$ for non-circular protein cross sections, with the (positive) constant of proportionality depending on the protein shape. The analytic estimates $\bar{G}_{\mathrm{analy}}$ obtained from Eq. (3.1) match $\bar{G}$ in Fig. 3.3 within approximately 10%, with particularly small magnitudes of the signed percent error $\xi_{\bar{G}}$ for the polygonal protein shapes in Fig. 3.3(d). Note that for protein sizes R comparable to the decay length λ we generally have $\xi_{\bar{G}} > 0$ in Fig. 3.3, indicating that protein self-interactions tend to lower the energy cost of protein-induced bilayer thickness deformations in Fig. 3.3.

The energy cost of protein-induced bilayer thickness deformations depends crucially on the unperturbed lipid bilayer thickness, which can be varied by changing the lipid chain length m in Eq. (2.4) [14, 21, 22, 40]. In Fig. 3.4 we plot $\bar{G}$ for clover-leaf [see

55
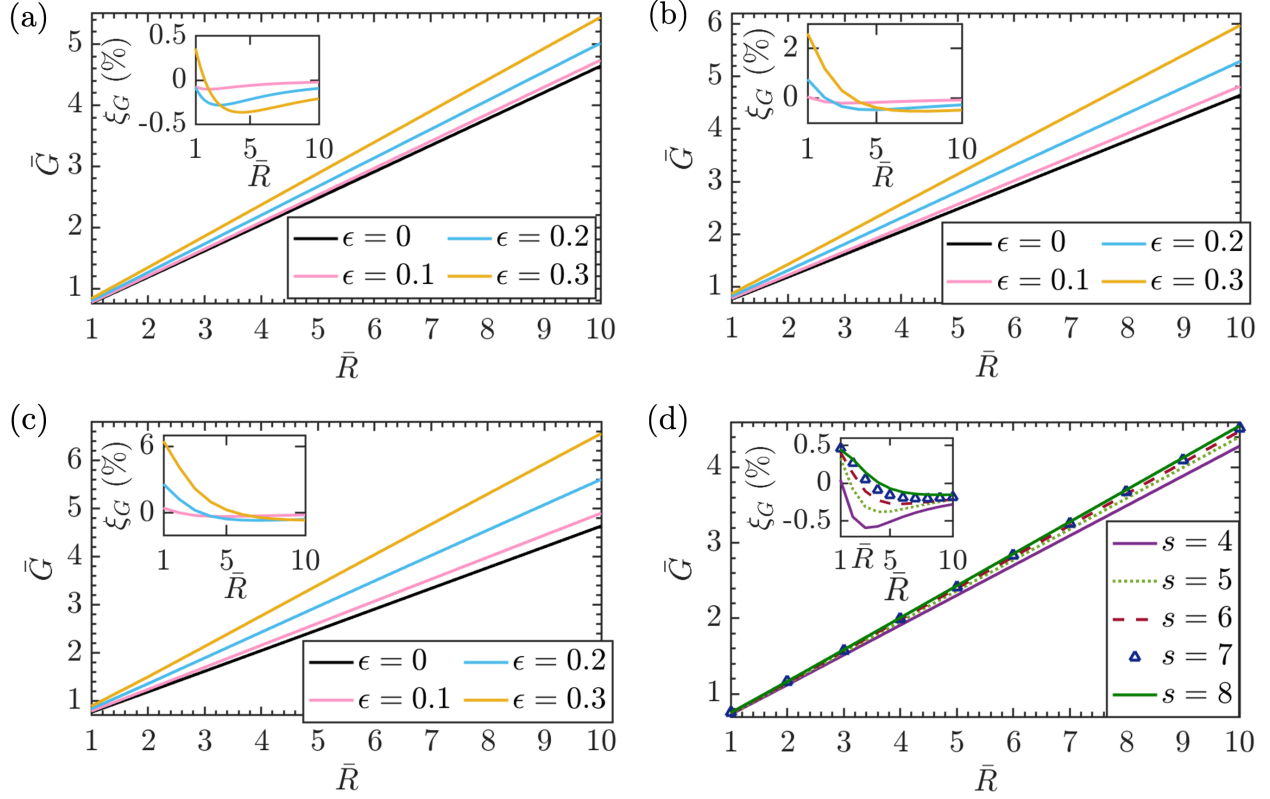
Figure 3.3: Bilayer thickness deformation energy $\bar{G}$ in Eq. (2.6) calculated using the BVM (see Sec. 2.2) as a function of protein size $\bar{R}$ for clover-leaf protein shapes with (a) $s = 3$, (b) $s = 4$, and (c) $s = 5$ in Eq. (2.17) with the indicated values of ϵ, and (d) polygonal protein shapes with the indicated values of s and $P = 5$ in Eq. (2.18). For all panels we set $\bar{U}\lambda = 0.3$ nm and $\bar{U}' = 0$ and $\tau = 0$. The insets show the signed percent error ξ_G in Eq. (3.5) for the corresponding analytic approximations $\bar{G}_{\text{analy}}$ in Eq. (3.1).

Figs. 3.4(a,b)] and polygonal [see Fig. 3.4(c)] protein shapes as a function of the lipid chain length m with $\bar{U}' = 0$. We used a protein hydrophobic thickness $\bar{W}\lambda = 3.8$ nm, which matches the unperturbed lipid bilayer thickness for $m \approx 16$. In Fig. 3.4(a) we consider clover-leaf protein shapes with different symmetries s and the same value of ϵ, while in Fig. 3.4(b) we consider clover-leaf protein shapes with different values of ϵ and the same symmetry s. Similarly as in Fig. 3.3 we find that deviations from a circular protein cross section increase $\bar{G}$. Furthermore, similarly as in Fig. 3.3, the dependence of $\bar{G}$ on m
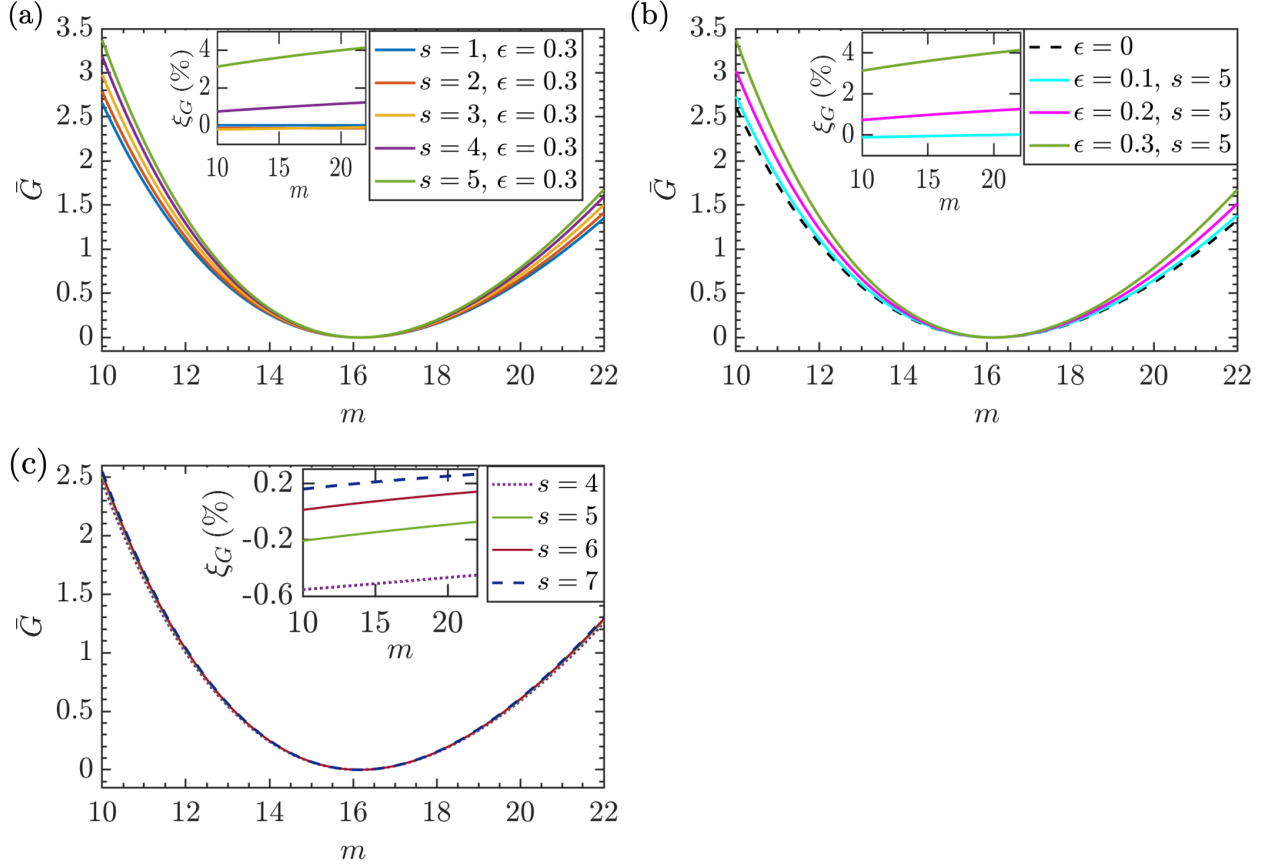
Figure 3.4: Bilayer thickness deformation energy $\bar{G}$ in Eq. (2.6) calculated using the BVM (see Sec. 2.2) as a function of lipid chain length m in Eq. (2.4) for (a) clover-leaf protein shapes with $\epsilon = 0.3$ and the indicated values of s, (b) clover-leaf protein shapes with $s = 5$ and the indicated values of ϵ, and (c) polygonal protein shapes with the indicated values of s and $P = 5$ in Eq. (2.18). For all panels we set $\tau = 0$, $\bar{U}' = 0$, $\bar{W}\lambda = 3.8\,\mathrm{nm}$ in Eq. (2.13), and $\bar{R}\lambda \approx 2.3\,\mathrm{nm}$. The insets show the signed percent error ξ_G in Eq. (3.5) for the corresponding analytic approximations $\bar{G}_{\mathrm{analy}}$ in Eq. (3.1). We always have $|\bar{U}| > 0$ for the m-discretization used here.

in Fig. 3.4 is very well captured by the analytic approximation $\bar{G}_{\mathrm{analy}}$ in Eq. (3.1), suggest-

ing that the increase in $\bar{G}$ for clover-leaf and polygonal protein cross sections compared

to circular protein cross sections results primarily from the increase in the length of the

bilayer-protein boundary $\bar{\Gamma}$ due to deviations from a circular protein cross section.

In Figs. 3.3 and 3.4 we set, in line with previous work on gramicidin channels and

MscL [23, 27, 102], $U' = 0$. As noted in Sec. 2.1, however, the most suitable choice for
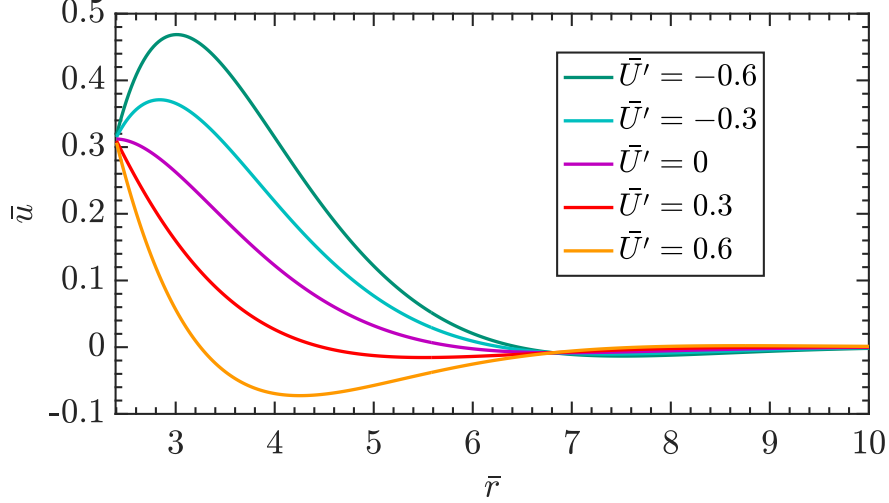
Figure 3.5: Bilayer thickness deformation profile $\bar{u}$ due to a protein with a circular cross section as a function of the radial distance from the protein center, $\bar{r} = r/\lambda$, obtained from the exact analytic solution in Eq. (2.8) with Eq. (2.9) for the indicated values of $\bar{U}'$. We set $\bar{U}\lambda = 0.3$ nm, $\tau = 0$, and $\bar{R}\lambda = 2.3$ nm.

the boundary conditions on the gradient of u at the bilayer-protein interface has been a matter of debate [21–25, 27–31, 39, 102, 118], and is likely to depend on the particular membrane protein and lipid species under consideration. In particular, U' may differ from zero or vary along the bilayer-protein interface, or U' may satisfy natural boundary conditions with U' being adjusted so as to minimize the bilayer thickness deformation energy. As illustrated in Fig. 3.5 for a membrane protein with circular cross section and constant $\bar{U}\lambda = 0.3$ nm, the value of U' can have a substantial effect on the shape of protein-induced lipid bilayer thickness deformations. In particular, for $U' \approx 0.3$ in Fig. 3.5 protein-induced lipid bilayer thickness deformations are seen to decay rapidly.

Plotting $\bar{G}$ as a function of U' for the scenario in Fig. 3.5 (see Fig. 3.6), we find that $\bar{G}$ is minimal for $U' \approx 0.28$ with, as suggested by $\bar{G}_{\text{analy}}$ in Eq. (3.1), an approximately quadratic dependence of $\bar{G}$ on U'. Allowing for non-circular protein cross sections we
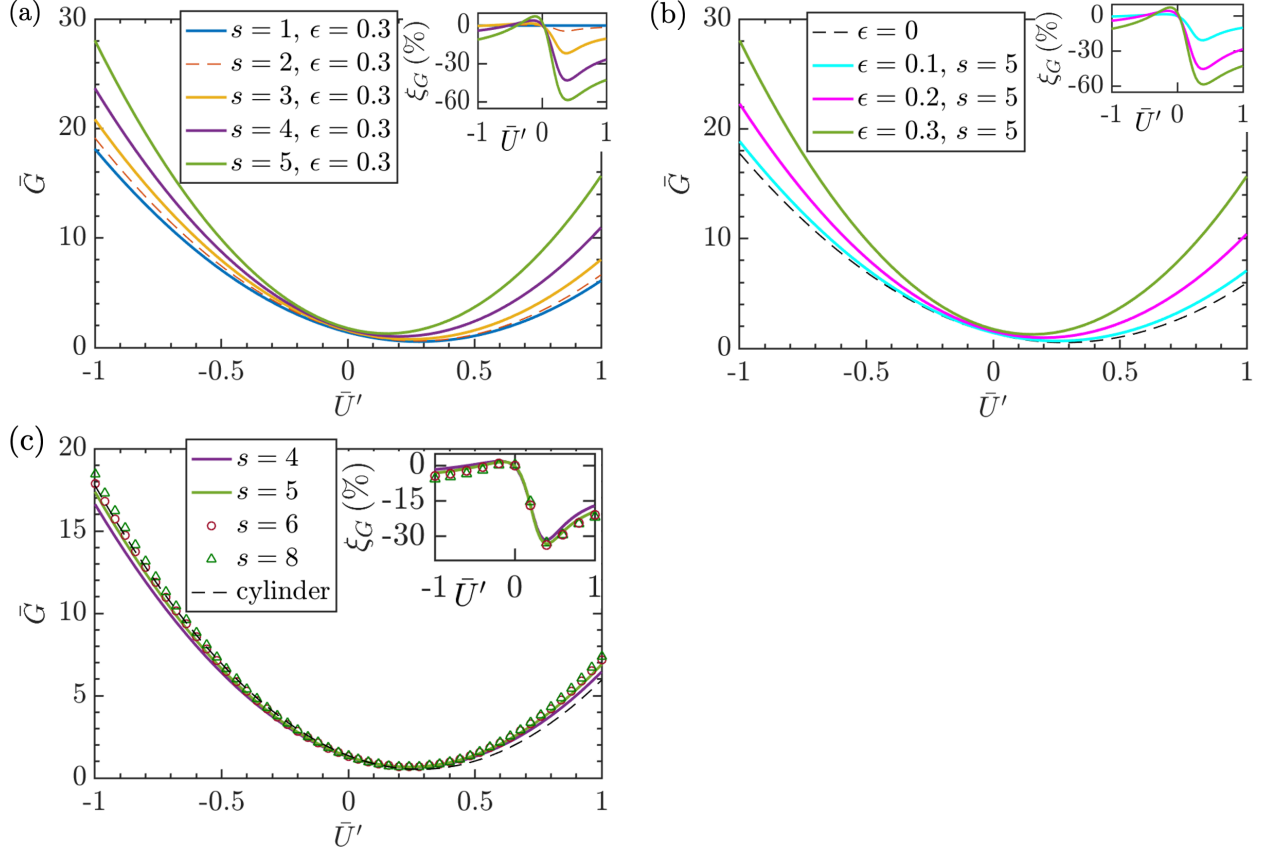
Figure 3.6: Bilayer thickness deformation energy $\bar{G}$ in Eq. (2.6) calculated using the BVM (see Sec. 2.2) as a function of the bilayer-protein contact slope $\bar{U}'$ for (a) clover-leaf protein shapes with $\epsilon = 0.3$ and the indicated values of s, (b) clover-leaf protein shapes with $s = 5$ and the indicated values of ϵ, and (c) polygonal protein shapes with the indicated values of s and $P = 5$, and cylindrical protein shapes with a circular cross section of radius $\bar{R}$. For all panels we set $\bar{R}\lambda = 2.3$ nm, $\bar{U}\lambda = 0.3$ nm, and $\tau = 0$. The insets show the signed percent error ξ_G in Eq. (3.5) for the corresponding analytic approximations $\bar{G}_{\text{analy}}$ in Eq. (3.1).

find that the optimal U' depends strongly, for large enough ϵ, on the symmetry of clover-leaf protein shapes [see Figs. 3.6(a,b)], but only weakly on the symmetry of polygonal protein shapes [see Fig. 3.6(c)]. Note that, for clover-leaf protein shapes, the optimal U' tend to shift towards $U' \approx 0$ compared to proteins with circular cross section. This can be understood by noting that, for clover-leaf protein shapes, the effective reduction in the size of the membrane footprint brought about by $U' \neq 0$ competes with contributions to the bilayer thickness deformation energy due to protein self-interactions. Conversely,

polygonal protein shapes only show weak self-interactions, resulting in minor shifts in the optimal U' compared to proteins with circular cross section. Finally, we note that the analytic estimates $\bar{G}_{\mathrm{analy}}$ in Eq. (3.1) tend to become less accurate for larger U', with up to $|\xi_G| \approx 60\%$ for the clover-leaf and polygonal shapes considered here [Fig. 3.6(insets)].

3.2.2   Variations in protein hydrophobic thickness

Membrane proteins are, in general, expected to show variations in their hydrophobic thickness along the bilayer-protein interface [184, 185]. For oligomeric membrane proteins, variations in protein hydrophobic thickness are expected to be periodic so as to reflect the protein symmetry. We employ here the sinusoidal variations of $U(\theta)$ in Eq. (2.15) as a generic model of variations in protein hydrophobic thickness, in which we denote the periodicity of $U(\theta)$ by w. We focus, for now, on zero bilayer-protein contact slopes, $U' = 0$ in Eq. (2.16), but return to the effects of angular variations in U' in Sec. 3.2.3.

Figure 3.7 shows that variations in $U(\theta)$ can have a strong impact on the energy cost of protein-induced bilayer thickness deformations, for non-circular as well as circular protein cross sections. The analytic estimate $\bar{G}_{\mathrm{analy}}$ in Eq. (3.1) is seen to approximately capture $\bar{G}$ in Fig. 3.7, but tends to become less accurate as the protein cross section exhibits greater deviations from a circular shape, with up to $|\xi_G| \approx 50\%$ for the clover-leaf and polygonal protein shapes considered here [Fig. 3.7(insets)]. Note that, for large enough w, $\bar{G}$ in Fig. 3.7 scales approximately as w^3 for all protein cross sections considered. This can be understood from $\bar{G}_{\mathrm{analy}}$ in Eq. (3.1) by noting that $\bar{E}_w \sim w^3$ at large w, and $\bar{\gamma} = 0$ if $U' = 0$.
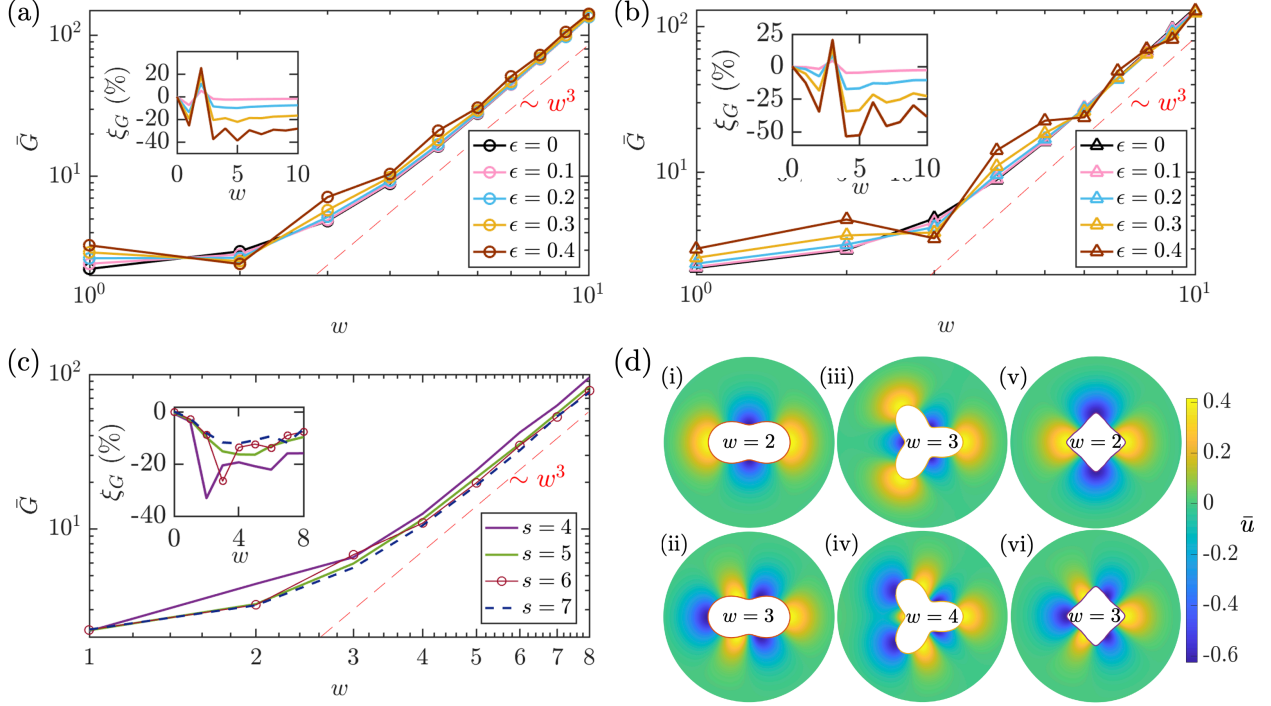
Figure 3.7: Bilayer thickness deformation energy $\bar{G}$ in Eq. (2.6) calculated using the BVM (see Sec. 2.2) as a function of the periodicity in protein hydrophobic thickness, w in Eq. (2.15), for (a) the clover-leaf protein shapes in Eq. (2.17) with $s = 2$ and the indicated values of ϵ, (b) the clover-leaf protein shapes in Eq. (2.17) with $s = 3$ and the indicated values of ϵ, and (c) the polygonal protein shapes in Eq. (2.18) with the indicated values of s and $P = 5$. For all panels we set $\bar{R}\lambda = 2.3$ nm, $\bar{U}_0\lambda = -0.1$ nm, $\bar{\beta}\lambda = 0.5$ nm, $\bar{U}' = 0$, and $\tau = 0$. The red dashed lines indicate the asymptotic scaling $\sim w^3$. The insets show the signed percent error ξ_G in Eq. (3.5) for the corresponding analytic approximations $\bar{G}_{\text{analy}}$ in Eq. (3.1). In panel (d) we show color maps of the protein-induced bilayer thickness deformations associated with $\epsilon = 0.4$ in panel (a) at (i) $w = 2$ and (ii) $w = 3$, with $\epsilon = 0.4$ in panel (b) at (iii) $w = 3$ and (iv) $w = 4$, and with $s = 4$ in panel (c) at (v) $w = 2$ and (vi) $w = 3$.

While, broadly speaking, variations in protein hydrophobic thickness are seen to increase $\bar{G}$ in Fig. 3.7 for all protein cross sections considered, the interplay of $U(\theta)$ and the shape of the protein cross section can yield comparatively favorable or unfavorable scenarios. For instance, depending on whether adjacent regions of the bilayer-protein boundaries in clover-leaf protein shapes yield bilayer thickness deformations of the same sign [see panels (i) and (iii) in Fig. 3.7(d)] or distinct signs [see panels (ii) and (iv) in Fig. 3.7(d)],

protein self-interactions can decrease or increase the energy of protein-induced bilayer thickness deformations. For polygonal protein shapes, we find that scenarios in which the maxima or minima of $U(\theta)$ coincide with the corners of the polygonal shapes [see panel (v) in Fig. 3.7(d)] tend to be unfavorable from an energetic perspective, as compared to scenarios in which the extrema of $U(\theta)$ tend to occur along the polygonal faces [see panel (vi) in Fig. 3.7(d)]. However, compared to the clover-leaf protein shapes considered in Fig. 3.7, the bilayer thickness deformation energy associated with the polygonal protein shapes in Fig. 3.7 depends only weakly on the interplay between $U(\theta)$ and the shape of the protein cross section.

3.2.3   Variations in bilayer-protein contact slope

Similarly as the variations in $U(\theta)$ considered in Sec. 3.2.2, $U'(\theta)$ in Eq. (2.16) will generally vary along the bilayer-protein interface. Such variations could come about, for instance, through the protein structure or the binding of peptides to some sections of the bilayer-protein interface [22, 147]. Alternatively, if the (normal) gradient of $\bar{u}$ obeys natural boundary conditions at the bilayer-protein interface, a non-circular protein cross section or variations in $U(\theta)$ may effectively induce variations in $U'(\theta)$. We employ here the simple model of $U'(\theta)$ in Eq. (2.16) to explore the effect of variations in $U'(\theta)$ on the energy cost of protein-induced lipid bilayer thickness deformations. For simplicity we thereby use a constant $\bar{U} > 0$.

Figure 3.8 illustrates the impact of variations in $U'(\theta)$ on the energy cost of protein-induced lipid bilayer thickness deformations. Similarly as in Fig. 3.7, the analytic estimate
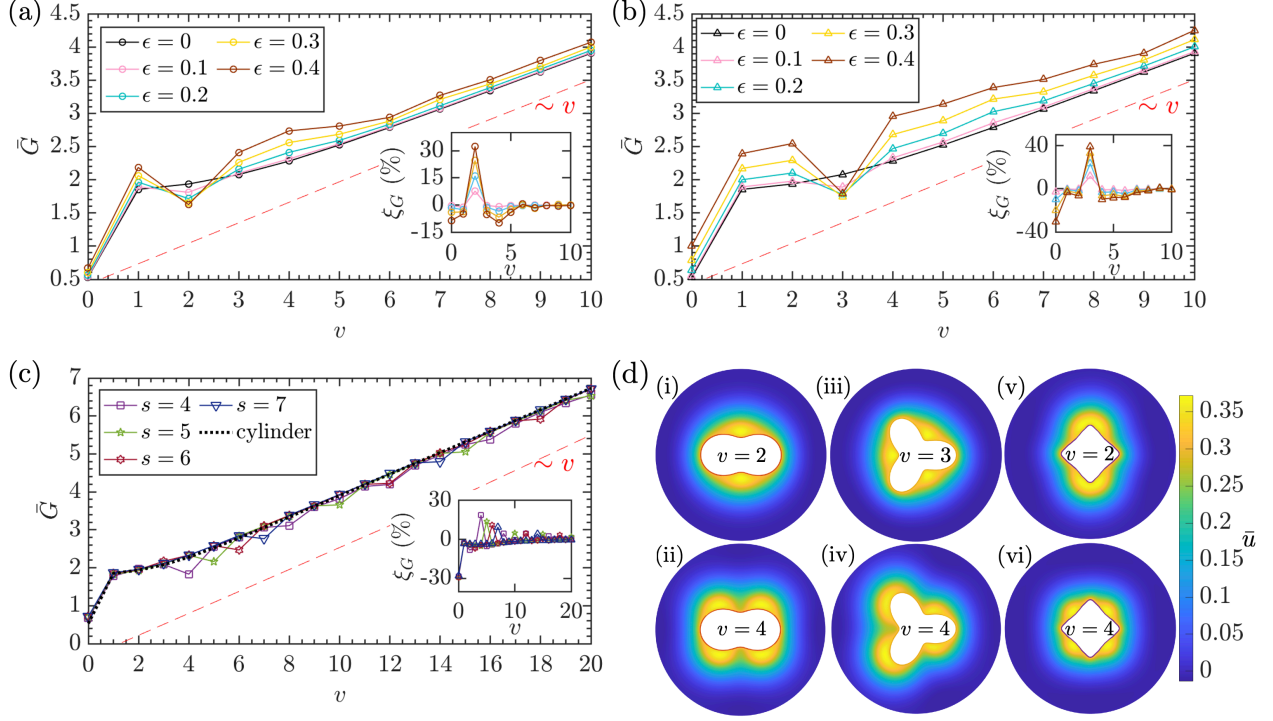
Figure 3.8: Bilayer thickness deformation energy $\bar{G}$ in Eq. (2.6) calculated using the BVM (see Sec. 2.2) as a function of the periodicity in the bilayer-protein contact slope, v in Eq. (2.16), for (a) the clover-leaf protein shapes in Eq. (2.17) with $s = 2$ and the indicated values of ϵ, (b) the clover-leaf protein shapes in Eq. (2.17) with $s = 3$ and the indicated values of ϵ, and (c) the polygonal protein shapes in Eq. (2.18) with the indicated values of s and $P = 5$. For all panels we set $\tau = 0$, $\bar{R}\lambda = 2.3$ nm, $\bar{U}\lambda = 0.3$ nm, $\bar{U}'_0 = 0$, and $\bar{\gamma} = 0.3$. The red dashed lines indicate the asymptotic scaling $\sim v$. The insets show the signed percent error ξ_G in Eq. (3.5) for the corresponding analytic approximations $\bar{G}_{\mathrm{analy}}$ in Eq. (3.1). In panel (d) we show color maps of the protein-induced bilayer thickness deformations associated with $\epsilon = 0.4$ in panel (a) at (i) $v = 2$ and (ii) $v = 4$, with $\epsilon = 0.4$ in panel (b) at (iii) $v = 3$ and (iv) $v = 4$, and with $s = 4$ in panel (c) at (v) $v = 2$ and (vi) $v = 4$.

$\bar{G}_{\mathrm{analy}}$ in Eq. (3.1) is seen to approximately capture $\bar{G}$ in Fig. 3.8, but tends to become less accurate with increasing deviation of the protein cross section from a circular shape, with up to $|\xi_G| \approx 40\%$ for the clover-leaf and polygonal shapes considered here [Fig. 3.8(insets)]. Note that, for large enough v, $\bar{G}$ in Fig. 3.7 scales approximately linearly with v, independent of the protein cross section considered. This can be understood from $\bar{G}_{\mathrm{analy}}$ in Eq. (3.1) by noting that $\bar{F}_v \sim v$ at large v. In analogy to Fig. 3.7 we find in Fig. 3.8 that, broadly speaking, variations in $U'(\theta)$ increase $\bar{G}$ for all protein cross sections considered.

However, the interplay of $U'(\theta)$ and the shape of the protein cross section can yield, similarly as in Fig. 3.7, comparatively favorable or unfavorable scenarios. In particular, for the clover-leaf protein shapes in Figs. 3.8(a) and 3.8(b), it tends to be energetically favorable for the minima of $\bar{U}'(\theta)$ to coincide with the minima of $\bar{C}(\theta)$, so as to make protein self-interactions more favorable, and the maxima of $\bar{U}'(\theta)$ to coincide with the maxima of $\bar{C}(\theta)$, so as to reduce the protein's membrane footprint. This configuration is achieved, for instance, when $v = s$ [see panels (i) and (iii) in Fig. 3.8(d)]. Conversely, it tends to be energetically unfavorable for the minima of $\bar{U}'(\theta)$ to coincide with the maxima of $\bar{C}(\theta)$, and vice versa, or for $\bar{U}'(\theta)$ and $\bar{C}(\theta)$ to be out of phase [see panels (ii) and (iv) in Fig. 3.8(d)]. For the polygonal protein shapes in Fig. 3.8(c), particularly favorable configurations tend to be achieved when the minima of $\bar{U}'(\theta)$ fall on the polygonal faces, rather than on the corners of the polygonal shapes [see panels (v) and (vi) in Fig. 3.8(d)].

3.3   Transitions in protein organization and shape

Section 3.2 demonstrates that protein-induced lipid bilayer thickness deformations show a strong dependence on protein shape, and that changes in protein shape can bring about changes in the bilayer thickness deformation energy $> 10\ k_B T$ in magnitude. In the present section we suggest possible implications of these results for the biophysical properties of membrane proteins. In particular, Sec. 3.3.1 explores the energetic contribution of lipid bilayer thickness deformations to the self-assembly of protein monomers into protein oligomers, and how changes in bilayer-protein interactions could destabilize

protein oligomers. In Sec. 3.3.2 we investigate the effect of lipid bilayer thickness deformations on transitions in protein conformational state that involve substantial changes in protein shape.

3.3.1 Self-assembly of protein oligomers

Complex molecular architectures of membrane proteins often arise from self-assembly of small protein subunits (monomers) into protein oligomers [5, 146]. While entropic effects are generally expected to oppose the self-assembly of membrane protein oligomers, bilayer-protein interactions can favor or oppose protein oligomerization depending on the lipid composition, protein shape, and membrane deformation mode considered [22, 24, 25, 30, 41, 57, 58, 60, 61, 157, 158, 161, 170, 178–183, 186–191]. In particular, the thermodynamic competition between different oligomeric states of membrane proteins depends crucially on how the energy per protein subunit changes with protein oligomeric state. If the hydrophobic thickness of the protein oligomers or monomers differs from the unperturbed hydrophobic thickness of the surrounding lipid bilayer, one set of contributions to the oligomerization energy is expected to arise from protein-induced bilayer thickness deformations [22, 24, 25, 30, 41, 57, 58, 60, 61, 157, 178–183, 191]. Other potential contributions to the oligomerization energy can arise, for instance, from lipid tilt deformations [161, 186, 187].

We illustrate here, in the context of protein-induced lipid bilayer thickness deformations, how contributions to the oligomerization energy due to bilayer-protein interactions can be calculated through the BVM. For simplicity, we thereby consider a protein oligomer

of symmetry s with a clover-leaf or polygonal cross section, and take the s (identical) competing protein monomers to have circular cross sections with the same total area as the protein oligomer, and no interactions between the monomers. Furthermore, we assume that the protein oligomers and monomers show constant values of U and U' along the bilayer-protein interface, with identical U for the protein oligomers and monomers and $U' = 0$ for the protein monomers. These assumptions could easily be lifted to describe more complex scenarios.

Figure 3.9 shows the difference between the (dimensionless) bilayer thickness deformation energies associated with protein oligomers and their corresponding monomers, $\Delta \bar{G}$, as a function of the lipid chain length m [see Fig. 3.9(a)] and the bilayer-oligomer contact slope U' [see Fig. 3.9(b)] for a variety of shapes of the oligomer cross section. The insets in Fig. 3.9 show the differences in the oligomerization energies obtained from the analytic approximation $\bar{G}_{\mathrm{analy}}$ in Eq. (3.1) and the BVM, $\Delta \bar{G}_\xi = \Delta \bar{G}_{\mathrm{analy}} - \Delta \bar{G}$. Equation (3.1) is seen to provide, for modest magnitudes of U and U', good estimates of the oligomerization energy. We generally have $\Delta G < 0$ in Fig. 3.9(a), indicating that protein-induced lipid bilayer thickness deformations support oligomerization. This can be understood from $\bar{G}_{\mathrm{analy}}$ by noting that the protein oligomers in Fig. 3.9(a) have a smaller circumference than their corresponding monomers. Interestingly, Fig. 3.9(b) shows that ΔG can become positive for large enough magnitudes of U' for the protein oligomer, which is thus destabilized. Such a change in U' could be achieved, for instance, through a transition in the conformational state of the oligomer or the binding of peptides to the oligomer [22, 147]. Figure 3.9 therefore suggests that protein-induced bilayer thickness deformations
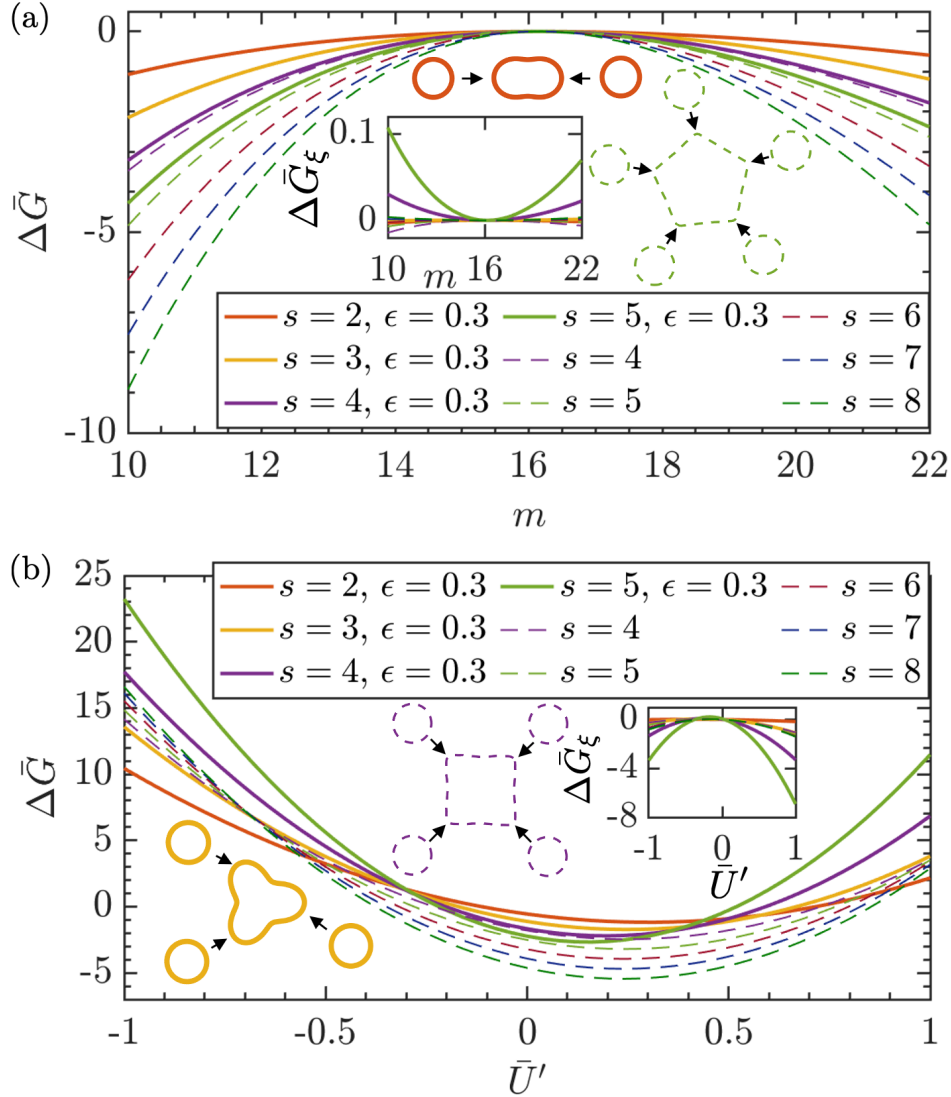
Figure 3.9: Difference between the lipid bilayer thickness deformation energies associated with protein oligomers of symmetry s and their corresponding s monomers, $\Delta\bar{G}$, calculated using the BVM (see Sec. 2.2) as a function of (a) the lipid chain length m in Eq. (2.4) and (b) the (constant) bilayer-oligomer contact slope U' in Eq. (2.14) for a variety of clover-leaf (solid curves) and polygonal (dashed curves) shapes of the protein oligomers. We took the protein monomers to have circular cross sections with $U' = 0$ and used the indicated values of s, with $\epsilon = 0.3$ for the clover-leaf oligomer shapes in Eq. (2.17) and $P = 5$ for the polygonal oligomer shapes in Eq. (2.18). For both panels, we set $\tau = 0$. We set $\bar{R}\lambda = 1$ nm for the monomer radii, and used identical cross-sectional areas of the oligomers and their corresponding monomers. We set $U' = 0$ in panel (a), $2\bar{a}\lambda = 3.2$ nm in panel (b), and used $\bar{W}\lambda = 3.8$ nm for the protein monomers and oligomers in all panels. The schematics in the insets illustrate transitions between monomers and oligomers for selected oligomeric shapes. The plots in the insets show the difference in the oligomerization energies obtained from the analytic approximation $\bar{G}_{\text{analy}}$ in Eq. (3.1) and the BVM, $\Delta\bar{G}_\xi = \Delta\bar{G}_{\text{analy}} - \Delta\bar{G}$, for each curve in the main panels.

could assist both in the assembly and disassembly of protein oligomers, and contribute $> 10\, k_B T$ to the energy budget of membrane protein oligomer assembly or disassembly.

3.3.2   Transitions in protein conformational state

To perform their biological functions, membrane proteins often have to transition between different conformational states. Such transitions in protein conformational state can be accompanied by changes in the cross-sectional shape of membrane proteins producing, in turn, changes in protein-induced lipid bilayer deformations. Membrane proteins can thus be regulated by lipid bilayer properties, such as the bilayer hydrophobic thickness [14, 21, 22, 192]. We illustrate here how the BVM can be used to calculate the contribution of lipid bilayer thickness deformations to the energy difference between two protein states with distinct cross-sectional shapes. For simplicity, we thereby take the two states of the membrane protein to show identical U and U' with U and U' both being constant along the bilayer-protein interface, and to have cross-sectional shapes with the same area. These assumptions could easily be lifted to provide detailed models of specific conformational transitions in membrane proteins, which may also involve more than just two protein states.

Figure 3.10 shows the difference between the lipid bilayer thickness deformation energies associated with the final and initial protein shapes indicated in the insets, $\Delta \bar{G}$, as a function of the lipid chain length m [see Figs. 3.10(a) and 3.10(b)] and the bilayer-protein contact slope U' [see Figs. 3.10(c) and 3.10(d)]. The insets in Fig. 3.10 show
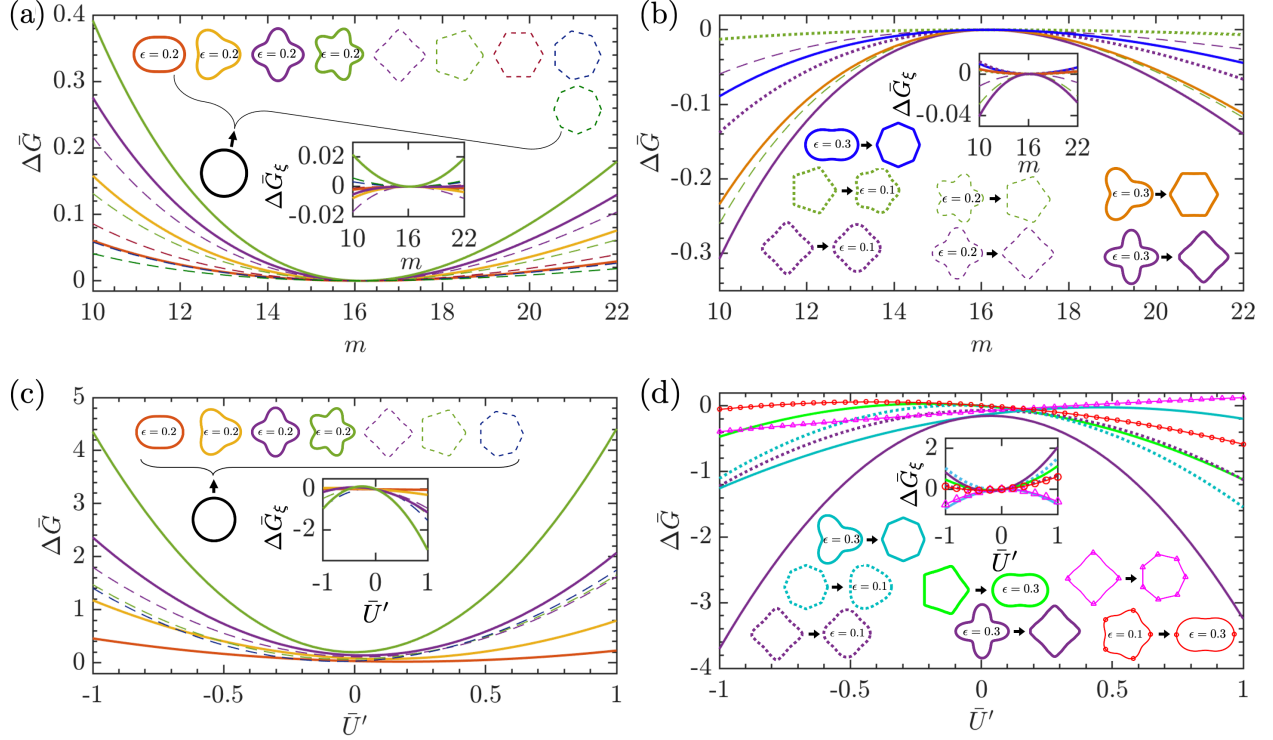
Figure 3.10: Difference between the lipid bilayer thickness deformation energies associated with the final and initial protein shapes indicated in the insets, $\Delta\bar{G}$, calculated using the BVM (see Sec. 2.2) as a function of (a,b) the lipid chain length m in Eq. (2.4) and (c,d) the (constant) bilayer-protein contact slope U' in Eq. (2.14). The values of ϵ associated with each clover-leaf shape in Eq. (2.17) are indicated in the insets, while for the polygonal protein shapes we set $P = 5$. We set $U' = 0$ in panels (a,b) and $2\bar{a}\lambda = 3.2$ nm in panels (c,d), and used $\bar{W}\lambda = 3.8$ nm and $\tau = 0$ for all panels. The cross sections of all protein shapes considered here have area $\pi\bar{R}^2$ with $\bar{R}\lambda = 2.3$ nm. The plots in the insets show the differences in the protein transition energies obtained from the analytic approximation $\bar{G}_{\mathrm{analy}}$ in Eq. (3.1) and the BVM, $\Delta\bar{G}_\xi = \Delta\bar{G}_{\mathrm{analy}} - \Delta\bar{G}$, for each curve in the main panels.

the corresponding differences in the protein transition energies obtained from the analytic approximation $\bar{G}_{\mathrm{analy}}$ in Eq. (3.1) and the BVM, $\Delta\bar{G}_\xi = \Delta\bar{G}_{\mathrm{analy}} - \Delta\bar{G}$. Similarly as in Fig. 3.9, Eq. (3.1) is seen to provide, for modest magnitudes of U and U', good estimates of $\Delta\bar{G}$ in Fig. 3.10. In Figs. 3.10(a) and 3.10(c) we consider idealized scenarios in which the initial protein shape shows a circular cross section, while the final protein state corresponds to a clover-leaf or polygonal protein shape. We find that bilayer thickness deformations generally inhibit such transitions in protein shape, $\Delta\bar{G} \geq 0$, which is easily

understood from $\bar{G}_{\mathrm{analy}}$ in Eq. (3.1) by noting that these transitions in protein shape are accompanied by an increase in protein circumference. In Fig. 3.10(b) we study $\Delta\bar{G}$ for transitions between proteins with non-circular cross sections. We thereby arranged the initial and final protein states such that $\Delta\bar{G} \leq 0$. Similarly as in Figs. 3.10(a) and 3.10(c), the results in Fig. 3.10(b) can be understood by noting that the transitions in protein shape in Fig. 3.10(b) are accompanied by a decrease in protein circumference. Note, in partic-ular, that the energetically favorable protein shapes in Fig. 3.10(b) tend to correspond to polygonal protein shapes or clover-leaf shapes with small ϵ.

Finally, we consider in Fig. 3.10(d) scenarios where the sign of $\Delta\bar{G}$ does not neces-sarily follow from the relative protein circumferences of the initial and final protein shapes, and may not be captured by G_{analy} in Eq. (3.1) for all the values of U and U' considered here. In particular, for the dotted teal, green, and red curves in Fig. 3.10(d) we chose the initial and final protein shapes so that their circumferences lie within 1% of each other, and the remaining protein shapes so that the final protein shape has a circumference that is substantially smaller than the circumference associated with the initial protein state, by at least 6%. The former sets of protein shapes yield a change of sign in $\Delta\bar{G}$ with U'. Three of the latter sets of protein shapes, corresponding to the teal, purple, and dotted purple curves in Fig. 3.10(d), always yield $\Delta\bar{G} \leq 0$, which can again be understood from $\bar{G}_{\mathrm{analy}}$ in Eq. (3.1), while the fourth, corresponding to the pink curve in Fig. 3.10(d), can yield a change of sign in $\Delta\bar{G}$ with U'. In analogy to Fig. 3.9(b) this suggests that, for certain protein shapes, modification of U' in a given (stable) protein conformational state through, for instance, peptide binding [22, 147] could trigger, mediated by protein-induced bilayer thickness deformations, a change in the protein conformational state. We note, however,

that for the protein shapes considered in Fig. 3.10(d) ΔG exceeds zero by not more than

a few $k_B T$.

Chapter 4

Thermosensing through membrane mechanics

This chapter proposes and develops a physical mechanism, based on protein-membrane mechanics, for the ability of cells to sense temperature changes, and illustrates and tests this mechanism in the context of three distinct bacterial and eukaryotic membrane proteins. In particular, we systematically explore the impact of temperature changes on the energetic cost of protein-induced lipid bilayer deformations. We begin by introducing a simple and straightforward temperature-dependent protein-membrane mechanical model, grounded in empirical data on phospholipid membranes (Sec. 4.1). This model lays the foundation for understanding how temperature influences protein-induced bilayer deformations. Next, we delve into how to model transitions in protein shape (Sec. 4.2), providing a framework for studying how temperature affects protein functionality. We then present the results of our model (Sec. 4.3), offering insights into the temperature-dependent activation energy of key sensory proteins, including bacterial chemoreceptors, MscL, and Piezo. In our discussion section (Sec. 4.4), we explore the implications of our findings in greater detail and consider their significance. Finally, in our concluding remarks (Sec. 6.3), we synthesize our findings, derive conclusions, and propose future

avenues for research within the domain of cellular thermosensation. We use, here, the term "protein sensor" to refer to a diverse range of temperature-responsive membrane proteins. In particular, we consider protein sensors that are ion channels, which transition between closed and open conformations, and chemoreceptors, which transition between on (ligand bound) and off (no ligand bound) states.

4.1 Modeling the effect of temperature changes on protein-induced bilayer deformations

We build our description of bilayer-protein interactions, on the established membrane-mechanical framework [21–23, 27, 28, 32–34, 49, 59, 102, 107, 110, 118, 119, 155, 156] discussed in Chapter 2 and Appendix B.1. For the purposes of this chapter it is convenient to use dimensional units $G/K_b \to \bar{G}$, $x/\lambda \to \bar{x}$, $y/\lambda \to \bar{y}$, $u/\lambda \to \bar{u}$, $a/\lambda \to \bar{a}$, $K_t\lambda^2/K_b \to \bar{K}_t$, and $\tau\lambda^2/K_b \to \bar{\tau}$. In particular, a variety of experiments have shown that bilayer mechanical properties change with temperature [15, 114–117]. A linear fit of experimental data on DOPC lipid bilayer thickness versus temperature (from Table 1 in Ref. [116]) yields the lipid bilayer half-thickness

$$a = -mT + a_0, \tag{4.1}$$

with $m = 0.0025 \ \mathrm{nm/K}$, and $a_0 = 2.10 \ \mathrm{nm}$ for DOPC lipid bilayers[*]. According to Eq. (4.1) and the associated experiments on DOPC lipid bilayers, a decreases from $a \approx 1.4 \ \mathrm{nm}$

---

[*]The variable m in Eq. (4.1) should not be mistaken for the variable m representing the lipid chain length in Eq. (2.4)—in particular, the lipid chain length Eq. (2.4) is a dimensionless integer.

to $a \approx 1.3$ nm in the temperature range $T = 10$–$50°$C. Similarly, experimental data on the temperature dependence of the bending rigidity K_b^ℓ of DOPC phospholipid bilayers suggests the phenomenological relation [116]

$$K_b^\ell = K_{b,\mathrm{rm}}^\ell e^{\frac{\varepsilon}{k_B}(\frac{1}{T} - \frac{1}{T_{\mathrm{rm}}})} \,, \tag{4.2}$$

where k_B is Boltzmann's constant, $K_{b,\mathrm{rm}}^\ell = 20\,k_B T_{\mathrm{rm}}$ is the bilayer bending rigidity at room temperature, and $\varepsilon = 7 \times 10^{-21}$ J, with the energy scale $k_B T_{\mathrm{rm}} = 4.11 \times 10^{-21}$ J for the room temperature $T_{\mathrm{rm}} = 25°$C; here we use the superscript ℓ to denote the lipid bilayer bending rigidity rather than the bending rigidity of the protein which we discuss, in the case of Piezo ion channels, in Sec. 4.2.3. In the temperature range $T = 10$–$50°$C, K_b^ℓ decreases from $K_b^\ell \approx 22\,k_B T_{\mathrm{rm}}$ to $K_b^\ell \approx 18\,k_B T_{\mathrm{rm}}$. The above measurements of a and K_b^ℓ allow estimation of the area deformation modulus via

$$K_a = 6\frac{K_b^\ell}{a^2} \,, \tag{4.3}$$

in accordance with the polymer brush model of the lipid bilayer [40, 116]. Assuming incompressibility of the lipid tail volume [193], we set, here, the thickness deformation modulus $K_t = K_a$. This assumption breaks down at extremely high or low temperatures at which lipid tails may undergo phase transitions and under high pressure, conditions affecting the volume and packing of lipid tails. In the temperature range $T = 10$–$50°$C, K_t then varies from $K_t \approx 68\,k_B T_{\mathrm{rm}}/\mathrm{nm}^2$ to $K_t \approx 63\,k_B T_{\mathrm{rm}}/\mathrm{nm}^2$.

While the values of K_b^ℓ and K_t measured for DOPC bilayers [116] are close to those measured for other phospholipid bilayers [22], bilayer hydrophobic thicknesses can vary to a greater extent depending on membrane composition. For instance, while $(m, a_0) = (0.0025 \text{ nm/K}, 2.10 \text{ nm})$ in Eq. (4.1) was found to correspond to DOPC bilayers, $(m, a_0) = (0.0025 \text{ nm/K}, 2.45 \text{ nm})$ in Eq. (4.1) yields a lipid bilayer half-thickness $a \approx 1.7 \text{ nm}$ at $T = 25°C$, which is consistent with measurements of the lipid bilayer hydrophobic core half-thickness of the *E. coli* cytoplasmic (*Eco*C) membrane [194]. Furthermore, m is generally also expected to vary with lipid composition. For instance, in *Bacillus subtilis* cytoplasmic membranes the membrane thickness was measured to linearly decrease with temperature with $(m, a_0) \approx (0.0087 \text{ nm/K}, 5.5 \text{ nm})$ [15].

To estimate the dependence of protein-induced lipid bilayer deformations on temperature changes we insert the empirical relations in Eqs. (4.1)–(4.3) into membrane elasticity theory discussed in Chapter 2. For simplicity, we thereby focus on the simple special cases with $U = \text{constant}$ and $U' = 0$ [23, 32, 118], while noting that the BVM approach developed in Chapter 2 could be applied to relax these assumptions. For all our calculations involving protein-induced lipid bilayer thickness we employ the BVM developed in Chapter 2, yielding errors of about 0.1% or less in G. For our calculations involving midplane deformations, which we assume to be axisymmetric here, we apply the formalism described in Appendix B.1.

4.2 Modeling transitions in protein shape

Changes in protein conformation are often accompanied by changes in protein shape, which can in turn result in changes in protein-induced lipid bilayer deformations. Seminal advances in experimental techniques such as x-ray crystallography and cryo-electron microscopy have significantly enhanced our understanding of membrane protein structure and the interaction of proteins with lipid bilayers [42–45, 48–53]. Though, in general, there can be intermediary states between deactivated and activated states of protein sensors, in our discussion we depict protein sensor activation as a straightforward transition from an off (closed) conformation to an on (open) conformation. While we recognize that this portrayal is, in general, a gross oversimplification [27, 59, 195], it effectively captures the core aspects of the temperature-dependent phenomena under consideration.

To describe the competition between open (on) and closed (off) states of protein sensors, a straightforward two-state Boltzmann model has proven to be useful for the systems considered here. At the core of this model is the channel opening probability:

$$P_o = \frac{1}{1 + e^{\Delta G/k_B T}} \, , \tag{4.4}$$

where ΔG is the energy difference between the open and closed states of the bilayer-protein system. In general, both the lipid bilayer (ΔG_ℓ) and protein (ΔG_p) components contribute to the total transition energy ΔG between any two protein conformations:

$$\Delta G = \Delta G_\ell + \Delta G_p \, , \tag{4.5}$$

where, from here on out, we distinguish the lipid bilayer deformation energy and protein internal energy with subscripts ℓ and p, respectively, and refer to the system state energy as G, without any subscripts (or superscripts). Recent studies suggest that ΔG_p may change significantly with temperature [50–52, 195–206]. Our focus here is to provide estimates of temperature-dependence changes in ΔG_ℓ, to put into place a framework for determing whether ΔG_p or ΔG_ℓ are dominant for a particular model system. In the following subsections we introduce the hydrophobic shape parameters for chemoreceptors and the ion channels MscL and Piezo, which we use as inputs for our calculations of ΔG_ℓ.

4.2.1 Chemoreceptor trimers

Traditionally, chemoreceptors have been recognized for their pivotal role in chemotaxis, a process enabling organisms, including bacteria like *Escherichia coli*, to effectively navigate their environments by detecting and responding to changes in chemical concentrations [207]. Numerous bacteria navigate a diverse range of environments using whip-like appendages known as flagella, and their movement is orchestrated by signals received from transmembrane chemoreceptors. This complex sensory system operates through a sophisticated signaling pathway [6, 45, 208–212]. When a chemoattractant binds to a chemoreceptor, it initiates a conformational change in the receptor. This, in turn, inhibits CheA, a kinase protein. CheA stops autophosphorylating and subsequently stops transferring the phosphate group to another protein called CheY. Dephosphorylated CheY does not bind to the bacterial flagellar motor and does not induce a change in its rotation direction. This lack of change in flagellar rotation direction ultimately controls the

bacterium's swimming behavior, allowing it to move towards favorable substances and away from harmful ones with remarkable precision in diverse environments.

Chemoreceptors have a conical shape and therefore induce midplane/curvature deformations in the surrounding lipid bilayer. However, a previous study [57] suggests that contributions due to bilayer midplane deformations typically amount to much less than $1\ k_B T_{\rm rm}$, an order of magnitude or more smaller than the contribution from bilayer thickness deformations. In the context of chemoreceptors, we therefore focus on protein-induced bilayer thickness deformations. Structural protein shape data collected by previous experiments suggest that the hydrophobic thicknesses of chemoreceptor on (ligand bound) and off (no ligand bound) states are about $W_{\rm off} = 4.21\ {\rm nm}$ and $W_{\rm on} = 4.05\ {\rm nm}$ [57, 213]. Thus, both states lead to a hydrophobic thickness mismatch U in Eq. (2.13) with $U < a$ for bilayer half-thicknesses $a = 1.35\ {\rm nm}$ and $a = 1.7\ {\rm nm}$, which approximately correspond to DOPC [116] and *Eco*C [194] membranes, respectively. This suggests that chemoreceptor-induced bilayer thickness deformations u satisfy $|u| < a$ and $|\nabla u| < 1$, and we may use Eq. (2.3) to accurately estimate bilayer deformation contributions to the chemoreceptor activation energy.

To utilize Eq. (2.3), we specify the boundary conditions in Eqs. (2.12)–(2.14), namely U and the protein-bilayer cross-section boundary curve $C(\theta)$ set by the shape of chemoreceptors. In particular, we consider chemoreceptor proteins that are oligomers composed of three smaller dimer proteins [45]. Based on cryoelectron tomography images, a simple coarse-grained model suggests that these chemoreceptor trimers exhibit a roughly three-leaf clover cross-sectional shape, with their hydrophobic thickness decreasing upon activation [57, 213]. This behavior resembles that of a button or switch. We describe
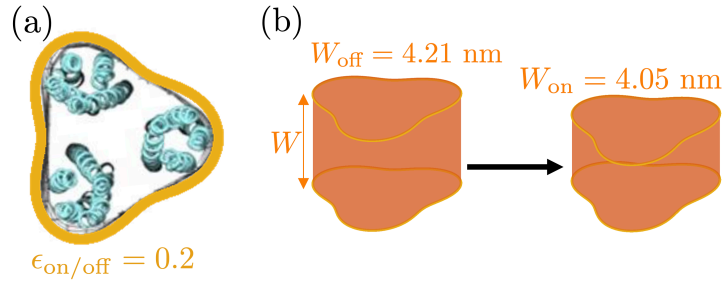
Figure 4.1: Schematic views of our hydrophobic shape model for chemoreceptor trimers. The molecular model of the chemoreceptor trimer in panel (a) is taken from Ref. [45] and the adjacent clover boundary curve was derived from Eq. (2.17) with $R_{\text{on/off}} = 3.1$ nm, $s_{\text{on/off}} = 3$, and $\epsilon_{\text{on/off}} = 0.2$ for both the on and off states. In panel (b), the decrease in chemoreceptor trimer hydrophobic thickness when activated is illustrated (not to scale) with $W_{\text{on}} = 4.05$ nm and $W_{\text{off}} = 4.21$ nm in Eq. (2.13) for the on and off states.

the cross-section shape of clover-leaf proteins using Eq. (2.17) with the estimated shape parameters $\epsilon = 0.2$, $R = 3.1$ nm, and $s = 3$ for both chemoreceptor off and on states [57, 213]. We show schematics of our shape model for chemoreceptor trimer on and off states in Figure 4.1.

4.2.2   MscL

Mechanosensitive channels are vital components for the cellular membranes, serving a crucial role in responding to mechanical stresses and preserving cell integrity. Among these channels, MscL emerges as a pivotal figure in the cellular physiology of bacteria. The prominence of MscL becomes evident when bacteria face a sudden drop in external osmolarity, leading to rapid water influx and subsequent cell swelling [8]. As this water influx causes the cell's volume to expand, the lipid bilayer of the cell membrane stretches and distorts, resulting in increased membrane tension. In response to this mechanical challenge, MscL assumes a pivotal role in preventing cell rupture and potential cell death. MscL possesses the remarkable ability to sense alterations in membrane tension, forming

a channel within the lipid bilayer akin to a safety valve. When the membrane tension exceeds a critical threshold due to hypoosmotic shock, MscL undergoes a conformational change, creating a pore-like structure within the membrane. This newly formed pore expedites the rapid efflux of solutes, including ions and osmolytes, which in turn reduces internal osmolarity and facilitates the exit of water, thus restoring the cell to its normal volume. Notably, MscL's opening is swift and reversible, ensuring its effectiveness under various mechanical stress conditions.

For MscL, we focus on its homopentamer homolog found in *Myobacterium Tuberculosis*. While MscL's closed state has been solved using x-ray crystallography techniques, its open state is still unresolved. However, several structural models have been proposed, analyzed, and show promising agreement with experimental data [14, 27, 59, 89, 91, 102, 168, 214].

During the transition from the closed ("off") state to the open ("on") state, structural studies suggest MscL changes its cross-sectional area A_p from $A_{p,\text{off}} = \pi R_{\text{off}}'^2$ to $A_{p,\text{on}} = \pi R_{\text{on}}'^2$ with, approximately, $R_{\text{off}}' = 2.3$ nm and $R_{\text{on}}' = 3.5$ nm. The shape of closed, pentameric MscL, $C(\theta)$, resembles a 5-leaf clover with $s = 5$ and $\epsilon = 0.22$ in Eq. (2.17). Based on previous structural models, we take here the open state of MscL to have a five-leaf clover cross-sectional shape $C(\theta)$ with $s = 5$ and $\epsilon = 0.11$ [59].

The alteration in MscL's cross-sectional dimensions and the closed-state hydrophobic thickness, measured at around Woff = 3.8 nm using its resolved structure [27, 42, 59], is well-documented. However, the precise hydrophobic thickness of its open state is still undetermined. Though several studies have suggested a likely decrease in MscL's
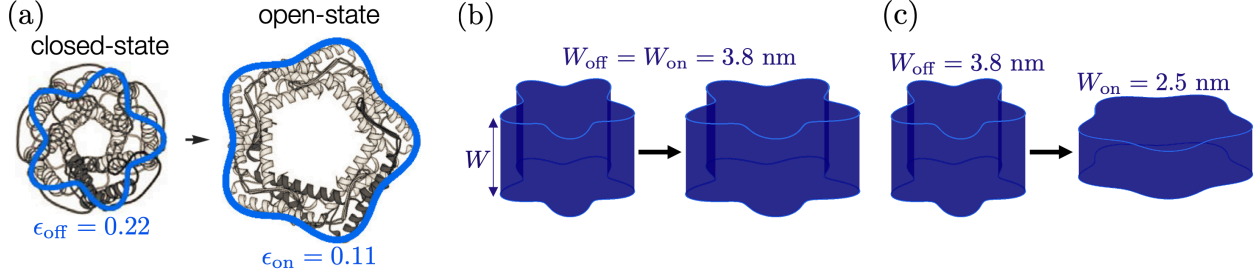
Figure 4.2: Schematic views of our hydrophobic shape model for MscL. The molecular models of MscL's closed and open states in panel (a) are taken from Ref. [59] and the superimposed clover boundary curves were derived from Eq. (2.17) with $R_{\text{off}} \approx 2.27$ nm and $R_{\text{on}} \approx 3.49$ nm, $s_{\text{on/off}} = 5$, and $\epsilon_{\text{off}} = 0.22$ and $\epsilon_{\text{on}} = 0.11$ for both the off (closed) and on (open) states. In panel (b), we show our model for MscL which ignores any change in hydrophobic thickness (not to scale) with $W_{\text{on}} = W_{\text{off}} = 3.8$ nm in Eq. 2.13 for the on and off states. In panel (c), we show our model for MscL with a decrease in hydrophobic thickness (not to scale) when activated with $W_{\text{on}} = 2.5$ nm and $W_{\text{off}} = 3.8$ nm in Eq. 2.13 for the on and off states.

hydrophobic thickness upon activation [42, 59, 91, 214], the extent of this reduction remains undetermined. To address this uncertainty, we explore two distinct possibilities. First, we focus on the change in the cross-sectional shape of MscL, ignoring the possible change in its hydrophobic thickness [102]. In this case, we maintain the thickness at $W_{\text{on}} = 3.8$ nm for the open state. in its open state MscL has a decreased hydrophobic thickness, $W_{\text{on}} = 2.5$ nm [42, 59, 91, 214]. We show schematics of our shape model for MscL on and off states in Figure 4.2.

For MscL, the lipid bilayer contribution ΔG_ℓ to the gating energy ΔG accounts for changes in the deformation of the lipid bilayer surrounding MscL, ΔG_ℓ^M. It also accounts for the work performed on the lipid bilayer under membrane tension as MscL expands its cross-sectional area to open up a pore in the membrane, $\Delta G_\ell^\tau = -\tau \Delta A_p$ with $\Delta A_p \approx 22$ nm. Estimates of ΔG_ℓ^M [27] suggest that the impact of MscL-induced bilayer midplane deformations on the gating energy of MscL is less than $1~k_B T_{\text{rm}}$, with the bilayer thickness deformation contribution being an order of magnitude or more larger.

Similarly to chemoreceptors, the hydrophobic thickness of MscL is expected to be near that of DOPC and EcoC membranes. We therefore focus here on contributions to the gating energy of MscL due to small protein-induced bilayer thickness deformations. Thus, we utilize Eq. (2.3), with the hydrophobic shape parameters discussed above, incorporated into the boundary conditions outlined in Eqs. (2.12)–(2.14) with Eq. (2.17), to estimate ΔG_ℓ^M.

4.2.3 Piezo

Since its discovery in 2010 [215], Piezo, a mechanosensor of eukaryotes, has emerged as a pivotal player in numerous physiological processes. For example, Piezo is located within the membranes of endothelial cells lining blood vessels [216]. When blood pressure rises from an acute increase in blood flow, causing increased shear stress on vessel walls, Piezo is activated due to elevated membrane tension. This activation appears to set off a cascade of events beginning with an increase in intracellular calcium concentration [217]. Piezo-induced calcium influx triggers intracellular signaling pathways leading to the production and release of nitric oxide (NO) by endothelial cells. NO, a potent vasodilator, relaxes smooth muscle cells in blood vessel walls, resulting in vasodilation. This, in turn, leads to reduced peripheral resistance and the regulation of blood pressure.

Recently, an in-depth investigation into the free membrane shape of lipid bilayer vesicles containing Piezo has yielded excellent agreement between the membrane footprint model [32, 38, 49, 107, 110, 111] and experimental data [110]—without any free parameters. These findings underscore specific characteristics of Piezo, including its intrinsic

curvature, membrane footprint, low stiffness, and expansive surface area. These features collectively contribute to Piezo's remarkable ability for low-threshold, high-sensitivity mechanical gating [111], providing compelling evidence of the intricate connection between Piezo's functionality and membrane mechanical properties.

Piezo's shape [218] has been determined through cryoelectron tomography experiments in lipid vesicles of different sizes, and a theoretical analysis [111] provided predictions for Piezo's shape in cell membranes. In its closed state, Piezo is described as having an intrinsic protein radius of curvature $R_0^p = 10.2$ nm and a room temperature bending rigidity $K_b^p(T = T_{\rm rm}) \approx 20\ k_B T_{\rm rm}$. Piezo bends the lipid bilayer to form a dome shape, composed of 25% protein and 75% lipid bilayer, that can be approximated as a spherical cap of area $S_{\rm cap} = 450$ nm^2, protruding into the cytoplasm, and with a radius of curvature R [111]. Piezo is believed to gate through a membrane dome mechanism [49, 107, 110, 111, 218], where membrane tension stabilizes Piezo towards a flatter state. In its closed state, Piezo thereby exhibits a smaller in-plane area compared to its flatter state when open, akin to MscL gating which also exhibits an in-plane area expansion upon opening from tension.

The boundary conditions at the Piezo dome-free membrane interface can be expressed in terms of Piezo's dome shape parameters R and $S_{\rm cap}$ [see also Eq. (B.1) in Appendix B.1], the cap angle

$$\alpha = \cos^{-1}\left(1 - \frac{S_{\rm cap}}{2\pi R^2}\right),\qquad(4.6)$$
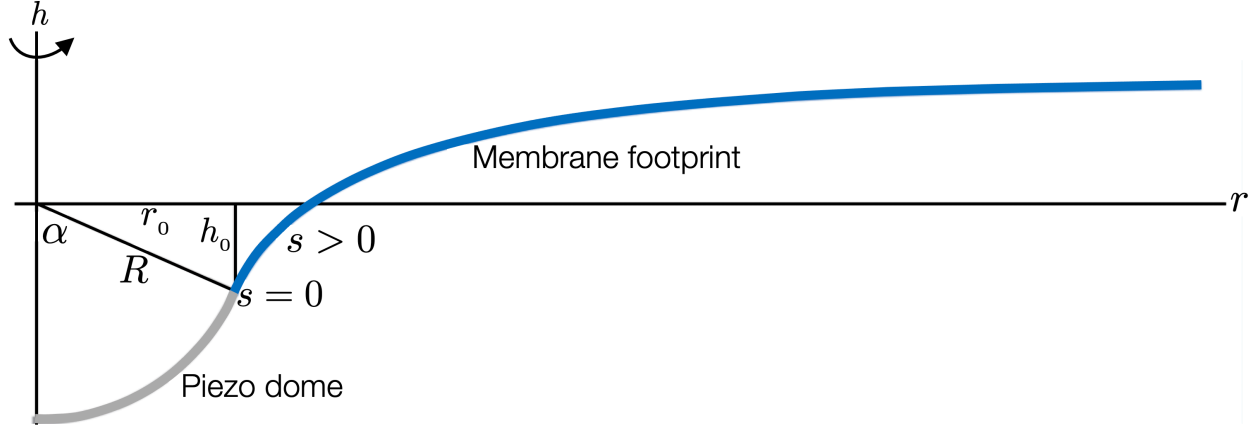
Figure 4.3: Cross-sectional view of Piezo-induced membrane deformations (adapted from Ref. [107]). The Piezo dome resembles a spherical cap with a fixed area $S_{\mathrm{cap}} = 450 \ \mathrm{nm}^2$. Key parameters include R (radius of curvature), $h = h_0$ and $r = r_0$ (central pore axis and radial coordinates at $s = 0$), s (arclength along Piezo's membrane footprint profile, $s = 0$ at the dome interface, $s > 0$ away from the dome), and α (cap angle). Deformations are assumed to diminish towards a flat membrane shape for large s.

in-plane cap radius

$$r_0 = R \sin \alpha \,, \tag{4.7}$$

and central pore axis coordinate of the interface of the Piezo dome and surrounding membrane

$$h_0 = -R \cos \alpha \,. \tag{4.8}$$

Following previous work [110, 111], we take the closed and open states of the Piezo dome to have the same area, with a radius of curvature

$$R_{\mathrm{off}} = R_0^p (1 + 3 K_b^\ell / K_b^p) \tag{4.9}$$

in the closed state and $R_{\mathrm{on}} = \infty$ in the open state. Figure 4.3 depicts the Piezo dome shape model and the membrane deformation profile using the arclength parametrization.

In our model, the activation energy of Piezo can be decomposed into several contributions. There are energetic contributions associated with flattening the deformations in the surrounding lipid bilayer ΔG_ℓ^M and the flattening of the Piezo dome ΔG_{cap}. We estimate ΔG_ℓ^M using Eq. (B.1).

ΔG_{cap} can be further decomposed into three separate contributions. One contribution comes from the change in the bilayer's in-plane area, under membrane tension, in flattening the Piezo dome,

$$\Delta G_{\text{cap}}^\tau = -\tau \Delta A_{\text{cap}} , \tag{4.10}$$

where $\Delta A_{\text{cap}} = S_{\text{cap}}^2 / 4\pi R_{\text{off}}^2$. Another contribution comes from bending the lipid bilayer part of the Piezo dome in to a flat configuration,

$$\Delta G_{\ell,\text{cap}}^b = -0.75 \frac{K_b^\ell}{2} S_{\text{cap}} \left(\frac{2}{R_{\text{off}}} \right)^2 , \tag{4.11}$$

with lipid bilayer bending rigidity K_b^ℓ. K_b^ℓ varies with temperature according to the relationship in Eq. (4.2).

The final contribution comes from bending Piezo's arms into a flat configuration,

$$\Delta G_{p,\text{cap}}^b = 0.25 \frac{K_b^p}{2} S_{\text{cap}} \left[\left(\frac{2}{R_0^p} \right)^2 - \left(\frac{2}{R_0^p} - \frac{2}{R_{\text{off}}} \right)^2 \right] , \tag{4.12}$$

with the piezo protein bending rigidity K_b^p. K_b^p was previously measured to be similar to K_b^ℓ at room temperature [111], so we maintain $K_b^p(T = T_{\text{rm}}) = K_{b,\text{rm}}^\ell = 20\ k_B T_{\text{rm}}$. Currently, to our knowledge, there is no available data on how K_b^p changes with temperature. However, in the study of soft materials, it is generally anticipated that material rigidity decreases with

increasing temperature, particularly over the range $T = 10$–$50°$C. Given the uncertainty regarding the impact of changes in temperature on K_b^p, we examined several different scenarios. The simplest approach is to assume K_b^p is independent of temperature [maintain $K_b^p(T) = 20~k_B T_{rm}$]. Alternatively, since $K_b^p = K_b^\ell$ at room temperature, this may indicate temperature effects K_b^p similarly as K_b^ℓ, so we also explore $K_b^p(T) = K_b^\ell(T)$. Additionally, we also consider the possibility of K_b^p having a stronger dependence on temperature than K_b^ℓ, in particular, twice as strong. So we set $K_b^p(T) = K_b^\ell(2\varepsilon \to \varepsilon, T)$[†].

4.3 Temperature-sensing through chemoreceptors and ion channels

4.3.1 Chemoreceptor activation

Based on the phenomenological relations in Eqs. (4.1)–(4.3), we have employed a simple membrane-mechanical model to estimate how changes in temperature might impact the activation of chemoreceptor trimers. Specifically, we have calculated the lipid bilayer deformation energy contribution ΔG_ℓ from the membrane surrounding the chemoreceptor to the transition from its off to on state. Though contributions due to membrane tension, namely changes in the bilayer's in-plane area and stretching deformations tangential to the bilayer leaflet surfaces in Eq. (2.3), can in general vary with temperature [113], their effect on the chemoreceptor activation energy is expected to be negligible in comparison to

---

[†]$K_b^\ell(2\varepsilon \to \varepsilon, T) = K_{b,rm}^\ell e^{\frac{2\varepsilon}{k_B}\left(\frac{1}{T} - \frac{1}{T_{rm}}\right)}$.

that of the hydrophobic thickness mismatch [57]. For this reason we ignore contributions due to membrane tension by setting $\tau = 0$.

We find that ΔG_ℓ decreases by roughly $8\ k_B T_{\rm rm}$ (equivalent to a decrease of approximately 14%) as temperature rises within the range of $T = 10\text{--}50°\text{C}$ in a DOPC bilayer [illustrated by the solid red curve in Fig. 4.4(a)]. To measure the impact of protein shape on these results, we performed analogous calculations using a circular cross-section with an area equivalent to that of the clover-leaf protein cross-section. The model of the chemoreceptor trimer with a circular cross-section yields a comparable shift in activation energy due to temperature increases over the same range, $T = 10\text{--}50°\text{C}$ [represented by the red dashed curve in Fig. 4.4(a)], signifying that our results do not depend significantly on the variations in cross-section shape of chemoreceptor trimers.

Furthermore, the decrease in ΔG_ℓ with rising temperature implies that the energy of the chemoreceptor trimer in the off state increases relative to its on state as temperature increases, ultimately favoring the chemoreceptor trimer's on state. The physical origin of these results lies in the significant energetic penalty associated with the chemoreceptor trimer hydrophobic thickness mismatch with the bilayer's unperturbed hydrophobic core in Eq. (2.3) (see Sec. 3.1 for details) [57, 59]. Note that if, the sole effect of temperature was a reduction in bending rigidity, K_b^ℓ, [as depicted by the cyan curve in Fig. 4.4(a)] or a decrease in thickness deformation modulus, K_t, [illustrated by the purple curve in Fig. 4.4(a)], then an increase in temperature would produce the opposite effect, favoring the off state with increasing temperature. In contrast, if rising temperature only caused a reduction in bilayer thickness, $2a$, the chemoreceptor trimer would remain biased towards
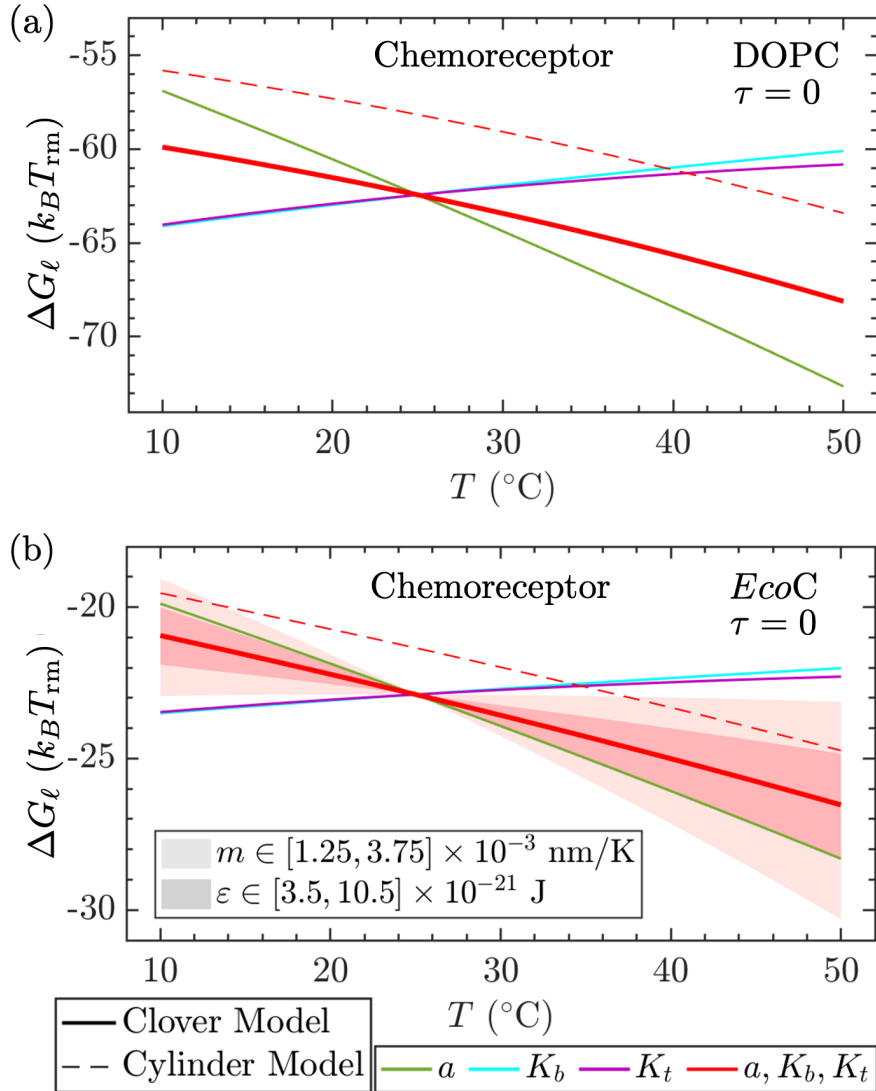
Figure 4.4: Estimates of the lipid bilayer deformation contribution to the chemoreceptor activation energy obtained using Eq. (2.3) with $\tau = 0$, are depicted for (a) DOPC and (b) *Eco*C membranes, as a function of temperature. Solid lines represent calculations employing the clover-leaf chemoreceptor trimer cross-section shape model described in Sec. 4.2.1, while dashed lines incorporate a cylinder cross-section shape with chemoreceptor trimer on and off states possessing equivalent cross-section areas to the corresponding clover cross-section shapes. The color legend below the panels indicates which parameters (a, K_b^ℓ, or K_t) were assigned the temperature relations in Eqs. (4.1)–(4.3) for DOPC lipid bilayers [116] and, by omission, which of these parameters were held constant at their respective values at room temperature $T_{rm} = 25°C$. In (b) *Eco*C membranes, a was modified using $a_0 = 2.45$ nm in Eq. (4.1). In panel (b), the lightly shaded region depicts the clover model solutions, with a 50% variation in m in Eq. (4.1), and the overlapping darker shaded region represents solutions with variations in ε by 50%.

the on state. Thus, the predicted bias of chemoreceptors towards the on state can be explained from the decrease in bilayer hydrophobic thickness with increasing temperature.

The dependence of the temperature variations on membrane thickness follows directly from the bilayer deformation energy's quadratic dependence on hydrophobic thickness mismatch U in Eq. (2.3) (see Chapter 3). The hydrophobic thicknesses of chemoreceptor trimers are larger than those of DOPC membranes, with the off state having a larger protein hydrophobic thickness compared to the on state. As the bilayer thins with rising temperature, U increases for both chemoreceptor off and on states by the same amount. However, the change in U^2 is greater for the chemoreceptor off state, resulting in a more substantial alteration in the energetic cost for the bilayer-chemoreceptor off state relative to the on state. Consequently, membrane thinning leads to a bias towards the chemoreceptor's on state[‡]. From this standpoint, chemoreceptor trimer switching conceptually resembles the gating of mechanosensitive ion channels, where the gating tension was observed to depend on lipid tail length [14].

Up to this point, we have assumed that the bilayer is DOPC. However, the measured hydrophobic thicknesses of DOPC bilayers [116] are less than the estimated hydrophobic thickness of the *Eco*C membrane. To account for an *Eco*C membrane, we have modified the relation in Eq. (4.1) as outlined in Sec. 4.1. Subsequently, we have recalculated the switching energy curves displayed in Fig. 4.4(a) [see Fig. 4.4(b)]. Our results in *Eco*C membranes exhibit qualitative similarity to those in DOPC membranes, with a

---

[‡]A similar biasing would emerge if $2a > W_{\text{off}} < W_{\text{on}}$ or $W_{\text{off}} > 2a > W_{\text{on}}$. If $W_{\text{off}} > 2a > W_{\text{on}}$, a decrease in a would reduce the hydrophobic mismatch, in Eq. (2.13), of the chemoreceptor trimer on state while increasing the hydrophobic mismatch of the off state, which would yield a more substantial biasing towards the chemoreceptor trimer on state. This implies that $W_{\text{off}} > W_{\text{on}}$ ensures that the decrease in membrane thickness with increasing temperature biases chemoreceptor trimers to the on state.

bias towards the chemoreceptor's on state at higher temperatures stemming from membrane thinning. Our model's predicted temperature-dependent ΔG_ℓ for chemoreceptors in *Eco*C membranes decreases by approximately $6\ k_B T_{\mathrm{rm}}$ (equivalent to a decrease of approximately 27%) over the temperature range $T = 10\text{--}50°\mathrm{C}$ [demonstrated by the solid red curve in Fig. 4.4(b)]. The predicted temperature-induced biasing of chemoreceptors towards their on state persists even under perturbations to the temperature-dependent relationship strength parameters, $m = 0.0025\mathrm{nm/K}$ [indicated by the light shaded region in Fig.4.4(a)], and $\varepsilon = 7 \times 10^{-21}\mathrm{J}$ [depicted by the dark shaded region in Fig.4.4(a)], in Eqs. (4.1)–(4.2), by up to 50%. This indicates that comparable outcomes are anticipated in membranes with somewhat different lipid compositions.

4.3.2   MscL gating

Much like in the case of chemoreceptors, we have utilized Eqs. (2.3), (2.11)–(2.14), (2.17), and (4.1)–(4.3), but this time incorporating the protein shape models for MscL [58, 59, 102], detailed in Section 4.2.2, to estimate the lipid bilayer deformation contribution ΔG_ℓ towards MscL's gating energy.

To focus on the temperature dependent bilayer mechanical parameters in Eqs. (4.1)–(4.3) (a, K_b^ℓ, K_t), we ignored membrane tension by setting $\tau = 0$. Thus, we set $\Delta G_\ell = \Delta G_\ell^M|_{\tau=0}$. Given that the cross-section boundary curve of MscL's open (on) state has a greater circumference than that of its off state, $\Delta G_\ell > 0$ (see Sec. 3.3.2 for details). If MscL's hydrophobic thickness does not change when activated and MscL's hydrophobic thickness is greater than that of the lipid bilayer's unperturbed thickness, such as in DOPC

and *Eco*C membranes, the hydrophobic thickness mismatch U in Eq. (2.13) increases as the membrane's unperturbed hydrophobic thickness decreases with increasing temperature. We also have the approximate scaling $\Delta G_\ell \sim U^2$ (see Sec. 3.1). We find that, due to an increase in hydrophobic thickness mismatch, ΔG_ℓ increases with increasing temperature. Note that if, the only effect of temperature was a decrease in bending rigidity, K_b^ℓ, [as depicted by the cyan curves in Figs. 4.5(a) and (b)] or a decrease in thickness deformation modulus, K_t, [illustrated by the purple curves in Fig. 4.5(a) and (b)], then an increase in temperature would produce the opposite effect, favoring the open (on) state with increasing temperature. In contrast, if increasing temperature only caused a decrease in the bilayer's unperturbed thickness, $2a$, MscL would remain biased towards the closed (off) state. Thus, our model predicts a bias in MscL towards the closed (off) state which can be explained from the decrease in the bilayer's unperturbed hydrophobic thickness with increasing temperature [§]. Since DOPC membranes being thinner than $EcoC$ bilayers, MscL has a larger hydrophobic mismatch in a DOPC bilayer. So ΔG_ℓ increases by a larger amount with increasing temperature in DOPC membranes. In particular, we found ΔG_ℓ increases by about $14\ k_B T_{\rm rm}$ in a DOPC bilayer, compared to $4\ k_B T_{\rm rm}$ in an $EcoC$ bilayer, with increasing temperature over the range $T = 10$–$50°$C.

If we, instead, assume $W_{\rm on} = 2.5$ nm [58, 59], we have $W_{\rm off} > 2a > W_{\rm on}$ in DOPC and *Eco*C membranes. So as the membrane hydrophobic thickness decreases, U increases with respect to the closed state and decreases with respect to the open state. Given the approximate scaling $G_\ell \sim U^2$ (see Sec. 3.1), as membrane hydrophobic thickness

---

[§]Conversely, if the bilayer's unperturbed thickness were greater than MscL, U would decrease as the bilayer thins with increasing temperature, reducing ΔG_ℓ.
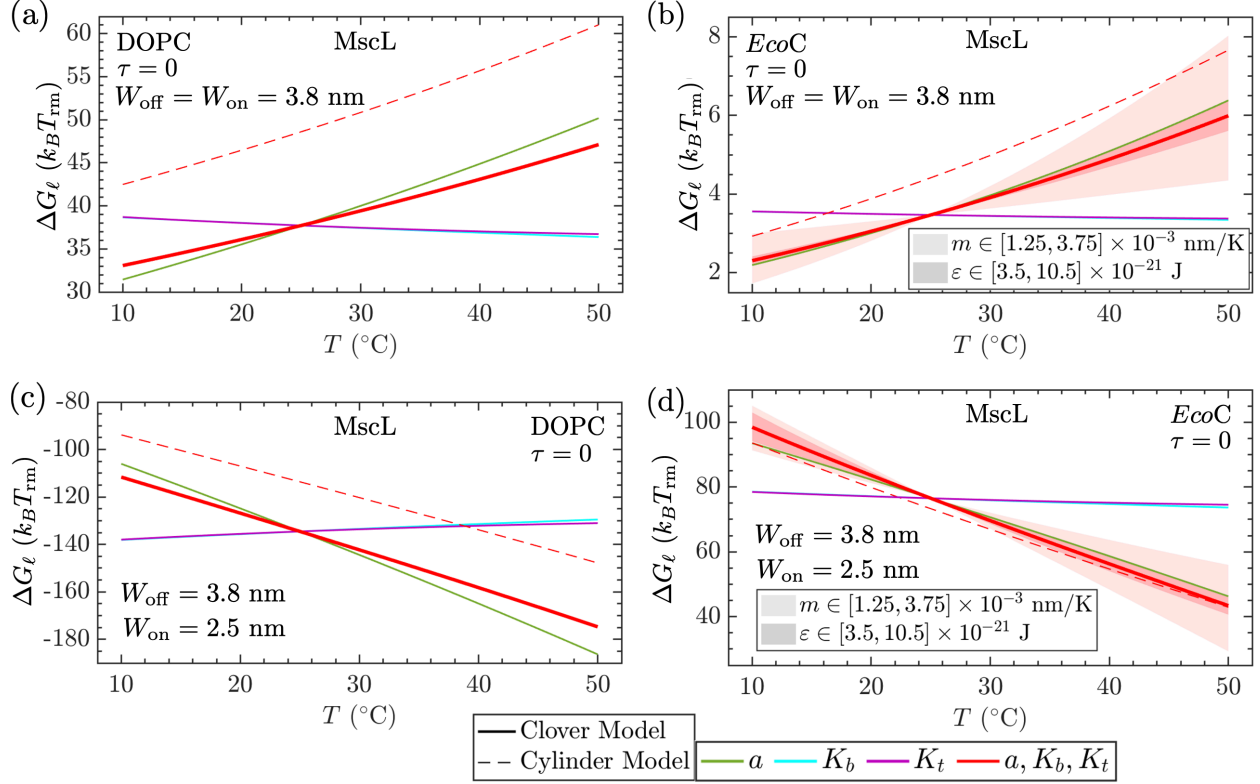
Figure 4.5: Estimates of the lipid bilayer deformation contribution to MscL's activation energy obtained using Eq. (2.3) with $\tau = 0$, are depicted for (a,c) DOPC and (b,d) *Eco*C membranes, as a function of temperature. In panels (a,b) we set $W_{\text{off}} = W_{\text{on}} = 3.8$ nm in Eq. (2.13), and in panels (c,d) we set $W_{\text{off}} = 3.8$ nm and $W_{\text{on}} = 2.5$ nm. In all panels, solid lines represent calculations employing the clover-leaf MscL cross-section shape models for MscL's open (on) and closed (off) states described in Sec. 4.2.2, while dashed lines incorporate a cylinder cross-section shape with MscL opened (on) and closed (off) states possessing equivalent cross-section areas to the corresponding clover cross-section shapes. The color legend below the panels indicates which parameters (a, K_b^ℓ, or K_t) were assigned the temperature relations in Eqs. (4.1)–(4.3) for DOPC lipid bilayers [116] and, by omission, which of these parameters were held constant at their respective values at room temperature $T_{\text{rm}} = 25°\text{C}$. In (b,d) *Eco*C membranes, a was modified using $a_0 = 2.45$ nm in Eq. (4.1). In panels (b,d), the lightly shaded region depicts the clover model solutions, with a 50% variation in m in Eq. (4.1), and the overlapping darker shaded region represents solutions with variations in ε by 50%.

decreases with increasing temperature, $G_{\ell,\text{on}}$ decreases while $G_{\ell,\text{off}}$ increases, yielding a decrease in ΔG_ℓ. In DOPC, we find that ΔG_ℓ decreases by about 63 $k_B T_{\text{rm}}$ and in EcoC, that ΔG_ℓ decreases by about 55 $k_B T_{\text{rm}}$ with increasing temperature over the range $T = 10$–$50°\text{C}$.

We performed analogous calculations using a circular cross-section model for MscL's closed and open states with radii 2.3 nm and 3.5 nm, respectively, which yield cross-section areas equivalent to the corresponding clover-leaf shape models we've already discussed (see dashed curves in Fig. 4.5). Using circular cross-sections, we found comparable shifts in ΔG_ℓ with increasing temperature over the range $T = 10$–$50°$C. This signifies that our results do not depend substantially on the variations in MscL's cross-section shape. Furthermore, these findings remain consistent even when the parameters m and ε in Eq. (4.1) and Eq. (4.2) are subject to variations, e.g., of 50%, as depicted by the lightly shaded regions in Fig. 4.5(b,d) for m and the darker shaded regions for ε.

We estimated the activation energy in Eq. (4.5) for MscL in an EcoC membrane, considering $\tau = 0.01, 0.1, 1\ k_B T_{\rm rm}/{\rm nm}^2$, as a function of temperature. Though, ΔG_p in Eq. (4.5) is not precisely known, MscL has been measured to have a channel opening probability $P_{\rm o} = 0.5$ at around $\tau \approx 2.7\ k_B T_{\rm rm}/{\rm nm}^2$ [22]. So we assign ΔG_p a value that yields $P_{\rm o} = 0.5$ in Eq. (4.4 at $\tau \approx 2.7\ k_B T_{\rm rm}/{\rm nm}^2$. For our calculations with $W_{\rm off} = W_{\rm on} = 3.8$ nm, this requires we set $\Delta G_p = 55\ k_B T_{\rm rm}$ [see Fig. 4.5(a)], and for our calculations with $W_{\rm off} = 3.8$ nm and $W_{\rm on} = 2.5$ nm, this requires we set $\Delta G_p = 0$ [see Fig. 4.5(c)].

In our models for MscL, ΔG_p is independent of temperature. So the changes in ΔG due to increasing temperature in Fig. 4.5(a,c) originate from ΔG_ℓ. For our calculations with $W_{\rm off} = W_{\rm on} = 3.8$ nm, we find that the contributions due to finite τ further increase ΔG_ℓ with increasing temperature. For example, at $\tau = 1\ k_B T_{\rm rm}/{\rm nm}^2$ ΔG_ℓ increases by $19\ k_B T_{\rm rm}$ with increasing temperature over the range $T = 10$–$50°$C [see blue curve in Fig. 4.5(a)], which is substantial compared to an increase of $4\ k_B T_{\rm rm}$ in $\Delta G_\ell|_\tau = 0$ [see

solid red curve in Fig. 4.4(b)]. So changes in temperature can have a significant effect on ΔG due to membrane tension.

In contrast, when we consider the hydrophobic thicknesses $W_{\mathrm{off}} = 3.8$ nm and $W_{\mathrm{on}} = 2.5$ nm for MscL's closed and open state, respectively, we find that incorporating a finite τ does not significantly impact the change in ΔG with increasing temperature [compare curves in Fig. 4.5(c) with the solid red curve in Fig. 4.4(d)]. Thus, the decrease in ΔG with increasing temperature in Fig. 4.5(c) is primarily attributed to the decrease in the bilayer's hydrophobic thickness, as we discussed previously when we considered $\tau = 0$.

Using Eq. (4.4), we calculated MscL's channel opening probability P_{o} as a function of τ at temperatures $T = 10, 30, 50°$C. We find that MscL's activation threshold membrane tension¶ increases by about 0.2 $k_B T_{\mathrm{rm}}/\mathrm{nm}^2$ (equivalent to about a 10% increase) with increasing temperature over the range $T = 10$–$50°$C, when we set $W_{\mathrm{off}} = W_{\mathrm{on}} = 3.8$ nm [see Fig. 4.6(c)]. In contrast, when we consider $W_{\mathrm{off}} = 3.8$ nm and $W_{\mathrm{on}} = 2.5$ nm, the activation threshold membrane tension decreases by about 2 $k_B T_{\mathrm{rm}}/\mathrm{nm}^2$ (equivalent to about a 60% decrease) with increasing temperature over the range $T = 10$–$50°$C [see Fig. 4.6(d)]. These findings remain consistent even when the parameters m and ε in Eq. (4.1) and Eq. (4.2), respectively, are varied by 50%, as indicated by the lightly shaded regions in Fig. 4.6(b,d) for m and the darker shaded regions for ε.
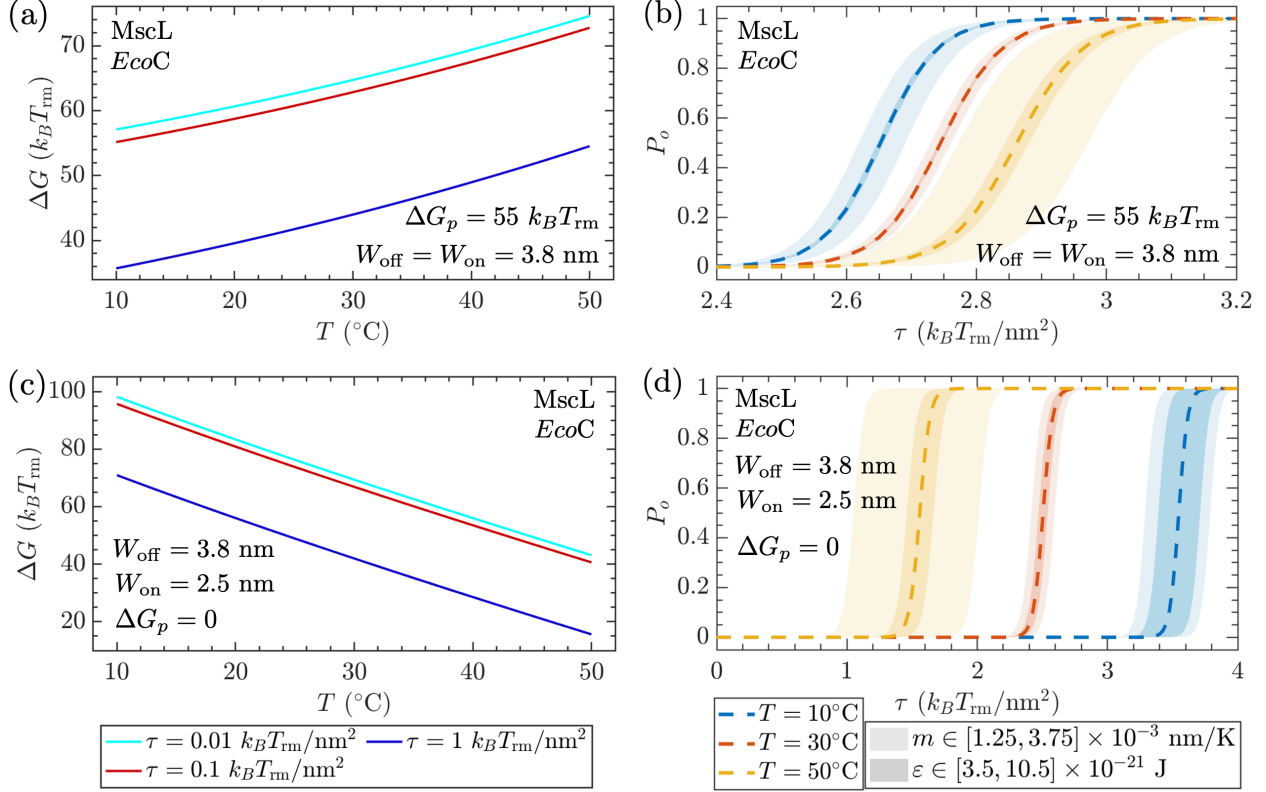
Figure 4.6: In panels (a,b), we depict estimates of MscL's activation energy in Eq. (4.5) in an *Eco*C membrane as a function of temperature, where we set the membrane tension τ to the values indicated by the color legend beneath panel (c). In panels (b,d) we show the opening channel probability in Eq. (4.4) for MscL in an *Eco*C membrane as a function of τ, where we set the temperature T to the values indicated in the color legend underneath panel (d), and the shaded regions. The shaded regions in panels (b,d) denote the range of solutions for 50% variations in m in Eq. (4.1) and ε in Eq. (4.2) as indicated in the greyscale legend underneath panel (d). In panels (a,b) we set $W_{\text{off}} = W_{\text{on}} = 3.8$ nm, and in panels (c,d) we set $W_{\text{off}} = 3.8$ nm and $W_{\text{on}} = 2.5$ nm in Eq. (2.13). In panels (a,b) we set $\Delta G_p = 55\ k_B T_{\text{rm}}$, and in panels (c,d) we set $\Delta G_p = 0$ in Eq. (4.5).

4.3.3 Piezo gating

We calculated the separate contributions to the activation energy of Piezo, $\Delta G = \Delta G_\ell^M + \Delta G_{\ell,\text{cap}}^\tau + \Delta G_{\ell,\text{cap}}^b + \Delta G_{p,\text{cap}}^b$ for the Piezo dome shape models discussed in Sec. 4.2.3.

If we assume $K_b^p(T) = 20\ k_B T_{\text{rm}}$ and membrane tension τ is finite, we find that ΔG_ℓ^M decreases approximately linearly with increasing temperature over the range $T = 10\text{–}50°\text{C}$

¶Throughout this thesis, we define the activation threshold of ion channels as the value for τ at which $P_\text{o} = 0.5$ in Eq. (4.4).
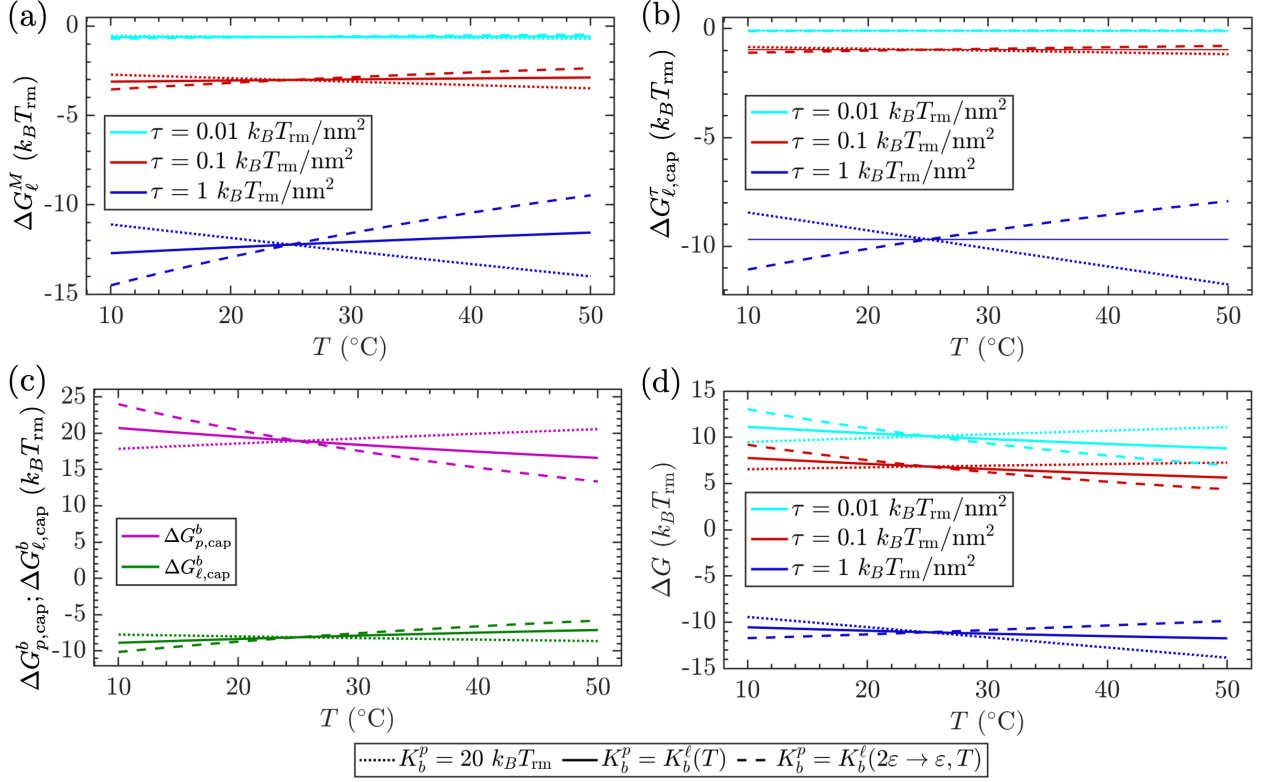
Figure 4.7: Estimates of (a) the change in deformation energy associated with the lipid bilayer surrounding the Piezo dome, ΔG_ℓ^M, (b) the change in the energy associated with the change in the Piezo dome's in-plane bilayer area under membrane tension, $\Delta G_{\ell,\mathrm{cap}}^\tau$, (c) the change in the bending energies associated with the lipid bilayer component of the Piezo dome, $\Delta G_{\ell,\mathrm{cap}}^b$ (green curves), and the protein component of the Piezo dome, $\Delta G_{p,\mathrm{cap}}^b$ (purple curves), and (d) the activation energy of Piezo at the membrane tension values indicated by the color legends and as functions of temperature. For our estimates of $\Delta G_\ell^M(T)$, in panel (a), we used Eq. (B.1) in the arc-length representation (see Sec. B.1 for details) with the boundary conditions in Eqs. (4.6)–(4.8), which we evaluated with $S_{\mathrm{cap}} = 450 \ \mathrm{nm}^2$ and $R_{\mathrm{off}}(T)$ in Eq. (4.9). For our estimates of $\Delta G_{\ell,\mathrm{cap}}^\tau(T)$, in panel (b), we used Eq. (4.10) which we evaluated with $S_{\mathrm{cap}} = 450 \ \mathrm{nm}^2$ and $R_{\mathrm{off}}(T)$ in Eq. (4.9). For our estimates of $\Delta G_{\ell,\mathrm{cap}}^b(T)$, in panel (c), we used Eq. (4.11), which we evaluated with $K_b^\ell(T)$ in Eq. (4.2), $S_{\mathrm{cap}} = 450 \ \mathrm{nm}^2$, and $R_{\mathrm{off}}(T)$ in Eq. (4.9). For our estimates of $\Delta G_{p,\mathrm{cap}}^b(T)$, in panel (c), we used Eq. (4.12), which we evaluated with the $K_b^p(T)$ that is indicated by the legend underneath all of the panels, $R_0^p = 10.2 \ \mathrm{nm}$, $S_{\mathrm{cap}} = 450 \ \mathrm{nm}^2$, and $R_{\mathrm{off}}(T)$ in Eq. (4.9). To evaluate $R_{\mathrm{off}}(T)$ in Eq. (4.9), we used $R_0^p = 10.2 \ \mathrm{nm}$, $K_b^\ell(T)$ in Eq. (4.2), and the $K_b^p(T)$ that is indicated by the legend underneath all of the panels. For our estimates of $\Delta G(T)$, in panel (d), we used $\Delta G(T) = \Delta G_\ell^M(T) + \Delta G_{\ell,\mathrm{cap}}^\tau(T) + \Delta G_{\ell,\mathrm{cap}}^b(T) + \Delta G_{p,\mathrm{cap}}^b(T)$.

[see dotted curves in Fig. 4.7(a)]. In particular, at $\tau = 1 \ k_B T_{\mathrm{rm}}/\mathrm{nm}^2$, ΔG_ℓ^M decreases by

about $3 \ k_B T_{\mathrm{rm}}$ over the range $T = 10$–50°C [see blue dotted curve in Fig. 4.7(a)]. Since

we assume in our model that Piezo's dome flattens out in its open state, the lipid bilayer also flattens out, so $G^M_{\ell,\mathrm{on}} = 0$. This implies that the decrease in ΔG^M_ℓ is due to an increase in $G^M_{\ell,\mathrm{off}}$. $G^M_{\ell,\mathrm{off}}$ increases since the Piezo dome curvature $(1/R_{\mathrm{off}})$ increases with increasing temperature. Since R_{off} in Eq. (4.9) depends linearly on the ratio K^ℓ_b/K^p_b and K^ℓ_b decreases with increasing temperature while we assume K^p_b remains constant, the Piezo dome curvature increases with increasing temperature. This implies that the more highly curved Piezo dome yields a larger $G^M_{\ell,\mathrm{off}}$ in our model. Thus, our model predicts that ΔG^M_ℓ decreases due to Piezo's dome curvature increasing with increasing temperature.

We calculated the contribution $\Delta G^\tau_{\ell,\mathrm{cap}}$ in Eq. (4.10), at finite τ, as a function of temperature [see dotted curves in Fig. 4.7(b)]. We find that $\Delta G^\tau_{\ell,\mathrm{cap}}$ decreases approximately linearly with increasing temperature. In particular, at $\tau = 1\ k_B T_{\mathrm{rm}}/\mathrm{nm}^2$ we find that $\Delta G^\tau_{\ell,\mathrm{cap}}$ decreases by about $3\ k_B T_{\mathrm{rm}}$ over the range $T = 10\text{--}50^\circ\mathrm{C}$ [see blue dotted curve in Fig. 4.7(b)]. Since Piezo's dome curvature increases with increasing temperature and $\Delta A_{\mathrm{cap}} \sim 1/R^2_{\mathrm{off}}$ in Eq. (4.10), ΔA_{cap} increases with increasing temperature. Thus, our model predicts that $\Delta G^\tau_{\ell,\mathrm{cap}}$ decreases with increasing temperature due to the decrease in bilayer in-plane area that accompanies the increase in Piezo dome curvature in its off state.

We calculated the contribution $\Delta G^b_{\ell,\mathrm{cap}}$ in Eq. (4.11) as a function of temperature [see green dotted curve in Fig. 4.7(c)]. We find that $\Delta G^b_{\ell,\mathrm{cap}}$ decreases approximately linearly with increasing temperature by about $1\ k_B T_{\mathrm{rm}}$ over the range $T = 10\text{--}50^\circ\mathrm{C}$. Since we assume in our model that Piezo's dome flattens out in its open state, the lipid bilayer also flattens out, so $G^b_{\ell,\mathrm{cap,on}} = 0$. This implies that the decrease in $\Delta G^b_{\ell,\mathrm{cap}}$ is due to an increase in $G^b_{\ell,\mathrm{cap,off}}$. $G^b_{\ell,\mathrm{cap,off}} \sim 1/R^2_{\mathrm{off}}$ [see Eq. (4.11)], so $G^b_{\ell,\mathrm{cap,off}}$ increases with

increasing Piezo dome curvature. Thus, our model predicts that $\Delta G^b_{\ell,\mathrm{cap}}$ decreases with increasing temperature due to the increase in Piezo's dome curvature.

We calculated the contribution $\Delta G^b_{p,\mathrm{cap}}$ in Eq. (4.12) as a function of temperature [see purple dotted curve in Fig. 4.7(c)]. We find that $\Delta G^b_{p,\mathrm{cap}}$ increases approximately linearly with increasing temperature by about $3\ k_B T_{\mathrm{rm}}$ over the range $T = 10$–$50°\mathrm{C}$. Since we assume in our model that Piezo's dome flattens out in its open state, the lipid bilayer also flattens out, so $G^b_{p,\mathrm{cap,on}} = 0.25 K^p_b S_{\mathrm{cap}} (2/R^p_0)^2/2$ is independent of temperature [see Eq. (4.12)]. This implies that the increase in $\Delta G^b_{p,\mathrm{cap}}$ is due to a decrease in $G^b_{p,\mathrm{off}}$. $G^b_{p,\mathrm{off}} \sim [(1/R^p_0) - (1/R_{\mathrm{off}})]^2$, with $1/R^p_0 > 1/R_{\mathrm{off}}$ [see Eq. (4.12)]. This implies that as the Piezo dome curvature increases, it increases towards the intrinsic curvature of Piezo $(1/R^p_0)$ and, consequently, $G^b_{p,\mathrm{off}}$ decreases. Thus, our model predicts that the increase in $\Delta G^b_{p,\mathrm{cap}}$ with increasing temperature is due to the Piezo dome curvature increasing towards Piezo's intrinsic curvature.

These results suggest that if we assume $K^p_b(T) = 20\ k_B T_{\mathrm{rm}}$ the lipid bilayer contribution biases Piezo towards its open state $[\Delta_T(\Delta G_\ell) = \Delta_T(\Delta G^M_\ell + \Delta G^\tau_{\ell,\mathrm{cap}} + \Delta G^b_{\ell,\mathrm{cap}}) < 0]^{\|}$ with increasing temperature, while the contribution due to the bending of Piezo's arms biases Piezo towards its off state $[\Delta_T(\Delta G_p) = \Delta_T(\Delta^b_{p,\mathrm{cap}}) > 0]$. At low tension ($\tau \lesssim 0.1\ k_B T_{\mathrm{rm}}/\mathrm{nm}^2$), $|\Delta_T(\Delta G_\ell)| < |\Delta_T(\Delta G_p)|$, so increasing temperature biases Piezo towards its off state, $\Delta_T(\Delta G) > 0$ [see cyan and red dotted curves in Fig. 4.7(d)]. At a sufficiently large membrane tension ($\tau \gtrsim 0.2\ k_B T_{\mathrm{rm}}/\mathrm{nm}^2$), $|\Delta_T(\Delta G_\ell)| > |\Delta_T(\Delta G_p)|$, so increasing

---

$^{\|}$The quantity $\Delta_T q$ represents the difference between q at $T = 50°\mathrm{C}$ and q at $T = 10°\mathrm{C}$ for the function q.

temperature biases Piezo towards its on state, $\Delta_T(\Delta G) < 0$ [see blue dotted curve in Fig. 4.7(d)].

Piezo's activation threshold was previously measured [111] to be about $\tau \approx 0.4\ k_B T_{\mathrm{rm}}/\mathrm{nm}^2$. We find that as temperature increases, this threshold decreases by about $0.05\ k_B T_{\mathrm{rm}}/\mathrm{nm}^2$ (roughly equivalent to about a 10% decrease) over the range $T = 10\text{--}50°\mathrm{C}$ [see Fig. 4.8(a)]. So our model suggests changes in temperature have a slight effect on Piezo's gating threshold if K_b^p does not depend on temperature. In our model, this effect is primarily attributed to the increase in Piezo dome curvature $(1/R_{\mathrm{off}})$ [see Eq. (4.9)] with increasing temperature.

If we consider, instead, that $K_b^p(T) = K_b^\ell(T)$, the Piezo dome curvature is independent of temperature, with $1/R_{\mathrm{off}} = 0.25/R_0^p$ [see Eq. (4.9)]. Assuming $K_b^p(T) = K_b^\ell(T)$, we calculated ΔG_ℓ^M as function of temperature [see solid curves in Fig. 4.7(a)]. We find that ΔG_ℓ^M increases approximately linearly with increasing temperature. In particulate, at $\tau = 1\ k_B T_{\mathrm{rm}}/\mathrm{nm}^2$, we find ΔG_ℓ^M increases by about $1\ k_B T_{\mathrm{rm}}$ over the temperature range $T = 10\text{--}50°\mathrm{C}$ [see blue solid curve in Fig. 4.7(a)]. Since our model assumes the Piezo dome is flat in its open state, we have $G_{\ell,\mathrm{on}}^M = 0$. This implies the increase in ΔG_ℓ^M is due to a decrease in $G_{\ell,\mathrm{off}}^M$. $G_{\ell,\mathrm{off}}^M \sim K_b^\ell$ [see Eq. (B.1)], so $G_{\ell,\mathrm{off}}^M$ decreases with increasing temperature since K_b^ℓ decreases with increasing temperature [see Eq. (4.2)]. In essence, the lipid bilayer becomes easier to bend. Thus, our model predicts that the increase in ΔG_ℓ^M with increasing temperature is due to the bilayer becoming easier to bend.

We calculated $\Delta G_{\ell,\mathrm{cap}}^\tau$ as function of temperature [see solid curves in Fig. 4.7(b)]. We find that $\Delta G_{\ell,\mathrm{cap}}^\tau$ is independent of temperature. This result is attributed to the Piezo dome curvature not changing with temperature. Since the Piezo dome curvature does not
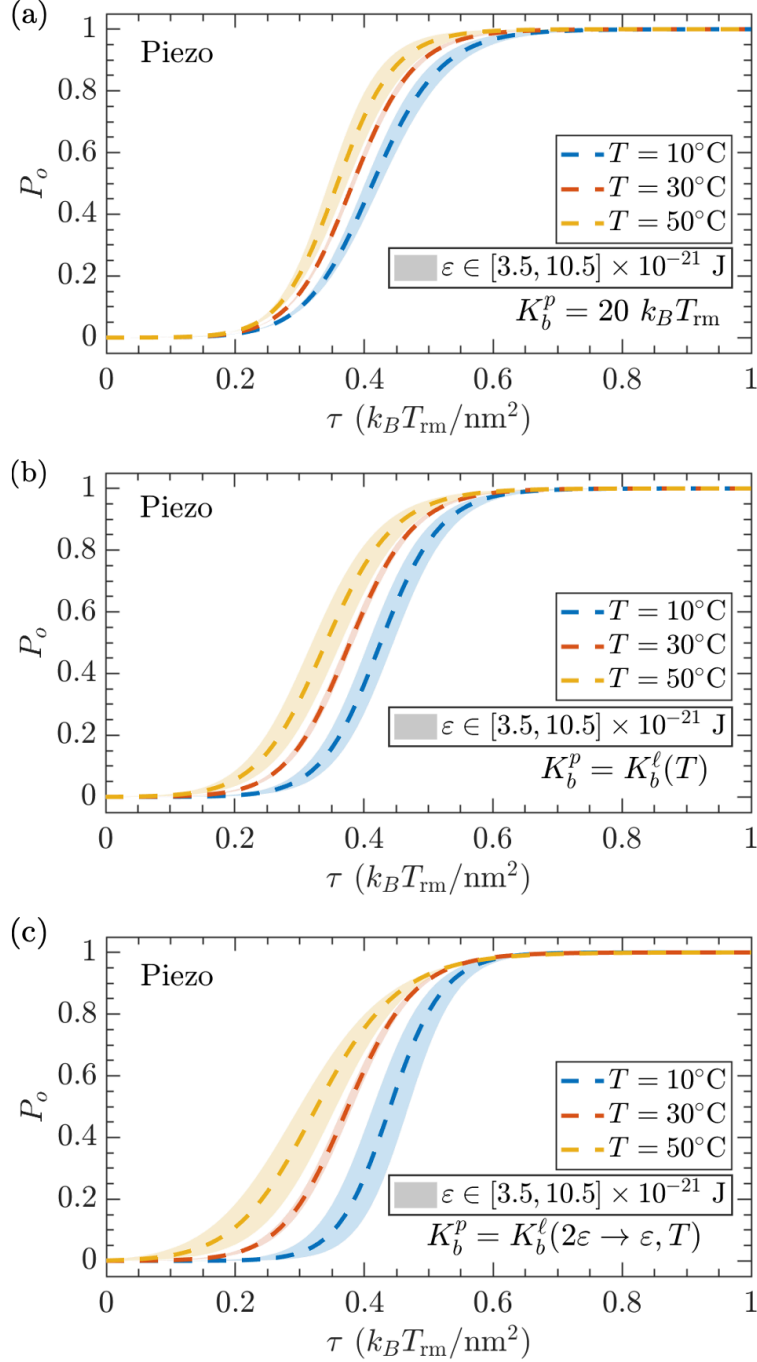
Figure 4.8: Estimates of channel opening probability in Eq. (4.4) for Piezo as a function of membrane tension and at the indicated values of temperature T, assuming (a) $K_b^p(T) = 20\ k_B T_{\rm rm}$, (b) $K_b^p(T) = K_b^\ell(T)$, and (c) $K_b^p(T) = K_b^\ell(2\varepsilon \to \varepsilon, T)$, with $K_b(T)$ calculated by Eq. (4.2). To evaluate $\Delta G = \Delta G_\ell^M + \Delta G_{\ell,\rm cap}^\tau + \Delta G_{\ell,\rm cap}^b + \Delta G_{p,\rm cap}^b$ in Eq. (4.4) we followed the caption of Fig. 4.7 to calculate all of its various contributions. The shaded regions denote the range of solutions that include 50% variations in ε about $\varepsilon = 7 \times 10^{-21}$ J at the temperatures indicated by the color legend in each panel.

change with temperature ΔA_p in Eq. (4.10) does not change with temperature. Thus our model predicts that $\Delta G_{\ell,\text{cap}}^{\tau}$ is independent of temperature since the Piezo dome curvature does not change with temperature when $K_b^p(T) = K_b^{\ell}(T)$.

We calculated $\Delta G_{\ell,\text{cap}}^{b}$ as a function of temperature [see solid green curve in Fig. 4.7(c)]. We find that $\Delta G_{\ell,\text{cap}}^{b}$ increases approximately linearly with increasing temperature by about $2\ k_B T_{\text{rm}}$ over the range $T = 10\text{--}50°\text{C}$. Since our model assumes the Piezo dome flattens out when it gates open, we have $G_{\ell,\text{cap,on}}^{b} = 0$. This implies the increase in $\Delta G_{\ell,\text{cap}}^{b}$ is due to a decrease in $G_{\ell,\text{cap,off}}^{b}$. $G_{\ell,\text{cap,off}}^{b} \sim K_b^{\ell}$ [see Eq. (4.11)], so $G_{\ell,\text{cap,off}}^{b}$ decreases with increasing temperature since K_b^{ℓ} decreases with increasing temperature [see Eq. (4.2)]. This amounts to the lipid bilayer becoming easier to bend with increasing temperature. Thus, our model predicts that the increase in $\Delta G_{\ell,\text{cap}}^{b}$ with increasing temperature is due to the bilayer becoming easier to bend.

We calculated the contribution $\Delta G_{p,\text{cap}}^{b}$ in Eq. (4.12) as a function of temperature [see purple solid curve in Fig. 4.7(c)]. We find that $\Delta G_{p,\text{cap}}^{b}$ decreases approximately linearly with increasing temperature by about $4\ k_B T_{\text{rm}}$ over the range $T = 10\text{--}50°\text{C}$. Since Piezo's dome curvature is independent of temperature, the dependence on temperature of $\Delta G_{p,\text{cap}}^{b}$ in encapsulated entirely in $K_b^p(T)$ ($\Delta G_{p,\text{cap}}^{b} \sim K_b^p$)[see Eq. (4.12)]. Since it is always the case that $1/R_0^p > 1/R_0^p - 1/R_{\text{off}}$ for finite R_{off}, in our model it is always true that $\Delta G_{p,\text{cap}}^{b} > 0$. Thus, our model predicts that $\Delta G_{p,\text{cap}}^{b}$ decreases with increasing temperature due to Piezo's arms becoming easier to bend.

If we assume $K_b^p(T) = K_b^{\ell}(T)$, our model results suggest that over the membrane tension range $\tau = 0\text{--}1\ k_B T_{\text{rm}}$, ΔG decreases with increasing temperature [see Fig. 4.7(d)]. Collecting our results for the effect of increasing temperature on the many contributions to

ΔG, we find that the lipid bilayer contribution ($\Delta G_\ell = \Delta_\ell^M + \Delta G_{\ell,\mathrm{cap}}^b$) biases Piezo towards its off state with increasing temperature while the protein contribution $\Delta G_p = \Delta G_{p,\mathrm{cap}}^b$ biases Piezo towards its on state. Over the membrane tension range $\tau = 0\text{--}1\ k_B T_{\mathrm{rm}}$, we have $|\Delta_T(\Delta G_\ell)| < |\Delta_T(\Delta G_p)|$, thus ΔG decreases with increasing temperature.

We calculated the channel opening probability in Eq. (4.4) of Piezo [see Fig. 4.8(b)]. We find that the activation threshold decreases by about $0.07\ k_B T_{\mathrm{rm}}/\mathrm{nm}^2$ (roughly equivalent to about a 20% decrease) with increasing temperature over the range $T = 10\text{--}50°\mathrm{C}$. Thus, if $K_b^p(T) = K_b^\ell(T)$, our model predicts changes in temperature can produce shifts in Piezo's activation threshold membrane tension that are on the same order of magnitude as the activation threshold.

We also explore the possibility that K_b^p decreases with increasing temperature at faster rate than K_b^ℓ. In particular, we assume $K_b^p = K_b^\ell(2\varepsilon \to \varepsilon, T)$ (see Sec. 4.2.3). We calculated ΔG_ℓ^M as function of temperature [see dashed curves in Fig. 4.7(a)]. We find that ΔG_ℓ^M increases approximately linearly with increasing temperature. In particulate, at $\tau = 1\ k_B T_{\mathrm{rm}}/\mathrm{nm}^2$, we find ΔG_ℓ^M increases by about $5\ k_B T_{\mathrm{rm}}$ over the temperature range $T = 10\text{--}50°\mathrm{C}$ [see blue dashed curve in Fig. 4.7(a)]. Since our model assumes the Piezo dome is flat in its open state, we have $G_{\ell,\mathrm{on}}^M = 0$. This implies the increase in ΔG_ℓ^M is due to a decrease in $G_{\ell,\mathrm{off}}^M$. $G_{\ell,\mathrm{off}}^M$ decreases since the Piezo dome curvature ($1/R_{\mathrm{off}}$) decreases with increasing temperature. Since R_{off} in Eq. (4.9) depends linearly on the ratio K_b^ℓ/K_b^p and K_b^p decreases at a faster rate with increasing temperature than K_b^ℓ, R_{off} increases with increasing temperature. Thus, the Piezo dome curvature decreases with increasing temperature. This implies that a less curved Piezo dome yields a smaller $G_{\ell,\mathrm{off}}^M$ in our model.

Thus, our model predicts that ΔG_ℓ^M increases due to Piezo's dome curvature decreasing with increasing temperature.

We calculated the contribution $\Delta G_{\ell,\mathrm{cap}}^\tau$ in Eq. (4.10), at finite τ, as a function of temperature [see dashed curves in Fig. 4.7(b)]. We find that $\Delta G_{\ell,\mathrm{cap}}^\tau$ increases approximately linearly with increasing temperature. In particular, at $\tau = 1\ k_B T_{\mathrm{rm}}/\mathrm{nm}^2$ we find that $\Delta G_{\ell,\mathrm{cap}}^\tau$ increases by about $3\ k_B T_{\mathrm{rm}}$ over the range $T = 10$–$50°\mathrm{C}$ [see blue dashed curve in Fig. 4.7(b)]. Since Piezo's dome curvature decreases with increasing temperature and $\Delta A_{\mathrm{cap}} \sim 1/R_{\mathrm{off}}^2$ in Eq. (4.10), ΔA_{cap} decreases with increasing temperature. Thus, our model predicts that $\Delta G_{\ell,\mathrm{cap}}^\tau$ increases with increasing temperature due to the increase in bilayer in-plane area that accompanies the decrease in Piezo dome curvature in its off state.

We calculated the contribution $\Delta G_{\ell,\mathrm{cap}}^b$ in Eq. (4.11) as a function of temperature [see green dashed curve in Fig. 4.7(c)]. We find that $\Delta G_{\ell,\mathrm{cap}}^b$ increases approximately linearly with increasing temperature by about $4\ k_B T_{\mathrm{rm}}$ over the range $T = 10$–$50°\mathrm{C}$. Since we assume in our model that Piezo's dome flattens out when it gates open, the lipid bilayer also flattens out, so $G_{\ell,\mathrm{cap,on}}^b = 0$. This implies that the increase in $\Delta G_{\ell,\mathrm{cap}}^b$ is due to an decrease in $G_{\ell,\mathrm{cap,off}}^b$. $G_{\ell,\mathrm{cap,off}}^b \sim 1/R_{\mathrm{off}}^2$ [see Eq. (4.11)], so $G_{\ell,\mathrm{cap,off}}^b$ decreases with decreasing Piezo dome curvature. Thus, our model predicts that $\Delta G_{\ell,\mathrm{cap}}^b$ increases with increasing temperature due to the decrease in Piezo's dome curvature.

We calculated the contribution $\Delta G_{p,\mathrm{cap}}^b$ in Eq. (4.12) as a function of temperature [see purple dashed curve in Fig. 4.7(c)]. We find that $\Delta G_{p,\mathrm{cap}}^b$ decreases approximately linearly with increasing temperature by about $11\ k_B T_{\mathrm{rm}}$ over the range $T = 10$–$50°\mathrm{C}$. Since we assume in our model that Piezo's dome flattens out when it gates open, the lipid bilayer

also flattens out, so $G^b_{p,\text{cap,on}} = 0.25 K^p_b S_{\text{cap}}(2/R^p_0)^2/2$ is independent of temperature [see Eq. (4.12)]. This implies that the decrease in $\Delta G^b_{p,\text{cap}}$ is due to an increase in $G^b_{p,\text{off}}$. $G^b_{p,\text{off}} \sim [(1/R^p_0) - (1/R_{\text{off}})]^2$, with $1/R^p_0 > 1/R_{\text{off}}$ [see Eq. (4.12)]. From this, it follows that as the Piezo dome curvature decreases, it decreases away from the intrinsic curvature of Piezo $(1/R^p_0)$ and, consequently, $G^b_{p,\text{off}}$ increases. Thus, our model predicts that the decrease in $\Delta G^b_{p,\text{cap}}$ with increasing temperature is due to the Piezo dome curvature decreasing away from Piezo's intrinsic curvature.

These results suggest that if we assume $K^p_b = K^\ell_b(2\varepsilon \to \varepsilon, T)$, the lipid bilayer contribution biases Piezo towards its closed state [$\Delta_T(\Delta G_\ell) = \Delta_T(\Delta G^M_\ell + \Delta G^\tau_{\ell,\text{cap}} + \Delta G^b_{\ell,\text{cap}}) > 0$] with increasing temperature, while the contribution due to the bending of Piezo's arms biases Piezo towards its on state [$\Delta_T(\Delta G_p) = \Delta_T(\Delta^b_{p,\text{cap}}) > 0$].

At low tension ($\tau \lesssim 0.1\ k_B T_{\text{rm}}/\text{nm}^2$), $|\Delta_T(\Delta G_\ell)| < |\Delta_T(\Delta G_p)|$, so increasing temperature biases Piezo towards its on state, $\Delta_T(\Delta G) < 0$ [see cyan and red dashed curves in Fig. 4.7(d)]. At a sufficiently large membrane tension ($\tau \gtrsim 1\ k_B T_{\text{rm}}/\text{nm}^2$), $|\Delta_T(\Delta G_\ell)| > |\Delta_T(\Delta G_p)|$, so increasing temperature biases Piezo towards its off state, $\Delta_T(\Delta G) > 0$ [see blue dashed curve in Fig. 4.7(d)].

Piezo's activation threshold was previously measured [111] to be about $\tau \approx 0.4\ k_B T_{\text{rm}}/\text{nm}^2$, at $\tau \sim 0.4\ k_B T_{\text{rm}}/\text{nm}^2$, our model give that increasing temperature biases Piezo towards it on state. We find that as temperature increases, Piezo's activation threshold decreases by about $0.13\ k_B T_{\text{rm}}/\text{nm}^2$ (roughly equivalent to about a 30% decrease) over the range $T = 10\text{--}50°\text{C}$ [see Fig. 4.8(a)]. So our model suggests that changes in temperature can have a substantial effect on Piezo's activation threshold if

$K_b^p = K_b^\ell(2\varepsilon \to \varepsilon, T)$. In our model, this effect is primarily attributed to the decrease in Piezo dome curvature ($1/R_{\text{off}}$) [see Eq. (4.9)] with increasing temperature.

The shaded regions in Fig. 4.8 denote the range of solutions for P_{o}, at the indicated temperatures, over which ε Eq. (4.2) was varied by 50% about the value 7×10^{-21} J. The shaded regions demonstrate that our results for the shifts in Piezo's activation curves with increasing temperature, in all the models we considered, are robust to variations in ε by as much as, e.g., 50%.

4.4   Connection to experiments

4.4.1   Chemoreceptors

Microorganisms have also long been recognized for their impressive capability to detect temperature variations and orient their movement in response to temperature gradients [13, 62–69, 219–223]. This ability to measure temperature gradients is vital for microorganisms to navigate towards optimal growth enviroments. While the molecular mechanisms underlying chemotaxis have been fairly well characterized and understood, the molecular mechanisms underpinning the thermosensing behavior remained elusive until experiments in recent decades began to shed light on the subject [13, 63–65, 68, 69, 222, 224]. Surprisingly, these investigations revealed that bacteria, including *E. coli*, repurpose some of the very same chemoreceptors they use for chemotaxis to carry out thermotaxis. Still, the physical mechanisms by which the chemoreceptors are activated by temperature have remained a mystery.

In this context, our model provides quantitative insights into the thermosensing capabilities of *E. coli* chemoreceptors within the framework of temperature-induced changes in lipid bilayer mechanics. Our findings indicate that alterations in bilayer properties, driven by temperature fluctuations, can exert a significant influence on the energetics of chemoreceptor activation. Over a biologically relevant temperature range of 10–$50°$C, our predictions suggest that moderate changes in temperature can induce variations of several $k_B T_{\rm rm}$ in the energetic contribution from protein-induced deformations in the *E. coli* cytoplasmic membrane to the chemoreceptor activation energy largely due to changes in membrane thickness. Importantly, this magnitude of variation is comparable to the changes in activation energy typically associated with chemoreceptor methylation, which are about 1 $k_B T_{\rm rm}$ per methylation site [209]. These findings suggest that regions characterized by locally elevated temperatures could act as areas with shorter bacterial run times or function as "sinks" for bacterial diffusion. This phenomenon might lead to a bias in bacterial motion toward higher temperatures. In essence, our model suggests that bacteria might be drawn to warmer regions due to the reduced activation energy for chemoreceptor-mediated responses that comes from a decrease in the contribution from the lipid bilayer deformations with increasing temperature. This aligns intriguingly with microfluid device experiments [13], which have indicated that bacteria tend to exhibit thermophilic behavior in response to moderate temperature gradients through the use of chemoreceptors.

4.4.2 MscL

Regarding MscL's temperature-dependent gating threshold in prokaryotic membranes, there is a paucity of available data. However, it is worth noting that over a decade ago, experimental evidence indicated that MscL's activation threshold decreases as temperature decreases when reconstituted in mammalian cells [225]. This suggests, at least in this particular investigation, that lower temperatures tend to bias MscL towards its open state. We found here that bilayer deformations bias MscL towards its open state at lower temperatures under two conditions: (1) MscL exhibits negligible change in hydrophobic thickness upon activation and (2) MscL's hydrophobic thickness exceeds that of the lipid bilayer. Currently, to our knowledge, there is a lack of adequate data regarding the thickness of mammalian cell membranes, preventing us from drawing any definite conclusions about the hydrophobic thickness in the reported study in mammalian cells [225]. The observed temperature dependence of MscL's activation threshold is intriguing, given the expectation that MscL exhibits a decrease in thickness when gated open [27, 42, 59, 91, 214], a point we wil return to later. Yet, we acknowledge that it is possible for tight binding lipids or peptides to act as structural co-factors that can effectively reduce the change in MscL's hydrophobic thickness when activated [22]. Assuming mammalian cell membranes are thinner than MscL, our findings suggest that MscL's effective hydrophobic thickness remains relatively constant during activation.

In contrast, if we assume that MscL's effective hydrophobic thickness decreases to a value thinner than the lipid bilayer when it gates open [27, 42, 59, 91, 214], our model predicts that MscL's activation threshold decreases with increasing temperature. In particular,

our model predicts MscL's activation threshold tension decreases by a couple $k_B T_{\rm rm}/{\rm nm}^2$ over the range $T = 10\text{–}50°{\rm C}$. While this result does not align with the experimental observations of MscL's activation threshold increasing with increasing temperature in mammalian cells [225], it is not unsupported. Since membrane hydrophobic thickness has been observed to decrease with increasing temperature [15, 116], predictions of MscL's activation threshold decreasing with increasing temperature align with the observations of MscL's activation threshold decreasing with decreasing membrane thickness [14, 22]. Moreover, there are also experiments that indicate that cell membrane rupture tension decreases with increasing temperature, albeit with limited available data [117]. These observations could be of biological significance if MscL's activation threshold was found to consistently remain just below that of the cell membrane rupture tension over the range of biologically relevant temperatures. This would be beneficial for bacteria given the potential for damage inflicted on the cell from the premature activation of MscL and, conversely, if MscL's activation was not accessible when needed.

Clearly, more data is needed to decipher MscL's functional dependence on temperature, but available experimental data and our calculations suggest that temperature may have a significant effect. Given the general principles on which our model is built, similar conclusions are expected to apply more broadly to other protein sensors.

4.4.3 Piezo

Recent electrophysiological experiments indicate that Piezo's activation is inhibited by cold temperatures and increased lipid bilayer rigidity [108, 226]. Since cold temperatures are expected to increase lipid bilayer rigidity, this suggests that Piezo's functional dependence on temperature is intricately linked to changes in lipid bilayer rigidity. Our model predicts that decreasing temperature (and increasing lipid bilayer rigidity) yields an increase in Piezo's activation threshold in qualitative agreement with experimental observations [108, 226]. This result follows regardless of whether we assumed the bending rigidity of Piezo's arms increases in colder temperatures or remains constant.

The shifts in Piezo's activation threshold with increasing temperature over the range $T = 10$–$50°C$, predicted by our model in terms of membrane tension, are on the same order of magnitude as Piezo's gating tension at room temperature $(\Delta\tau \sim -0.1 \ k_B T_{\mathrm{rm}}/\mathrm{nm}^2)$. Furthermore, our calculations indicate that these shifts are anticipated to be more substantial if the bending rigidity of Piezo's arms exhibits a faster rate of decrease with increasing temperature. These findings suggest that temperature can have a significant impact on the functionality of Piezo ion channels. Moreover our results indicate that the lipid bilayer rigidity may provide a general physical mechanism by which transmembrane mechanosensors can sense changes in temperature.

Chapter 5

Physical mechanism for the self-assembly of emerin nanodomains at the inner nuclear membrane

This chapter proposes and develops a physical mechanism for the self-assembly and stabilization of emerin nanodomains observed in experiments [12]. The chapter is organized as follows. In Sec. 5.1 we develop the general mathematical form of the reaction-diffusion equations we employ to model emerin nanodomains, and present a linear stability analysis to obtain the general mathematical conditions on the reaction rate constants and diffusion coefficients for which they yield a Turing instability. In Sec. 5.2 we introduce our physical model, based on a Turing mechanism, for the self-assembly and stabilization of emerin nanodomains. In Sec. 5.2.1 we demonstrate how the molecular reactions relevant for emerin nanodomains can be expressed mathematically in terms of our reaction-diffusion equations. In Sec. 5.3 we employ our reaction-diffusion model to predict key properties of emerin nanodomains observed in experiments. We summarize our conclusions in Sec. 6.4.

5.1 Reaction-diffusion equations and linear stability analysis

Here we present the mathematical framework of our reaction-diffusion system, where $I(x, y, t)$ and $A(x, y, t)$ represent dynamic molecular concentration fields along the INM governed by the reaction-diffusion equations

$$\frac{\partial I}{\partial t} = \mathrm{F}(I, A) + \nu_I \left[(1 - A) \nabla^2 I + I \nabla^2 A \right] \tag{5.1}$$

and

$$\frac{\partial A}{\partial t} = \mathrm{G}(I, A) + \nu_A \left[(1 - I) \nabla^2 A + A \nabla^2 I \right], \tag{5.2}$$

which involve the cubic polynomials F and G describing the reaction dynamics of the I and A molecule populations (see Sec. 5.2.1). The diffusion coefficients, ν_I and ν_A, dictate the dispersion rates of these molecular complexes. Notably, we impose here the constraint $0 \leq I + A \leq 1$, which accounts for the finite sizes [227] of I and A complexes in the confined INM area, on all reaction and diffusion processes; we thereby scale I and A to represent the local fractional coverage of INM area. This constraint produces the non-linear modifications to the standard diffusion terms $\nu_I \nabla^2 I$ and $\nu_A \nabla^2 A$ in Eqs. (5.1) and (5.2).

A Turing instability, also known as a diffusion-driven instability, was theorized by Alan Turing [140, 141], as a generic mechanism for nonequilibrium pattern formation from random initial conditions. For our model to support a Turing instability [9, 11, 120–122, 140–

144], Eqs. (5.1) and (5.2) must exhibit a non-trivial homogeneous fixed point, represented as $(I, A) = (\bar{I}, \bar{A})$. For a non-trivial homogeneous fixed point, both $\bar{I}$ and $\bar{A}$ should not equal 0 or 1. We have

$$\mathrm{F}\left(\bar{I}, \bar{A}\right) = 0, \qquad \mathrm{G}\left(\bar{I}, \bar{A}\right) = 0, \tag{5.3}$$

In the absence of diffusion, random perturbations of this fixed point decay over time. Our perturbation can be represented as a planar wave with small amplitude,

$$\vec{\delta f}(x, y, t) = \begin{pmatrix} \delta I \\ \delta A \end{pmatrix} = \begin{pmatrix} \hat{\delta I} \\ \hat{\delta A} \end{pmatrix} e^{\lambda t} e^{i \cdot \vec{\kappa} \cdot \vec{r}}, \tag{5.4}$$

where λ characterizes whether the perturbation grows or decays, $\vec{\kappa} = (\kappa_x, \kappa_y)^{\mathrm{T}}$ is the perturbation's spatial wavevector, and $\vec{r} = (x, y)^{\mathrm{T}}$. Introducing random perturbations of the I and A concentration fields about $I = \bar{I}$ and $A = \bar{A}$, $\vec{\delta f}$ and setting $\nu_I = \nu_A = 0$, we have from Eqs. (5.1)–(5.3) that

$$\frac{\partial \vec{\delta f}(x, y, t)}{\partial t} = \bar{\bar{\mathbf{J}}} \vec{\delta f}(x, y, t), \tag{5.5}$$

with the homogeneous stability matrix

$$\bar{\bar{\mathbf{J}}} = \begin{pmatrix} I_{11} & I_{12} \\ A_{21} & A_{22} \end{pmatrix} \equiv \begin{pmatrix} \frac{\partial \mathrm{F}}{\partial I}\big|_{(I,A)=(\bar{I},\bar{A})} & \frac{\partial \mathrm{F}}{\partial A}\big|_{(I,A)=(\bar{I},\bar{A})} \\ \frac{\partial \mathrm{G}}{\partial I}\big|_{(I,A)=(\bar{I},\bar{A})} & \frac{\partial \mathrm{G}}{\partial A}\big|_{(I,A)=(\bar{I},\bar{A})} \end{pmatrix}, \tag{5.6}$$

to leading order in $\vec{\delta f}$. Substitution of this representation of the perturbation $\vec{\delta f}$ into Eq. (5.5) leads to the eigenvector equation

$$\bar{\mathbf{J}} \cdot \vec{\delta f}\left(t\right) = \lambda \vec{\delta f}\left(t\right) , \tag{5.7}$$

For the perturbation $\vec{\delta f}$ to decay with time, Eq. (5.7) must yield two negative eigenvalues ($\lambda_0^{\pm} < 0$). One finds that the condition

$$\mathrm{Tr}[\bar{\mathbf{J}}] = I_{11} + A_{22} < 0 \tag{5.8}$$

guarantees one negative eigenvalue, while the condition

$$\mathrm{Det}[\bar{\mathbf{J}}] = I_{11}A_{22} - I_{12}A_{21} > 0 \tag{5.9}$$

ensures that both eigenvalues share the same sign. Consequently, Eqs. (5.8) and (5.9) ensure the stability of the reaction-only system under (spatially homogeneous) perturbations.

The subsequent stage in our analysis involves introducing diffusion into our system and investigating the joint conditions on the reaction-diffusion processes in the system leading to a Turing instability. In the presence of diffusion with $\nu_I \neq \nu_A$, random perturbations of the fixed point $(I, A) = \left(\bar{I}, \bar{A}\right)$ trigger pattern formation via a Turing instability.

Introducing random perturbations of the I and A concentration fields about $I = \bar{I}$ and $A = \bar{A}$, $\vec{\delta f}$, we have from Eqs. (5.1)–(5.3) that

$$\frac{\partial \vec{\delta f}\,(x,y,t)}{\partial t} = \left(\bar{\mathbf{J}} + \bar{\mathbf{D}} \cdot \nabla^2\right) \vec{\delta f}\,(x,y,t)\;, \tag{5.10}$$

with the coefficients of the diffusive terms in matrix

$$\bar{\mathbf{D}} = \begin{pmatrix} \nu_I \left(1 - \bar{A}\right) & \bar{I} \\ \bar{A} & \nu_A \left(1 - \bar{I}\right) \end{pmatrix}, \tag{5.11}$$

to leading order in $\vec{\delta f}$. Substitution of this representation of the perturbation $\vec{\delta f}$ into Eq. (5.10) leads to the eigenvector equation

$$\left(\bar{\mathbf{J}} - \kappa^2 \bar{\mathbf{D}}\right) \vec{\delta f}\,(t) = \lambda \vec{\delta f}\,(t)\;. \tag{5.12}$$

For a Turing instability, the perturbation $\vec{\delta f}$ must not decay with time. The perturbation $\vec{\delta f}$ decays with time if $\mathrm{Tr}\left[\bar{\mathbf{J}} - \kappa^2 \bar{\mathbf{D}}\right] < 0$ and $\mathrm{Det}\left[\bar{\mathbf{J}} - \kappa^2 \bar{\mathbf{D}}\right] > 0$, so, for their to be a Turing instability, one or both of these conditions must not be satisfied.

The terms within $\bar{\mathbf{D}}$ in Eq. (5.11) are positive, since $(I, A) = \left(\bar{I}, \bar{A}\right)$ is a non-trivial homogeneous fixed point and $0 \leq I + A \leq 1$. Thus $\mathrm{Tr}\left[\bar{\mathbf{J}} - \kappa^2 \bar{\mathbf{D}}\right] = I_{11} + A_{22} - \kappa^2 \left[\nu_I \left(1 - \bar{A}\right) + \nu_A \left(1 - \bar{I}\right)\right] < 0$. This implies, for a Turing instability, we require $\mathrm{Det}\left[\bar{\mathbf{J}} - \kappa^2 \bar{\mathbf{D}}\right] < 0$.

$\mathrm{Det}\left[\bar{\mathbf{J}} - \kappa^2 \bar{\mathbf{D}}\right] = \mathrm{A}\kappa^4 - \mathrm{B}\kappa^2 + \mathrm{C} < 0$, with $\mathrm{A} = 4\nu_I \nu_A \left(1 - \bar{I} - \bar{A}\right)$, $\mathrm{B} = \nu_I \left[A_{22} \left(1 - \bar{A}\right) - A_{21}\bar{I}\right] + \nu_A \left[I_{11} \left(1 - \bar{I}\right) - I_{12}\bar{A}\right]$, and $\mathrm{C} = \mathrm{Det}\left[\bar{\mathbf{J}}\right]$. So $\mathrm{Det}\left[\bar{\mathbf{J}} - \kappa^2 \bar{\mathbf{D}}\right]$

is a quadratic function in κ^2. Note that $\mathrm{A} > 0$ since $(I, A) = (\bar{I}, \bar{A})$ is a non-trivial homogeneous fixed point and $0 \leq I + A \leq 1$. Therefore, $\mathrm{Det}\left[\bar{\mathbf{J}} - \kappa^2\bar{\mathbf{D}}\right]$ is a convex parabolic function in κ^2, with its vertex at $\kappa^2 = \mathrm{B}/2\mathrm{A}$. To have $\mathrm{Det}\left[\bar{\mathbf{J}} - \kappa^2\bar{\mathbf{D}}\right] < 0$, the vertex of $\mathrm{Det}\left[\bar{\mathbf{J}} - \kappa^2\bar{\mathbf{D}}\right]$ must lie below the κ^2-axis. Since $\mathrm{C} = \mathrm{Det}[\bar{\mathbf{J}}] > 0$ [see Eq. (5.9)], this can only be true if $\mathrm{B}^2 - 4\mathrm{AC} > 0$, and thus we have the condition

$$\left\{\nu_I\left[A_{22}\left(1 - \bar{A}\right) - A_{21}\bar{I}\right] + \nu_A\left[I_{11}\left(1 - \bar{I}\right) - I_{12}\bar{A}\right]\right\}^2 - 4\nu_I\nu_A\left(1 - \bar{I} - \bar{A}\right)\mathrm{Det}\left[\bar{\mathbf{J}}\right] > 0\,.$$

(5.13)

The perturbation $\vec{\delta f}$ has a finite spatial frequency κ, so for a Turing instability, κ must be real where $\mathrm{Det}\left[\bar{\mathbf{J}} - \kappa^2\bar{\mathbf{D}}\right] < 0$. This is the case if the intercepts $\kappa_\pm^2 > 0$. $\kappa_\pm^2 > 0$ if $B > 0$, and consequently we have the condition

$$\nu_I\left[A_{22}\left(1 - \bar{A}\right) - A_{21}\bar{I}\right] + \nu_A\left[I_{11}\left(1 - \bar{I}\right) - I_{12}\bar{A}\right] > 0\,. \tag{5.14}$$

The range $\left(\kappa_-^2, \kappa_+^2\right)$ signifies a band of unstable perturbation modes that give rise to a Turing instability. An estimate of the characteristic scale arising from the Turing instability can be calculated from the midpoint of this band, denoted as κ_m^2, which corresponds to the vertex of $\mathrm{Det}\left[\bar{\mathbf{J}} - \kappa^2\bar{\mathbf{D}}\right]$, $\kappa_m = \sqrt{\mathrm{B}/2\mathrm{A}}$ [121]. The characteristic length scale is determined by

$$\ell_c = \frac{2\pi}{\kappa_m} = 2\pi\sqrt{\frac{2\nu_I\nu_A(1 - \bar{I} - \bar{A})}{\nu_I[A_{22}(1 - \bar{A}) - A_{21}\bar{I}] + \nu_A[I_{11}(1 - \bar{I}) - I_{12}\bar{A}]}}\,. \tag{5.15}$$

5.2 Physical model of emerin nanodomains

Here we develop a physical model of the self-assembly of emerin nanodomains at the INM. Our model serves three related purposes: (a) to explain how wild-type emerin nanodomains form when no force is applied, (b) to predict how wild-type emerin nanodomain properties change under force application based on experimental data on changes in emerin diffusion under force application, and (c) to trace observed changes in emerin organization in mutated forms of emerin to changes in key reaction or diffusion processes.

Experiments have revealed two distinct populations of fast and slowly diffusing emerin at the INM [12]. On this basis, we consider in our model two distinct types of emerin-NBP complexes, fast and slowly diffusing emerin-NBP complexes. We assume that there are fast diffusing emerin that on their own cannot assemble molecular complexes, but can do so by interacting with other emerin or NBPs. We refer to these emerin and NBP molecular components, collectively, as $\varnothing$. On the one hand, emerin can interact with other emerin or NBPs to form molecular complexes that can transiently assemble into higher-order structures, resulting in a local increase in the molecule concentration at the INM. Such molecular complexes therefore *activate* increased molecule concentrations at the INM, and we denote them by A. We assume that the diffusion of A complexes is slowed down substantially by their interactions with other emerin and with molecular binding partners, and therefore associate A complexes with the slowly diffusing emerin populations seen in experiments [12]. We set their diffusion coefficient to $\nu_A = \nu_{\mathrm{slow}}$ (see Sec. 5.3 for data).

On the other hand, we assume that emerin can also form transient complexes that only show weak interactions with potential molecular binding partners and do not form higher-order structures*, thus locally *inhibiting* increased molecule concentrations at the INM through steric constraints. We denote these molecular complexes by I. We assume that, compared to A complexes, the diffusion of I complexes is less affected by interactions with potential molecular binding partners, and therefore associate I complexes with the more rapidly diffusing emerin populations seen in experiments. We set their diffusion coefficient to $\nu_I = \nu_{\text{fast}}$ (see Sec. 5.3 for data). Note that I complexes may contain a single emerin molecule or multiple emerin molecules. For instance, the EDMD-associated P183H mutation yields spontaneous formation of emerin dimers that are long-lived enough to be tracked in microscopy experiments, and seem unable to form higher-order structures [12, 127]. The diffusion properties of these P183H dimers are relatively similar to those found for emerin monomers that are not part of higher-order structures [12].

Given experimental uncertainties, and to keep our model as general as possible, we do not specify the exact stoichiometry of A and I complexes in terms of emerin molecules or NBPs. A and I complexes may therefore correspond to a range of molecular structures, and are defined by their reaction and diffusion properties rather than their detailed molecular composition. The precise diffusion properties of A and I complexes are likely to depend on their detailed molecular composition. A more detailed model of emerin nanodomain self-assembly would therefore allow for more than just two types of molecular complexes. We also note that, since experiments suggest that the regime of slow emerin

---

*Possibly, because emerin or NBPs are present in these complexes at stoichiometries or in molecular conformations that are inconsistent with the assembly of higher-order structures.

diffusion applies predominantly to emerin inside emerin nanodomains, we implicitly make here the assumption that emerin nanodomains are dominated by A, rather than I, complexes. Our model calculations are consistent with this assumption (see Sec. 5.3).

To understand the spontaneous formation of emerin nanodomains within the framework of our model, consider a local fluctuation in the molecule concentrations at the INM that produces a local excess of the activating molecule species. Due to the reaction properties of the activating molecule species, the molecule concentrations of both activators and inhibitors will subsequently be increased at that membrane location. Since it is assumed that $\nu_I > \nu_A$, the inhibiting molecule species diffuse faster out of this membrane region than the activating molecule species, producing a positive feedback in which local molecule concentrations of both the activating and inhibiting molecule species are locally increased. Finally, a steady state is reached when enough of the inhibiting molecules diffuse into the membrane regions from the surrounding membrane so that the local concentrations of activating and inhibiting molecule species balance each other.

At the most basic level, I and A complexes may both spontaneously assemble or disassemble. Since, at least in wild-type systems, the self-assembly of emerin into nanodomains seems to rely on interactions with A complexes (see below), we assume that the disassembly of I and A is much faster than their spontaneous assembly. For simplicity, we therefore set the spontaneous assembly rates of both I and A to be equal to zero

for wild-type emerin (but see Sec. 5.3.4.1) while allowing for the spontaneous dissociation reactions

$$I \xrightarrow{f_1} \varnothing \,, \tag{5.16}$$

$$A \xrightarrow{g_1} \varnothing \,, \tag{5.17}$$

where f_1 and g_1 denote decay rate constants. The rate constants f_1 and g_1 fix the time scales associated with the reaction and diffusion properties of the I and A populations in our model of emerin nanodomain self-assembly.

In the absence of direct experimental measurements of f_1 and g_1, we fix f_1 and g_1 through a simple physical argument inspired by the mathematics of Turing instabilities [140]. Note that, in the absence of reactions increasing the I and A concentrations, f_1 and g_1 in Eqs. (5.16) and (5.17) yield estimates for the root-mean-square displacements (RMSDs) of the I and A populations over their lifetime at the membrane, $2\sqrt{\nu_I/f_1}$ and $2\sqrt{\nu_A/g_1}$. We assume that the I population can globally explore the system and, hence, diffuse over the characteristic scale of emerin nanodomains (~ 20 nm), while the A population stays localized over molecular scales. We therefore set $f_1 = 30$ s^{-1} and $g_1 = 30f_1$ resulting, for wild-type systems under no mechanical stress, in RMSDs of about 16 nm and 1 nm for the I and A populations. While we use these values of f_1 and g_1 throughout, we find that f_1 or g_1 can be changed by as much as 50%, or even more, to obtain emerin nanodomains with similar properties.

Based on the experimental observation that emerin can form higher-order structures, we assume that the presence of A at a particular membrane location increases the likelihood that additional emerin complexes assemble at that membrane location. This could, for instance, result from the preferential recruitment of NBPs to membrane regions with elevated A concentrations, from a direct binding of A to emerin monomers, or from a local slowing down of emerin diffusion in membrane regions with elevated A concentrations. We allow here for both the possibility that an A complex can facilitate the assembly of another A complex,

$$A + \varnothing \xrightarrow{g_2} 2A \,, \tag{5.18}$$

and, oppositely, for the possibility that a newly formed emerin complex is unable to form higher-order structures,

$$A + \varnothing \xrightarrow{f_2} A + I \,. \tag{5.19}$$

In the case of emerin complexes that can form higher-order structures, we also allow for the possibility that two emerin complexes present in a particular membrane region can interact to facilitate the formation of a third emerin complex,

$$2A + \varnothing \xrightarrow{f_3} 3A \,. \tag{5.20}$$

Note that, mathematically, the above reaction provides the only fundamental distinction between I and A, together with our assumption that A can locally increase the concentration of I, but not vice versa. Equations (5.18)–(5.20) thus encapsulate our model assumptions about the key reaction properties of A and, by extension, I complexes underlying emerin nanodomain self-assembly.

To achieve a non-trivial steady-state distribution of emerin, decay and creation rates across multiple emerin complexes must take comparable magnitudes. In particular, due to the slow diffusion rates of A complexes, the decay and creation rates of different A complexes must be approximately equal to each other so that a non-trivial steady state can be achieved. Furthermore, as mentioned above, we expect from experiments that emerin nanodomains are predominantly composed of A, rather than I, complexes. We therefore expect f_2 in Eq. (5.19) to be smaller than f_1 in Eq. (5.16). For the calculations described here we set $f_2 = f_1/2$, but other choices $f_2 \lesssim f_1$ give similar results. In the most basic picture, we expect g_1 and g_2 in Eqs. (5.17) and (5.18) to take similar magnitudes, and we therefore set $g_2 = g_1$. Since the reactions in Eqs. (5.18) and (5.19) correspond to first-order reactions, while the reaction in Eq. (5.20) corresponds to a second-order reaction, we generally expect g_3 to be substantially smaller than g_1 and g_2. We set here $g_3 = g_2/15 = 2f_1$ for wild-type emerin under no mechanical stress. Again, we find that other choices for $g_1 \approx g_2$ and $g_3 \ll g_2$ give similar results.

In all reaction (and diffusion) processes that locally increase the molecule concentration at the INM, we include steric factors inhibiting the formation of emerin complexes in crowded membrane regions (or their diffusion to such membrane regions) such that the sum of the dimensionless I and A concentration fields, $(I + A)$ with $I = I(x, y, t)$ and

$A = A(x, y, t)$, cannot exceed 1 anywhere in the system (see Sec. 5.1). Thus, $I(x, y, t)$ and $A(x, y, t)$ represent the fraction of the free membrane area covered by I and A complexes.

5.2.1 Reaction kinetics of emerin nanodomains

Equations (5.16), (5.17), (5.19), and (5.20) provide the key reactions entering our model of emerin nanodomain self-assembly. In particular, the reactions $I \rightarrow \varnothing$ and $A \rightarrow \varnothing$ in Eqs. (5.16) and (5.17) represent the spontaneous disassembly of I and A complexes. Conversely, the reactions $A + \varnothing \rightarrow A + I$, $A + \varnothing \rightarrow 2A$, and $2A + \varnothing \rightarrow 3A$ in Eqs. (5.19), (5.18), and (5.20) represent the assembly of I and A complexes, which we take to be catalyzed by A complexes. We mathematically account for these reactions in the reaction-diffusion equations in Eqs. (5.1) and (5.2) through the formalism of chemical dynamics [140–144],

$$\mathrm{F}(I, A) = -f_1 I + f_2 (1 - I - A) A \tag{5.21}$$

and

$$\mathrm{G}(I, A) = -g_1 A + g_2 (1 - I - A) A + g_3 \left(\frac{1 - I - A}{1 - \bar{I} - \bar{A}} \right) \frac{A^2}{\bar{A}} \tag{5.22}$$

with

$$\bar{A} = \frac{f_1 (g_2 - g_1 + g_3)}{f_1 g_2 + f_2 (g_1 - g_3)}, \qquad \bar{I} = \frac{f_2}{f_1} \left(\frac{g_1 - g_3}{g_2} \right) \bar{A}. \tag{5.23}$$

For instance, the decay of I and A complexes into emerin and NBPs is characterized by the terms $-f_1 I$ and $-g_1 A$ in F and G. We consider steric effects by imposing the constraint $0 \leq I + A \leq 1$, leading to a reduction in the relevant reaction rates by a factor of

$(1 - I - A)$. The reaction $A + \varnothing \to A + I$, represented by the term $+ f_2 (1 - I - A) A$ in F, and the reactions $A + \varnothing \to 2A$ and $2A + \varnothing \to 3A$, represented by the terms $+ g_2 (1 - I - A) A$ and $+ g_3 [A^2 (1 - I - A)] / [(1 - \bar{I} - \bar{A}) \bar{A}]$ in G, model the activation of elevated concentrations of I complexes by A complexes and the self-activation of A complexes.

As explained in Section 5.2, our Turing model assumes that the I complexes act as inhibitors and A complexes as activators, leading to $I_{11} < 0$ and $A_{22} > 0$ in Eq. (5.6), respectively. Note that the evaluation of I_{11} in Eq. (5.6), utilizing Eq. (5.21), results in the condition

$$I_{11} = -f_1 - f_2 \bar{A} < 0 \,, \tag{5.24}$$

Since our model does not have any reactions for which I complexes stabilize other I complexes, we have that I complexes have the property inhibiting other I complexes through steric repulsion, $I_{11} < 0$, due to their finite size. Utilizing Eq. (5.22) to assess A_{22} in Eq. (5.6) yields the following condition for a Turing instability,

$$A_{22} = -g_1 + g_2 \left(1 - \bar{I} - 2\bar{A}\right) + g_3 \left[2 - \frac{\bar{A}}{1 - \bar{I} - \bar{A}} \right] > 0 \,. \tag{5.25}$$

The reaction $2A + \varnothing \to 3A$ represents the minimal reaction capable of yielding $A_{22} > 0$ in our model. We note here that the reaction $A + \varnothing \to 2A$ is insufficient for the self-activation of A complexes since it would fail to give $A_{22} > 0$ in our model.

Consider that, as per the conditions outlined in Sec. 5.1, we must have $I_{11} A_{22} - I_{12} A_{21} > 0$ [refer to Eq. (5.9)]. Consequently, it follows that I_{12} and A_{21} must possess

opposite signs. In our model, we do not have any reaction in which I complexes stabilize A complexes. Thus, we find, by evaluating A_{21} in Eq. (5.6) and utilizing Eq. (5.22), that

$$A_{21} = -g_2\bar{A} - g_3\bar{A}/(1 - \bar{I} - \bar{A}) < 0\,. \tag{5.26}$$

Notably, in our model, the reaction $A+\varnothing \rightarrow A+I$ embodies the simplest scenario wherein I complexes are stabilized by A complexes. Evaluating I_{12} in Eq. (5.6), using Eq. (5.21), yields the following condition for a Turing instability,

$$I_{12} = f_2\left(1 - \bar{I} - 2\bar{A}\right) > 0\,. \tag{5.27}$$

The reaction terms in F and G are such that the reaction rate constants f_1, f_2, g_1, g_2, and g_3 are all expressed in units of s^{-1}. For emerin nanodomain self-assembly to occur through a Turing instability, these reaction rates, for a given, observed set of values of the I and A diffusion coefficients ν_I and ν_A, must satisfy the mathematical constraints in Eqs. (5.8), (5.9), (5.13), (5.14), and (5.24)–(5.27).

5.2.2   Numerical implementation

The reaction and diffusion processes considered in our model imply, via the Turing mechanism for nonequilibrium pattern formation [140], a characteristic length scale ℓ_c, which can be estimated through a linear stability analysis (see Sec. 5.1) [121] and which we corroborate through numerical solutions of our reaction-diffusion equations. The corresponding characteristic diameter of emerin nanodomains, ℓ_Φ, is given by $\ell_\Phi \approx \ell_c/2$.

Similarly, the characteristic time scale for the self-assembly of emerin nanodomains, τ, can be estimated as $\tau \approx \ell_c^2/\nu_A$, where $\nu_A < \nu_I$ is the diffusion coefficient of the slower molecule species (A complexes) considered in our model. However, due to uncertainties in our estimates of f_1 and g_1, which fix the time scales associated with I and A (see Sec. 5.2), as well as the mean-field character of the formulation of our model [11], we only attach limited physical significance to the values of τ obtained from our model calculations, and show τ for completeness.

For our numerical solutions of the reaction-diffusion Eqs. (5.1) and (5.2), we employed the *DifferentialEquations* library in Julia [228, 229]. We compared numerical solutions obtained with a range of solvers—including *BS3*, *Tsit5*, *Runge-Kutta*, and *GMRES*—and found similar results. The numerical solutions shown here were obtained using the *GMRES* solver. We used periodic boundary conditions with a system size $400 \times 400 \text{ nm}^2$, which is significantly larger than the size of emerin nanodomains observed in experiments [12]. Smaller system sizes approaching the size of emerin nanodomains can yield finite-size artifacts in the emerin patterns generated by our model.

The numerical solutions presented in (Sec. 5.3) were obtained from initial conditions that were perturbed randomly about the homogeneous steady state of the system, $(I, A) = (\bar{I}, \bar{A})$, setting the diffusion coefficients $\nu_I = \nu_{\text{fast}}$ and $\nu_A = \nu_{\text{slow}}$ (see Fig. 5.1 for data of ν_{fast} and ν_{slow} for each system considered here), and utilizing the reaction rate constants in Sec. 5.3 for each individual system discussed. Random perturbations were drawn from a uniform distribution over $[-0.0005, 0.0005]$. Note that the reaction rates in our model fix the homogeneous steady state $(I, A) = (\bar{I}, \bar{A})$ of the system (see Sec. 5.2.1) and were chosen for each system considered here to satisfy the constraints for a Turing instability

	WT	WT; force	Q133H	P183H	Δ95-99	Δ95-99; force
$\nu_{\text{fast}}\ (\mu\text{m}^2/s)$	2×10^{-3}	4×10^{-3}	3×10^{-3}	1.5×10^{-3}	1×10^{-3}	no data
$\nu_{\text{slow}}\ (\mu\text{m}^2/s)$	3×10^{-4}	6×10^{-4}	4×10^{-4}	1×10^{-4}	1.5×10^{-4}	no data
$\ell_\Phi\ (\text{nm})$	22	50	18	35	null	74
$\ell_\Phi\ (\text{nm})$	22±11	60±13	19±12	35±12	null	75±20
$F_\Phi/F_\Phi^{\text{WT}}$	1	0.67	1.55	0.39	null	0.38
$F_\Phi/F_\Phi^{\text{WT}}$	1	0.56	1.49	0.27	null	0.24

☐ data from experiments   ☐ reaction-diffusion model predictions

Figure 5.1: Table comparing experimental data on emerin [12] (orange) and predictions of our reaction-diffusion model (emerin nanodomain diameter, ℓ_Φ, and ratio of the fraction of emerin nanodomain area covered by I and A complexes relative to that of the wild type system under no mechanical stress, $F_\Phi/F_\Phi^{\text{WT}}$) (red) for the various emerin systems in Fig. 5.2 and the Δ95-99 system under no mechanical stress. For Δ95-99 systems under no mechanical stress, emerin nanodomains were not observed to self-assemble in experiments [12] and were not predicted to self-assemble by our model. So, for the Δ95-99 system under no mechanical stress, we specify "null" for $F_\Phi/F_\Phi^{\text{WT}}$ and ℓ_Φ.

in Eqs. (5.8), (5.9), (5.13), (5.14), (5.24)–(5.27), with the exception of our solutions for the Δ95-99 emerin system under no mechanical stress. Our model for the Δ95-99 emerin system under no mechanical stress does not yield a Turing pattern due to not satisfying the constraints for a Turing instability. In Sec. 5.2.1 we express the reaction scheme used to obtain our numerical solutions in Sec. 5.3 in a form that, for mathematical convenience, explicitly involves the homogeneous steady state $(I, A) = (\bar{I}, \bar{A})$, with all reaction rates having units of s^{-1}. We used a 150×150 grid for all numerical solutions, and checked that a finer grid produced similar results. The steady states solutions provided in Sec. 5.3 correspond to times $t = 100\tau$ in our numerical solutions.

To calculate the average joint concentration of $(I + A)$ inside emerin nanodomains, F_Φ, we first find, for a given nanodomain, the grid point associated with the maximum of $(I + A)$ in the steady state of the system. We then average $(I + A)$ over all grid points

within a radius $\ell_\Phi/2$, rounded to the nearest multiple of the grid spacing, about this (local) maximum of $(I + A)$. We repeat this algorithm for four additional emerin nanodomains and average over five nanodomains to obtain F_Φ. We found that this last step was, strictly speaking, not necessary, with F_Φ evaluated over a single nanodomain and F_Φ evaluated over multiple nanodomains yielding similar results.

5.3 Results

5.3.1 Wild-type system under no mechanical stress

For wild-type ("WT") systems under no mechanical stress, we find that our model yields spontaneous self-assembly of emerin nanodomains from random initial conditions. In the steady state of the system, we find that the emerin nanodomains obtained from our model have a characteristic diameter $\ell_\Phi \approx 22$ nm, in good agreement with 22 ± 11 nm in diameter observed in experiments [12] [see Figs. 5.1 and 5.2(a)]. Thus, our model yields spontaneous self-assembly of emerin nanodomains with a size that is consistent with experimental observations. Our model also predicts that the fraction of available emerin nanodomain area covered by I and A complexes is $F_\Phi \approx 0.15$. This is comparable to the mean fractional area of emerin nanodomains covered by emerin, approximately 3–15%, suggested by previously published data [12] and further unpublished experimental estimates [230]. As expected, our numerical solutions yield elevated concentrations of A complexes compared to I complexes in emerin nanodomains [Fig. 5.2(a)].
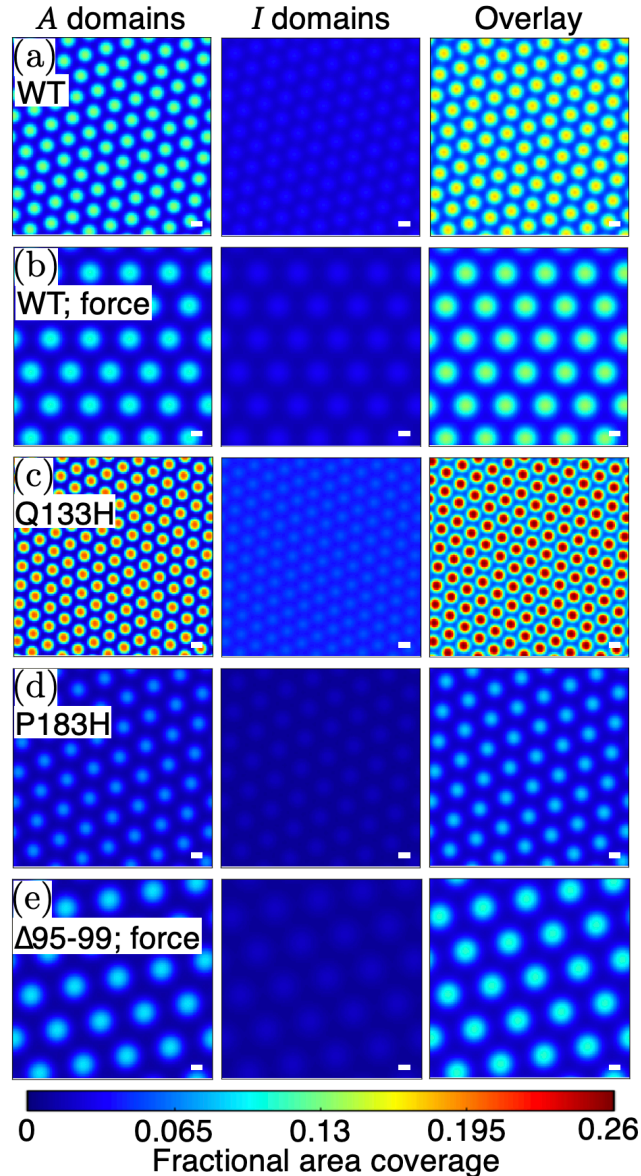
Figure 5.2: Colormaps depict numerical solutions for A, I, and $(A + I)$ (overlay) calculated from our emerin nanodomain self-assembly model (see Sec. 5.2.2 for numerical implementation), where I and A denote fields for the fraction of the INM area locally covered by I and A complexes, respectively. The colorbar scale indicates the values of the fields A, I, or $(A + I)$. We show model solutions for wild-type systems (a) with and (b) without mechanical stress, (c) Q133H systems without mechanical stress, (d) P183H systems without mechanical stress, and (e) $\Delta 95\text{-}99$ systems under mechanical stress. Diffusion coefficients ν_I and ν_A are as indicated in Fig. 5.1 with $\nu_A = \nu_{\text{slow}}$ and $\nu_I = \nu_{\text{fast}}$. The reaction rates f_1, f_2, g_1, g_2, and g_3 utilized in our calculations are discussed in (a) Sec. 5.2, (b) Sec. 5.3.2, (c) Sec. 5.3.3, (d) Sec. 5.3.4, and (e) Sec. 5.3.6. The colormaps depict numerical solutions at the corresponding time $t = 100\,\tau$ (see Sec. 5.2.2), with (a) $\tau \approx 6$ s, (b) $\tau \approx 17$ s, (c) $\tau \approx 3$ s, (d) $\tau \approx 50$ s, (e) $\tau \approx 74$ s.

Though our model's output aligns closely with experimental findings in several ways, our model exhibits some disparities with experiments which can be potentially explained. For instance, our model predicts $F_\Phi \approx 0.15$ which lies within experimental margins for emerin area coverage of nanodomains, but is on the high side. Since we impose steric constraints so that $0 \leq I + A \leq 1$, if I and A were to cover the entire free INM area in emerin nanodomains, we would have $F_\Phi = 1$. Assuming the steric constraints on I and A are set by emerin rather than other components, $F_\Phi = f$ corresponds to an average fractional area coverage f of emerin in the nanodomain. Our numerical solutions yield $f \approx 15\%$ inside emerin nanodomains, while experiments suggest a range 3–15%, referring to the fractional area coverage of emerin alone. This implies that steric constraints on I and A in our model arise not only from emerin but also from other interacting molecule species, supporting our assumption that I and A complexes involve both emerin and NBPs.

Additionally, the model generates closely spaced emerin nanodomains, approximately 10 nm apart and consistently 22 nm in diameter. In contrast, experimental emerin nanodomains exhibit variations in size, shape, and spacing, often exceeding 10 nm between them [12]. However, this discrepancy is unsurprising, since, by definition, our mean-field model inherently lacks the molecular noise present in actual molecular reactions and diffusion [231]. In the INM, variations in nanodomain properties likely arise from heterogeneous INM composition involving molecule species other than emerin and NBPs and fluctuations in NBP properties. We note that the I domains of our model have a broader profile than the A domains they overlap, which is a characteristic of the Turing mechanism, where the outward diffusing flow of the fast inhibitor I complexes balances the surge of

emerin complexes at the center of nanodomains and stabilizes the nanodomains. Due to the close spacing between emerin nanodomains, the I domains exhibit linkage.

Lastly, our numerical solutions yield an area coverage of $(I + A)$ of about 4% outside emerin nanodomains. This is substantially higher than the expected mean local fractional area covered by emerin outside emerin nanodomains ($\lesssim 2\%$) [12, 230]. Here, again, we note that our model generates closely spaced emerin nanodomains with an inter-domain distance of around $10\ \mathrm{nm}$, in contrast to experiments which often reveal larger spacings between nanodomains, likely due to disruptions in the noisy INM environment [12]. So, when comparing our model's results on $(I + A)$ outside emerin nanodomains to experimental findings, it's important to focus on closely spaced nanodomains. Experimentally observed emerin density maps, albeit somewhat blurred by rendering effects, suggest that emerin density is notably higher between closely spaced emerin nanodomains. Together with our model's more stringent steric constraints on I and A, which tend to overestimate the local emerin density, this could explain why our model shows somewhat elevated values of $(I + A)$ outside emerin nanodomains compared to experimentally observed mean emerin concentrations outside these nanodomains.

5.3.1.1 Crowding effects due to emerin monomers

Emerin monomers cover $\sim 0.1\%$ of the INM [230]. To test the possible effect of steric constraints due to emerin monomers on our model predictions, we accounted for a "background" concentration of emerin monomers by including a modified steric repulsion term $(1 - I - A - m)$ in the reaction-diffusion dynamics considered here, with a constant fractional area $m = 0.002 = 0.2\%$ of emerin monomers. Inserting $m = 0.002$ into our

model and leaving all other model parameters unchanged resulted in slightly smaller nanodomains, of diameter $\ell_\Phi \approx 21$ nm as opposed to the value $\ell_\Phi \approx 22$ nm obtained with $m = 0$, and a slight increase in the nanodomain coverage by I and A complexes, from $F_\Phi \approx 15\%$ to $F_\Phi \approx 17\%$. Thus, as expected, steric effects due to emerin monomers seem to have little impact on the self-assembly of emerin nanodomains in our model.

For completeness, we tested whether steric effects due to emerin monomers could be effectively compensated by decreasing the creation rate of I ("crowder") complexes, from $f_2 = f_1/2$ to $f_2 = 0.44 f_1$. These adjustments yielded results that were nearly identical to those obtained with the corresponding system with $m = 0$ [see Fig. 5.1 and Fig. 5.2(a)]. Using values of m smaller or not much greater than $m = 0.002$ also yielded similar results as in Fig. 5.2(a). By increasing m to values substantially greater than $m = 0.002$ (e.g., $m = 0.004$), which effectively leads to a crowding out of I and A complexes, a transition to stripe patterns can be obtained in our model.

5.3.2 Wild-type system under mechanical stress

Wild-type systems under mechanical stress ("WT; force") were observed to exhibit emerin nanodomains with an increased diameter 60 ± 12 nm, but a density of emerin inside nanodomains that was reduced by about 40% compared to unperturbed wild-type systems [12]. Interestingly, it was thus found that while the density of emerin in emerin nanodomains is decreased by mechanical stress, the overall number of emerin molecules in nanodomains is increased. Our model of emerin nanodomain self-assembly provides a simple explanation of these observations.

Experiments suggest that, possibly due to a disruption in the interactions between emerin and NBPs by mechanical force, the diffusion coefficients ν_A and ν_I are approximately doubled in the perturbed system compared to the unperturbed system [12] [see Fig. 5.1]. In our model, this adjustment results in an increase in the diameter of emerin nanodomains by about a factor of $\sqrt{2}$ ($\sim 40\%$)[†], while the fractional area of emerin nanodomains occupied by I and A complexes remains unchanged. This suggests that the observed changes in ν_I and ν_A can partially, but not completely, account for the observed changes in emerin nanodomains under mechanical stress.

As noted above, experiments show that mechanical stress tends to decrease the emerin density in nanodomains. A physical interpretation of this observation is that mechanical stress diminishes interactions between emerin and NBPs necessary for the formation of higher-order emerin structures. To test whether such a modification of the reaction dynamics can explain the observed changes in nanodomain size, we decreased the reaction rate g_3, which parameterizes the formation of higher-order emerin structures in our model, $2A + \varnothing \to 3A$, by a factor of $1/2$, to $g_3 = f_1$. As shown in Fig. 5.1 and Fig. 5.2(b), this perturbation resulted in an increase in the characteristic emerin nanodomain diameter to $\ell_\Phi \approx 50$ nm. Importantly, with this decrease in g_3 we found that the fractional area of emerin nanodomains occupied by I and A complexes was $F_\Phi \approx 0.1$, which amounts to $F_\Phi / F_\Phi^{\mathrm{WT}} \approx 0.7$ [‡]. Thus, the observed increases in the emerin diffusion coefficients together with a reduction in the effective rate for the formation of higher-order

---

[†]This can be understood by noting that ℓ_c in Eq. (5.15) scales with the square roots of ν_I and ν_A [121].
[‡]Using $g_3 = 0.9f_1$ yields $\ell_\Phi \approx 56$ nm and $F_\Phi / F_\Phi^{\mathrm{WT}} \approx 0.6$, further aligning model outcomes with experimental observations.

emerin structures seem to underlie the observed changes in emerin nanodomains under mechanical stress.

5.3.3 Q133H mutation

Experiments indicate that the EDMD-associated Q133H mutation of emerin decreases emerin's interactions with nuclear actin, resulting in an increased mobility of emerin as well as increased formation of higher-order emerin structures [12, 136, 232–234]. It was found experimentally that, under no mechanical stress, the Q133H mutation yields emerin nanodomains of statistically similar size to the wild-type system under no mechanical stress and leads to an increase in the density of emerin in nanodomains by approximately 50% compared to the wild-type system under no mechanical stress [12]. Our model can account for these observations.

It was found in experiments that, for Q133H emerin, the rapidly- and slowly-diffusing emerin populations have diffusion coefficients of approximately $\nu_{\mathrm{fast}} = 3 \times 10^{-3}~\mu\mathrm{m}^2/\mathrm{s}$ and $\nu_{\mathrm{slow}} = 4 \times 10^{-4}~\mu\mathrm{m}^2/\mathrm{s}$, respectively [12]. Proceeding as for wild-type emerin, we thus set $\nu_A = \nu_{\mathrm{slow}}$ and $\nu_I = \nu_{\mathrm{fast}}$ for Q133H emerin. We find that these changes in the diffusion coefficients of I and A complexes result in a slight increase in the diameter of emerin nanodomains, by approximately[§] 10%, with no appreciable change in the fractional area of emerin nanodomains occupied by I and A complexes. Thus, the changes in the diffusion properties observed for Q133H emerin do not account for the observed changes in the overall properties of emerin nanodomains.

[§]Again, this can be understood from the scaling of ℓ_c in Eq. (5.15) with the diffusion coefficients ν_I and ν_A [121].

We hypothesized that, possibly due to its decreased interactions with nuclear actin, Q133H emerin has an increased propensity to interact with other Q133H emerin as well as with NBPs to form higher-order structures. In our model, A complexes capture interactions between emerin and NBPs that can yield higher-order emerin structures, while I complexes passively inhibit the formation of higher-order emerin structures through steric constraints. We therefore assume that, compared to A complexes formed from wild-type emerin, all reaction rates associated with A complexes formed from Q133H emerin are increased, including the reaction $A+\varnothing \to A+I$, while reactions solely involving I complexes are not affected. In the specific reaction scheme considered here (see Sec. 5.2), the reaction $I \to \varnothing$ with rate f_1 is the only reaction not directly involving A complexes. Thus, we take f_1 to be unaffected by the Q133H mutation while, for simplicity, we increase all other reaction rates in the model—f_2, g_1, g_2, and g_3—by the same factor. Figs. 5.1 and 5.2(c) shows the resulting model results obtained with an increase by 30% in the reaction rates f_2, g_1, g_2, and g_3 compared to the wild-type system under no mechanical stress.

With the above assumptions, our model yields Q133H emerin nanodomains with $\ell_\Phi \approx 18\,\mathrm{nm}$ [see Figs. 5.1 and Fig. 5.2(c)]. Furthermore, we find that $F_\Phi \approx 0.23$, which amounts to $F_\Phi/F_\Phi^{\mathrm{WT}} \approx 1.5$. These model results are in good agreement with the aforementioned experiments on the Q133H emerin system [12].

5.3.4 P183H mutation

The EDMD-associated P183H mutation of emerin is thought to yield more pronounced interactions between emerin and NBPs than wild-type emerin [131, 135, 136], which are

believed to slow down the diffusion of P183H emerin compared to wild-type emerin and disrupt the formation of higher-order emerin complexes—possibly due to incorrect stoichiometries or arrangements of emerin and NBPs in supramolecular complexes. Experiments show that P183H emerin can form dimers that diffuse significantly faster than other P183H oligomers [12]. P183H dimers seem to be unable to efficiently form higher-order emerin structures [12, 127]. It was found experimentally that, under no mechanical stress, the P183H mutation yields larger emerin nanodomains than the wild-type system under no mechanical stress, with an emerin nanodomain diameter of approximately 35 ± 12 nm (compared to approximately 22 ± 11 nm for the wild-type system under no mechanical stress), and a reduction in the density of emerin in nanodomains by approximately 70% compared to the wild-type system under no mechanical stress [12]. Thus, contrary to the Q133H mutation, the P183H mutation of emerin *increases* the nanodomain size while *decreasing* F_Φ. Combining insights gleaned from the wild-type system under mechanical stress (see Sec. 5.3.2) and Q133H emerin (see Sec. 5.3.3), our model is able to account for these observations.

It was found in experiments that, for P183H emerin, the rapidly- and slowly-diffusing emerin populations have diffusion coefficients of approximately $\nu_{\text{fast}} \approx 1.5 \times 10^{-3}$ $\mu\text{m}^2/\text{s}$ and $\nu_{\text{slow}} \approx 1 \times 10^{-4}$ $\mu\text{m}^2/\text{s}$, respectively [12]. On this basis, we set here $\nu_I = \nu_{\text{fast}}$ and $\nu_A = \nu_{\text{slow}}$. These changes to our model produced, compared to the wild-type system under no mechanical stress, a decrease in ℓ_Φ by approximately[¶] 50% with an increase in F_Φ by about[‖] 30% compared to the wild-type system under no mechanical stress. Thus, similarly

---

[¶]Again, this can be understood from the scaling of ℓ_c in Eq. (5.15) with the diffusion coefficients ν_I and ν_A [121].

[‖]This can be understood by noting that, compared to the wild-type system, the ratio ν_A/ν_I is decreased in the P183H system, thus facilitating larger concentrations of A and, hence, I inside emerin nanodomains.

as for Q133H emerin (see Sec. 5.3.3), the changes in the diffusion properties observed for P183H emerin do not account for the observed changes in the overall properties of emerin nanodomains.

As mentioned above, experiments suggest that P183H emerin shows, compared to wild-type emerin, a reduced ability to self-assemble into higher-order structures. Following similar reasoning as for Q133H emerin, we therefore *decreased* the rates associated with all "activating" reactions in our model. In particular, we now decreased (rather than increased) the rates f_2, g_1, g_2, and g_3 by 30% compared to the wild-type system under no mechanical stress. This adjustment to our model produced emerin nanodomains that were about 18 nm in diameter, and reduced F_Φ by about 20% compared to the wild-type system under no mechanical stress. Thus, such a global reduction in all rates associated with reactions involving A complexes decreased, consistent with experimental observations, $\langle I + A \rangle$, but also decreased (rather than increased) the nanodomain size.

In analogy to the wild-type system under mechanical stress (see Sec. 5.3.2), we hypothesized that the P183H mutation has a more pronounced effect on the formation of higher-order emerin structures. Decreasing g_3 to $g_3 = f_1/2$, we found that the nanodomain diameter increased to $\ell_\Phi \approx 35$ nm and $F_\Phi/F_\Phi^{\mathrm{WT}}$ decreased to about 0.4 [see Figs. 5.1 and 5.2(d)]**. Thus, with the values of ν_I and ν_A measured for P183H emerin, we are able to account for the aforementioned experiments on the P183H emerin system [12] via a reduction in the rates of all reactions involving A complexes, with a more

---

**If we use $g_3 = 0.6f_1$ rather than $g_3 = f_1/2$ and decrease f_2, g_1, and g_2 by 35% rather than 30% compared to the wild-type system under no mechanical stress, our model produces P183H emerin nanodomains with $\ell_\Phi \approx 32$ nm and $F_\Phi/F_\Phi^{\mathrm{WT}} \approx 0.3$, further improving the agreement between model results and experimental observations.

pronounced reduction in the reaction rate associated with the formation of higher-order emerin complexes.

5.3.4.1 Spontaneous dimerization

P183H emerin has a higher propensity to dimerize than wild-type emerin. In particular, P183H emerin can dimerize even at the outer nuclear membrane in the absence of emerin nanodomains [12]. This observation suggests that P183H dimers, which are represented by I complexes in our model, can form spontaneously in the absence of A complexes. To test to what extent our model predictions change if one allows for the spontaneous formation of dimers, we extended our reaction scheme in Sec. 5.2.1 to allow for the reaction $\varnothing \rightarrow I$ with reaction rate f_0 in units of s^{-1}. This modifies F to

$$\text{F}(I, A) = f_0 \bar{I} \left(\frac{1 - I - A}{1 - \bar{I} - \bar{A}} \right) - f_1 I + f_2 (1 - I - A) A \tag{5.28}$$

with

$$\bar{A} = \frac{(f_1 - f_0)(g_2 - g_1 + g_3)}{g_2(f_1 - f_0) + f_2(g_1 - g_3)}, \qquad \bar{I} = \frac{f_2(g_1 - g_3)}{g_2(f_1 - f_0)} \bar{A}. \tag{5.29}$$

We found that such a modified reaction scheme can yield similar results for P183H emerin as described above. For instance, setting $f_0 = 0.1 f_1$, decreasing f_2 from $f_2 = 0.35 f_1$ to $f_2 = 0.25 f_1$ to compensate for the additional creation of I complexes through the reaction $\varnothing \rightarrow I$, and setting $g_3 = 0.6 f_1$ rather than $g_3 = f_1/2$ produces results similar to those in Figs. 5.1 and 5.2(d).

5.3.5 $\triangle$95-99 **mutant system under no mechanical stress**

Experiments indicate that the EDMD-associated $\triangle$95-99 mutation of emerin yields an approximately random emerin distribution across the INM at no mechanical stress, with little or no domain formation and $\triangle$95-99 emerin covering a fractional area $\lesssim 2\%$ of the INM [12]. $\triangle$95-99 emerin is thought to exhibit reduced interactions with some NBPs (e.g., lamin A/C and/or nuclear actin) [128, 131, 135]. This conclusion is also supported by experiments on wild-type emerin, which show that depletion of NBPs results in impaired formation of higher-order emerin structures in the INM [12]. Based on our results on P183H emerin (see Sec 5.3.4), our model is able to account for these observations.

It was found in experiments that the mobility of $\triangle$95-99 emerin on the INM is reduced by approximately a factor of two compared to wild-type emerin under no mechanical stress, $\nu_{\text{fast}} \approx 1 \times 10^{-3} \ \mu\text{m}^2/\text{s}$ and $\nu_{\text{slow}} \approx 1.5 \times 10^{-4} \ \mu\text{m}^2/\text{s}$ [12] (see Fig. 5.1). We thus set $\nu_I = \nu_{\text{fast}}$ and $\nu_A = \nu_{\text{slow}}$ in our model. This adjustment to our model results in a decrease in the diameter of emerin nanodomains by about[††] 30%, while F_Φ is decreased by about 20% compared to the wild-type system. Thus, the observed decrease in ν_A and ν_I is not sufficient to account for the severely impaired self-assembly of emerin nanodomains observed for the $\triangle$95-99 mutation of emerin.

As mentioned above, experiments suggest that $\triangle$95-99 emerin has a decreased propensity to self-assemble into higher-order structures. Following similar reasoning as for P183H emerin, we therefore decreased the rates associated with all "activating" reactions in our model. Interestingly we find that, for the diffusion coefficients measured for $\triangle$95-99

[††]Again, this can be understood from the scaling of ℓ_c in Eq. (5.15) with the diffusion coefficients ν_I and ν_A [121].

emerin, a decrease in the rates f_2, g_1, g_2, and g_3 by as little as 20% compared to the un-perturbed wild-type emerin system leads to a destabilization of emerin nanodomains and results, in our mean-field model, in a homogeneous steady state. In particular, proceed-ing as for P183H emerin and decreasing f_2, g_1, and g_2 by 30% while decreasing g_3 from $g_3 = 2f_1$ to $g_3 = f_1/2$ (see Sec 5.3.4) resulted in a homogeneous steady state of the sys-tem with $\langle I + A \rangle \approx 2\%$. As discussed above, we expect the value of $\langle I + A \rangle$ obtained from our model to yield an upper bound on the fractional area coverage of emerin, because I and A involve not only emerin but also NBPs. Our model results for $\Delta 95$-99 emerin under no mechanical stress are therefore consistent with experimental observations [12].

5.3.6 $\Delta 95$-99 **mutant system under mechanical stress**

Experiments indicate that application of mechanical stress to the $\Delta 95$-99 emerin sys-tem ("$\Delta 95$-99; force") results in the self-assembly of emerin nanodomains with approxi-mate diameter 75 ± 20 nm and emerin densities about 25% compared to the unperturbed wild-type emerin system [12]. Based on the wild-type emerin system under mechanical stress (see Sec. 5.3.2) we modified our model of the unperturbed $\Delta 95$-99 emerin system (see Sec. 5.3.5) to capture the mechanically stressed state of the $\Delta 95$-99 emerin system.

From experimental observations of the perturbed state of the wild-type emerin sys-tem, we expect the mobility of $\Delta 95$-99 emerin to increase when the system is put under mechanical stress [12]. However, it was initially not clear how exactly mechanical per-turbation of the $\Delta 95$-99 system impacts the values of ν_I and ν_A. Assuming that A com-plexes formed from $\Delta 95$-99 emerin respond similarly to mechanical stress as A complexes

formed from wild-type emerin, we double ν_A to $\nu_A = 3 \times 10^{-4} \ \mu\mathrm{m}^2/\mathrm{s}$. Furthermore, we hypothesize that the diffusion rate of I complexes may respond more strongly to mechanical stress than the diffusion rate of A complexes[‡‡]—this could, for instance, be the case if the combined effects of the Δ95-99 mutation and application of mechanical stress largely decouple I complexes from their potential binding partners—as indicated by the large diameter of the nanodomains observed (75 ± 20 nm), since ℓ_c depends on $\sqrt{\nu_I}$. We find that with, for instance, $\nu_I = 6 \times 10^{-3} \ \mu\mathrm{m}^2/\mathrm{s}$, Δ95-99 emerin self-assemble into nanodomains with $\ell_\Phi \approx 53$ nm and $F_\Phi/F_\Phi^{\mathrm{WT}} \approx 0.5$.

These results are broadly consistent with published experimental data on the Δ95-99 emerin system under mechanical stress [12]. Closer agreement between model results and experimental observations can be obtained by assuming, in analogy to the wild-type emerin system under mechanical stress (see Sec. 5.3.2), that mechanical stress also modifies the reaction rate for $2A + \varnothing \rightarrow 3A$ in the Δ95-99 system. For instance, if we decrease g_3 from $g_3 = f_1/2$ to $g_3 = 0.35f_1$ we find Δ95-99 emerin nanodomains with $\ell_\Phi \approx 74$ nm and $F_\Phi/F_\Phi^{\mathrm{WT}} \approx 0.4$ [see Figs. 5.1 and 5.2(e)][§§].

Interestingly, the diffusion coefficients of the Δ95-99 emerin system have recently been measured [230] after we had made our initial predictions, and found them to be $\nu_{\mathrm{fast}} \approx 6 \times 10^{-3} \ \mu\mathrm{m}^2/\mathrm{s}$ and $\nu_{\mathrm{slow}} \approx 4 \times 10^{-4} \ \mu\mathrm{m}^2/\mathrm{s}$, which agree quite close with our predictions. We found if we change $\nu_A = 3 \times 10^{-4} \ \mu\mathrm{m}^2/\mathrm{s}$ to $\nu_A = 4 \times 10^{-4} \ \mu\mathrm{m}^2/\mathrm{s}$ to better align with these new measurements, and do not decrease g_3 to $g_3 = 0.35f_1$, we get similar results

---

[‡‡]Simply doubling ν_I to $\nu_I = 2 \times 10^{-3} \ \mu\mathrm{m}^2/\mathrm{s}$ in our model, yields a homogeneous steady state of I and A complexes, which does not align with experimental observations that mechanical perturbation of the Δ95-99 emerin system evokes the formation of nanodomains [12].

[§§]Decreasing g_3 to $g_3 = 0.34f_1$, rather than to $g_3 = 0.35f_1$, yields nanodomains with $\ell_\Phi \approx 77$ nm and $F_\Phi/F_\Phi^{\mathrm{WT}} \approx 0.3$, further improving the agreement between model results and experimental observations.

as described above, with $\ell_\Phi \approx 71$ nm and $F_\Phi/F_\Phi^{\mathrm{WT}} \approx 0.4$. Since our initial prediction for ν_I

was based on the nanodomain diameter, these results further support a direct correlation

between emerin nanodomain properties and emerin reaction-diffusion characteristics.

Chapter 6

Overview and conclusions

This chapter offers summaries and conclusions for each of Chapters 2 through 5 and discusses potential future research directions suggested by our findings.

6.1 Overview and conclusions of Chapter 2

In Chapter 2 we introduced a novel BVM for lipid bilayer deformations based on the elasticity theory of protein-induced lipid bilayer thickness deformations [21–25, 27–34, 36–40]. In Sec. 2.1, we discussed the bilayer thickness deformation energy, in Eq. 2.3 and demonstrated how we incorporate the hydrophobic shape parameters of proteins in the boundary conditions in Eqs. 2.12–2.14 to fix the lipid bilayer thickness deformation energy. In Sec. 2.2 we described in detail our BVM for bilayer thickness deformations, tested it against FEM solutions, and discussed how the BVM can be used to calculate protein-induced lipid bilayer thickness deformations and their associated elastic energy for general protein shapes. We also introduced a measure of accuracy [see Eq. (2.25)

in Sec. 2.2.1], and APDs to optimize the efficiency and accuracy [see Sec. 2.2.2] of our BVM.

Our BVM permits the construction of analytic series solutions of protein-induced lipid bilayer deformations for arbitrarily large deviations from a circular protein cross section, albeit can become computationally limited by the available floating point precision of numbers utilized (see Appendix A.2). In addition to the membrane protein cross section, our BVM allows for a breaking of rotational symmetry about the protein center through angular variations in the boundary conditions along the bilayer-protein interface—in particular, for the scenarios considered in Chapters 2 and 3, in the protein hydrophobic thickness and in the bilayer-protein contact slope along the bilayer-protein boundary. Our BVM reproduces available analytic solutions for membrane proteins with circular cross section [23, 27, 30, 58, 59, 118] and yields, for membrane proteins with non-circular cross section, excellent agreement with numerical, finite element solutions.

A limitation of the BVM arises for protein shapes that show extreme deviations from circular symmetry, in which case BVM solutions tend to involve a large number of terms and, hence, become increasingly intractable. In such cases it may be advisable to modify the APD method for the distribution of boundary points employed in Chapters 2–4, so as to reduce the number of terms required in the lipid bilayer thickness deformation field in Eq. (2.20) with Eq. (2.21). While we have focused here on bilayer thickness deformations, it would be interesting to use a BVM approach analogous to that employed in Chapters 2–4 to construct analytic series solutions for other modes of protein-induced lipid bilayer deformations such as, for instance, bilayer midplane or lipid tilt deformations [22, 32–38, 54–56, 107, 153, 154, 158–161, 163, 186, 187]. On this basis one could,

for instance, further investigate how anisotropic membrane protein shapes can give rise to anisotropic membrane elastic properties [54, 55]. Furthermore, it would be interesting to construct BVM solutions for membrane proteins embedded in bilayers with heterogeneous lipid composition [162, 235–239]. Notably, for calculating long-ranged lipid bilayer deformations due to proteins of non-circular cross-section shape, the BVM may offer a convenient and computationally efficient approach. In particular, as membrane tension approaches zero, leading to theoretically infinite decay lengths for midplane deformations, numerical techniques like FDM and FEM can become computationally infeasible, whereas the BVM remains viable.

6.2   Overview and conclusions of Chapter 3

In Chapter 3 we investigated the significance of protein shape in protein-induced lipid bilayer thickness deformations. Based on the BVM solutions, in Sec. 3.1, we formulated a simple analytic approximation of the lipid bilayer thickness deformation energy associated with general protein shapes [see Eq. (3.1) with Eq. (3.2)]. Through our BVM and analytic approximation of the lipid bilayer thickness deformation energy, we surveyed the dependence of protein-induced lipid bilayer thickness deformations on protein shape in Sec. 3.2. We then applied our BVM and analytic approximation to investigate the impact of protein shape in the assembly of transmembrane protein oligomers [see Sec. 3.3.1] and transitions in transmembrane protein conformational states [see Sec. 3.3.2]. Here we provide the conclusions of studies in regards to the impact of protein shape on lipid bilayer deformations.

We find that, for modest deviations from rotational symmetry, our analytic approximation of the lipid bilayer thickness deformation energy is in good agreement with BVM solutions. These results suggest that, to a first approximation, the effect of membrane protein shape on the energy of bilayer thickness deformations can be understood based on the length of the circumference of non-circular protein cross sections. Moreover, our survey of the dependence of protein-induced lipid bilayer thickness deformations on protein shape reveals that protein shape tends to have a large effect on the energy of protein-induced lipid bilayer thickness deformations, typically shifting the bilayer deformation energy by more than 10 $k_B T$.

In the case of non-circular protein cross sections, we find that protein self-interactions provide an important motif for the energy of protein-induced lipid bilayer thickness deformations. Such self-interactions arise for invaginations in the protein cross section, from overlaps in the bilayer deformations induced at different sections of the bilayer-protein interface. The basic phenomenology of membrane protein self-interactions can be understood by drawing analogies with bilayer-thickness-mediated interactions between proteins [22, 24, 25, 30, 41, 57, 58, 60, 61, 157, 161, 178–183]. In particular, membrane protein self-interactions can effectively lower the energy cost of protein-induced lipid bilayer thickness deformations for proteins with constant bilayer-protein hydrophobic mismatch and zero bilayer-protein contact slope. For non-zero bilayer-protein contact slopes, or for variations in the bilayer-protein hydrophobic mismatch or in the bilayer-protein contact slope along the bilayer-protein interface, protein self-interactions can yield dramatic shifts in the bilayer thickness deformation energy. Thus, the interplay between the cross-sectional shape of membrane proteins, protein hydrophobic thickness, and bilayer-protein contact

slope yields a rich energy landscape of protein-induced lipid bilayer thickness deformations. Interestingly, the hydrophobic thickness or bilayer-protein contact slope of membrane proteins may be modified in cells through, for instance, protein mutations, changes in lipid composition, or the binding of peptides at the bilayer-protein interface, while protein oligomerization and transitions in protein conformational state tend to change the cross-sectional shape of membrane proteins. The results described here therefore suggest general physical mechanisms for how protein shape couples to the function, regulation, and organization of membrane proteins.

6.3 Overview and conclusions of Chapter 4

In Chapter 4 we introduced a simple model of the effect of temperature changes on protein-induced elastic bilayer deformations to explore the intricate relationship between temperature, membrane mechanics, and the activation energies of key sensory proteins. In Sec. 4.1 we described, based on experimental measurements, how temperature changes modify key bilayer mechanical properties. In Sec. 4.2 we developed, based on previous work [27, 57, 59, 102, 107, 110, 111], membrane-mechanical models of transitions in the conformational states of bacterial chemoreceptor trimers, MscL ion channels, and Piezo ion channels. In Sec. 4.3 we combined the methodologies developed in Secs. 3.1 and 4.2 to quantify the effect of temperature changes on the conformational states of chemroeceptors, MscL, and Piezo. In Sec. 4.4 we discussed the implications of our finding for chemoreceptor thermotaxis and tempertaure-dependent shifts in the gating thresholds of MscL and Piezo.

Temperature, being a fundamental environmental factor, significantly influences cellular physiology, impacting decision-making processes in microorganisms and the response of multicellular organisms. Our research sought to understand how alterations in membrane mechanical properties induced by temperature changes can impact the activation energies of pivotal proteins involved in cellular perception. Our findings highlight several critical aspects of the interplay between temperature and membrane protein conformational state. Most notably, we found that temperature variations can induce substantial changes in the energy cost of protein-induced lipid bilayer deformations, with magnitudes on the order of several $k_B T_{\mathrm{rm}}$ to tens of $k_B T_{\mathrm{rm}}$. These results suggest a role for membrane elastic properties in bacterial thermosensation.

Our findings suggest that the effect of increasing temperature on lipid bilayer deformations may be sufficient for the activation of chemoreceptors in *E. coli*, which aligns with their observed thermophilic response [13]. We also found changes in temperature may produce significant shifts in the activation energy of MscL through changes in membrane thickness. These results are based on measurements of the temperature dependence of the membrane hydrophobic thickness of DOPC lipid bilayers, representing synthetic and pure lipid compositions [116]. However, biological membranes generally have highly heterogeneous compositions. Interestingly, measurements of the *Bacillus subtilis* membrane thickness dependence on temperature have revealed a decrease rate in membrane thickness that is three-fold faster than that used in our model based on measurements of DOPC bilayers [15, 116]. This observation suggests that our calculations for estimating the effect of changes in temperature on chemoreceptors and MscL in E. coli cytoplasmic membranes are conservative. Thus we may expect the functionality of chemoreceptors

and MscL to have a stronger dependence on temperature through membrane mechanics than that suggested by our results.

We have predicted that Piezo's gating tension increases with decreasing temperature, which we can trace back to the observed increase in lipid bilayer bending rigidity with decreasing temperature. Interestingly, these results align with experimental observations [108, 226] on the dependence of Piezo gating on temperature and bilayer bending rigidity, suggesting that membrane rigidity may provide a membrane property through which proteins can sense variations in temperature.

The results of our investigation in Chapter 4 indicates that certain transmembrane proteins can detect variations in temperature through alterations in membrane thickness. Interestingly, there is substantial evidence suggesting that DesK, a transmembrane protein known for its temperature-sensing ability, gauges temperature changes by monitoring variations in membrane thickness [15, 43, 44, 46, 47, 70–79, 94, 95, 98–100, 240, 241]. Thus, it would be intriguing to conduct a quantitative analysis, akin to our investigations on chemoreceptors and MscL, to assess the influence of temperature-induced membrane thickness variations on DesK's activation energy.

Beyond our focus on MscL and Piezo, the realm of thermosensation encompasses other mechanosensors with intriguing temperature-sensitive attributes. Among these, TREK/TRAK channels have emerged as notable examples. These mammalian channels are known to be gated by membrane tension and several have been shown to be activated either through increases in temperature or through decreases in temperature [48, 83, 84, 96, 97, 242–244]. These observations highlight the multifaceted nature of mechanosensors, which can also double as thermosensors, suggesting that the interplay

between membrane mechanics and temperature sensitivity extends beyond the proteins we explored in this study [48].

Another well-known group of thermosensors is the Transient Receptor Potential (TRP) channels which also double as chemoreceptors in mammalian cells [16, 52, 80–82]. In recent years, mounting evidence has supported the hypothesis that TRPs are intrinsically activated by temperature, owing to a temperature-dependent protein molar heat capacity mechanism and, perhaps, also contributions due to bilayer-protein interactions [52, 195, 196]. Structural studies suggest significant conformational changes in TRPs upon activation [51, 53, 195–206, 245, 246], aligning with the principles of thermodynamics, which predict that substantial changes in protein molar heat capacities are associated with substantial structural changes.

In addition to temperature-sensing through thermodynamic properties intrinsic to TRP proteins, there is evidence suggesting that membrane mechanics may play a secondary role in temperature sensing in TRP channels. For instance, experiments have shown that alterations in membrane composition can influence the temperature activation thresholds of TRPs [196, 245]. Notably, enriching the membrane with cholesterol leads to significant increases in the activation temperature in TRVP1, causing shifts of several degrees Celsius [196]. In these experiments, it was reported that the cholesterol enrichment of the cell membrane resulted in an increase in membrane stiffness and a decrease in membrane fluidity. So the observed increase in the activation temperature in TRVP1 due to cholesterol enrichment may be attributed to an increase in membrane rigidity and a decrease in membrane fluidity. In this context and in light of the results described in Chapter 4,

it would be interesting to see experiments measuring the effect of changing membrane thickness on TRP activation.

We acknowledge the complex nature of temperature sensing mechanisms in cells—in particular, experimental difficulties associated with isolating temperature sensing mechanisms from the effects of temperature on other physiological parameters, and the need to devise experimental techniques for this purpose. Perhaps, in analogy to studies on mechanosensitive ion channels [14, 22], one potential experimental approach for assessing whether bilayer mechanics plays a role in thermosensing could involve compensating for temperature-induced changes in bilayer mechanical properties by altering the lipid composition. For example, according to the results obtained in Chapter 4, chemoreceptor trimers are increasingly biased towards the "on" state with increasing temperature. This prediction critically depends on the observed decrease in lipid bilayer thickness with increasing temperature. It might thus be possible to test the role of bilayer mechanics in the thermosensitive behavior of chemoreceptors by counterbalancing temperature-induced variations in lipid bilayer thickness through adjustments in lipid tail length.

Overall, we find here that changes in membrane mechanical properties—in particular, lipid bilayer thickness and rigidity—can substantially impact the activation energies of various protein sensors. Our calculations, which utilized a simple temperature-dependent membrane mechanical model, underscore the potential significance of membrane mechanical properties as crucial contributors to the temperature sensing abilities of key sensory proteins, including chemoreceptors, MscL, and Piezo. Thus, our work suggests that the elastic coupling of lipid bilayer properties and membrane protein conformational state

may provide a generic physical mechanism for temperature sensing through membrane mechanics.

6.4   Overview and conclusions of Chapter 5

In Chapter 5, we investigated the mechanisms governing nuclear adaptation to mechanical stress, with a specific focus on the critical role played by emerin proteins and protein mutations associated with EDMD. We also examined the implications of EDMD mutations on this process. Our work led to the development of a simple framework for understanding the self-assembly and stabilization of emerin nanodomains at the INM. In Sec. 5.1 we introduced of the general mathematical structure of the reaction-diffusion equations used here, and carried out a linear stability analysis of these equations to identify the conditions leading to Turing patterns in our model. In Sec. 5.2, we developed in detail our physical model of emerin nanodomain self-assembly. In Sec. 5.3, we combined experimental measurements and simple estimates of the reaction and diffusion parameters in our model to predict emerin nanodomain formation, and compared these predictions to experimental observations.

Our model of emerin nanodomain self-assembly links emerin's diffusion and reaction characteristics to key physical attributes of emerin nanodomains, such as their size and fractional area coverd by emerin. We were able to show that our model accurately predicts the emerin nandomain size and emerin fractional area coverage for a variety of experimental conditions corresponding to mutations and changes in mechanical stress based on observations of changes in emerin reaction and diffusion properties. Furthermore, we

were also able to show that our model accurately predicts the diffusion coefficients of the Δ95-99 mutant emerin system under mechanical stress based on the nanodomain diameter and the wild-type emerin system's response to mechanical stress. This model also explained how these properties change in response to mechanical stress and emerin mutations. Our model suggests that emerin nanodomain self-assembly is rooted in a Turing instability exhibited by the two distinct emerin populations observed at INM: a rapidly-diffusing emerin population that locally inhibits increases in the emerin concentration at the membrane through steric repulsion, and slowly-diffusing emerin population locally binds emerin and NBPs to further increase the emerin concentration at memrbane locations with elevated emerin concentration. Our results emphasize the critical role of rapidly-diffusing emerin in the self-assembly of stable emerin nanodomains. The work described in Chapter 5 thus helps to illuminate the fundamental mechanisms underlying the formation and physical characteristics of emerin nanodomains, offering insight into nuclear adaptation to mechanical perturbations and key features of EDMD-associated mutations or emerin.

References

[1]   D. M. Engelman. "Membranes are more mosaic than fluid". In: *Nature* 438 (Dec. 2005), pp. 578–580. DOI: 10.1038/nature04394.

[2]   H. T. McMahon and J. L. Gallop. "Membrane curvature and mechanisms of dynamic cell membrane remodelling". In: *Nature* 438.7068 (Nov. 2005), pp. 590–596. DOI: 10.1038/nature04396.

[3]   M. R. Villarreal. *Fluid Mosaic Model of a Cell Membrane*. File: Cell_membrane_detailed_diagram_en.svg. 2007. URL: https://en.wikipedia.org/wiki/Fluid_mosaic_model#/media/File:Cell_membrane_detailed_diagram_en.svg (visited on 11/04/2023).

[4]   R. Phillips, J. Kondev, J. Theriot, and H. Garcia. *Physical biology of the cell*. Second. Garland Science, 2013. ISBN: 9780815344506.

[5]   K. R. Vinothkumar and R. Henderson. "Structures of membrane proteins". In: *Quarterly Reviews of Biophysics* 43.1 (Feb. 2010), pp. 65–158. DOI: 10.1017/s0033583510000041.

[6]   M. D. Baker, P. M. Wolanin, and J. B. Stock. "Signal transduction in bacterial chemotaxis". In: *BioEssays* 28.1 (2005), pp. 9–22. DOI: 10.1002/bies.20343.

[7]   L. M. P. Chataigner, N. Leloup, and B. J. C. Janssen. "Structural Perspectives on Extracellular Recognition and Conformational Changes of Several Type-I Transmembrane Receptors". In: *Frontiers in Molecular Biosciences* 7 (Aug. 2020). DOI: 10.3389/fmolb.2020.00129.

[8]   V. J. Flegler, T. Rasmussen, and B. Böttcher. "How Functional Lipids Affect the Structure and Gating of Mechanosensitive MscS-like Channels". In: *International Journal of Molecular Sciences* 23.23 (Dec. 2022), p. 15071. DOI: 10.3390/ijms232315071.

[9] Y. Li, O. Kahraman, and C. A. Haselwandter. "Stochastic lattice model of synaptic membrane protein domains". In: *Physical Review E* 95.5 (May 2017). DOI: 10.1103/physreve.95.052406.

[10] S. E. Kotob. "Review Article: An Overview of Cellular Signal Transduction Pathway". In: *Biomedical Journal of Scientific & Technical Research* 38.2 (Aug. 2021). DOI: 10.26717/bjstr.2021.38.006133.

[11] E. Law, Y. Li, O. Kahraman, and C. A. Haselwandter. "Stochastic self-assembly of reaction-diffusion patterns in synaptic membranes". In: *Physical Review E* 104.1 (July 2021). DOI: 10.1103/physreve.104.014403.

[12] A. Fernandez, M. Bautista, L. Wu, and F. Pinaud. "Emerin self-assembly and nucleoskeletal coupling regulate nuclear envelope mechanics against stress". In: *Journal of Cell Science* 135.6 (Mar. 2022). DOI: 10.1242/jcs.258969.

[13] A. Paulick, V. Jakovljevic, S. Zhang, M. Erickstad, A. Groisman, Y. Meir, W. S. Ryu, N. S. Wingreen, and V. Sourjik. "Mechanism of bidirectional thermotaxis in Escherichia coli". In: *eLife* 6 (Aug. 2017). DOI: 10.7554/elife.26607.

[14] E. Perozo, A. Kloda, D. M. Cortes, and B. Martinac. "Physical principles underlying the transduction of bilayer deformation forces during mechanosensitive channel gating". In: *Nature Structural Biology* 9.9 (Aug. 2002), pp. 696–703. DOI: 10.1038/nsb827.

[15] M. E. Inda, R. G. Oliveira, D. de Mendoza, and L. E. Cybulski. "The Single Transmembrane Segment of Minimal Sensor DesK Senses Temperature via a Membrane-Thickness Caliper". In: *Journal of Bacteriology* 198.21 (Nov. 2016). Ed. by A. M. Stock, pp. 2945–2954. DOI: 10.1128/jb.00431-16.

[16] A. Patapoutian, A. M. Peier, G. M. Story, and V. Viswanath. "ThermoTRP channels and beyond: mechanisms of temperature sensation". In: *Nature Reviews Neuroscience* 4.7 (July 2003), pp. 529–539. DOI: 10.1038/nrn1141.

[17] G. van Meer, D. R. Voelker, and G. W. Feigenson. "Membrane lipids: where they are and how they behave". In: *Nat. Rev. Mol. Cell Bio.* 9 (Feb. 2008), pp. 112–124. DOI: 10.1038/nrm2330.

[18] P. L. Yeagle. *The membranes of cells*. London: Academic Press, 2016. ISBN: 978-0-12-800047-2.

[19] E. Sezgin, I. Levental, S. Mayor, and C. Eggeling. "The mystery of membrane organization: composition, regulation and roles of lipid rafts". In: *Nat. Rev. Mol. Cell Biol.* 18.6 (June 2017), pp. 361–374. DOI: 10.1038/nrm.2017.16.

[20] T. Sych, Y. Mély, and W. Römer. "Lipid self-assembly and lectin-induced reorganization of the plasma membrane". In: *Philosophical Transactions of the Royal Society B: Biological Sciences* 373.1747 (Apr. 2018), p. 20170117. DOI: 10.1098/rstb.2017.0117.

[21] O. S. Andersen and R. E. Koeppe. "Bilayer Thickness and Membrane Protein Function: An Energetic Perspective". In: *Annual Review of Biophysics and Biomolecular Structure* 36.1 (June 2007), pp. 107–130. DOI: 10.1146/annurev.biophys.36.040306.132643.

[22] R. Phillips, T. Ursell, P. Wiggins, and P. Sens. "Emerging roles for lipids in shaping membrane-protein function". In: *Nature* 459.7245 (May 2009), pp. 379–385. DOI: 10.1038/nature08147.

[23] H.W. Huang. "Deformation free energy of bilayer membrane and its effect on gramicidin channel lifetime". In: *Biophysical Journal* 50.6 (Dec. 1986), pp. 1061–1070. DOI: 10.1016/s0006-3495(86)83550-0.

[24] N. Dan, P. Pincus, and S. A. Safran. "Membrane-induced interactions between inclusions". In: *Langmuir* 9.11 (Nov. 1993), pp. 2768–2771. DOI: 10.1021/la00035a005.

[25] N. Dan, A. Berman, P. Pincus, and S. A. Safran. "Membrane-induced interactions between inclusions". In: *Journal de Physique II* 4.10 (Oct. 1994), pp. 1713–1725. DOI: 10.1051/jp2:1994227.

[26] A. Ben-Shaul. "Molecular Theory of Chain Packing, Elasticity and Lipid-Protein Interaction in Lipid Bilayers". In: *Handbook of Biological Physics*. Elsevier, 1995, pp. 359–401. DOI: 10.1016/s1383\textendash8121(06)80024\textendash2.

[27] P. Wiggins and R. Phillips. "Membrane-Protein Interactions in Mechanosensitive Channels". In: *Biophysical Journal* 88.2 (Feb. 2005), pp. 880–902. DOI: 10.1529/biophysj.104.047431.

[28] T. S. Ursell, J. Kondev, D. Reeves, P. A. Wiggins, and R. Phillips. "The Role of Lipid Bilayer Mechanics in Mechanosensation". In: *Mechanosensitivity in Cells and Tissues 1: Mechanosensitive Ion Channels*. Ed. by Andre Kamkin and Irina Kiseleva. Springer Verlag, 2008, pp. 37–70.

[29] S. Mondal, G. Khelashvili, J. Shan, O. S. Andersen, and H. Weinstein. "Quantitative modeling of membrane deformations by multihelical membrane proteins: application to G-protein coupled receptors". In: *Biophys. J.* 101.9 (Nov. 2011), pp. 2092–2101. DOI: 10.1016/j.bpj.2011.09.037.

[30] O. Kahraman, P. D. Koch, W. S. Klug, and C. A. Haselwandter. "Bilayer-thickness-mediated interactions between integral membrane proteins". In: *Physical Review E* 93 (4 Apr. 2016), p. 042410. DOI: 10.1103/physreve.93.042410.

[31] D. Argudo, N. P. Bethel, F. V. Marcoline, C. W. Wolgemuth, and M. Grabe. "New Continuum Approaches for Determining Protein-Induced Membrane Deformations". In: *Biophysical Journal* 112.10 (May 2017), pp. 2159–2172. DOI: 10.1016/j.bpj.2017.03.040.

[32] W. Helfrich. "Elastic Properties of Lipid Bilayers: Theory and Possible Experiments". In: *Zeitschrift für Naturforschung C.* 28.11–12 (Dec. 1973), pp. 693–703. DOI: 10.1515/znc-1973-11-1209.

[33] P. B. Canham. "The minimum energy of bending as a possible explanation of the biconcave shape of the human red blood cell". In: *J. Theor. Biol.* 26.1 (Jan. 1970), pp. 61–81. DOI: 10.1016/S0022-5193(70)80032-7.

[34] E. A. Evans. "Bending resistance and chemically induced moments in membrane bilayers". In: *Biophys. J.* 14.12 (Dec. 1974), pp. 923–931. DOI: 10.1016/S0006-3495(74)85959-X.

[35] M. Fošnarič, A. Iglič, and S. May. "Influence of rigid inclusions on the bending elasticity of a lipid membrane". In: *Phys. Rev. E* 74 (5 Nov. 2006), p. 051503. DOI: 10.1103/PhysRevE.74.051503.

[36] J. Zimmerberg and M. M. Kozlov. "How proteins produce cellular membrane curvature". In: *Nat. Rev. Mol. Cell Biol.* 7.1 (Jan. 2006), pp. 9–19. DOI: 10.1038/nrm1784.

[37] T. R. Weikl. "Membrane-mediated cooperativity of proteins". In: *Ann. Rev. Phys. Chem.* 69 (Apr. 2018), pp. 521–539. DOI: 10.1146/annurev-physchem-052516-050637.

[38] M. Young, A. H. Lewis, and J. Grandl. "Physics of mechanotransduction by Piezo ion channels". In: *J. Gen. Physiol.* 154.7 (May 2022), e202113044. DOI: 10.1085/jgp.202113044.

[39] J. -B. Fournier. "Microscopic membrane elasticity and interactions among membrane inclusions: interplay between the shape, dilation, tilt and tilt-difference modes". In: *Eur. Phys. J. B* 11 (Sept. 1999), pp. 261–272. ISSN: 1434–6036. DOI: 10.1007/s100510050937.

[40] W. Rawicz, K. C. Olbrich, T. McIntosh, D. Needham, and E. Evans. "Effect of Chain Length and Unsaturation on Elasticity of Lipid Bilayers". In: *Biophysical Journal* 79.1 (July 2000), pp. 328–339. DOI: 10.1016/s0006-3495(00)76295-3.

[41] T. Ursell, K. C. Huang, E. Peterson, and R. Phillips. "Cooperative Gating and Spatial Organization of Membrane Proteins through Elastic Interactions". In: *PLoS Comp. Bio.* 3 (May 2007), pp. 0803–0812.

[42] G. Chang, R. H. Spencer, A. T. Lee, M. T. Barclay, and D. C. Rees. "Structure of the MscL Homolog from Mycobacterium tuberculosis: A Gated Mechanosensitive Ion Channel". In: *Science* 282.5397 (Dec. 1998), pp. 2220–2226. DOI: 10.1126/science.282.5397.2220.

[43] A. K. Park, S. M. Bong, J. H. Moon, and Y. M. Chi. "Crystallization and preliminary X-ray crystallographic studies of DesR, a thermosensing response regulator in a two-component signalling system from *Streptococcus pneumoniae*". In: *Acta Crystallographica Section F Structural Biology and Crystallization Communications* 65.7 (June 2009), pp. 727–729. DOI: 10.1107/s1744309109023082.

[44] D. Albanesi, M. Martín, F. Trajtenberg, M. C. Mansilla, A. Haouz, P. M. Alzari, D. de Mendoza, and A. Buschiazzo. "Structural plasticity and catalysis regulation of a thermosensor histidine kinase". In: *Proceedings of the National Academy of Sciences* 106.38 (Sept. 2009), pp. 16185–16190. DOI: 10.1073/pnas.0906699106.

[45] J. Liu, B. Hu, D. R. Morado, S. Jani, M. D. Manson, and W. Margolin. "Molecular architecture of chemoreceptor arrays revealed by cryoelectron tomography of Escherichia coli minicells". In: *Proceedings of the National Academy of Sciences* 109.23 (May 2012), E1481–E1488. DOI: 10.1073/pnas.1200781109.

[46] M. E. Inda, M. Vandenbranden, A. Fernández, D. de Mendoza, J.-M. Ruysschaert, and L. E. Cybulski. "A lipid-mediated conformational switch modulates the thermosensing activity of DesK". In: *Proceedings of the National Academy of Sciences* 111.9 (Feb. 2014), pp. 3579–3584. DOI: 10.1073/pnas.1317147111.

[47] E. Saita, L. A. Abriata, Y. T. Tsai, F. Trajtenberg, T. Lemmin, A. Buschiazzo, M. Dal Peraro, D. de Mendoza, and D. Albanesi. "A coiled coil switch mediates cold sensing by the thermosensory protein DesK". In: *Molecular Microbiology* 98.2 (Aug. 2015), pp. 258–271. DOI: 10.1111/mmi.13118.

[48] M. Lolicato, P. M. Riegelhaupt, C. Arrigoni, K. A. Clark, and D. L. Minor. "Transmembrane Helix Straightening and Buckling Underlies Activation of Mechanosensitive and Thermosensitive K2P Channels". In: *Neuron* 84.6 (Dec. 2014), pp. 1198–1212. DOI: 10.1016/j.neuron.2014.11.017.

[49] Y. R. Guo and R. MacKinnon. "Structure-based membrane dome mechanism for Piezo mechanosensitivity". In: *eLife* 6 (Dec. 2017). DOI: 10.7554/elife.33660.

[50] D. H. Kwon, F. Zhang, Y. Suo, J. Bouvette, M. J. Borgnia, and S.-Y. Lee. "Heat-dependent opening of TRPV1 in the presence of capsaicin". In: *Nature Structural & Molecular Biology* 28.7 (July 2021), pp. 554–563. DOI: 10.1038/s41594-021-00616-3.

[51] K. D. Nadezhdin, A. Neuberger, Y. A. Trofimov, N. A. Krylov, V. Sinica, N. Kupko, V. Vlachova, E. Zakharian, R. G. Efremov, and A. I. Sobolevsky. "Structural mechanism of heat-induced opening of a temperature-sensitive TRP channel". In: *Nature Structural & Molecular Biology* 28.7 (July 2021), pp. 564–572. DOI: 10.1038/s41594-021-00615-4.

[52] G. Fernández-Ballester, A. Fernández-Carvajal, and A. Ferrer-Montiel. "Progress in the Structural Basis of thermoTRP Channel Polymodal Gating". In: *International Journal of Molecular Sciences* 24.1 (Jan. 2023), p. 743. DOI: 10.3390/ijms24010743.

[53] X. Wang, Y. Li, H. Wei, Z. Yang, R. Luo, Y. Gao, W. Zhang, X. Liu, and L. Sun. "Molecular architecture and gating mechanisms of the Drosophila TRPA1 channel". In: *Cell Discovery* 9.1 (Apr. 2023). DOI: 10.1038/s41421-023-00527-1.

[54] J. B. Fournier. "Nontopological Saddle-Splay and Curvature Instabilities from Anisotropic Membrane Inclusions". In: *Phys. Rev. Lett.* 76 (23 June 1996), pp. 4436–4439. DOI: 10.1103/PhysRevLett.76.4436.

[55] V. Kralj-Iglič, V. Heinrich, S. Svetina, and B. Žekš. "Free energy of closed membrane with anisotropic inclusions". In: *The European Physical Journal B* 10.1 (July 1999), pp. 5–8. DOI: 10.1007/s100510050822.

[56] M. Fošnarič, K. Bohinc, D. R. Gauger, A. Iglič, V. Kralj-Iglič, and S. May. "The Influence of Anisotropic Membrane Inclusions on Curvature Elastic Properties of Lipid Membranes". In: *Journal of Chemical Information and Modeling* 45.6 (Nov. 2005), pp. 1652–1661. DOI: 10.1021/ci050171t.

[57] C. A. Haselwandter and N. S. Wingreen. "The Role of Membrane-Mediated Interactions in the Assembly and Architecture of Chemoreceptor Lattices". In: *PLoS Computational Biology* 10.12 (Dec. 2014). Ed. by J. M. Haugh, e1003932. DOI: 10.1371/journal.pcbi.1003932.

[58] C. A. Haselwandter and R. Phillips. "Directional interactions and cooperativity between mechanosensitive membrane proteins". In: *EPL (Europhysics Letters)* 101.6 (Mar. 2013), p. 68002. DOI: 10.1209/0295-5075/101/68002.

[59] Christoph A. Haselwandter and Rob Phillips. "Connection between Oligomeric State and Gating Characteristics of Mechanosensitive Ion Channels". In: *PLoS Computational Biology* 9.5 (May 2013). Ed. by A. V. Morozov, e1003055. DOI: 10.1371/journal.pcbi.1003055.

[60] O. Kahraman, P. D. Koch, W. S. Klug, and C. A. Haselwandter. "Architecture and Function of Mechanosensitive Membrane Protein Lattices". In: *Scientific Reports* 6.1 (Jan. 2016), p. 19214. DOI: 10.1038/srep19214.

[61] O. Kahraman, W. S. Klug, and C. A. Haselwandter. "Signatures of protein structure in the cooperative gating of mechanosensitive ion channels". In: *EPL (Europhysics Letters)* 107.4 (Aug. 2014), p. 48004. DOI: 10.1209/0295-5075/107/48004.

[62] K. Maeda, Y. Imae, J. I. Shioi, and F. Oosawa. "Effect of temperature on motility and chemotaxis of Escherichia coli". In: *Journal of Bacteriology* 127.3 (Sept. 1976), pp. 1039–1046. DOI: 10.1128/jb.127.3.1039-1046.1976.

[63] H. Salman, A. Zilman, C. Loverdo, M. Jeffroy, and A. Libchaber. "Solitary Modes of Bacterial Culture in a Temperature Gradient". In: *Physical Review Letters* 97.11 (Sept. 2006). DOI: 10.1103/physrevlett.97.118101.

[64] H. Salman and A. Libchaber. "A concentration-dependent switch in the bacterial response to temperature". In: *Nature Cell Biology* 9.9 (Aug. 2007), pp. 1098–1100. DOI: 10.1038/ncb1632.

[65] E. Paster and W. S. Ryu. "The thermal impulse response of *Escherichia coli*". In: *Proceedings of the National Academy of Sciences* 105.14 (Apr. 2008), pp. 5373–5377. DOI: 10.1073/pnas.0709903105.

[66] M. Demir, C. Douarche, A. Yoney, A. Libchaber, and H. Salman. "Effects of population density and chemical environment on the behavior of *Escherichia coli* in shallow temperature gradients". In: *Physical Biology* 8.6 (Nov. 2011), p. 063001. DOI: 10.1088/1478-3975/8/6/063001.

[67] M. Demir and H. Salman. "Bacterial Thermotaxis by Speed Modulation". In: *Biophysical Journal* 103.8 (Oct. 2012), pp. 1683–1690. DOI: 10.1016/j.bpj.2012.09.005.

[68] A. Yoney and H. Salman. "Precision and Variability in Bacterial Temperature Sensing". In: *Biophysical Journal* 108.10 (May 2015), pp. 2427–2436. DOI: 10.1016/j.bpj.2015.04.016.

[69] C.-Y. Yang, M. Erickstad, L. Tadrist, E. Ronan, E. Gutierrez, J. Wong-Ng, and A. Groisman. "Aggregation Temperature of Escherichia coli Depends on Steepness of the Thermal Gradient". In: *Biophysical Journal* 118.11 (June 2020), pp. 2816–2828. DOI: 10.1016/j.bpj.2020.02.033.

[70] P. S. Aguilar, J. E. Cronan, and D. de Mendoza. "A *Bacillus subtilis* Gene Induced by Cold Shock Encodes a Membrane Phospholipid Desaturase". In: *Journal of Bacteriology* 180.8 (Apr. 1998), pp. 2194–2200. DOI: 10.1128/jb.180.8.2194-2200.1998.

[71] P. S. Aguilar, P. Lopez, and D. de Mendoza. "Transcriptional Control of the Low-Temperature-Inducible *des* Gene, Encoding the Δ^5 Desaturase of *Bacillus subtilis*". In: *Journal of Bacteriology* 181.22 (Nov. 1999), pp. 7028–7033. DOI: 10.1128/jb.181.22.7028-7033.1999.

[72] P. S. Aguilar. "Molecular basis of thermosensing: a two-component signal transduction thermometer in Bacillus subtilis". In: *The EMBO Journal* 20.7 (Apr. 2001), pp. 1681–1691. DOI: 10.1093/emboj/20.7.1681.

[73] D. Albanesi, M. C. Mansilla, and D. de Mendoza. "The Membrane Fluidity Sensor *DesK* of *Bacillus subtilis* Controls the Signal Decay of Its Cognate Response Regulator". In: *Journal of Bacteriology* 186.9 (May 2004), pp. 2655–2663. DOI: 10.1128/jb.186.9.2655-2663.2004.

[74] M. C. Mansilla, L. E. Cybulski, D. Albanesi, and D. de Mendoza. "Control of Membrane Lipid Fluidity by Molecular Thermosensors". In: *Journal of Bacteriology* 186.20 (Oct. 2004), pp. 6681–6688. DOI: 10.1128/jb.186.20.6681-6688.2004.

[75] R. J. Rowbury. "Intracellular and Extracellular Components as Bacterial Thermometers, and Early Warning against Thermal Stress". In: *Science Progress* 88.2 (May 2005), pp. 71–99. DOI: 10.3184/003685005783238426.

[76] I. Digel, P. Kayser, and G. M. Artmann. "Molecular Processes in Biological Thermosensation". In: *Journal of Biophysics* 2008 (May 2008), pp. 1–9. DOI: 10.1155/2008/602870.

[77] B. Klinkert and F. Narberhaus. "Microbial thermosensors". In: *Cellular and Molecular Life Sciences* 66.16 (May 2009), pp. 2661–2676. DOI: 10.1007/s00018-009-0041-3.

[78] C. Arrigoni and D. L. Minor. "Global versus local mechanisms of temperature sensing in ion channels". In: *Pflügers Archiv - European Journal of Physiology* 470.5 (Jan. 2018), pp. 733–744. DOI: 10.1007/s00424-017-2102-z.

[79] A. Ramón, A. Esteves, C. Villadóniga, C. Chalar, and S. Castro-Sowinski. "A general overview of the multifactorial adaptation to cold: biochemical mechanisms and strategies". In: *Brazilian Journal of Microbiology* 54.3 (July 2023), pp. 2259–2287. DOI: 10.1007/s42770-023-01057-4.

[80] M. J. Caterina, M. A. Schumacher, M. Tominaga, T. A. Rosen, J. D. Levine, and D. Julius. "The capsaicin receptor: a heat-activated ion channel in the pain pathway". In: *Nature* 389.6653 (Oct. 1997), pp. 816–824. DOI: 10.1038/39807.

[81] M. J. Caterina, T. A. Rosen, M. Tominaga, A. J. Brake, and D. Julius. "A capsaicin-receptor homologue with a high threshold for noxious heat". In: *Nature* 398.6726 (Apr. 1999), pp. 436–441. DOI: 10.1038/18906.

[82] S.-E. Jordt, D. D. McKemy, and D. Julius. "Lessons from peppers and peppermint: the molecular logic of thermosensation". In: *Current Opinion in Neurobiology* 13.4 (Aug. 2003), pp. 487–492. DOI: 10.1016/s0959-4388(03)00101-6.

[83] J. A. Lamas, L. Rueda-Ruzafa, and S. Herrera-Pérez. "Ion Channels and Thermosensitivity: TRP, TREK, or Both?" In: *International Journal of Molecular Sciences* 20.10 (May 2019), p. 2371. DOI: 10.3390/ijms20102371.

[84] L. Rueda-Ruzafa, S. Herrera-Pérez, A. Campos-Ríos, and J. A. Lamas. "Are TREK Channels Temperature Sensors?" In: *Frontiers in Cellular Neuroscience* 15 (Oct. 2021). DOI: 10.3389/fncel.2021.744702.

[85] J. P. Ding and B. G. Pickard. "Modulation of mechanosensitive calcium-selective cation channels by temperature". In: *The Plant Journal* 3.5 (May 1993), pp. 713–720. DOI: 10.1111/j.1365-313x.1993.00713.x.

[86] S. I. Sukharev, P. Blount, B. Martinac, F. R. Blattner, and C. Kung. "A large-conductance mechanosensitive channel in E. coli encoded by mscL alone". In: *Nature* 368.6468 (Mar. 1994), pp. 265–268. DOI: 10.1038/368265a0.

[87] C. C. Häse, A. C. Le Dain, and B. Martinac. "Purification and Functional Reconstitution of the Recombinant Large Mechanosensitive Ion Channel (MscL) of Escherichia coli". In: *Journal of Biological Chemistry* 270.31 (Aug. 1995), pp. 18329–18334. DOI: 10.1074/jbc.270.31.18329.

[88] S. I. Sukharev, W. J. Sigurdson, C. Kung, and F. Sachs. "Energetic and Spatial Parameters for Gating of the Bacterial Large Conductance Mechanosensitive Channel, MscL". In: *The Journal of General Physiology* 113.4 (Apr. 1999), pp. 525–540. DOI: 10.1085/jgp.113.4.525.

[89] S. Sukharev, M. Betanzos, C.-S. Chiang, and H. R. Guy. "The gating mechanism of the large mechanosensitive channel MscL". In: *Nature* 409.6821 (Feb. 2001), pp. 720–724. DOI: 10.1038/35055559.

[90] S. Sukharev. "Purification of the Small Mechanosensitive Channel of Escherichia coli (MscS): the Subunit Structure, Conduction, and Gating Characteristicsin Liposomes". In: *Biophysical Journal* 83.1 (July 2002), pp. 290–298. DOI: 10.1016/s0006-3495(02)75169-2.

[91] E. Perozo, D. M. Cortes, P. Sompornpisut, A. Kloda, and B. Martinac. "Open channel structure of MscL and the gating mechanism of mechanosensitive channels". In: *Nature* 418.6901 (Aug. 2002), pp. 942–948. DOI: 10.1038/nature00992.

[92] T. Rosenbaum and L. D. Islas. "Structure and mechanism in prokaryotic mechanosensitive channels". In: *Current Opinion in Structural Biology* 13.4 (Aug. 2003), pp. 432–442. DOI: 10.1016/s0959-440x(03)00106-4.

[93] V. Belyy, K. Kamaraju, B. Akitake, A. Anishkin, and S. Sukharev. "Adaptive behavior of bacterial mechanosensitive channels is coupled to membrane mechanics". In: *Journal of General Physiology* 135.6 (May 2010), pp. 641–652. DOI: 10.1085/jgp.200910371.

[94] K. S. Ramamurthi. "Signal Transduction: Bacterial Thermometer Works by Measuring Membrane Thickness". In: *Current Biology* 20.17 (Sept. 2010), R707–R709. DOI: 10.1016/j.cub.2010.07.010.

[95] L. E. Cybulski, M. Martín, M. C. Mansilla, A. Fernández, and D. de Mendoza. "Membrane Thickness Cue for Cold Sensing in a Bacterium". In: *Current Biology* 20.17 (Sept. 2010), pp. 1539–1544. DOI: 10.1016/j.cub.2010.06.074.

[96] S. G. Brohawn, E. B. Campbell, and R. MacKinnon. "Physical mechanism for gating and mechanosensitivity of the human TRAAK K+ channel". In: *Nature* 516.7529 (Dec. 2014), pp. 126–130. DOI: 10.1038/nature14013.

[97] S. G. Brohawn, Z. Su, and R. MacKinnon. "Mechanosensitivity is mediated directly by the lipid membrane in TRAAK and TREK1 K+ channels". In: *Proceedings of the National Academy of Sciences* 111.9 (Feb. 2014), pp. 3614–3619. DOI: 10.1073/pnas.1320768111.

[98] E. A. Saita and D. de Mendoza. "Thermosensing via transmembrane protein–lipid interactions". In: *Biochimica et Biophysica Acta (BBA) - Biomembranes* 1848.9 (Sept. 2015), pp. 1757–1764. DOI: 10.1016/j.bbamem.2015.04.005.

[99] E. Saita, D. Albanesi, and D. de Mendoza. "Sensing membrane thickness: Lessons learned from cold stress". In: *Biochimica et Biophysica Acta (BBA) - Molecular and Cell Biology of Lipids* 1861.8 (Aug. 2016), pp. 837–846. DOI: 10.1016/j.bbalip.2016.01.003.

[100] L. E. Cybulski, J. Ballering, A. Moussatova, M. E. Inda, D. B. Vazquez, T. A. Wassenaar, D. de Mendoza, D. P. Tieleman, and J. A. Killian. "Activation of the bacterial thermosensor DesK involves a serine zipper dimerization motif that is modulated by bilayer thickness". In: *Proceedings of the National Academy of Sciences* 112.20 (May 2015), pp. 6353–6358. DOI: 10.1073/pnas.1422446112.

[101]   C. Kung, B. Martinac, and S. Sukharev. "Mechanosensitive Channels in Microbes". In: *Annual Review of Microbiology* 64.1 (Oct. 2010), pp. 313–329. DOI: 10.1146/annurev.micro.112408.134106.

[102]   P. Wiggins and R. Phillips. "Analytic models for mechanotransduction: Gating a mechanosensitive channel". In: *Proceedings of the National Academy of Sciences* 101.12 (Mar. 2004), pp. 4071–4076. DOI: 10.1073/pnas.0307804101.

[103]   S. S. Ranade, R. Syeda, and A. Patapoutian. "Mechanically Activated Ion Channels". In: *Neuron* 87.6 (Sept. 2015), pp. 1162–1179. DOI: 10.1016/j.neuron.2015.08.032.

[104]   A. H. Lewis and J. Grandl. "Mechanical sensitivity of Piezo1 ion channels can be tuned by cellular membrane tension". In: *eLife* 4 (Dec. 2015). DOI: 10.7554/elife.12088.

[105]   C. D. Cox, C. Bae, L. Ziegler, S. Hartley, V. Nikolova-Krstevski, P. R. Rohde, C.-A. Ng, F. Sachs, P. A. Gottlieb, and B. Martinac. "Removal of the mechanoprotective influence of the cytoskeleton reveals PIEZO1 is gated by bilayer tension". In: *Nature Communications* 7.1 (Jan. 2016). DOI: 10.1038/ncomms10366.

[106]   R. Syeda, M. N. Florendo, C. D. Cox, J. M. Kefauver, J. S. Santos, B. Martinac, and A. Patapoutian. "Piezo1 Channels Are Inherently Mechanosensitive". In: *Cell Reports* 17.7 (Nov. 2016), pp. 1739–1746. DOI: 10.1016/j.celrep.2016.10.033.

[107]   C. A. Haselwandter and R. MacKinnon. "Piezo's membrane footprint and its contribution to mechanosensitivity". In: *eLife* 7 (Nov. 2018). DOI: 10.7554/elife.41968.

[108]   W. Zheng, Y. A. Nikolaev, E. O. Gracheva, and S. N. Bagriantsev. "Piezo2 integrates mechanical and thermal cues in vertebrate mechanoreceptors". In: *Proceedings of the National Academy of Sciences* 116.35 (Aug. 2019), pp. 17547–17555. DOI: 10.1073/pnas.1910213116.

[109]   J. M. Kefauver, A. B. Ward, and A. Patapoutian. "Discoveries in structure and physiology of mechanically activated ion channels". In: *Nature* 587.7835 (Nov. 2020), pp. 567–576. DOI: 10.1038/s41586-020-2933-1.

[110]   C. A. Haselwandter, Y. R. Guo, Z. Fu, and R. MacKinnon. "Quantitative prediction and measurement of Piezo's membrane footprint". In: *Proceedings of the National Academy of Sciences* 119.40 (Sept. 2022). DOI: 10.1073/pnas.2208027119.

[111] C. A. Haselwandter, Y. R. Guo, Z. Fu, and R. MacKinnon. "Elastic properties and shape of the Piezo dome underlying its mechanosensory function". In: *Proceedings of the National Academy of Sciences* 119.40 (Sept. 2022). DOI: 10.1073/pnas.2208034119.

[112] G. Vaisey, P. Banerjee, A. J. North, C. A. Haselwandter, and R. MacKinnon. "Piezo1 as a force-through-membrane sensor in red blood cells". In: *eLife* 11 (Dec. 2022). DOI: 10.7554/elife.82621.

[113] E. Sackmann. "Physical Basis of Self-Organization and Function of Membranes: Physics of Vesicles". In: *Handbook of Biological Physics*. Elsevier, 1995, pp. 213–304. DOI: 10.1016/s1383-8121(06)80022-9.

[114] G. Niggemann, M. Kummrow, and W. Helfrich. "The Bending Rigidity of Phosphatidylcholine Bilayers: Dependences on Experimental Method, Sample Cell Sealing and Temperature". In: *Journal de Physique II* 5.3 (Mar. 1995), pp. 413–425. DOI: 10.1051/jp2:1995141.

[115] Z. V. Leonenko, E. Finot, H. Ma, T. E. S. Dahms, and D. T. Cramb. "Investigation of Temperature-Induced Phase Transitions in DOPC and DPPC Phospholipid Bilayers Using Temperature-Controlled Scanning Force Microscopy". In: *Biophysical Journal* 86.6 (June 2004), pp. 3783–3793. DOI: 10.1529/biophysj.103.036681.

[116] J. Pan, S. Tristram-Nagle, N. Kučerka, and J. F. Nagle. "Temperature Dependence of Structure, Bending Rigidity, and Bilayer Interactions of Dioleoylphosphatidylcholine Bilayers". In: *Biophysical Journal* 94.1 (Jan. 2008), pp. 117–124. DOI: 10.1529/biophysj.107.115691.

[117] W. Rawicz, B.A. Smith, T. J. McIntosh, S. A. Simon, and E. Evans. "Elasticity, Strength, and Water Permeability of Bilayers that Contain Raft Microdomain-Forming Lipids". In: *Biophysical Journal* 94.12 (June 2008), pp. 4725–4736. DOI: 10.1529/biophysj.107.121731.

[118] C. Nielsen, M. Goulian, and O. S. Andersen. "Energetics of Inclusion-Induced Bilayer Deformations". In: *Biophysical Journal* 74.4 (Apr. 1998), pp. 1966–1983. DOI: 10.1016/s0006-3495(98)77904-4.

[119] C. Nielsen and O. S. Andersen. "Inclusion-Induced Bilayer Deformations: Effects of Monolayer Equilibrium Curvature". In: *Biophysical Journal* 79.5 (Nov. 2000), pp. 2583–2604. DOI: 10.1016/s0006-3495(00)76498-8.

[120] C. A. Haselwandter, M. Calamai, M. Kardar, A. Triller, and R. A. da Silveira. "Formation and Stability of Synaptic Receptor Domains". In: *Physical Review Letters* 106.23 (June 2011). DOI: 10.1103/physrevlett.106.238104.

[121] C. A. Haselwandter, M. Kardar, A. Triller, and R. A. da Silveira. "Self-assembly and plasticity of synaptic domains through a reaction-diffusion mechanism". In: *Physical Review E* 92.19 (Sept. 2015). DOI: 10.1103/PhysRevE.92.032705.

[122] O. Kahraman, Y. Li, and C. A. Haselwandter. "Stochastic single-molecule dynamics of synaptic membrane protein domains". In: *EPL (Europhysics Letters)* 115.6 (Sept. 2016), p. 68006. DOI: 10.1209/0295-5075/115/68006.

[123] A. Stubenvoll, M. Rice, A. Wietelmann, M. Wheeler, and T. Braun. "Attenuation of Wnt/β-catenin activity reverses enhanced generation of cardiomyocytes and cardiac defects caused by the loss of emerin". In: *Human Molecular Genetics* 24.3 (Sept. 2014), pp. 802–813. DOI: 10.1093/hmg/ddu498.

[124] E. Markiewicz, K. Tilgner, N. Barker, M. van de Wetering, H. Clevers, M. Dorobek, I. Hausmanowa-Petrusewicz, F. C. S. Ramaekers, J. L. V. Broers, W. M. Blankesteijn, G. Salpingidou, R. G. Wilson, J. A. Ellis, and C. J. Hutchison. "The inner nuclear membrane protein Emerin regulates β-catenin activity by restricting its accumulation in the nucleus". In: *The EMBO Journal* 25.14 (July 2006), pp. 3275–3285. DOI: 10.1038/sj.emboj.7601230.

[125] Z. Dedeic, M. Cetera, T. V. Cohen, and J. M. Holaska. "Emerin inhibits Lmo7 binding to the *Pax3* and *MyoD* promoters and expression of myoblast proliferation genes". In: *Journal of Cell Science* 124.10 (May 2011), pp. 1691–1702. DOI: 10.1242/jcs.080259.

[126] J. M. Holaska, S. Rais-Bahrami, and K. L. Wilson. "Lmo7 is an emerin-binding protein that regulates the transcription of emerin and many other muscle-relevant genes". In: *Human Molecular Genetics* 15.23 (Oct. 2006), pp. 3459–3472. DOI: 10.1093/hmg/ddl423.

[127] J. M. Berk, D. N. Simon, C. R. Jenkins-Houk, J. W. Westerbeck, L. M. Grønning-Wang, C. R. Carlson, and K. L. Wilson. "Emerin intermolecular links to emerin and BAF". In: *Journal of Cell Science* (Jan. 2014). DOI: 10.1242/jcs.148247.

[128] I. Herrada, C. Samson, C. Velours, L. Renault, C. Östlund, P. Chervy, D. Puchkov, H. J. Worman, B. Buendia, and S. Zinn-Justin. "Muscular Dystrophy Mutations Impair the Nuclear Envelope Emerin Self-assembly Properties". In: *ACS Chemical Biology* 10.12 (Oct. 2015), pp. 2733–2742. DOI: 10.1021/acschembio.5b00648.

[129] J. M. Berk, S. Maitra, A. W. Dawdy, J. Shabanowitz, D. F. Hunt, and K. L. Wilson. "O-Linked β-N-Acetylglucosamine (O-GlcNAc) Regulates Emerin Binding to Barrier to Autointegration Factor (BAF) in a Chromatin- and Lamin B-enriched "Niche"". In: *Journal of Biological Chemistry* 288.42 (Oct. 2013), pp. 30192–30209. DOI: 10.1074/jbc.m113.503060.

[130] J. M. K. Mislow, J. M. Holaska, M. S. Kim, K. K. Lee, M. Segura-Totten, K. L. Wilson, and E. M. McNally. "Nesprin-1α self-associates and binds directly to emerin and lamin A in vitro". In: *FEBS Letters* 525.1-3 (July 2002), pp. 135–140. DOI: 10.1016/s0014-5793(02)03105-8.

[131] J. M. Berk, K. E. Tifft, and K. L. Wilson. "The nuclear envelope LEM-domain protein emerin". In: *Nucleus* 4.4 (July 2013), pp. 298–314. DOI: 10.4161/nucl.25751.

[132] L. Clements, S. Manilal, D. R. Love, and G. E. Morris. "Direct Interaction between Emerin and Lamin A". In: *Biochemical and Biophysical Research Communications* 267.3 (Jan. 2000), pp. 709–714. DOI: 10.1006/bbrc.1999.2023.

[133] M. Sakaki, H. Koike, N. Takahashi, N. Sasagawa, S. Tomioka, K. Arahata, and S. Ishiura. "Interaction between Emerin and Nuclear Lamins". In: *Journal of Biochemistry* 129.2 (Feb. 2001), pp. 321–327. DOI: 10.1093/oxfordjournals.jbchem.a002860.

[134] E. A. Fairley, J. Kendrick-Jones, and J. A. Ellis. "The Emery-Dreifuss muscular dystrophy phenotype arises from aberrant targeting and binding of emerin at the inner nuclear membrane". In: *Journal of Cell Science* 112.15 (Aug. 1999), pp. 2571–2582. DOI: 10.1242/jcs.112.15.2571.

[135] K. K. Lee, T. Haraguchi, R. S. Lee, T. Koujin, Y. Hiraoka, and K. L. Wilson. "Distinct functional domains in emerin bind lamin A and DNA-bridging protein BAF". In: *Journal of Cell Science* 114.24 (Dec. 2001), pp. 4567–4573. DOI: 10.1242/jcs.114.24.4567.

[136] F. Haque, D. Mazzeo, J. T. Patel, D. T. Smallwood, J. A. Ellis, C. M. Shanahan, and S. Shackleton. "Mammalian SUN Protein Interaction Networks at the Inner Nuclear Membrane and Their Role in Laminopathy Disease Processes". In: *Journal of Biological Chemistry* 285.5 (Jan. 2010), pp. 3487–3498. DOI: 10.1074/jbc.m109.071910.

[137] R. C. Roberts, A. J. Sutherland-Smith, M. A. Wheeler, O. N. Jensen, L. J. Emerson, I. I. Spiliotis, C. G. Tate, J. Kendrick-Jones, and J. A. Ellis. "The Emery-Dreifuss muscular dystrophy associated-protein emerin is phosphorylated on serine 49 by protein kinase A". In: *FEBS Journal* 273.19 (Oct. 2006), pp. 4562–4575. DOI: 10.1111/j.1742-4658.2006.05464.x.

[138]   C. Guilluy, L. D. Osborne, L. Van Landeghem, L. Sharek, R. Superfine, R. Garcia-Mata, and K. Burridge. "Isolated nuclei adapt to force and reveal a mechanotransduction pathway in the nucleus". In: *Nature Cell Biology* 16.4 (Mar. 2014), pp. 376–381. DOI: 10.1038/ncb2927.

[139]   Y. Hirano, M. Segawa, F. S. Ouchi, Y. Yamakawa, K. Furukawa, K. Takeyasu, and T. Horigome. "Dissociation of Emerin from Barrier-to-autointegration Factor Is Regulated through Mitotic Phosphorylation of Emerin in a Xenopus Egg Cell-free System". In: *Journal of Biological Chemistry* 280.48 (Dec. 2005), pp. 39925–39933. DOI: 10.1074/jbc.m503214200.

[140]   A. M. Turing. "The chemical basis of morphogenesis". In: *Philosophical Transactions of the Royal Society of London. Series B, Biological Sciences* 237.641 (Aug. 1952), pp. 37–72. DOI: 10.1098/rstb.1952.0012.

[141]   M. C. Cross and P. C. Hohenberg. "Pattern formation outside of equilibrium". In: *Reviews of Modern Physics* 65.3 (July 1993), pp. 851–1112. DOI: 10.1103/revmodphys.65.851.

[142]   H. Meinhardt. *Models of Biological Pattern Formation (Academic Press, London, 1982)*. May 1982.

[143]   D. Walgraef. *Spatio-Temporal Pattern Formation*. Springer New York, 1997. DOI: 10.1007/978-1-4612-1850-0.

[144]   I. R. Epstein and J. A. Pojman. *An Introduction to Nonlinear Chemical Dynamics*. Oxford University Press, Nov. 1998. DOI: 10.1093/oso/9780195096705.001.0001.

[145]   K. D. Polyzos. "Detection and recognition of aerial targets via RADAR data processing, machine learning techniques and neural networks". PhD thesis. Feb. 2019.

[146]   L. R. Forrest. "Structural symmetry in membrane proteins". In: *Ann. Rev. Biophys.* 44 (June 2015), pp. 311–337. DOI: 10.1146/annurev-biophys-051013-023008.

[147]   T. M. Suchyna, S. E. Tape, R. E. Koeppe, O. S. Andersen, F. Sachs, and P. A. Gottlieb. "Bilayer-dependent inhibition of mechanosensitive channels by neuroactive peptide enantiomers". In: *Nature* 430.6996 (July 2004), pp. 235–240. DOI: 10.1038/nature02743.

[148]   N. Mobashery, C. Nielsen, and O. S. Andersen. "The conformational preference of gramicidin channels is a function of lipid bilayer thickness". In: *FEBS Lett.* 412.1 (Nov. 1997), pp. 15–20. DOI: 10.1016/s0014-5793(97)00709-6.

[149] J. Yuan, F. Jin, T. Glatter, and V. Sourjik. "Osmosensing by the bacterial PhoQ/PhoP two-component system". In: *Proc. Natl. Acad. Sci. U. S. A.* 114.50 (Dec. 2017), E10792–E10798. DOI: 10.1073/pnas.1717272114.

[150] U. Seifert. "Configurations of fluid membranes and vesicles". In: *Advances in Physics* 46.1 (Feb. 1997), pp. 13–137. DOI: 10.1080/00018739700101488.

[151] S. Safran. *Statistical Thermodynamics of Surfaces, Interfaces, and Membranes*. Boulder: Westview Press, 2003. DOI: 10.1201/9780429497131.

[152] D. Boal. *Mechanics of the Cell*. Cambridge University Press, 2012. DOI: 10.1017/CBO9781139022217.

[153] M. Goulian, R. Bruinsma, and P. Pincus. "Long-range forces in heterogeneous fluid membranes". In: *Europhys. Lett.* 22.2 (Apr. 1993), pp. 145–150. DOI: 10.1209/0295-5075/22/2/012.

[154] T. R. Weikl, M. M. Kozlov, and W. Helfrich. "Interaction of conical membrane inclusions: Effect of lateral tension". In: *Physical Review E* 57 (6 June 1998), pp. 6988–6995. DOI: 10.1103/physreve.57.6988.

[155] P. Helfrich and E. Jakobsson. "Calculation of deformation energies and conformations in lipid membranes containing gramicidin channels". In: *Biophysical Journal* 57.5 (May 1990), pp. 1075–1084. DOI: 10.1016/s0006-3495(90)82625-4.

[156] A. Ring. "Gramicidin channel-induced lipid membrane deformation energy: influence of chain length and boundary conditions". In: *Biochimica et Biophysica Acta (BBA) - Biomembranes* 1278.2 (Jan. 1996), pp. 147–159. DOI: 10.1016/0005-2736(95)00220-0.

[157] Y. Jiang, B. Thienpont, V. Sapuru, R. K. Hite, J. S. Dittman, J. N. Sturgis, and S. Scheuring. "Membrane-mediated protein interactions drive membrane protein organization". In: *Nat. Commun.* 13.1 (Nov. 2022), pp. 1–14.

[158] V. Kralj-Iglič, S. Svetina, and B. Žekž. "Shapes of bilayer vesicles with membrane embedded molecules". In: *European Biophysics Journal* 24.5 (Sept. 1996), pp. 311–321. DOI: 10.1007/bf00180372.

[159] W. Helfrich and J. Prost. "Intrinsic bending force in anisotropic membranes made of chiral molecules". In: *Phys. Rev. A* 38 (6 Sept. 1988), pp. 3065–3068. DOI: 10.1103/PhysRevA.38.3065.

[160] S. May, Y. Kozlovsky, A. Ben-Shaul, and M. M. Kozlov. "Tilt modulus of a lipid monolayer". In: *The European Physical Journal E* 14.3 (July 2004), pp. 299–308. DOI: 10.1140/epje/i2004\textendash10019\textendashy.

[161] K. Bohinc, V. Kralj-Iglič, and S. May. "Interaction between two cylindrical inclusions in a symmetric lipid bilayer". In: *The Journal of Chemical Physics* 119.14 (Oct. 2003), pp. 7435–7444. DOI: 10.1063/1.1607305.

[162] A. Shrestha, O. Kahraman, and C. A. Haselwandter. "Regulation of membrane proteins through local heterogeneity in lipid bilayer thickness". In: *Physical Review E* 102.6 (Dec. 2020). DOI: 10.1103/physreve.102.060401.

[163] M. Abramowitz and I. A. Stegun. *Handbook of Mathematical Functions with Formulas, Graphs, and Mathematical Tables*. ninth Dover printing, tenth GPO printing. New York City: Dover, 1964.

[164] R. Courant and D. Hilbert. *Methods of Mathematical Physics*. New York: Interscience Publishers Inc., 1953. DOI: 10.1002/9783527617210.

[165] B. van Brunt. *The Calculus of Variations*. Springer, New York, 2004. DOI: 10.1007/b97436.

[166] D. E. Elmore and D. A. Dougherty. "Investigating Lipid Composition Effects on the Mechanosensitive Channel of Large Conductance (MscL) Using Molecular Dynamics Simulations". In: *Biophysical Journal* 85.3 (Sept. 2003), pp. 1512–1524. DOI: 10.1016/s0006-3495(03)74584-6.

[167] D. A. Doyle. "The Structure of the Potassium Channel: Molecular Basis of K+ Conduction and Selectivity". In: *Science* 280.5360 (Apr. 1998), pp. 69–77. DOI: 10.1126/science.280.5360.69.

[168] S. Sukharev, S. R. Durell, and H. R. Guy. "Structural Models of the MscL Gating Mechanism". In: *Biophysical Journal* 81.2 (Aug. 2001), pp. 917–936. DOI: 10.1016/s0006-3495(01)75751-7.

[169] U. Bernchou, J. Brewer, H. S. Midtiby, J. H. Ipsen, L. A. Bagatolli, and A. C. Simonsen. "Texture of Lipid Bilayer Domains". In: *Journal of the American Chemical Society* 131.40 (Oct. 2009), pp. 14130–14131. DOI: 10.1021/ja903375m.

[170] S. May and A. Ben-Shaul. "A molecular model for lipid-mediated interaction between proteins in membranes". In: *Phys. Chem. Chem. Phys.* 2 (20 Aug. 2000), pp. 4494–4502. DOI: 10.1039/B003570J.

[171] Z. Liu, C. S. Gandhi, and D. C. Rees. "Structure of a tetrameric MscL in an expanded intermediate state". In: *Nature* 461 (Sept. 2009), pp. 120–124. DOI: 10.1038/nature08277.

[172] A. Robert. "Fourier Series of Polygons". In: *The American Mathematical Monthly* 101.5 (May 1994), pp. 420–428. DOI: 10.1080/00029890.1994.11996967.

[173] K. Atkinson. *An introduction to numerical analysis*. New York: Wiley, 1988. ISBN: 0471624896.

[174] L. Trefethen. *Numerical linear algebra*. Philadelphia: Society for Industrial and Applied Mathematics, 1997. ISBN: 0898713617.

[175] F. Johansson. "Arb: efficient arbitrary-precision midpoint-radius interval arithmetic". In: *IEEE Transactions on Computers* 66 (8 2017), pp. 1281–1292. DOI: 10.1109/TC.2017.2690633.

[176] MATLAB. *(R2021a)*. Natick, Massachusetts: The MathWorks, Inc., 2021.

[177] L. Dagum and R. Menon. "OpenMP: an industry standard API for shared-memory programming". In: *Computational Science & Engineering, IEEE* 5.1 (1998), pp. 46–55.

[178] T. A. Harroun, W. T. Heller, T. M. Weiss, L. Yang, and H. W. Huang. "Experimental evidence for hydrophobic matching and membrane-mediated interactions in lipid bilayers containing gramicidin". In: *Biophys. J.* 76.2 (Feb. 1999), pp. 937–945.

[179] R. L. Goforth, A. K. Chi, D. V. Greathouse, L. L. Providence, R. E. Koeppe II, and O. S. Andersen. "Hydrophobic coupling of lipid bilayer energetics to channel function". In: *J. Gen. Physiol.* 121.5 (May 2003), pp. 477–493.

[180] A. V. Botelho, T. Huber, T. P. Sakmar, and M. F. Brown. "Curvature and hydrophobic forces drive oligomerization and modulate activity of rhodopsin in membranes". In: *Biophys. J.* 91.12 (Dec. 2006), pp. 4464–4477.

[181] S. L. Grage, A. M. Keleshian, T. Turdzeladze, A. R. Battle, W. C. Tay, R. P. May, S. A. Holt, S. A. Contera, M. Haertlein, M. Moulin, P. Pal, P. R. Rohde, T. V. Forsyth, A. Watts, K. C. Huang, A. S. Ulrich, and B. Martinac. "Bilayer-mediated clustering and functional interaction of MscL channels". In: *Biophys. J.* 100.5 (Mar. 2011), pp. 1252–1260.

[182] D. Milovanovic, A. Honigmann, S. Koike, F. Göttfert, G. Pähler, M. Junius, S. Müller, U. Diederichsen, A. Janshoff, H. Grubmüller, H. J. Risselada, C. Eggeling, S. W. Hell, G. van den Bogaart, and R. Jahn. "Hydrophobic mismatch sorts SNARE proteins into distinct membrane domains". In: *Nat. Comm.* 6 (Jan. 2015), p. 5984.

[183] A. M. Pollard and V. Sourjik. "Transmembrane region of bacterial chemoreceptor is capable of promoting protein clustering". In: *J. Biol. Chem.* 293.6 (Feb. 2018), pp. 2149–2158.

[184]   D. Krepkiy, M. Mihailescu, J. A. Freites, E. V. Schow, D. L. Worcester, K. Gawrisch, D. J. Tobias, S. H. White, and K. J. Swartz. "Structure and hydration of membranes embedded with voltage-sensing domains". In: *Nature* 462.7272 (Nov. 2009), pp. 473–479. DOI: 10.1038/nature08542.

[185]   Y. Sonntag, M. Musgaard, C. Olesen, B. Schiøtt, J. V. Møller, P. Nissen, and L. Thøgersen. "Mutual adaptation of a membrane protein and its lipid bilayer during conformational changes". In: *Nature Communications* 2.1 (May 2011), p. 304. DOI: 10.1038/ncomms1307.

[186]   S. Marčelja. "Lipid-mediated protein interaction in membranes". In: *Biochimica et Biophysica Acta (BBA) - Biomembranes* 455.1 (Nov. 1976), pp. 1–7. ISSN: 0005–2736. DOI: https://doi.org/10.1016/0005\textendash2736(76)90149\textendash8.

[187]   P. Laguë, M. J. Zuckermann, and B. Roux. "Lipid-Mediated Interactions between Intrinsic Membrane Proteins: Dependence on Protein Size and Lipid Composition". In: *Biophysical Journal* 81.1 (July 2001), pp. 276–284. ISSN: 0006–3495. DOI: https://doi.org/10.1016/S0006\textendash3495(01)75698\textendash6.

[188]   K. Bohinc, A. Iglič, and S. May. "Self-assembly of linear aggregates on curved membranes". In: *Europhysics Letters* 71.1 (May 2005), p. 145. DOI: 10.1209/epl/i2004\textendash10528\textendash3.

[189]   V.S. Markin. "Lateral organization of membranes and cell shapes". In: *Biophysical Journal* 36.1 (Oct. 1981), pp. 1–19. ISSN: 0006–3495. DOI: https://doi.org/10.1016/S0006\textendash3495(81)84713\textendash3.

[190]   S. Svetina B. Božič V. Kralj-Iglič. "Coupling between vesicle shape and lateral distribution of mobile membrane inclusions". In: *Phys. Rev. E* 73 (4 Apr. 2006), p. 041915. DOI: 10.1103/PhysRevE.73.041915.

[191]   O. Kahraman and C. A. Haselwandter. "Thermodynamic competition between membrane protein oligomeric states". In: *EPL* 116.2 (Nov. 2016), p. 28005. DOI: 10.1209/0295-5075/116/28005.

[192]   R. Rusinova, C. He, and O. S. Andersen. "Mechanisms underlying drug-mediated regulation of membrane protein function". In: *Proc. Natl. Acad. Sci.* 118.46 (Nov. 2021), e2113229118. DOI: 10.1073/pnas.2113229118.

[193]   A.-F. Bitbol, D. Constantin, and J.-B. Fournier. "Bilayer Elasticity at the Nanoscale: The Need for New Terms". In: *PLoS ONE* 7.11 (Nov. 2012). Ed. by H. W. van Veen, e48306. DOI: 10.1371/journal.pone.0048306.

[194] K. Mitra, I. Ubarretxena-Belandia, T. Taguchi, G. Warren, and D. M. Engelman. "Modulation of the bilayer thickness of exocytic pathway membranes by membrane proteins rather than cholesterol". In: *Proceedings of the National Academy of Sciences* 101.12 (Mar. 2004), pp. 4083–4088. DOI: 10.1073/pnas.0307332101.

[195] D. E. Clapham and C. Miller. "A thermodynamic framework for understanding temperature sensing by transient receptor potential (TRP) channels". In: *Proceedings of the National Academy of Sciences* 108.49 (Nov. 2011), pp. 19492–19497. DOI: 10.1073/pnas.1117485108.

[196] B. Liu, K. Hui, and F. Qin. "Thermodynamics of Heat Activation of Single Capsaicin Ion Channels VR1". In: *Biophysical Journal* 85.5 (Nov. 2003), pp. 2988–3006. DOI: 10.1016/s0006-3495(03)74719-5.

[197] J. Yao, B. Liu, and F. Qin. "Kinetic and Energetic Analysis of Thermally Activated TRPV1 Channels". In: *Biophysical Journal* 99.6 (Sept. 2010), pp. 1743–1753. DOI: 10.1016/j.bpj.2010.07.022.

[198] F. Yang, Y. Cui, K. Wang, and J. Zheng. "Thermosensitive TRP channel pore turret is part of the temperature activation pathway". In: *Proceedings of the National Academy of Sciences* 107.15 (Mar. 2010), pp. 7083–7088. DOI: 10.1073/pnas.1000357107.

[199] S. E. Kim, A. Patapoutian, and J. Grandl. "Single Residues in the Outer Pore of TRPV1 and TRPV3 Have Temperature-Dependent Conformations". In: *PLoS ONE* 8.3 (Mar. 2013). Ed. by S. A. Simon, e59593. DOI: 10.1371/journal.pone.0059593.

[200] B. Liu and F. Qin. "Single-residue molecular switch for high-temperature dependence of vanilloid receptor TRPV3". In: *Proceedings of the National Academy of Sciences* 114.7 (Feb. 2017), pp. 1589–1594. DOI: 10.1073/pnas.1615304114.

[201] A. Sánchez-Moreno, E. Guevara-Hernández, R. Contreras-Cervera, G. Rangel-Yescas, E. Ladrón-de-Guevara, T. Rosenbaum, and L. D. Islas. "Irreversible temperature gating in trpv1 sheds light on channel activation". In: *eLife* 7 (June 2018). DOI: 10.7554/elife.36372.

[202] A. K. Singh, L. L. McGoldrick, L. Demirkhanyan, M. Leslie, E. Zakharian, and A. I. Sobolevsky. "Structural basis of temperature sensation by the TRP channel TRPV3". In: *Nature Structural & Molecular Biology* 26.11 (Oct. 2019), pp. 994–998. DOI: 10.1038/s41594-019-0318-7.

[203] M. Kim, N. J. Sisco, J. K. Hilton, C. M. Montano, M. A. Castro, B. R. Cherry, M. Levitus, and W. D. Van Horn. "Evidence that the TRPV1 S1-S4 membrane domain contributes to thermosensing". In: *Nature Communications* 11.1 (Aug. 2020). DOI: 10.1038/s41467-020-18026-2.

[204] I. Díaz-Franulic, N. Raddatz, K. Castillo, F. D. González-Nilo, and R. Latorre. "A folding reaction at the C-terminal domain drives temperature sensing in TRPM8 channels". In: *Proceedings of the National Academy of Sciences* 117.33 (Aug. 2020), pp. 20298–20304. DOI: 10.1073/pnas.2004303117.

[205] B. Liu and F. Qin. "Identification of a helix–turn–helix motif for high temperature dependence of vanilloid receptor TRPV2". In: *The Journal of Physiology* 599.21 (Oct. 2021), pp. 4831–4844. DOI: 10.1113/jp282073.

[206] A. Mugo, R. Chou, F. Chin, B. Liu, Q.-X. Jiang, and F. Qin. "A suicidal mechanism for the exquisite temperature sensitivity of TRPV1". In: *Proceedings of the National Academy of Sciences* 120.36 (Aug. 2023). DOI: 10.1073/pnas.2300305120.

[207] J. Adler. "Chemotaxis in Bacteria". In: *Annual Review of Biochemistry* 44.1 (June 1975), pp. 341–356. DOI: 10.1146/annurev.bi.44.070175.002013.

[208] W. Wang and S.-H. Kim. "Chemotaxis Receptor in Bacteria". In: *Handbook of Cell Signaling*. Elsevier, 2010, pp. 195–200. DOI: 10.1016/b978-0-12-374145-5.00029-2.

[209] T. S. Shimizu, Y. Tu, and H. C. Berg. "A modular gradient-sensing network for chemotaxis in Escherichia coli revealed by responses to time-varying stimuli". In: *Molecular Systems Biology* 6.1 (Jan. 2010), p. 382. DOI: 10.1038/msb.2010.37.

[210] B. Hu and Y. Tu. "Precision Sensing by Two Opposing Gradient Sensors: How Does Escherichia coli Find its Preferred pH Level?" In: *Biophysical Journal* 105.1 (July 2013), pp. 276–285. DOI: 10.1016/j.bpj.2013.04.054.

[211] K. J. Watts, A. Vaknin, C. Fuqua, and B. I. Kazmierczak. "New Twists and Turns in Bacterial Locomotion and Signal Transduction". In: *Journal of Bacteriology* 201.20 (Oct. 2019). Ed. by A. M. Stock. DOI: 10.1128/jb.00439-19.

[212] K. Hadjidemetriou, S. K., C. K. Cassidy, and P. Zhang. "Mechanisms of *E. coli* chemotaxis signaling pathways visualized using cryoET and computational approaches". In: *Biochemical Society Transactions* 50.6 (Nov. 2022), pp. 1595–1605. DOI: 10.1042/bst20220191.

[213] T. Boldog and G. L. Hazelbauer. "Accessibility of introduced cysteines in chemoreceptor transmembrane helices reveals boundaries interior to bracketing charged residues". In: *Protein Science* 13.6 (June 2004), pp. 1466–1475. DOI: 10.1110/ps.04648604.

[214] A. M. Powl, J. M. East, and A. G. Lee. "Lipid-Protein Interactions Studied by Introduction of a Tryptophan Residue: The Mechanosensitive Channel MscL". In: *Biochemistry* 42.48 (Nov. 2003), pp. 14306–14317. DOI: 10.1021/bi034995k.

[215] B. Coste, J. Mathur, M. Schmidt, T. J. Earley, S. Ranade, M. J. Petrus, A. E. Dubin, and A. Patapoutian. "Piezo1 and Piezo2 Are Essential Components of Distinct Mechanically Activated Cation Channels". In: *Science* 330.6000 (Oct. 2010), pp. 55–60. DOI: 10.1126/science.1193270.

[216] S. S. Ranade, Z. Qiu, S.-H. Woo, S. S. Hur, S. E. Murthy, S. M. Cahalan, J. Xu, J. Mathur, M. Bandell, B. Coste, Y.-S. J. Li, S. Chien, and A. Patapoutian. "Piezo1, a mechanically activated ion channel, is required for vascular development in mice". In: *Proceedings of the National Academy of Sciences* 111.28 (June 2014), pp. 10347–10352. DOI: 10.1073/pnas.1409233111.

[217] S. P. Wang, R. Chennupati, H. Kaur, A. Iring, N. Wettschureck, and S. Offermanns. "Endothelial cation channel PIEZO1 controls blood pressure by mediating flow-induced ATP release". In: *Journal of Clinical Investigation* 126.12 (Oct. 2016), pp. 4527–4536. DOI: 10.1172/jci87343.

[218] Y.-C. Lin, Y. R. Guo, A. Miyagi, J. Levring, R. MacKinnon, and S. Scheuring. "Force-induced conformational changes in PIEZO1". In: *Nature* 573.7773 (Aug. 2019), pp. 230–234. DOI: 10.1038/s41586-019-1499-2.

[219] K. B. Raper. "Pseudoplasmodium formation and organization in Dictyostelium discoideum". In: *Journal of the Elisha Mitchell Scientific Society* 56.2 (Dec. 1940), pp. 241–282. URL: https://www.jstor.org/stable/24333970.

[220] J. T. Bonner, W. W. Clarke, C. L. Neely, and M. K. Slifkin. "The orientation to light and the extermely sensitive orientation to temperature gradients in the slime mold Dictyostelium discoideum". In: *Journal of Cellular and Comparative Physiology* 36.2 (Oct. 1950), pp. 149–158. DOI: 10.1002/jcp.1030360203.

[221] K. L. Poff and M. Skokut. "Thermotaxis by pseudoplasmodia of Dictyostelium discoideum." In: *Proceedings of the National Academy of Sciences* 74.5 (May 1977), pp. 2007–2010. DOI: 10.1073/pnas.74.5.2007.

[222] T. Mizuno and Y. Imae. "Conditional inversion of the thermoresponse in Escherichia coli". In: *Journal of Bacteriology* 159.1 (July 1984), pp. 360–367. DOI: 10.1128/jb.159.1.360-367.1984.

[223] A. Bahat and M. Eisenbach. "Sperm thermotaxis". In: *Molecular and Cellular Endocrinology* 252.1-2 (June 2006), pp. 115–119. DOI: 10.1016/j.mce.2006.03.027.

[224] S. Nishiyama, T. Umemura, T. Nara, M. Homma, and I. Kawagishi. "Conversion of a bacterial warm sensor to a cold sensor by methylation of a single residue in the presence of an attractant". In: *Molecular Microbiology* 32.2 (Apr. 1999), pp. 357–365. DOI: 10.1046/j.1365-2958.1999.01355.x.

[225] J. F. Doerner, S. Febvay, and D. E. Clapham. "Controlled delivery of bioactive molecules into live cells using the bacterial mechanosensitive channel MscL". In: *Nature Communications* 3.1 (Aug. 2012). DOI: 10.1038/ncomms1999.

[226] L. O. Romero, A. E. Massey, A. D. Mata-Daboin, F. J. Sierra-Valdez, S. C. Chauhan, J. F. Cordero-Morales, and V. Vásquez. "Dietary fatty acids fine-tune Piezo1 mechanical response". In: *Nature Communications* 10.1 (Mar. 2019). DOI: 10.1038/s41467-019-09055-7.

[227] Y. Li, O. Kahraman, and C. A. Haselwandter. "Distribution of randomly diffusing particles in inhomogeneous media". In: *Physical Review E* 96.3 (Sept. 2017). DOI: 10.1103/physreve.96.032139.

[228] J. Bezanson, A. Edelman, S. Karpinski, and V. B. Shah. "Julia: A Fresh Approach to Numerical Computing". In: *SIAM Review* 59.1 (Jan. 2017), pp. 65–98. DOI: 10.1137/141000671.

[229] C. Rackauckas and Q. Nie. "Differential Equations.jl—a performant and feature-rich ecosystem for solving differential equations in Julia". In: *Journal of Open Research Software* 5.1 (2017). DOI: 10.5334/jors.151.

[230] F. Pinaud. personal communication. May 9, 2023.

[231] T. Butler and N. Goldenfeld. "Robust ecological pattern formation induced by demographic noise". In: *Physical Review E* 80.3 (Sept. 2009). DOI: 10.1103/physreve.80.030902.

[232] I. Holt, L. Clements, S. Manilal, and G. E. Morris. "How Does a g993t Mutation in the Emerin Gene Cause Emery–Dreifuss Muscular Dystrophy?" In: *Biochemical and Biophysical Research Communications* 287.5 (Oct. 2001), pp. 1129–1133. DOI: 10.1006/bbrc.2001.5708.

[233] L. Bengtsson and K. L. Wilson. "Multiple and surprising new functions for emerin, a nuclear membrane protein". In: *Current Opinion in Cell Biology* 16.1 (Feb. 2004), pp. 73–79. DOI: 10.1016/j.ceb.2003.11.012.

[234] J. M. Holaska, A. K. Kowalski, and K. L. Wilson. "Emerin Caps the Pointed End of Actin Filaments: Evidence for an Actin Cortical Network at the Nuclear Inner Membrane". In: *PLoS Biology* 2.9 (Aug. 2004). Ed. by M. W. Kirschner, e231. DOI: 10.1371/journal.pbio.0020231.

[235] S. Leibler and D. Andelman. "Ordered and curved meso-structures in membranes and amphiphilic films". In: *J. Phys. France* 48 (Nov. 1987), pp. 2013–2018. DOI: 10.1051/jphys:0198700480110201300.

[236] P. Sens and S. A. Safran. "Inclusions induced phase separation in mixed lipid film". In: *Eur. Phys. J. E* 1 (2 Feb. 2000), pp. 237–248. DOI: 10.1007/s101890050026.

[237] E. Schäffer and U. Thiele. "Dynamic domain formation in membranes: Thickness-modulation-induced phase separation". In: *Eur. Phys. J. E* 14 (June 2004), pp. 169–175. DOI: 10.1140/epje/i2003-10147-x.

[238] S. A. Rautu, G. Rowlands, and M. S. Turner. "Membrane Composition Variation and Underdamped Mechanics near Transmembrane Proteins and Coats". In: *Phys. Rev. Lett.* 114 (9 Mar. 2015), p. 098101. DOI: 10.1103/physrevlett.114.098101.

[239] A. Shrestha, O. Kahraman, and C. A. Haselwandter. "Mechanochemical coupling of lipid organization and protein function through membrane thickness deformations". In: *Phys. Rev. E* 105 (5 May 2022), p. 054410. DOI: 10.1103/PhysRevE.105.054410.

[240] M. P. Bhate, K. S. Molnar, M. Goulian, and W. F. DeGrado. "Signal Transduction in Histidine Kinases: Insights from New Structures". In: *Structure* 23.6 (June 2015), pp. 981–994. DOI: 10.1016/j.str.2015.04.002.

[241] L. A. Abriata, D. Albanesi, M. Dal Peraro, and D. de Mendoza. "Signal Sensing and Transduction by Histidine Kinases as Unveiled through Studies on a Temperature Sensor". In: *Accounts of Chemical Research* 50.6 (May 2017), pp. 1359–1366. DOI: 10.1021/acs.accounts.6b00593.

[242] H. Bang, Y. Kim, and D. Kim. "TREK-2, a New Member of the Mechanosensitive Tandem-pore K$^+$ Channel Family". In: *Journal of Biological Chemistry* 275.23 (June 2000), pp. 17412–17419. DOI: 10.1074/jbc.m000445200.

[243] D. Kang, C. Choe, and D. Kim. "Thermosensitivity of the two-pore domain K$^+$ channels TREK-2 and TRAAK". In: *The Journal of Physiology* 564.1 (Mar. 2005), pp. 103–116. DOI: 10.1113/jphysiol.2004.081059.

[244] V. Viatchenko-Karpinski, J. Ling, and J. G. Gu. "Characterization of temperature-sensitive leak K$^+$ currents and expression of TRAAK, TREK-1, and TREK2 channels in dorsal root ganglion neurons of rats". In: *Molecular Brain* 11.1 (July 2018). DOI: 10.1186/s13041-018-0384-5.

[245] E. Cao, J. F. Cordero-Morales, B. Liu, F. Qin, and D. Julius. "TRPV1 Channels Are Intrinsically Heat Sensitive and Negatively Regulated by Phosphoinositide Lipids". In: *Neuron* 77.4 (Feb. 2013), pp. 667–679. DOI: 10.1016/j.neuron.2012.12.016.

[246] F. Zhang, A. Jara-Oseguera, T.-H. Chang, C. Bae, S. M. Hanson, and
       K. J. Swartz. "Heat activation is intrinsic to the pore domain of TRPV1". In:
       Proceedings of the National Academy of Sciences 115.2 (Dec. 2017). DOI:
       10.1073/pnas.1717192115.

[247] M. Ma and C. A. Haselwandter. "Self-assembly of polyhedral bilayer vesicles from
       Piezo ion channels". In: *Phys. Rev. E* 104 (3 Sept. 2021), p. 034410. DOI:
       10.1103/PhysRevE.104.034410.

[248] Wolfram Research Inc. *Mathematica, Version 12.0*. Champaign, IL, 2019.

Appendices

A Supplemental material for Chapter 2

A.1 Computational implementation of the boundary value method

The general solution for the bilayer thickness deformation field in Eq. (2.20) with Eq. (2.21) involves modified Bessel functions of the second kind, K_n, of any order n [163]. $K_n(x)$ can vary rapidly with x, leading to numerical overflow and large round-off (floating point) errors [173]. These numerical issues are compounded by error propagation in the arithmetic operations necessary for solving the linear system of equations imposing the bilayer-protein boundary conditions in the BVM [173, 174]. In particular, if the values of the matrix $\mathbf{A}$ in Eq. (2.24) vary over many orders of magnitude, which is typically the case for the scenarios considered here, the resulting propagation of floating point errors can be catastrophic. These problems are ameliorated through the APD method, which effectively reduces the number of terms required in the series in Eq. (2.20) with Eq. (2.21), as well as LU decomposition with partial pivoting of $\mathbf{A}$ [173, 174], which reduces the pairing of matrix elements that differ over many orders of magnitude.

We solved the linear system of equations in Eq. (2.24) in C++ using F. Johansson's arbitrary precision library for C/C++, *Arb* [175], which includes built-in functions for LU decomposition with partial pivoting. Importantly, *Arb* also includes Bessel functions with support for complex arguments. The linear system of equations in Eq. (2.24) encompasses $4N + 2$ independent equations. As N is increased in Eq. (2.20) with Eq. (2.21), solving Eq. (2.24) therefore becomes increasingly intensive from a computational perspective. To improve the computational efficiency of our calculations, we use *OpenMP* multi-threading [177] to spread computations across multiple CPU cores.

As discussed in Sec. 2.2, the APD method involves the gap factor Ω in Eq. (2.28), which we optimized so that the boundary error $\eta_{b'} \leq 0.1\%$ in Eq. (2.25) and we obtained changes in G and $\eta_{b'}$ of no more than $10^{-5}\%$ as the numerical precision was increased. A suitable choice for Ω thus allows construction of accurate solutions through Eq. (2.20) with Eq. (2.21) at lower orders N, thus improving the numerical performance of the BVM. For example, Fig. A.1 shows $\eta_{b'}$ as a function of Ω for clover-leaf protein shapes with symmetries $s = 1$ [see Fig. A.1(a)] and $s = 3$ [see Fig. A.1(b)], with constant U and U' along the bilayer-protein interface. The solutions in Fig. A.1 were computed at the indicated orders N in Eq. (2.20) with Eq. (2.21). Figure A.1 illustrates how the optimal gap factor Ω converges with increasing N. For clover-leaf protein shapes we generally find that the optimal Ω increases with increasing ϵ. For the scenarios considered here we also find that, for a given N in Eq. (2.20) with Eq. (2.21) and shape of the protein cross section, the optimal Ω changes only weakly if one allows for variations in U or U' along the bilayer-protein interface.
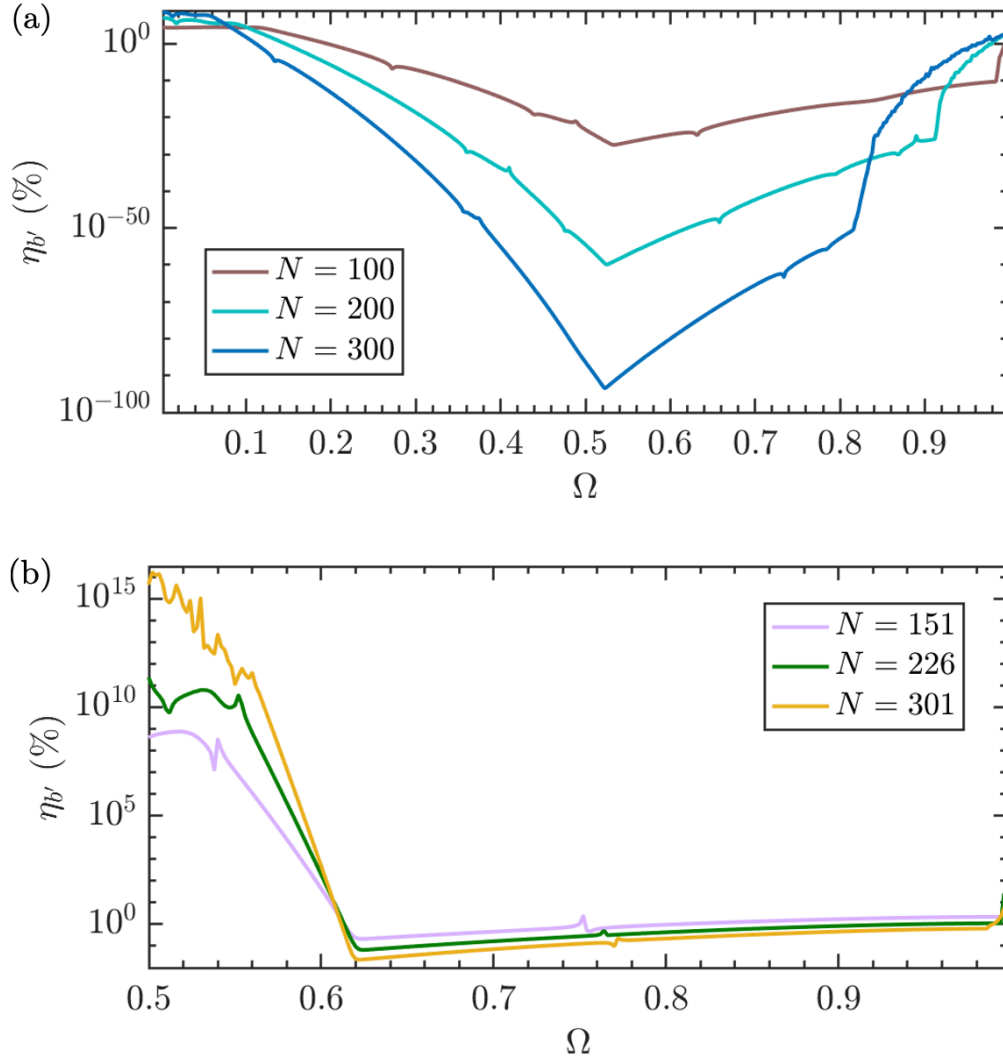
Figure A.1: Boundary error $\eta_{b'}$ in Eq. (2.25) in BVM calculations (see Sec. 2.2) for cloverleaf protein shapes with (a) $s = 1$ and $\epsilon = 0.54$ in Eq. (2.17) and (b) $s = 3$ and $\epsilon = 0.38$ in Eq. (2.17) as a function of the gap factor Ω in Eq. (2.28). We set $R \approx 2.3\,\mathrm{nm}$, $U = 0.3\,\mathrm{nm}$, and $U' = 0$. For ease of comparison we used, for each curve, the indicated, fixed values of N in Eq. (2.20) with Eq. (2.21).

A.2   Numerical precision

For the numerical calculations of the lipid bilayer thickness deformation energy G in Eq. (2.26) presented in this thesis, we generally used numbers with precision (substantially) greater than double precision (64 bits) [175], so as to meet the numerical precision criteria described in Sec. 2.2 with the boundary error $\eta_{b'} \leq 0.1\%$ in Eq. (2.25) and changes

in G and $\eta_{b'}$ of no more than $10^{-5}\%$ as the numerical precision is increased (see also Appendix A.1). However, many programming languages do not have built-in support for numerical precision greater than double precision. To illustrate the extent to which double precision calculations could be used to approximate the BVM results described here, we plot in Fig. A.2 the bilayer thickness deformation energy G [see Fig. A.2(a)] and the corresponding boundary error $\eta_{b'}$ [see Fig. A.2(b)] versus bit precision for several clover-leaf protein symmetries s and the indicated values of ϵ. As described in Appendix A.1, the results in Fig. A.2 were obtained with F. Johansson's arbitrary precision library for C/C++, *Arb* [175]. We have $\eta_{b'} \leq 0.1\%$ in Fig. A.2 as the floating point precision is increased beyond double precision, with changes in G and $\eta_{b'}$ of no more than $10^{-5}\%$. For the clover-leaf protein shapes considered in this thesis, we generally find that numerical precision greater than double precision is required for large s or large ϵ. For the polygonal protein shapes considered in this thesis, we find that a numerical precision greater than double precision is generally required to meet the numerical precision criteria described in Sec. 2.2.
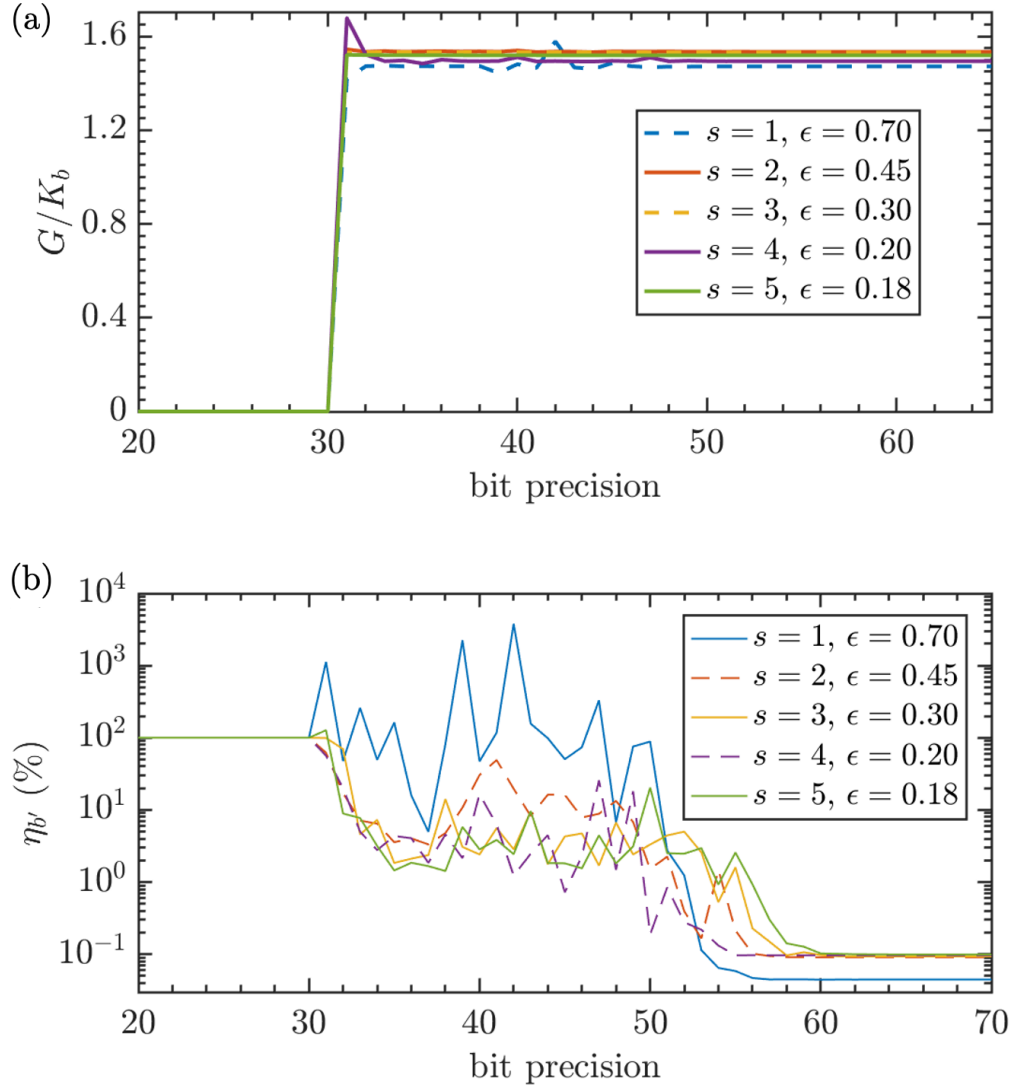
Figure A.2: (a) Lipid bilayer thickness deformation energy G in Eq. (2.26) calculated using the BVM (see Sec. 2.2) and (b) corresponding boundary error $\eta_{b'}$ in Eq. (2.25) for clover-leaf protein shapes as a function of the bit precision employed in the numerical computations. We used the indicated values of s and ϵ in Eq. (2.17), and $R \approx 2.3$ nm, $U = 0.3$ nm, and $U' = 0$. For ease of comparison we used for $s = 1$ the fixed values $N = 20$ in Eq. (2.20) with Eq. (2.21) and $\Omega = 0.726$ in Eq. (2.28), $N = 48$ and $\Omega = 0.62$ for $s = 2$, $N = 72$ and $\Omega = 0.52$ for $s = 3$, $N = 90$ and $\Omega = 0.552$ for $s = 4$, and $N = 125$ and $\Omega = 0.45$ for $s = 5$.

B Supplemental material for Chapter 4

B.1 Axisymmetric bilayer midplane deformations

We assume that, for given bilayer-protein boundary conditions and membrane mechanical properties, the minimum of the bilayer midplane deformation energy [32–34]

$$G = \frac{K_b}{2} \int dA \left(c_1 + c_2 \right)^2 - \tau \Delta A \,, \tag{B.1}$$

with K_b as the lipid bilayer bending rigidity, determines the dominant lipid bilayer shape. We thereby, we assume the bilayer to be asymptotically flat at a large distance away from the bilayer-protein boundary. Equation (B.1) considers the (mean curvature) energy due to bending of the bilayer midplane and the change in its projected in-plane area ΔA under membrane tension τ, where c_1 and c_2 represent the local principal curvatures of the bilayer midplane surface.

Solving the nonlinear shape (Euler-Lagrange) equations for bilayer midplane deformations is, in general, a very challenging mathematical problem. However, if the deformations are axisymmetric, we can reformulate the problem using the arc-length parametrization of surfaces and accurately calculate G in Eq. (B.1). We follow here Refs. [107, 110, 111, 247]. The axial symmetry allows us to parameterize the bilayer midplane shape solely as a function of the arc-length s measured along the midplane deformation profile. The bilayer midplane deformation field $h(s)$ represents the vertical coordinate parallel to the axial line of symmetry (the h-axis), $r(s)$ denotes the radial coordinate perpendicular to the h-axis, and $\psi(s)$ is the angle between the tangent to the bilayer midplane surface and

the r-axis. The assumption of a smooth membrane surface at $s = 0$ yields the following boundary conditions [107, 110, 111, 247]:

$$\psi(0) \equiv \alpha\,, \tag{B.2}$$

$$r(0) \equiv r_0\,, \tag{B.3}$$

and

$$h(0) \equiv h_0\,, \tag{B.4}$$

where r_0, h_0, and α are determined by the shape of the bilayer-protein boundary. The Hamiltonian formalism allows us to derive a set of first-order differential equations whose solutions yield the stationary lipid bilayer shapes. We numerically solved these equations using Mathematica's $FindRoot$ command with a shooting method as described in greater detail in a previous work [247, 248].

C   Supplemental material for Chapter 5

C.1   Molecule distributions in emerin nanodomains from spatially heterogeneous diffusion coefficients

Experimental data on emerin systems under various conditions, including mutations and mechanical stress [12], suggests that emerin cluster at the INM to form stable nanodomains that coincide with regions in diffusion maps with slowed-down diffusion (diffusion coefficient $\nu_{\mathrm{slow}} \approx 3 \times 10^{-4} \mu\mathrm{m}^2/\mathrm{s}$ in wild-type systems under no mechanical stress), while membrane regions outside emerin nanodomains show faster diffusion of emerin (diffusion coefficient $\nu_{\mathrm{fast}} \approx 2 \times 10^{-3} \mu\mathrm{m}^2/\mathrm{s}$ in wild-type systems under no mechanical stress). In particular, for wild type emerin systems under no mechanical stress, 56% of the emerin population at the INM were shown to be fast diffusers. Moreover, local cluster maps of the emerin revealed that emerin nanodomains roughly cover 15% of the INM area and the relative density of emerin inside nanodomains was shown to be about 6. In this appendix we show that, treating the INM as a two-dimensional medium with the observed differences in diffusion coefficients [227], one finds steady state molecular concentrations of emerin inside nanodomains, ρ_{slow}, and their relative densities inside nanodomains, $\langle N_{\mathrm{slow}} \rangle / \langle N_{\mathrm{fast}} \rangle$, at the INM that roughly agree with experiments, at least in the case of mechanically unperturbed wild-type systems.

C.1.1 Free diffusion

If no steric constraints are considered and if the particles do not interact with each other, our system corresponds to standard, "free" diffusion with spatially heterogeneous diffusion coefficients [227]. For now, we will not directly incorporate effects connected to molecular crowding, and focus on the free diffusion of emerin molecules. Starting with the (stochastic) master equation (ME) describing emerin diffusion, we obtained exact analytic solutions of the steady-state distributions of emerin molecules. Solutions of the ME at steady state correspond to zero net molecular fluxes across the nanodomain boundaries. The steady-state solution of our model necessarily corresponds to uniform (average) distributions of molecules inside and outside nanodomains. In particular, our exact analytic solution of the ME shows that, in the steady state of the system, the fraction of emerin molecules inside nanodomains is given by

$$\rho_{\mathrm{slow}} = \left(1 + \frac{\Gamma_{\mathrm{fast}}}{\Gamma_{\mathrm{slow}}}\right)^{-1}, \tag{C.1}$$

where, in free diffusion, Γ_{slow} and Γ_{fast} are the characteristic times randomly diffusing emerin molecules spend inside and outside emerin nanodomains, respectively. Thus, for freely diffusing molecules we have $\Gamma = \mathrm{A}/\nu$, where A is the area of the membrane region characterized by the diffusion coefficient ν. Thus, for our free-diffusion emerin system we have $\rho_{\mathrm{slow}} = \left[1 + (\mathrm{A}_{\mathrm{fast}}/\mathrm{A}_{\mathrm{slow}})/(\nu_{\mathrm{fast}}/\nu_{\mathrm{slow}})\right]^{-1}$ with $\mathrm{A}_{\mathrm{slow}}$ and $\mathrm{A}_{\mathrm{fast}}$ as the total areas of the membrane regions inside and outside nanodomains, respectively. Assuming nanodomains cover 15% of the availabile INM area and the diffusion coefficients are $\nu_{\mathrm{slow}} = 3 \times 10^{-4} \ \mu\mathrm{m}^2/\mathrm{s}$ and $\nu_{\mathrm{fast}} = 2 \times 10^{-3} \ \mu\mathrm{m}^2/\mathrm{s}$, for wild-type emerin systems under

no mechanical stress, Eq. (C.1) yields the steady state fraction of freely diffusing emerin inside nanodomains at the INM $\rho_{\mathrm{slow}} \approx 54\%$. This aligns well with the experimental measurement of 56% [12].

The density of emerin molecules inside nanodomains is $\langle N_{\mathrm{slow}} \rangle = \rho_{\mathrm{slow}} M / \mathrm{A}_{\mathrm{slow}}$, where M is the total number of emerin molecules at the INM. Likewise, the molecular density of emerin outside nanodomains is $\langle N_{\mathrm{fast}} \rangle = \rho_{\mathrm{fast}} M / \mathrm{A}_{\mathrm{fast}}$, with $\rho_{\mathrm{fast}} = 1 - \rho_{\mathrm{slow}}$. So, the relative molecular density of emerin inside nanodomains is

$$\frac{\langle N_{\mathrm{slow}} \rangle}{\langle N_{\mathrm{fast}} \rangle} = \frac{\rho_{\mathrm{slow}}}{\rho_{\mathrm{fast}}} \frac{\mathrm{A}_{\mathrm{fast}}}{\mathrm{A}_{\mathrm{slow}}} \, , \qquad (\mathrm{C.2})$$

Inserting, Eq. (C.1) into Eq. (C.2) and simplifying yields $\langle N_{\mathrm{slow}} \rangle / \langle N_{\mathrm{fast}} \rangle = \nu_{\mathrm{fast}} / \nu_{\mathrm{slow}}$, and so the ME predicts that the relative molecular density of emerin inside emerin nanodomains is governed by the ratio of emerin diffusion coefficients outside to inside emerin nanodomains. For wild type emerin systems under no mechanical stress, this ratio evaluates to about 7 which aligns with the corresponding value of this ratio, ≈ 6, implied by experiments [12].

We also calculated ρ_{slow} and $\langle N_{\mathrm{slow}} \rangle / \langle N_{\mathrm{fast}} \rangle$, using Eqs. (C.1)–(C.2), for wild type emerin systems under mechanical stress, Q133H emerin systems under no mechanical stress, P183H emerin systems under no mechanical stress, and $\Delta 95\text{-}99$ emerin systems under no mechanical stress and mechanical stress, assuming their emerin nanodomains cover 15% of the INM, like wild type emerin systems under no mechanical stress, and using the diffusion coefficients for ν_{slow} and ν_{fast} measured in experiments [12] and summarized in Fig. C.1. We also summarize the results of our free-diffusion model in Fig. C.1.

	WT	WT; force	Q133H	P183H	Δ95-99	Δ95-99; force
ν_{fast} $(\mu\text{m}^2/s)$	2×10⁻³	4×10⁻³	3×10⁻³	1.5×10⁻³	1×10⁻³	6×10⁻³
ν_{slow} $(\mu\text{m}^2/s)$	3×10⁻⁴	6×10⁻⁴	4×10⁻⁴	1×10⁻⁴	1.5×10⁻⁴	3×10⁻⁴
ρ_{slow} $(\%)$	54	54	57	73	54	78
ρ_{slow} $(\%)$	56	46	53	54	46	no data
$\langle N_{\text{slow}}\rangle/\langle N_{\text{fast}}\rangle$	7	7	8	15	null	20
$\langle N_{\text{slow}}\rangle/\langle N_{\text{fast}}\rangle$	6	4	9	2	null	2

▨ data from experiments	▨ parameter estimates
▨ free diffusion model predictions	

Figure C.1: Table comparing experimental data [12] (orange), estimated parameters (blue), free diffusion model predictions (fraction of emerin molecules that are slow diffusers, ρ_{slow}, and relative emerin molecule density inside nanodomains, $\langle N_{\text{slow}}\rangle/\langle N_{\text{fast}}\rangle$) (green) wild-type emerin systems under no mechanical stress ("WT") and mechanical stress ("WT; force"), Q133H and P183H mutant emerin systems under no mechanical stress, and $\Delta 95\text{-}99$ mutant emerin systems under no mechanical stress ("$\Delta 95\text{-}99$") and mechanical stress ("$\Delta 95\text{-}99$; force").

For ρ_{slow}, our predictions roughly agree with experiments for all cases considered. For $\langle N_{\text{slow}}\rangle/\langle N_{\text{fast}}\rangle$, our predictions roughly agree with experiments for wild-type and Q133H emerin systems under no mechanical stress, but our predictions generally fail to describe experiments if mechanical force is applied to the system or if emerin is mutated so as to impair emerin's ability to cluster [12]. when the system in subjected to mechanical stress or mutations which greatly impair emerin's clustering potential [12]. Our results suggest that the deficient clustering potential of these systems is greatly hindered by the alteration in interactions with nuclear binding partners imparted by force and mutations.

Equation (C.1) suggests that the steady-state fractions of emerin molecules concentrated inside nanodomains depend only on the fraction of available INM area covered by nanodomains and on the relative diffusion coefficients inside and outside nanodomains, and are independent of the detailed arrangement and shape of nanodomains [227]. By

construction, our simple model is unable to to predict the self-assembly or size of emerin nandomains, which we address through the reaction-diffusion model described in Chapter [5].

C.1.2   Diffusion in crowded membranes

Our model is readily extended to directly account for steric repulsion arising from the finite size of emerin molecules, in which case the effective diffusion rates also depend on the number of emerin molecules occupying the "target" sites of randomly diffusing emerin molecules. In particular, steric constraints due to the finite size of emerin molecules imply that, locally, the membrane area can only accommodate some finite number of emerin molecules, which is expected to modify the results in Sec. [C.1.1]. To model emerin steric repulsion, we assume that the rates of diffusion processes locally increasing the molecule number are $\propto (1 - N)$, where the field $N(x, y, t)$ is the local fractional INM area covered by emerin molecules. We thereby take $N(x, y, t)$ to be normalized so that $0 \leq N \leq 1$ [227].

Similarly as in Sec. [C.1.1] we directly solved the ME defining our model of diffusion in crowded membranes in the steady state to obtain the steady-state fractions of emerin molecules inside emerin nanodomains, yielding $\Gamma_{\text{slow}} = A_{\text{slow}}/\mu_{\text{slow}}$ and $\Gamma_{\text{fast}} = A_{\text{fast}}/\mu_{\text{fast}}$ [227], where

$$\mu_{\text{fast}} = \frac{-b + (b^2 - 4ac)^{1/2}}{2a} \tag{C.3}$$

and

$$\mu_{\text{slow}} = \left[1 + \frac{\nu_{\text{fast}}}{\nu_{\text{slow}}} \left(\frac{1 - \mu_{\text{fast}}}{\mu_{\text{fast}}} \right) \right]^{-1}, \tag{C.4}$$

with

$$a = -\mathrm{A}_{\mathrm{slow}} \left(\frac{\nu_{\mathrm{fast}} - \nu_{\mathrm{slow}}}{\nu_{\mathrm{fast}} \nu_{\mathrm{slow}}} \right), \; b = \frac{\mathrm{A}_{\mathrm{slow}}}{\nu_{\mathrm{slow}}} + \frac{\mathrm{A}_{\mathrm{fast}}}{\nu_{\mathrm{fast}}} + \langle N \rangle \left(\frac{\nu_{\mathrm{fast}} - \nu_{\mathrm{slow}}}{\nu_{\mathrm{fast}} \nu_{\mathrm{slow}}} \right), \; c = -\frac{\langle N \rangle}{\nu_{\mathrm{slow}}}. \quad \text{(C.5)}$$

We find, as in Sec. C.1.1, that the direct solution of the ME for our system with steric constraints depends on the ratio of membrane area inside and outside emerin nanodomains and on the ratio of the diffusion coefficients measured inside and outside emerin nanodomains, and is independent of detailed emerin nanodomain properties such as the shape or number of emerin nanodomains. Furthermore, as in Sec. C.1.1, the ME describing diffusion in crowded membranes implies, in the steady state, uniform (average) concentrations of emerin inside and outside nanodomains. Importantly, and contrary to the case of free diffusion, the steady-state fractions of emerin inside emerin nanodomains and, consequently, the relative densities of emerin inside emerin nanodomains now depend on the fractional INM area covered by emerin molecules $\langle N \rangle$.

In wild-type emerin systems under no mechanical stress, increasing the fraction of the INM area covered by emerin molecules, in our model, leads to a decrease in the steady-state fractions and relative molecular densities inside emerin nanodomains [Fig. C.2(a,b)]. For example, when $\langle N \rangle = 0.02$, an upper bound suggested by counting experiments [230], $\rho_{\mathrm{slow}} \approx 53\%$ in the steady state, corresponding to $\langle N_{\mathrm{slow}} \rangle / \langle N_{\mathrm{fast}} \rangle \approx 6$. We found similar minor decreases in mutant and mechanically stressed emerin systems.

While incorporation of steric constraints yields somewhat improved agreement between model predictions and experimental observations (see Fig. C.1), we also find that steric constraints only tend to have a minor effect on the emerin distributions at the INM.
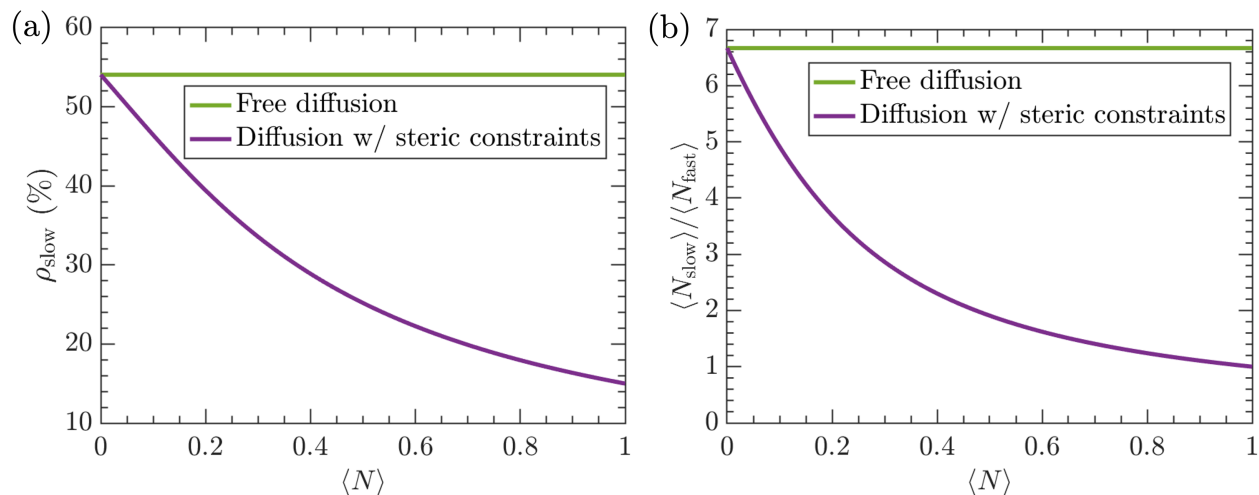
Figure C.2: Diffusion-only models applied to wild-type emerin systems under no mechanical stress. Steady-state (a) fractions of emerin molecules inside emerin nanodomains, ρ_{slow}, and (b) relative densities of emerin molecules inside emerin nanodomains, $\langle N_{\text{slow}} \rangle / \langle N_{\text{fast}} \rangle$, as a function of the global fractional INM area covered by emerin molecules, $\langle N \rangle$, assuming free diffusion (green curves) and diffusion with steric constraints linear in the local fractional INM area covered by emerin molecules N (purple curves). All results were obtained through direct solution of the ME (see Ref. [227]), with the analytical solutions shown in (a) Eq. (C.1) and (b) Eq. (C.2).

In contrast, our reaction-diffusion model requires steric repulsion for the self-assembly and stabilization of emerin nanodomains through a Turing mechanism (see Chapter 5). We also note that, according to the results discussed here, these steric effects alone cannot explain the relatively low molecular densities of emerin within nanodomains seen in experiments of various mutant emerin type systems [12]. This suggests that the observed relative densities of emerin inside and outside emerin nanodomains depend on the interactions of emerin with its nuclear binding partners at the INM. Additionally, emerin's diffusion properties alone cannot explain the characteristic shape, size, and self-assembly of emerin nanodomains, highlighting the necessity of reactions for a more accurate description of these properties.